UNIVERSITY OF NEWCASTLE-UPON-TYNE
DEPARTMENT OF MARINE TECHNOLOGY

DRAG, BOUNDARY-LAYER AND ROUGHNESS CHARACTERISTICS OF MARINE SURFACES COATED WITH ANTIFOULINGS

MAXIM CANDRIES

A Thesis submitted for the degree of Doctor of Philosophy
December 2001

Dedicated to my Parents

Abstract

The overall aim of this investigation is to compare the drag, boundary-layer and roughness characteristics of two state-of-the-art antifoulings: a Tin-free Self-Polishing Co-Polymer (SPC) and a Foul Release silicone elastomer. These coatings are currently the most satisfactory alternatives to Tri-butyl Tin SPC systems which will be banned from application by 2003. This is basically an experimental study with drag, boundary-layer and roughness measurements being carried out in parallel.

Drag measurements of the two different antifoulings have been carried out in three sets of towing tank experiments, of which two involved flat plates of different size and one involved a wave-piercing catamaran model. Both sets of flat plate experiments demonstrate that the frictional resistance is lower for the Foul Release surface than for the tin-free SPC surface. The catamaran model experiments show that the application of the Foul Release system by rollering increases the drag compared to the Tin-free SPC system.

Boundary-layer measurements have been carried out by means of Laser Doppler Velocimetry on a 2.1m long flat plate set-up with a 1m long interchangeable test surface. A significant difference in frictional resistance is observed between the sprayed Foul Release surface and the other two painted surfaces. The ratio of the inner to the outer part of the boundary layer is fractionally smaller for the sprayed Foul Release system than for the two other coated surfaces.

Roughness measurements of the tested surfaces have been carried out both with a stylus instrument and with an optical measurement system. A moving average filter is applied on the measured digital roughness profiles to filter out the long-wavelength waviness of the plates. It is shown that for short cut-off lengths (2.5mm) both the amplitude and texture parameters of the Foul Release are significantly different from the Tin-free SPC coating.

The roughness and drag findings have been correlated by a semi-empirical method which assumes that the coated surfaces obey the Colebrook-White law in the transitional flow regime. A characteristic roughness measure which incorporates both amplitude and texture characteristics of the coated surface is introduced and correlated to the boundary-layer roughness function. The experiments show that from a qualitative point of view a typical application by the same operator of a newly sprayed Foul Release system will result in less added drag than a newly applied Tin-free SPC system.

Acknowledgements

I would like to thank my supervisor Prof. Mehmet Atlar for all his guidance, advice and encouragement throughout this work. It has always been a pleasure and an honour to work under him, and I hope this is reflected in this work.

My sincere gratitude also goes to Dr. Colin Anderson at International Coatings Ltd. for his ceaseless help with this work and for his continuous encouragement.

This research project was funded by EPSRC Research Grant No. 98316366, by International Coatings Ltd and by the Engineering Design Centre at the University of Newcastle-upon-Tyne. The experiments at CEHIPAR were made possible by the European Community programme CEHMAR, which promotes the mobility and opportunities of researchers. The experiments at the Denny Tank were made possible by kind permission of the University of Strathclyde. The roughness measurements were made with the Hull Roughness Analyser of International Coatings Ltd. and with the optical measurement system at the Akzo Nobel Technology Centre.

Throughout this work I have had the good fortune to come in contact with many interesting people and I am indebted to the following people for their help with this work:

- The staff and colleagues at the Department of Marine Technology and at EDC, particularly Mr. Ian Paterson and Mr. Richard Carter.
- The people at International Coatings Ltd., particularly Dr. Catherine McGurk, Ms. Val Horrigan and Ms. Nicola Towns for the application of the paint systems.
- Dr. Trevor Wills at the Akzo Nobel Technology Centre.
- Mr. Sabino Quirros and Mr. Josú Intxaurraga for their superivision of the paint application at CEHIPAR.
- The staff at CEHIPAR, particularly Dr. Jaime Masip, Mr. Antonio Guerrero, Mr. José Maria Riola, Mr. Orencio Lozano, Mr. Ramon Querada, Mr. Luis and Mr. Domingo Bañuelos.
- The technical staff at the Denny Tank, particularly Mr. Charlie Kaye. Dr. Turan of the University of Strathclyde, and Mr. Davies of Aluminium Shipbuilders Ltd.
- Mr. Jaryczewski and Mr. Hassall at Dantec Corp., and Mr. Graham Small for manufacturing the boundary-layer plate.

- Dr. Robert Townsin for his insightful comments and for proof-reading this work.
- The students who carried out experiments in extension to this work, Mr. Pazouki in particular.
- The people at Flowtech International AB, particularly Dr. Carl-Erik Janson, Dr. Leif Broberg, Prof. Lars Larsson and Mr. Michael Leer-Andersen.
- Dr. Stewart Evans, Dr. Andy Birchenough and Dr. Jeremy Thomason at the Department of Marine Sciences.
- Prof. Balachandar at the University of Saskatchewan, Dr. Schultz at the US Naval Academy, Dr. Tachie at the University of Toronto, Prof. Gören and Prof. Odabasi at Istanbul Technical University, Prof Semenov and Dr. Kulik at the Siberian Branch of Russian Academy of Sciences, Dr. Choi at Nottingham University, Prof Escudier at Liverpool University, Prof. Carpenter at Warwick University, Dr. Milne at 3AM Ltd., Dr. Kattan at Safinah, Dr. Bertram at HSVA, Mrs. Otto at WWF Germany and Dr. Wark at the Office of Naval Research. For their comments on the boundary-layer experiments, I am also grateful to Dr. Thornhill at the National Research Council Canada, Dr. Spalart at Boeing, Mr. Poggi at the Polytechnical University of Turin, Mr. Duranti at Computational Dynamics Ltd. and Dr. Martinuzzi at the University of Western Ontario.

Finally, I would like to thank my family and loved ones for their support and encouragement.

Maxim Candries
19 October 2001

Table of contents

Nomenclature

AHR	Average Hull Roughness
B	Breadth (Chapter 3)
B (= 5.0)	Smooth-wall log law constant
B_0	General log law constant
B_1	Hydraulically smooth Colebrook-White constant (see Eq. 4.36)
C	Velocity defect law intercept
C_0	Fully rough flow constant (see Equation 4.35)
C_1	Fully rough Colebrook-White constant (see Equation 4.36)
C_A	ITTC correlation allowance
C_B	Block coefficient
$c_f = 2\tau_w/(\rho U_e^2)$	Local frictional resistance coefficient
$C_F = R_F/(^1/_2\rho S U_e^2)$	Frictional resistance coefficient
$C_{F,ITTC} = 0.075/(\log Re-2)^2$	Frictional resistance coefficient according to the ITTC 1957 model-ship correlation line
C_P	Prismatic coefficient
$C_T = R_T/(^1/_2\rho S U_e^2)$	Total resistance coefficient
C_V	Viscous resistance coefficient
C_{VP}	Viscous pressure resistance coefficient
C_W	Wave-making resistance coefficient
D	Half the number of zero-crossings over the cut-off length
De	Density of extrema
Dz	Density of zero-crossings
E, E_1	Spectral energy
f	Frequency
FD	Fractal Dimension
$Fn = U_e/\sqrt{gL}$	Froude number
G	Clauser's shape parameter
h	A characteristic measure of roughness
$H = \delta_1/\theta$	Shape factor
h'	Musker's roughness parameter
h_s	Sand grain size
k	Form factor (1+k) (Chapter 3)

k, k_1	Wave number
Ku	Kurtosis
L	Length of a plate or ship
L	Evaluation length of a roughness profile (Chapter 6)
L_c	Cut-off length (or long wavelength cut-off)
$L_{c,e}$	Effective cut-off length
L_u, L_v	Streamwise and wall-normal integral length scale
$m = B_1/C_1$	Factor in the Colebrook-White law
m_n	Spectral moments of order n
m_n'	Cumulative spectral moment of order n
m_0(var)	Variance of height distribution
m_2(var)	Variance of slope distribution
m_4(var)	Variance of curvature distribution
n_{mean}	Mean data-rate
p(z)	Probability density
P	Pressure (Chapter 4)
P(ω)	Power spectral density function
$Re = U_e \cdot L/\nu$	Reynolds number of a ship or at the trailing edge of a plate
$Re_x = U_e \cdot x/\nu$	Reynolds number
$Re_{\delta 1} = U_e \cdot \delta_1/\nu$	Displacement thickness Reynolds number
$Re_\theta = U_e \cdot \theta/\nu$	Momentum thickness Reynolds number
Ra	Centre-line average roughness height
Rq	RMS roughness height
RMS	Root Mean Square
Rt	Highest peak to lowest valley height
Rt50	Highest peak to lowest valley roughness height for a 50mm cut-off length
R_T	Total measured resistive force
Rz	Vertical separation of the average of the 5 highest peaks and the average of the 5 lowest valleys
R(τ)	Autocovariance function
S	Wetted surface
S(τ)	Structure function (Chapter 6)
Sa	Mean absolute slope angle
Sk	Skewness
Sq	RMS slope angle
T	Draught
$Tu = \frac{\sqrt{(\overline{u'^2} + \overline{v'^2})/2}}{U_e}$	Free-stream turbulence
U_e	Free-stream velocity
U_τ	Shear velocity
U, V	Average velocity components (streamwise and wall-normal)
u', v'	Instantaneous velocity components
$-\overline{u'v'}$	Reynolds stress (divided by ρ)
w	Wake function

WPA	Water Plane Area
x	Streamwise distance from the leading edge of the plate
y	Normal distance from the wall
z_i	i-th height reading of a surface profile
α, β, ...	Dimensionless roughness parameters (Chapter 4, 7)
$\alpha = m_0 m_4 / m_2^2$	Bandwidth parameter (Chapter 6, 7)
α	Statistical significance level (Chapter 5)
$\alpha(1) = (De/Dz)^2$	Bandwidth parameter via Longuet-Higgins (1957)
$\alpha(2)$	Bandwidth parameter calculated via bandwidth parameters and Fractal Dimension (cf. Chapter 6)
$\alpha(3) = Rq^2 m_4(var) / m_2(var)^2$	Bandwidth parameter calculated with the variances of height, slope and curvature
χ	Nikuradse's form of the roughness function
χ_r	Constant value of Nikuradse's roughness function in the fully rough flow regime
$\delta = \delta_{0.99}$	Boundary-layer thickness
Δ	Clauser's boundary-layer thickness parameter
δ_1	Displacement thickness
Δa	Mean absolute slope
ΔC_F	Added frictional drag
$\Delta P/P$	Power savings
Δq	RMS slope
ΔU^+	Roughness function
ε	Distance from virtual to actual origin at the wall (error in origin)
κ (= 0.41)	von Karman constant
λa	Average wavelength
λ_{PC}	Peak Count wavelength
μ	Dynamic viscosity
μ_n	Central moments of the probability density function of order n
ν	Kinematic viscosity
θ	Momentum thickness
Π	Wake parameter
ρ	Density
$\rho(\tau)$	Autocorrelation function
τ	Shear stress (Chapter 4)
τ	Time or spatial delay (Chapters 5, 6)
$\tau_{0.5}$	0.5 correlation length
$\tau_{1/e}$	1/e correlation length
τ_w	Wall shear stress
ω	Wavenumber
ω_h	Higher bandwidth limit
ω_L	Lower bandwidth limit
∇	Displacement
$^+$	Non-dimensionalised in wall units: multiplied by U_τ/ν for length parameters and by $1/U_\tau$ for velocities

Chapter 1: Introduction

> The great empty hulls with swept holds, just out of dry-dock, with their paint glistening freshly, sat high-sided with ponderous dignity alongside the wooden jetties.
>
> J. Conrad, *The Mirror of the Sea, XXXV*, 1915.

Antifouling paint systems are an essential component of an economic seagoing vessel. The repercussions of fouling are well known. Fouling increases the frictional resistance which makes up 80-90% of the total resistance of cargo carriers and tankers (Lackenby, 1962), and generally more than 50% for high-speed craft. Consequently the required shaft power rises steeply if fouling occurs and increases of 30% have been reported for cross-channel ferries with only moderate fouling (Aertssen, 1961). From an environmental point of view this leads to an undesirable increase of fuel consumption and exhaust emissions. Moreover, there is also concern on the effect of invasive species on local ecosystems.

Antifouling paint technology has come a long way since the days of Joseph Conrad (quoted above) when ships had to be dry-docked every six months in order to keep the hull in an acceptable condition (Bengough and Shepheard, 1943). Presently, the most widely applied type of antifoulings are Self-Polishing Co-polymers (SPC) which use the toxin Tri-Butyl Tin (TBT). They are very effective and give satisfactory performance for up to 5 years. They work by gradually leaching the toxin to kill off any organisms that have attached to the surface. However, this toxin dissolves very slowly in seawater (Milne, 1991) and can therefore damage non-target organisms which live on the coastline (e.g. oysters). TBT-SPC antifoulings have now come under such environmental scrutiny that the International Maritime Organisation has decided to ban their application by 2003. This means that shortly 75% of the world fleet will have to be coated with an alternative antifouling system.

Two types of antifouling may exhibit the same satisfactory performance for a period of 5 years and they form the subject of this study: Tin-free SPC and Foul Release systems. Tin-free SPC systems work by the same principle but use copper as main toxin. Foul Release systems are non-toxic and made of silicone elastomers of low surface energy. This low surface energy inhibits the ability of fouling organisms to attach strongly to the surface. Any

organisms that do attach are washed off by hydrodynamic shear forces when the vessel is cruising fast enough.

Foul Release systems were commercialised in the 1990s for high-speed craft and upon application, some interesting observations were made. For example, it has been reported that the application of a Foul Release system on a 36-metre fast catamaran ferry in 1996 resulted in an increase of 2-3 knots in all weather conditions compared to 1995 when it was coated with a conventional antifouling. Each journey (of approximately 1 hour) was about five minutes shorter in 1996 with an overall fuel consumption reduction of 12%, i.e. more than 20,000 litres/month (Millett and Anderson, 1997). These observations led to a research project set up at the University of Newcastle-upon-Tyne which evolved into the present work.

The philosophy behind this work is to present a systematic experimental study of the drag, boundary-layer and roughness characteristics of antifouling technology and bring the findings together in a qualitative manner. This will allow to draw some specific conclusions, and will identify those areas which may need further research. The ultimate aim of correlating roughness and drag is to predict the added resistance for a full-scale ship caused by the application of a specific coating system if sufficient details on the topography of that coating are known. However, to calculate such quantitative predictions falls beyond the scope of this work and will require the collection of comprehensive in-service data to validate against.

This study is pursued experimentally in order to obtain systematic data regarding the characteristics of the antifoulings. To the Author's knowledge, such a study has not yet been undertaken for Tin-free SPC coatings or Foul Release systems. The study of the boundary-layer and roughness characteristics is complex and not well understood. Both the turbulent boundary layer and the roughness characteristics of an irregular rough surface are difficult to study because they are random in nature. Consequently, semi-empirical theories have been developed which require the input of empirical data. Numerical methods which do not require such input are not yet mature and are currently unable to resolve the issues with which this study is concerned.

This study has to tackle several experimental difficulties. It is particularly difficult to obtain reliable data for the roughness function of low-drag surfaces, in which category these coatings fall. The effect of roughness on the turbulent boundary layer has traditionally been studied for (mostly regular) roughness which causes very high added drag, and which is not particularly relevant in relation to a ship hull surface. Sand roughness is the best-known example of this. These surfaces, however, allow the observation of very clear differences in

the boundary layer. As a surface gets smoother, it becomes more difficult to pick up these differences. Because it is the objective of this work to study newly painted surfaces, the application of the paint systems throughout this work will be of very good to excellent quality. This means that these surfaces are nearer to being *hydraulically smooth*, which implies that the roughness effects do not protrude through the viscous sublayer and disturb the flow, avoiding added drag altogether.

On the other hand, more sophisticated flow measuring devices have emerged. In this work, state-of-the-art Laser Doppler Velocimetry (LDV) will be used to study the boundary-layer characteristics of surfaces coated with antifoulings, which to the Author's knowledge is new. This equipment allows non-intrusive and potentially more accurate measurements than for example pitot tubes or hot-wire anemometry would allow, and should therefore be able to pick up differences even for these very smooth surfaces.

This work is therefore set up as a systematic experimental study with five principal objectives in mind.

The first objective is to present a clear literature review on modern antifouling technology with particular attention to Foul Release technology and its specific surface properties, which is presented in Chapter 2. The impending ban on TBT-SPC coatings and the repercussions on the requirements for satisfactory alternatives are discussed. Both antifouling systems investigated in this research are described in their context and the effect of paint application on ship performance in general is reviewed.

The second objective is to investigate whether Foul Release systems systematically exhibit lower drag than Tin-free SPC systems. Within the framework of this objective, Chapter 3 contains the results of three sets of towing tank experiments which have been carried out with the two different coatings in order to directly measure any differences in total resistance. The first set comprises experiments carried out at the University of Newcastle-upon-Tyne with a 2.55m long plate. The second set of experiments was carried out at CEHIPAR, Spain, with a 6.3m long plate. The third set of experiments was carried out at Dumbarton, Scotland, with a 2.72m long wave-piercing catamaran model. Assuming that the wave resistance is unaffected by the application of coatings, the differences in frictional resistance are compared. Attention is paid to the application details of the paint systems and the roughness measurements taken with the standard stylus instrument for use on ship hulls, known as the *BMT Hull Roughness Analyser*.

A systematic investigation of the turbulent boundary-layer characteristics of the coated surfaces forms the third objective of this study. The boundary layer is the thin layer of fluid close to the wall where the velocity decreases from the free-stream value to zero at the wall and where the friction between body and fluid is produced. A literature review of rough-wall boundary layers and the related theory is first presented in Chapter 4. The theory presented in Chapter 4 is used in Chapter 5 for the analysis of two sets of water tunnel experiments which have been carried out with Laser Doppler Velocimetry (LDV). The first set of experiments was carried out in the Emerson Cavitation Tunnel and investigated the boundary-layer characteristics of 5 different surfaces: a smooth steel reference surface; a Tin-free SPC surface; a Foul Release surface applied by both spraying and rollering; and a surface covered with sand-grit. The distinction between spraying and rollering the Foul Release system is made in order to study the effect of application on the boundary-layer and friction characteristics. The sand-grit surface is included in order to investigate one test surface operating in the fully rough flow region. In order to confirm the findings and to study the boundary-layer characteristics at slightly higher free stream-velocities, the second set of experiments was carried out for three different surfaces in the CEHIPAR Cavitation Tunnel with a similar set-up. The most important scaling factor for boundary-layer measurements is the friction velocity. This parameter is determined by two different methods: an outer layer similarity method, known as the *Hama method*, and the Reynolds stress method which evaluates the friction velocity in the constant stress region of the boundary layer. When plotted in inner co-ordinates, a rough surface will exhibit a shift in the mean velocity which is known as the *velocity loss function* or *roughness function*. This parameter indicates how much drag is added when compared against a smooth surface. In addition, the turbulence intensities, spectra and autocorrelation functions are also measured and compared for the different surfaces.

A systematic study of the roughness characteristics is the fourth objective of this study. Chapter 6 reviews general concepts and definitions of roughness characterisation and contains an extensive analysis of the roughness characteristics of the painted surfaces tested in Chapters 3 and 5. Small sample plates painted alongside the tested surfaces, so that they would be representative of the surface condition of the tested surfaces, are analysed using a UBM optical measurement system. This equipment provides digital roughness profiles which allow the determination of both amplitude and texture parameters. Several of these parameters are known to be related to each other and these relationships are examined. The data are

compared for the different surfaces and are related to a database of other painted surfaces which has been collected in the 1980s by the Ship Performance Group at the University of Newcastle-upon-Tyne. In addition, the build-up with each coat of a typical scheme for each of the two antifoulings is examined.

The fifth objective is to investigate whether there is a correlation between the roughness and drag characteristics of the coated surfaces. Chapter 7 reviews a semi-empirical method used for this purpose and brings together the experimental findings of Chapters 3 and 5 and the roughness analysis of Chapter 6. It is assumed that the roughness function of any surface coated with an antifouling obeys the Colebrook-White law in the transitional flow region. This reduces the semi-empirical method to finding a characteristic roughness measure which correlates the roughness functions of different surfaces. Several characteristic roughness measures are examined and evaluated for the present data. The use and suitability of the Colebrook-White law is discussed and some considerations are given concerning the general correlation between roughness and drag for both regular and irregular roughness.

Finally, Chapter 8 summarises the entire work presented in this thesis and contains a recapitulation with regards to the objectives formulated here. Suggestions for further work are also included.

Five appendices present the calculation of the wave resistance by CFD for the resistance experiments, the principles and errors of LDV measurements, the uncertainty analysis of the boundary-layer measurements, plots of the boundary-layer measurements and roughness profiles.

Chapter 2: Literature review on antifoulings

2.1 Introduction

This Chapter reviews the literature on present-day antifouling coatings and their effect on ship performance. By providing such a review, this Chapter aims to highlight some important differences between Tin-free SPC and Foul Release systems and to refine the overall objectives of this work which have been described in Chapter 1.

Although various techniques have been developed and applied to control fouling (Fischer et al., 1984; Czimmek and Sandor, 1985; Krstajic et al., 1992), this review concentrates on antifouling coatings since paint technology is undoubtedly the most effective and widely applied antifouling method.

Fouling is the undesirable growth of organisms on artificial structures immersed in seawater, of which the most visible form is macrofouling such as barnacles and seaweed. Fouling control is necessary in order to prevent drag increase and consequently increased power requirements and fuel consumption in order to keep the same service speed. Fouling may also hasten corrosion (Edyvean, 1982) and reduce propeller efficiency (Kan et al., 1958; Mosaad, 1986). Worldwide, the cost of keeping marine fouling at bay is estimated to at least 1.4 billion dollars a year (Clare, 1995). For conventional ships, 50-80% of the resistance is caused by friction between the water and the wetted surface of the ship. The smooth, wetted surface of a newly built ship has a roughness of about 80-130 μm. However, the roughness of a surface fouled with for example green algae can easily exceed 1000 μm, causing enormous added resistance. Williams (1923) mentions an increase of 300% for the resistance of a heavily fouled plate as compared to when it was towed in a clean condition. Schultz and Swain (1998, 1999, 2000) carried out LDV water tunnel experiments with flat plates fouled by algae and found an increase in frictional resistance of 125%.

This Chapter briefly reviews the process of fouling in Section 2.2. TBT-SPC systems and the problematic issues associated with them are discussed in Section 2.3. Section 2.4 and Section 2.5 respectively review toxic and non-toxic alternatives to TBT-SPC systems. In Section 2.6, the influence of antifouling paint systems on paint performance is discussed. Section 2.7 contains the conclusions on the literature review and a refinement of the overall objectives formulated in Chapter 1.

2.2 Fouling

The process of fouling is generally divided into four stages, as illustrated in Figure 2.1 (From Davis and Williamson, 1995).

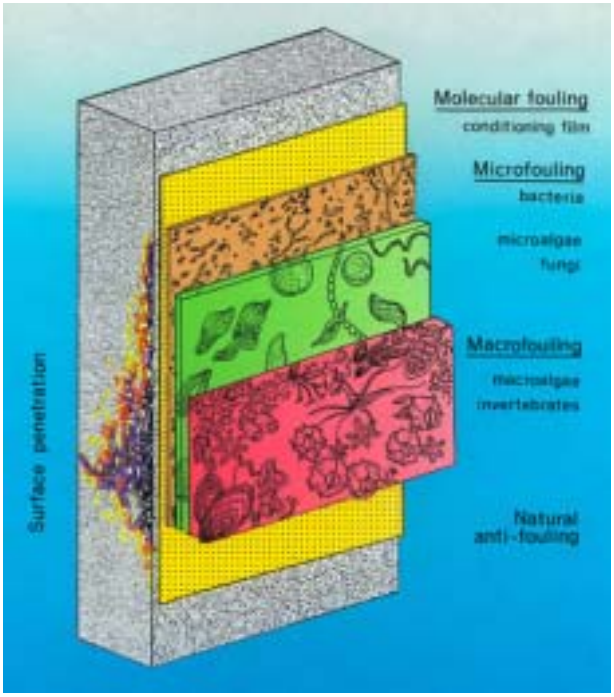

Figure 2.1. Build-up of marine biofouling (from Davis and Williamson, 1995).

Fouling starts from the moment the ship is immersed in seawater. The hull rapidly accumulates dissolved organic matter and molecules such as polysaccharides, proteins and protein fragments (Egan, 1987). This conditioning process is regarded as the first stage of fouling. It begins within seconds, stabilises within hours, and sets the scene for later fouling stages. The genesis of fouling almost invariably occurs when the ship is at rest, most commonly in port. Ports differ considerably in their tendency to cause fouling (British Maritime Technology - BMT, 1986) and the problem of fouling is more severe in tropical waters (Stevens, 1937). The nature of the fouling depends on the species of animal and plant life present in the water, the salinity and temperature of the water, the degree of illumination of the hull surface, the season when berthing takes place and the time spent in port.

When a conditioning film has been formed, bacteria and unicellular organisms such as diatoms then sense the surface and settle on it, forming a microbial film (Fletcher and Chamberlain, 1975). This second stage of fouling involves the secretion of muco-polysaccharides, and generally eases the way for macrofouling settlement (Fischer et al., 1984). This slime already has a significant impact on the ship's performance, as first discussed by McEntee (1915). The influence of slime films on ship resistance was reviewed in the Author's MSc Dissertation (Candries, 1998), which is summarised here.

A separate section was devoted to the effect of slime fouling in the standard work on antifouling for the first half of the 20th century, *Marine Fouling and its Prevention* (Woods Hole Oceanographic Institute - WHOI, 1952). Experiments coated with different paints, showed that after 10 days' exposure an increased resistance of more than 10% was measured, which was attributed to the effects of the slime film.

Watanabe et al. (1969), in recognition of the fact that paints appeared to make no impression on slime, examined the effects on frictional resistance arising directly from the presence of slime, and it was concluded that a significant increase in resistance will occur as a result of the formation of slime.

Loeb et al. (1984) measured the effect of several different types of microbial slimes on the drag of rotating discs of different materials and roughnesses. Results showed that the discs' friction drag increased with 10 to 20%. Based on similarity law characterisation methods, a drag increase of 5 to 8% was thus predicted at 40 knots for smooth planes.

Lewthwaite et al. (1985) developed a technique for determining the local skin friction of a ship's hull under seagoing conditions. Using a small pitot type probe, detailed measurements of the boundary-layer velocity profile and hence the local skin friction were obtained (see also Chapter 4). As the hull became covered with a dense slime film but remained virtually free of weed and shell growth, an increase in skin friction of about 80% was recorded together with a 15% speed loss.

Some interesting experiments were carried out by coating a flat plane with an agar-gel of different concentrations (El-Labbad, 1986). Agar is a substance derived from micro-algae, and the agar-gel would be representative of different kinds of slime films. A plane coated by a 3 mm thick agar-gel with a concentration of 0.5% would correspond to fouling by a light to moderate slime film, and a concentration of 1% to heavy slime. Towing tests showed that the frictional resistance coefficient was increased 4-11% and 13-21% respectively.

The US Navy carried out power trials after underwater cleaning of a frigate. A significant change in power consumption was measured after the removal of a 22-month old mature slime layer, ranging from 8-18% and the maximum speed of the test ship, was increased after cleaning by about 1 knot (Bohlander, 1991).

Schultz and Swain (1998, 1999, 2000) investigated the effect of biofilms on the turbulent boundary layer structure by comparing the boundary layer velocity characteristics of different surfaces with a two-component Laser Doppler Velocimeter (cf. Chapter 5). They found that the skin friction coefficient was dependent on not only the biofilm thickness but also on its morphology. An average increase in the skin friction coefficient for slime films with a mean thickness of 163μm and 347μm before testing was 33% and 68% respectively. The average increase for a surface dominated by filamentous green algae (Enteromorpha spp.) with a mean thickness of 310μm was 187% (Schultz and Swain, 1998).

The presence of adhesive exudates and the roughness of irregular microbial colonies enables the settling of more particles and organisms. These are likely to include algal spores, marine fungi and protozoa. The transition from a microbial film to a more complex community that typically includes multicellular primary producers, grazers and decomposers is regarded as the third stage of fouling (Davis and Williamson, 1995; Bertram, 2000).

The final stage involves the settlement and growth of macro-algal and animal fouling. Green algae, mainly *Enteromorpha*, as shown in Figure 2.2, can grow up to 150mm long in a band a few meters wide at the waterline. It grows rapidly and scrubbing it off can trigger an even more vigorous growth within a few weeks. Brown algae, mainly *Ectocarpus* as shown in Figure 2.3, grow further down the side of the hull. Both these algal species have an extraordinary reproductive potential and an ability to withstand widespread fluctuations in environmental conditions such as desiccation and salinity (Callow et al., 1986). Animal fouling, such as shell fouling as shown in Figure 2.3 may consist of barnacles, mussels, polyzoans, and tubeworms. As mentioned, weed and shell fouling decrease the ship's performance drastically and should definitely be avoided.

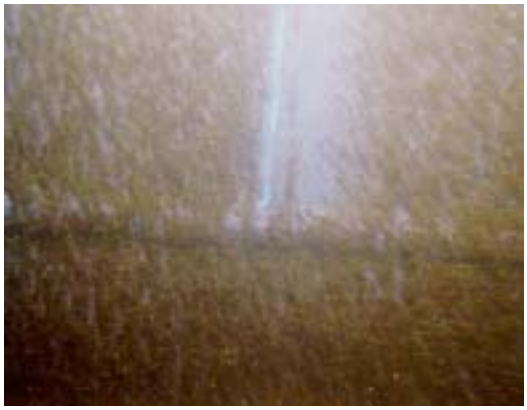

Figure 2.2. Fouling green algae (Anderson, 2000)

Figure 2.3. Fouling brown algae (Anderson, 2000)

Ship fouling is most commonly prevented by the use of antifouling paints. These usually contain biocides that are released during the lifetime of the coatings, creating a concentration of biocide within a surface micro-layer of water adjacent to the paint surface, thus preventing settlement of juvenile fouling organisms. There are over 4000 marine fouling species, therefore the biocides used in antifouling paints must have a wide spectrum of activity to cover such a diversity of organisms (Anderson, 2000).

Figure 2.4. Shell fouling (Clare, 1995)

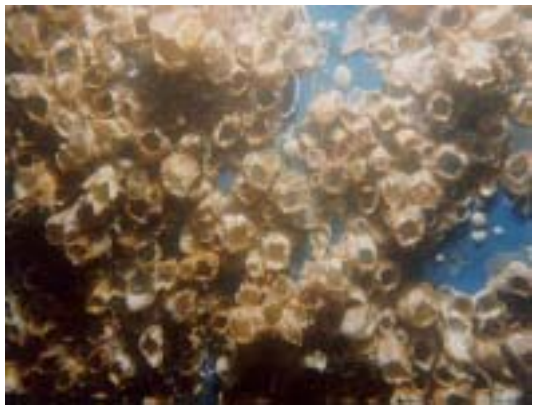

Figure 2.5. Fouling acorn barnacles (Anderson, 2000)

2.3 Antifouling and the impending TBT ban

2.3.1 General concepts of paint technology

Paint can be described as a liquid material capable of being applied or spread over a solid surface on which it subsequently dries or hardens to form a continuous adherent film. Paints are mixtures of many raw materials, each of which in turn has been manufactured to give certain specific properties. Paints basically consist of three major components and many additives which are included in minor proportions. The major components are the binder (other terms used include: vehicle, medium, resin, film former or polymer), pigment and solvent. Of these only the first two form the final dry paint film. Solvent, which leaves the film by evaporation, is necessary to facilitate application and initial film formation. Binders are the film-forming components of paint. They are predominant in determining the principal characteristics of the coating, both physical and chemical. Pigments are fine powders dispersed into binder and can have several functions: anticorrosive pigments prevent corrosion by chemical and electrochemical means, barrier pigments increase impermeability of the paint film and colouring pigments give permanent colour.

A ship bottom is generally coated with two types of paint, whereby a first anticorrosive coat serves as a priming surface for the subsequent antifouling coats.

2.3.2 Historical development of antifouling

Coatings have been applied since Antiquity. A very early record on the use of some form of paint on ship's hulls can be found in the translation from the Aramaic of a papyrus of about 412 BC concerning the repairs of a boat of that date (Culver and Grant, 1924, p. 48):

> "And that the arsenic and sulphur have been well mixed with Chian oil thou broughtest back on thy last voyage and the mixture evenly applied to the vessel's sides that she may speed through the blue waters freely and without impediment?"

In the 3rd century BC, the ancient Greeks used tar and wax to coat ship bottoms. From the 13th to 15th century, pitch, oil, resin, and tallow were used to protect ships. In his life of Columbus, Morison (1942, p. 124) mentions that:

> "All ships' bottoms were covered with a mixture of tallow and pitch in the hope of discouraging barnacles and teredos, and every few months a vessel had to be hove-down and graved on some convenient beach. This was done by careening her alternately on each side, cleaning off the marine growth, repitching the bottom and paying the seams."

During the following centuries, the main form of protection for wooden ships was copper sheathing or the use of a mixture containing sulphur and arsenic. It was not until the development of iron hulls that copper sheathing was abandoned because of serious galvanic problems (WHOI, 1952).

In 1625 William Beale was the first to file a patent for a paint composition containing iron powder, copper and cement. In 1670, Philip Howard and Francis Watson patented a paint consisting of tar, resin, and beeswax. In 1791, William Murdock patented a varnish mixed with iron sulphide and zinc powder, using arsenic as antifoulant (WHOI, 1952).

The number of patents proliferated in the second half of the 19th century - more than 300 patents were registered by 1870 - but all these paints had little to no effect over a very limited time. Mallet (1872, p.129) stated:

> "…it is probable that under no other head in the whole range of the Patent Office Records is such a mass of ignorance, absurdity and charlatanry exhibited, as in these antifouling patents. One or two of the best have proved palliatives (no more can be said for any of them), and are for want as yet of anything better, more or less in practical use. The writer refrains from particularizing those that to his observation seem best or next best; but the vast mass of these 'compositions' are worthless or hurtful – several are more worthy of the name of 'impositions'; and some even of the most recently patented are grotesque in their ignorant absurdity, - as for instance, one in which a farrago of the soluble drastic purgatives (such as colocynth) of the apothecary's shop is mixed up with incompatible resinous fluids, to scare away the unhappy zoöphytes."

The basic principle of these toxic antifouling paints, however, still holds today: some toxic substance is mixed with the paint to kill off fouling organisms by some kind of leaching mechanism (Lewes, 1889; Holzapfel, 1904). The latter is the key factor in the success of present-day antifoulings and was at the time problematic. As Mallet (1872, 120) put it:

> "The necessary balance between adhesion and slow diffusion or washing away thru the water of the poisonous soap is too delicate for practice. Either the soap adheres firmly and does not wash away enough to keep off fouling or it washes away so fast as soon to be all gone."

Salts of copper, arsenic, or mercury were popular biocides. Binders included turpentine oil, naphtha, and benzene. Linseed oil, shellac, tar, and various kinds of resin were used as matrix. In 1854, James McInnes patented the first practical composition to come into widespread general use. It used copper sulphate as toxin in a metallic soap composition, which was applied hot over a quick-drying priming paint of rosin varnish and iron oxide

pigment. Soon after, a similar 'hot plastic paint' known as 'Italian Moravian' was developed which was a rosin and copper compound. It was one of the best paints of that time and was used well into the 20th century. In 1863, James Tarr and Augustus Wonson were given a US patent for antifouling paint using copper oxide and tar (WHOI, 1952). In 1885, Zuisho Hotta was given the first Japanese patent for an antifouling paint made of lacquer, powdered iron, red lead, persimmon tannin, and other ingredients (Bertram, 2000). These paints, although reasonably successful, were expensive and had a short life-span.

In 1906, the US Navy decided to manufacture its own antifouling coatings and tested shellac and hot plastic paints at Norfolk Navy Yard (WHOI, 1952). From 1911 to 1921 more experiments were performed both to find substitutes for scarce materials such as mercuric oxide and to improve the paints (Williams, 1923; WHOI, 1952). In 1926, the US Navy developed a hot plastic paint, using coal tar or rosin as binder and copper or mercuric oxides as toxins. Hot plastic paint required some heating facility which made application difficult (WHOI, 1952). Consequently, 'cold plastic paints' were developed which dry by evaporation of the solvent and which were easier to apply (Graham, 1947). These paints already effectively decreased fouling and the time between dry-docking for re-painting was extended to 18 months.

Major changes in antifouling paint technology came about after the Second World War with the advent of a wide range of new industrial chemicals like synthetic petroleum-based resins and organotins (ca.1962) and with the introduction of abrasive blasting of steel and prefabrication. Considerations of safety and health and the introduction of airless spraying caused the demise of organo-mercurials and organo-arsenicals (Milne, 1982). While the physical integrity of the paints ameliorated markedly, the lifetime of these 'free association' or 'conventional' antifoulings remained limited because the release rate for the biocides was uncontrolled and tended to be rapid initially, with the effect wearing off after 12 to 24 months when the biocides had leached out of the paint (Milne, 1990). This situation changed completely, however, with the introduction of Tributyl-Tin Self-Polishing Co-Polymers in 1974.

2.3.3 Tri-Butyl-Tin Self-Polishing Co-polymers (TBT-SPCs)

Currently, about 75% of all ship hulls in the world are coated with TBT-SPCs (Anderson, 1993; Anderson, 2000). TBT-SPC coatings consist of an acrylic co-polymer as the film-forming component of the paint, with the TBT biocide chemically bonded to the polymer. In the finished paint product other biocides are included, usually copper compounds and 'booster biocides', along with additives and solvent (Anderson and Hunter, 2000).

On immersion, a reaction, which is confined to the top few nanometers of the paint surface, occurs between seawater and the TBT copolymer which releases the TBT and the other biocides present. The chemical reaction results in the formation of a water-soluble reaction product, which is then able to dissolve away, resulting in the surface 'polishing' away with time, thus steadily releasing the other biocides. The rate of biocide release is controlled by this chemical reaction and it has been finely tuned over the past 25 years in order to minimise cost and to maximise lifetime. Moreover, the biocide release rate can be tailored to the requirements of a specific vessel type. The lifetime of TBT-SPCs is directly related to the thickness of coating applied, and in-service lifetimes of up to 5 years are easily achievable (Anderson, 1993; Anderson and Hunter, 2000; Anderson, 2000).

The fact that the reaction only occurs at the surface, and not in the bulk film, was at the time an important breakthrough in antifouling technology. Since it is purely a surface reaction, the 'leached layer' which is depleted of biocides, is very thin (usually less than 20μm), which allows for an unimpaired and steady biocide release. The 'polishing rate' is directly related to speed, but one of the most important benefits of TBT-SPCs compared to other antifouling systems, is that the polishing continues when the ship is stationary and most prone to foul (Anderson and Hunter, 2000; Anderson, 2000).

The paint film of TBT-SPC products is mechanically strong, and is able to withstand extreme environmental conditions. This makes it ideal for use during the long periods of exposure to the atmosphere which can occur during newbuilding.

The biocidal potency and wide spectrum activity against fouling organisms of the TBT-Copper-booster biocide combination, coupled with the precisely controlled release rate, allows vessels coated with TBT SPC products to maintain a high level of fouling control for long periods. Typical records show that over 90% of vessels with high-performance TBT SPC products return to dry-dock in a satisfactory condition, at the end of the specified lifetime of the paint scheme applied (Anderson and Hunter, 2000).

2.3.4 The impending ban on TBT-SPCs

Over the years, TBT-SPC systems have come under increasing environmental scrutiny. In the early 1980s it became clear that organotin not only killed fouling organisms, but because of its very slow decomposition particularly in sediments, TBT also had toxic effects on a wide range of other marine species, particularly molluscs such as whelks and oysters. In marine harbours that were contaminated with TBT at concentrations of parts per billion, whelks were starting to show sex-changing disorders, and oysters developed abnormally thick shells. Similar effects were also detected in the vicinity of maintenance and repair dry-docks where wash-down water contaminated with TBT was released untreated into the marine environment. Within a few years, some whelk species had disappeared from many harbours and marinas along the North Sea.

As a consequence of these observations, the use of TBT in all antifouling products applied on vessels which were smaller than 25m was banned in 1989 in the European Union (and as early as 1982 in France) and similar bans were introduced throughout the world. In addition, a summary of the current antifouling regulations worldwide (Hunter and Cain, 1996; Champ, 2000) shows that in most countries all antifoulings applied on a ship hull require registration, that TBT antifoulings must have a release rate of less than 4 μg of TBT per cm^2 per day and that in certain countries washing water and blasting abrasive used to prepare TBT antifoulings should be collected and treated as a hazardous waste. In Japan, the guidelines on TBT-containing antifoulings have effectively banned application since 1990.

The change in legislation concerning small craft had a positive environmental effect. Assessments of water, sediments and shellfish taken from areas where TBT had previously been detected indicated falling levels of TBT. Biological recovery was observed in coastal dogwhelk and oyster populations. At present, it is considered that elevated levels of TBT and consequent biological effects are restricted to specific localised ‘hotspots’, i.e. coastal areas adjacent to dry-docking operations or within busy commercial harbours and ports.

Some people have argued that the implementation of legislation reducing the release of contaminated water from dry-docks in the hotspots where TBT concentrations are relatively high, and a ban on the use of TBT on coastal vessels will reduce the levels of TBT sufficiently to justify the continuation of the use of TBT products on deep-sea vessels (Hunter and Cain, 1996). The Marine Environment Protection Committee (MEPC) of the International Maritime Organisation (IMO), however, has taken a more radical stance and has published

mandatory regulations to ban the use of toxic antifouling paints containing all organotins such as TBT, despite much debate.

The objections to ban TBT not only come from shipowners (who will have to pay more for Tin-free antifouling alternatives) but also from biologists and environmentalists. The argument centres on the viability of the alternatives to TBT, assuming that the systems currently do not deliver the same satisfactory antifouling performance (Evans et al., 2000). If the performance is not as good, fouling will increase the frictional resistance of a ship and increase fuel consumption and air pollution. From an economical point of view, there are also secondary factors such as more frequent repair dockings and effects on freight rates and transport costs (Strandenes, 2000). There has also been much concern about *invasive species*. If fouling organisms can attach to a ship hull, they can migrate to other waters and cause damage to local eco-systems. A recent spectacular example of the damage that invasive species can afflict is *Caulerpa Taxifolia* (the so-called 'killer weed') in the Mediterranean, where the migration was not due to dysfunctional antifouling systems but to an accidental spill of aquarium water at the Oceanographic Museum of Monaco (See for example Thibaut and Meinesz, 2000). However, as will be seen in the following sections, the alternatives to TBT-SPC studied in this work are claimed by their manufacturers to give 5 years satisfactory performance.

The MEPC resolution ensures a global prohibition on the application of organotin compounds by 2003 and a complete prohibition of these biocides by 2008. The resolution was submitted to a full diplomatic IMO convention and on 5 October 2001 the "IMO Convention on Control of Harmful Anti-fouling Systems on Ships" was adopted (IMO, 2001).

The decision to ban TBT is of great importance to the marine industry since 75% of antifoulings on existing ships will have to be replaced over the next couple of years. The major topics of concern are the treatment of dockyard wastewater, the enforcement of the ban and the practical logistics involved in removing all of the TBT-SPC coatings by 2008 (MER, 1999). Sealer coats applied over the TBT-SPC coatings is one possibility. It is interesting to note that the tiecoat of the Foul Release systems studied in Chapter 5, which acts as a strong link coat to allow the application and subsequent adhesion of the topcoat, can also serve as such a sealer coat (MER, 2001).

2.4 Toxic alternatives to TBT-SPC systems: CDPs and Tin-free SPCs

Several systems have been developed which use other biocides to replace TBT. Most of these systems are based on copper as the main biocide. In terms of the mechanisms involved, Brady (2000) distinguishes three types: Controlled Depletion Polymers which are based on a hydration mechanism, SPCs which work by hydrolysis and coatings which work by an ion exchange mechanism. The latter type is not discussed here.

2.4.1 Controlled Depletion Polymers (CDPs)

Controlled Depletion Polymer antifoulings are derived from traditional 'soluble matrix' (or saponifying) antifoulings, which were popular before the advent of TBT-SPCs. CDP antifoulings are formulated using rosin, which is a substance obtained from trees. Rosin has been used for well over a century by antifouling paint chemists, and is used because it is slightly soluble in seawater, which enables the paint film to slowly dissolve or 'solubilise' and thus release the biocides contained in the coating matrix. Rosin is a cheap renewable resource, but it does have some drawbacks: it is a brittle material, and if too much is used in the coating it can cause cracking and detachment. In order to overcome this, CDP systems include modern reinforcing polymer resins, such as acrylics, vinyls, polyesters or polyamides. Care has to be taken not to include these polymers at too high a level since they are water insoluble, and addition of too much would retard the solubilisation process and so prevent biocide release (Milne, 1991).

Another drawback of rosin arises from the fact that, unlike the TBT-SPC polymers, it cannot prevent seawater penetration into the depth of the coating. As the seawater penetrates further and further into the bulk of the CDP film, a large leached layer can develop, which slows down biocide release and which eventually leads to the attachment of fouling. In CDP systems, this is most commonly seen as green algae on the vertical sides (Anderson and Hunter, 2000). Prior to the advent of TBT-SPC systems, it was well known that the leached layer was the rate-controlling and lifetime-limiting step in all antifouling formulation work. Once it is formed, the only way to remove it is either by in-water scrubbing, or by high-pressure freshwater washing in dry-dock. If it is not removed prior to overcoating, it can lead to detachment and increased roughness at subsequent dockings.

Given the above disadvantages inherent in rosin, CDP systems based on it cannot match the longevity and fouling control performance of TBT-SPC systems and are typically limited to a lifespan of 36 months (Anderson and Hunter, 2000). For this reason, the present investigation and the remainder of this thesis will deal only with two alternatives to TBT-SPCs which do match their longevity and performance: Tin-free SPCs and Foul Release systems.

2.4.2 Tin-free Self-Polishing Co-polymers

As discussed in Section 2.3.3, the success behind the TBT-SPCs is the precise polishing rate, which is a direct result of the chemical reaction which occurs in seawater. In order to mimic the chemistry of TBT in seawater, a series of acrylic polymers have been synthesized. The three main types are copper acrylate, silyl acrylate and zinc acrylate. Only the first type is discussed here.

The first of these to be introduced commercially was the copper acrylate system, launched in 1990 under the brand name 'Ecoloflex SPC' by Nippon Paint Marine Coatings in response to the ban of TBT in Japan that year. The copper acrylate polymer reacts with seawater in exactly the same way as the TBT co-polymer, producing a soluble micro-layer at the paint surface, resulting in the gradual polishing of the coating. This mechanism ensures that there is no leached layer built up over time, and that the biocides in the system are released in a controlled way thus enabling long-term fouling protection. The coatings have a lifetime proportional to the thickness applied (Anderson and Hunter, 2000). The polishing rates of the three types of toxic antifoulings which have been discussed are compared in Figure 2.6, which shows that Tin-free SPC systems also exhibit a non-zero polishing rate at zero speed.

The biocides in the Tin-free SPC systems studied in this work are copper oxide as main biocide and zinc pyrithione as booster biocide since copper alone is vulnerable to diatom and algal fouling. Like TBT, several booster biocides have come under increasing environmental scrutiny, but, unlike TBT, zinc pyrithione is degraded and becomes non-toxic quickly after release from the coating, therefore having much less impact on the marine environment (Evans et al., 2000).

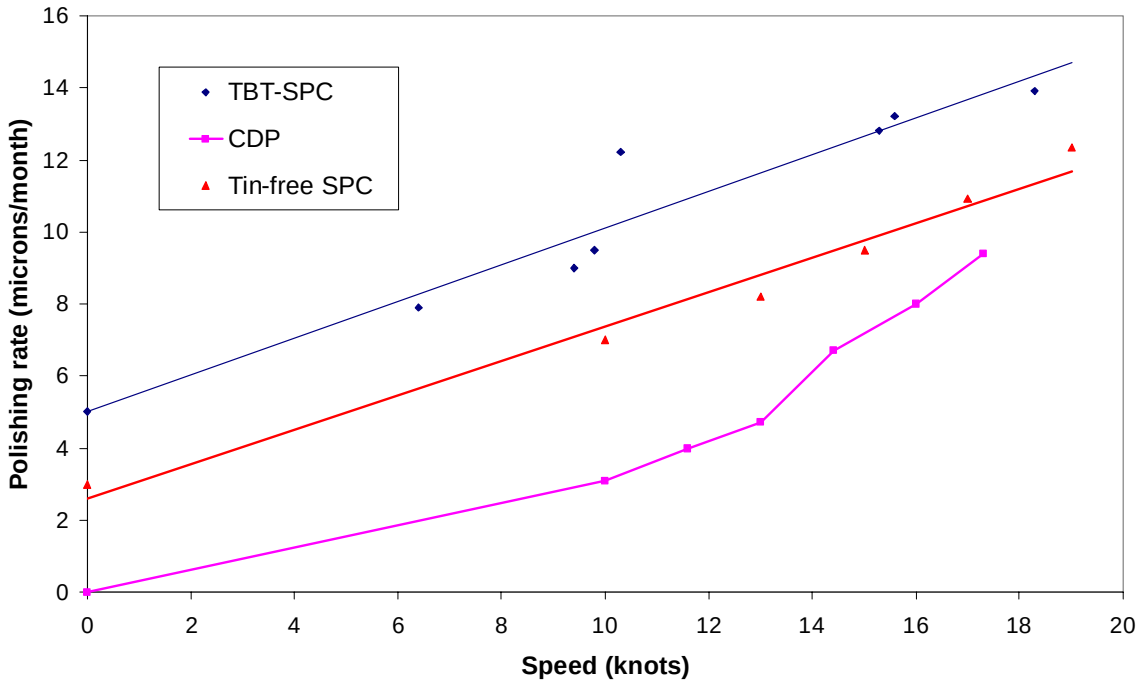

Figure 2.6. Polishing rates of toxic antifoulings (Data courtesy of International Coatings Ltd.)

Data from the manufacturers of the Tin-free SPC systems studied here show that to date, they have been applied to the complete underwater hull of 1813 commercial vessels greater than 4000dwt (Anderson, *pers. comm. 7/9/2001*) and that "at present there are more than a dozen ships currently in-service with five year Ecoloflex SPC systems applied to the entire underwater hull. One of these has now completed 53 months in-service and a recent underwater inspection showed that performance was good. The Royal Australian Navy has also been carrying out long-term testing of Ecoloflex SPC on Patrol Boats, and after 64 months Ecoloflex SPC showed exactly equivalent performance to the standard TBT-SPC product used. This was far superior to the other tin-free products tested, which were all of the CDP type." (Anderson and Hunter, 2000).

2.5 Non-toxic alternatives to TBT systems: Foul Release technology

There is no doubt that from an environmental point of view, antifoulings which do not rely on the use of toxins are desirable. Several of the booster biocides used in Tin-free alternatives have come under environmental scrutiny, and there are even worries about how relatively large amounts of copper itself (even though necessary in trace amounts for normal cellular function) might affect ecosystems (Claisse and Alzieu, 1993). The most established non-toxic antifouling systems rely on Foul Release (or low adherence) technology.

The use of non-toxic surfaces or the concept of low adherence to protect against fouling is not new and was already considered in the 19th century (WHOI, 1952, pp. 226-227), but these concepts were not put into practical use. The first version of the Foul Release system studied in this work was actually patented almost simultaneously with TBT-SPCs, in the early 1970s (Milne, *pers. comm. 6/9/2000*). However the efficacy and commercial benefits delivered by TBT-SPCs was such that the research on Foul Release technology lagged behind for many years. The development of Foul Release systems started in earnest in the late 1980s, as the demand for faster delivery times for passengers and cargoes increased, and as vessels with increased design speeds were developed. This also coincided with the move to ban TBT antifoulings, as mentioned in Section 2.3.4.

The majority of the Foul Release systems that are in use today are silicone materials based on polydimethylsiloxane (PDMS). Fluorinated polymers were for a long time also considered to be successful candidates for Foul Release technology (Griffith, 1985; Brady et al., 1989), but several trials showed disappointing results and they are not further considered here.

PDMS is a heterogeneous molecule with an extremely flexible backbone, which allows the polymer chain to readily adapt to the lowest surface energy configuration. The free energy of a surface, hereafter named *surface energy*, is the excess energy of the molecules on the surface compared with the molecules in the thermodynamically-homogeneous interior. The size of the surface energy represents the capability of the surface to interact spontaneously with other materials (Brady, 1997; Vincent and Bausch, 1997). The surface energy and the critical surface tension are determined by comprehensive contact angle analysis, or in other words, by measuring the *wettability* of the surface. The surface tension of a variety of diagnostic liquids is related to the cosines of the angles that the liquid droplets make with the

coated surface (Baier et al., 1997). The surface energy of PDMS in air is 23mN/m, which is a direct result of the low intermolecular forces between the methyl groups which allow the surface to adapt to the lowest surface energy configuration (Brady, 1997). The surface energy and the associated contact angles change on prolonged immersion in (sea)water. The contact angles decrease and the surface becomes less hydrophobic. This is attributed mainly to structural rearrangement of the surface accompanying adsorption of water and of a conditioning layer from dissolved organic material. The settlement of organisms from seawater significantly lowers the contact angle and renders the surface more hydrophilic (Estarlich et al., 2000).

It has long been noted that hydrophobic surfaces do not foul rapidly (WHOI, 1952). Systematic experiments carried out in the early 1970s have examined the adhesion of barnacles and other marine organisms on substrata with different surface energy. It was found that surfaces with a free surface energy of 23mN/m in air were least prone to foul (Baier, 1970; Meyer et al., 1988), as shown in Figure 2.7. This may be explained by the fact that a surface, of whatever composition or surface free energy in air, acquires a conditioning layer very rapidly when placed in seawater. The conditioning layer, which has the same composition for all surfaces regardless of their chemical nature, is mainly made up of glycoproteins and polysaccharides, which act as glue for fouling organisms (Brady, 1997; Baier, 1970). A surface free energy of 23-25mN/m in air, which is equal to the minimum in Figure 2.7, has the lowest interfacial tension with solutions of biological macromolecules and gives the minimum driving force for adsorbtion (Brady, 1997).

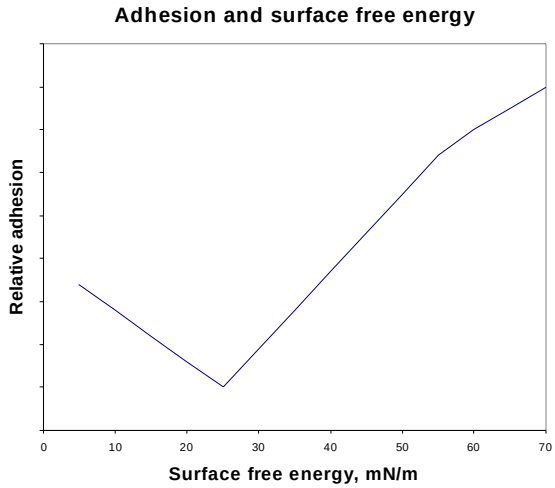

Figure 2.7. The 'Baier curve': the relationship between surface free energy (in air) and adhesion (after Brady, 1997)

Moreover, research in the early 70s, investigating the adhesion of fouling organisms to surfaces with different free energy, found that algal fouling released more easily from silicone elastomers with a surface energy of 23mN/m. Barnacles could be removed under the pressure of a water jet only from the silicone elastomer (Baier, 1970; Meyer et al., 1988). Thus, a surface free energy of 23-25mN/m in air ensures the lowest possible bonding strength of fouling organisms to surfaces and offers the possibility for easy removal of these organisms, either mechanically or hydrodynamically.

Brady and Singer (2000) found experimentally that the relative adhesion of fouling organisms on a material does not solely depend on the surface free energy, but is directly proportional to $\sqrt{E\gamma_c}$, whereby E is the elastic modulus of the material, and γ_c its surface energy. This parameter for silicone materials is at least an order of magnitude smaller than for other materials. The thickness of the coating is also an important factor, with thinner coatings favouring the adhesion of organisms (Singer et al., 2000).

According to American Standard for Testing and Materials (ASTM) D5618-94, the foul(ing)-release properties of coatings are evaluated by measuring the adhesion of barnacles in shear (Schultz et al., 1999). Barnacles are macrofouling organisms that will eventually attach very firmly to a submerged surface and allow quantification of adhesion on surfaces. Towing experiments have been carried out with fouled test surfaces towed behind a motorboat to determine the free-stream velocities required for the release of fouling from silicone coatings with known barnacle adhesion strength (Kovach and Swain, 1998). The barnacle shear adhesion strength for the Foul Release test panels was an order of magnitude lower than the shear adhesion strength found on other surfaces. From the measurements of the shear adhesion strength, the speed at which the barnacles would release from the surface was predicted at 12 and 20 knots for two different Foul Release systems. The towing tests, shown in Figure 2.8, demonstrated that Foul Release coatings with low barnacle adhesion strengths will hydrodynamically self-clean and that there is a good correlation between the predicted and observed velocities at which fouling will release (Kovach and Swain, 1998; Schultz et al., 1999).

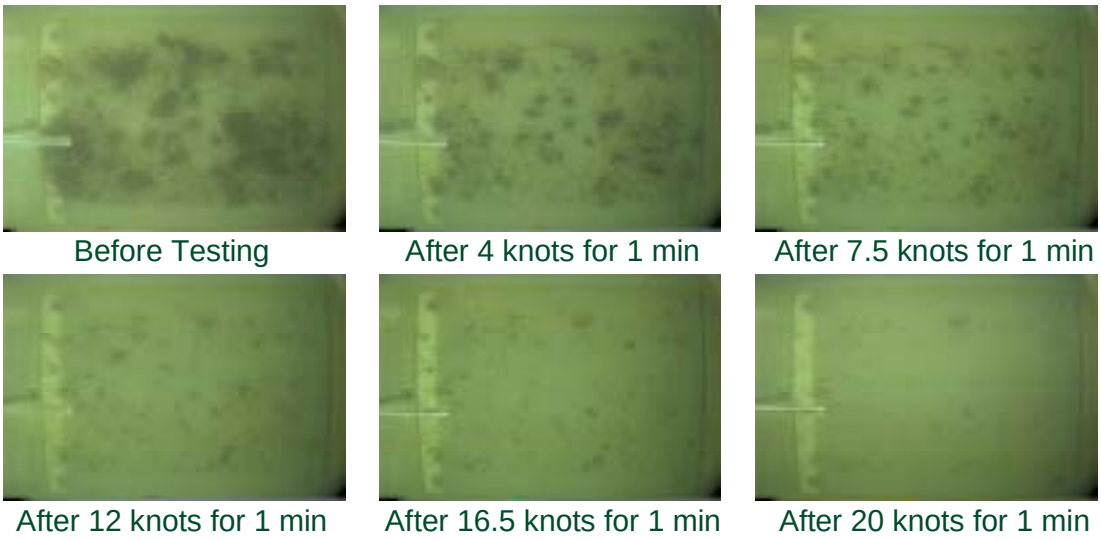

Figure 2.8. Demonstration of the release of fouling organisms under increasing hydrodynamic shear forces.

One of the main motivations behind this research is the recognition that 'smoothness' is a very important factor for an effective Foul Release surface. Surface energy and the surface area available for adsorption and attachment increase with 'roughness'. The valleys of rough surfaces are penetrated by marine adhesives and hence foulants will more readily attach (WHOI, 1952; Crisp and Walker, 1985). This is known as the *thigmotactic* nature of fouling organisms. Moreover, the foulants also find shelter from shear and abrasion in the crevices and thus roughness also poses a threat to the hydrodynamical removal of the organisms (Brady, 1997).

The relationship between low surface energy (or water-repellency) and roughness, however, is not so straightforward. A good example of this is the 'Lotus Effect' (Bathlott and Neinhuis, 1997; Neinhuis and Barthlott, 1997; Forbes, 2001). Certain plant surfaces stay clean because water droplets do not cling to the surface and carry away dirt particles. The water-repellency of the surface is caused by the presence of microstructures, together with the hydrophobic properties of a wax on the plant, as shown in Figure 2.9 and Figure 2.10. The Lotus Effect is not relevant as antifouling technique (because the air entrapped in the microstructures diffuses over time in water, thus annihilating the self-cleaning effect), but interestingly, highly water-repellent surfaces studied in fluid mechanics and based on similar microstructures, as shown in Figure 2.11 and Figure 2.12, exhibit the property of being drag-reducing in the laminar flow regime (Watanabe et al., 1996; Watanabe et al., 1999). Drag

reduction does not occur in the turbulent flow regime but the transition from laminar-to-turbulent flow is slightly delayed by the surfaces (cf. Chapter 4).

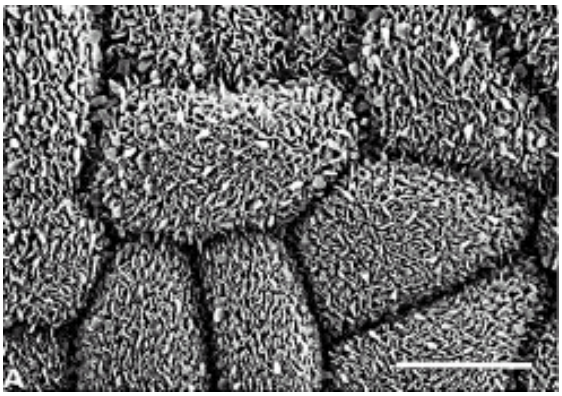

Figure 2.9. Water-repellent leaf surface of *hypericum aegypticum* (From Neinhuis and Barthlott, 1997). Bar = 20μm.

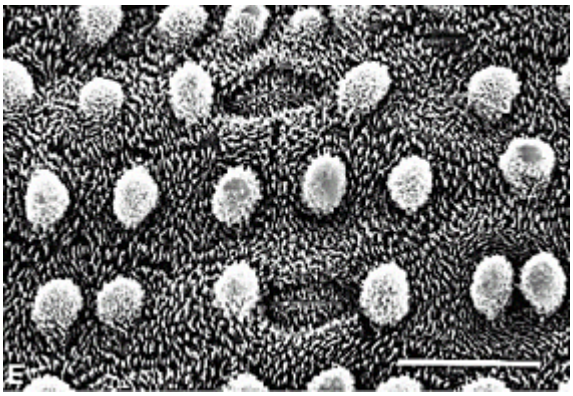

Figure 2.10. Water-repellent leaf surface of *gladiolus watsonioides* (From Neinhuis and Barthlott, 1997). Bar = 20μm.

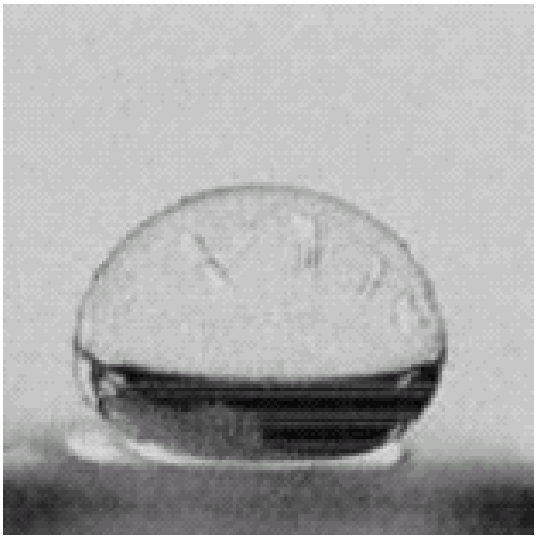

Figure 2.11. Water droplet on a highly water-repellent wall (From Watanabe et al., 1999).

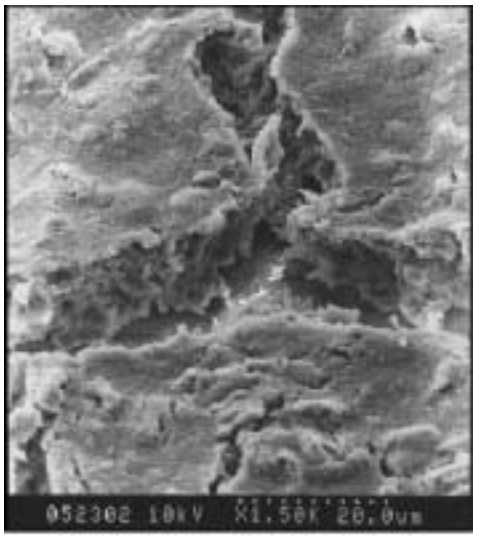

Figure 2.12. Micrograph of a highly water-repellent wall (From Watanabe et al. 1999). Same scale as in Figure 2.9.

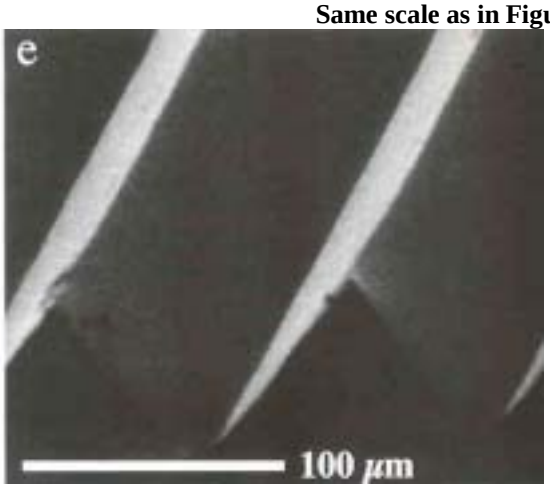

Figure 2.13. Riblets moulded in PDMS with 70μm high structures (From Berntsson et al., 2000).

Another interesting aspect of the Foul Release surfaces studied here is that they are made of silicones like *compliant coatings*, which are also capable of delaying transition from the laminar to the turbulent flow regime (Gad-el-Hak, 1986, 1996, 1998). Moreover, these surfaces, popularly compared to dolphin skin, are capable of reducing drag in turbulent flows by dampening out turbulence production in the boundary layer. The first experiments were carried out by Kramer (1957, 1960, 1961, 1962) in the late 1950s with claims of up to 60% drag reduction. Semenov (1972, 1996) developed a methodology to select the optimum material properties of a compliant coating and achieved up to 17% drag reduction by towing a test body in a lake. Experiments with the same test model carried out in the Emerson Cavitation Tunnel (cf. Chapter 5) by Choi et al. (1997), achieved up to 7% drag reduction.

The drag-reducing properties of compliant coatings and the interesting relationship between wettability and drag, which was already considered by Lamble (1936), led Lackenby (1962) almost 40 years ago to recommend further research whereby "silicones would now seem an obvious choice as non-wetting agents" and they were a motivating background for the present research.

At the end of the Author's MSc Dissertation (Candries, 1998), it was concluded from a literature review on seawater drag reduction techniques that an essential prerequisite for success is to overcome the problem of fouling and that is therefore worthwhile to pursue their integration with Foul Release systems. Since then, research carried out in Sweden has been published whereby grooved surfaces or *riblets* are made of PDMS, shown in Figure 2.13 (Berntsson et al., 2000). This research was initially carried out to investigate the influence of the texture of grooved surfaces on fouling and showed that, depending on the inclination of the riblets, fouling was reduced significantly compared to a smooth reference surface. Fouling surfaces therefore do not always prefer to settle on rough surfaces. Moreover, depending on the flow alignment, riblets have the potential of reducing drag in turbulent flows by up to 10% (cf. Section 7.6)

Just how 'smoothness' and 'roughness' can be defined and described in terms of surface metrology parameters will be investigated in Chapter 6. Consequently, a study will be carried out in Chapter 7 to assess whether there is a correlation between the 'roughness' of a Foul Release and its drag as measured from towing tank (Chapter 3) and water tunnel (Chapter 5) experiments.

Initially, there were concerns about the mechanical strength of silicone elastomers which may therefore not be durable enough to survive on a ship's hull (Kohl and Singer, 1999). However, the Foul Release systems studied in this work are two-layer systems which are considerably tougher than a single-layer silicone elastomer system (Griffith and Bultman, 1997). The two-layer system has a silicone elastomer *topcoat* applied to a stiffer *tiecoat* which consists of a silicone elastomer blended with co-polymers.

Some commercial Foul Release systems contain a silicone oil that migrates from the bulk of the coating to the surface. Fouling then settles on the oil rather than on the surface of the coating, which is known as the 'weak boundary layer' (Vincent and Bausch, 1997; Brady, 1997). The joint between oil and coating is weak and easily breaks off. The oil migrates into the water taking early stages of fouling with it. There are two major drawbacks to this approach. Firstly, the silicone oils are lost, usually within two years in temperate waters, with several consequences. The mechanical properties of the coating deteriorate significantly and sharply, and the coating becomes brittle and cracks. Consequently, the weak boundary layer is no longer formed, fouling is able to settle and adhere with tenacity, and the coating eventually must be replaced. A second drawback is that silicone oils are released into the environment (Brady, 2000). Although PDMS has demonstrated no adverse effects on a wide range of marine species (Stevens et al., 2001), a policy of no release of silicone oils into the environment is ecologically more sound.

The Foul Release coatings studied in this work do not contain silicone oil and purely rely on the hydrophobic nature of the surface which minimises the adhesion of fouling (Callow et al., 1986). Data from the paint manufacturers show that the Foul Release systems studied in this work to date have been applied on 15 ships of more than 4000dwt and on more than 100 smaller vessels, mainly fast ferries (Anderson, *pers. comm. 7/9/2001*).

Foul Release technology is not the only non-toxic concept which has been investigated or commercialised. A fair deal of attention and research has been devoted to chemical inhibition which occurs in natural antifouling processes. The search for antifouling compounds from marine organisms began in earnest in the 1970s based on the observation that certain marine plants and animals, such as seaweeds and sponges, naturally resist fouling. Barnacles and bryozoans do not attach to these sessile organisms while they are alive and fouling occurs only when these organisms die and no longer produce the chemical defences (Matias, 2001). Some organisms are totally devoid of even the first stages of biofilm

formation involving bacteria and microalgae. Several compounds have been identified that might repel or inhibit fouling organisms. For a compound to be truly effective, it should have a non-toxic mode of action, be active at low concentrations, break down rapidly to non-polluting substances, be effective against a broad spectrum of biofouling organisms and be compatible with coating systems (Clare, 1996; Swain, 1999). Moreover, the cost of producing such a compound synthetically should not be too excessive. A number of promising compounds have been identified by several researchers (Cowling et al., 2000; Matias, 2000). These compounds are also toxic when they occur in very large quantities, but their toxicity is 2 to several orders of magnitude lower than TBT, whereas copper is only an order of magnitude less toxic than TBT (Cowling et al., 2000). Successful incorporation of these compounds in a coating system and subsequent evaluation of performance, however, is still in a research phase.

Another concept are the so-called fibrecoats which aim to deter fouling by attaching short fibres (ca. 1mm long) with an epoxy glue in a dense pattern (200 fibres/mm^2). The fibres are electrostatically charged and when the coating is submerged into water, it is assumed that the fibres are moved by currents, thus creating a spiny surface which is permanently in motion (Watermann et al., 2001).

2.6 The importance of antifouling on ship performance

2.6.1 The condition of a ship bottom

This Section briefly discusses the importance of antifouling on ship performance. Milne (1990) estimated that the cost of not doing anything against fouling would amount to 40% of the total marine transport fuel consumption. He further estimated that the advent of TBT-SPC systems due to their efficacy (with consequent fuel savings from better fouling prevention and lower rate of roughness increase) and longer lifetime (with consequent savings in dry-docking costs and extended service time) saved $2.5 \cdot 10^9$\$ compared with conventional antifoulings. This improvement had been achieved at little extra cost but resulted from the efficiency with which similar amounts of equally expensive biocides had been deployed to much better effect.

Thanks to better antifouling systems a ship now returns to dry-dock with its hull in much better condition than, say, 30 years ago. Nevertheless, it is in worse condition than when it first left dry-dock and deterioration of the surface condition implies fuel penalties. Most damage to a painted hull surface occurs during ship handling within harbour and is likely to occur at every berthing, for example, cable and anchor damage, the nosing of tugs, fender damage and bottom abrasions. This mechanical damage accounts for the increasing roughness of ships in service and explains why the average hull roughness of SPC systems increases with time (at about 10-20 microns per year) whereas the undamaged painted SPC surface gets smoother due to its polishing action (Townsin et al., 1980; Townsin et al., 1981; Sakamoto et al., 1983). The average hull roughness increase is much higher for CDP systems (Nygren, 2001). Clearly, a service with more frequent berthings, such as high-speed ferries, puts a surface at greater risk.

The sources of roughness on a hull are manifold. Beside mechanical damage and coating build-up over the years, paint system failures (e.g. blistering, detachment from metal) are a major contributor. In a survey of 272 vessels, Townsin et al. (1981) found that the amount of mechanical damage varied according to ship type and that it covered between 3.6 and 7.3% of the total area, whereas paint failure damage was fairly independent of ship type and covered about 2% of the total area. Corrosion is generally only a minor source of roughness.

In an extensive survey of ship hull roughness, Byrne (1980) found that the average hull roughness of newbuildings was 129μm. The sides are generally rougher than the bottom.

Contrary to expectation perhaps, Townsin et al. (1980) mention that 68% of the hulls increased in roughness during dry-docking when re-blasting was omitted. Re-blasting, however, can render the surface to 'nearly new' condition if corrosion has not occurred. Observed causes were thixotropy of the paint (resulting in poor flow characteristics of the applied paint), poor paint application standards including inadequate hull cleaning, adverse environmental conditions and the limited dimensions of the dry-dock relative to the ship.

Paint application is often a 'bottleneck process', which can take up to 30% of total man-hours during ship production. Careful planning and better integration of the application process will not only increase a shipyard's productivity, it may also improve the quality of the finished surface (Baldwin, 1997). Good paint application and the avoidance of paint system failures has an important effect on its increase in roughness compared to a smooth unpainted surface. For example, one of the worst paint system failures is 'dry overspray' which occurs when the painters hold the nozzles of the pole gun too far from the hull in order to cover the surfaces more quickly. As a consequence, clouds of droplets harden before they reach the surface and in bad cases the final coat is a dense array of paint globules similar to and as rough as sand (Grigson, 1992).

The importance of roughness on ship performance is discussed in Section 1.1.1, but first the instrument by which an average hull roughness (AHR) value is obtained will be described in the following Section.

2.6.2 Description of the BMT Hull Roughness Analyser

For the last 50 years, the roughness of the ship hull surfaces has mainly been measured using the BMT (British Maritime Technology) Hull Roughness Analyser and its earlier version the BSRA (British Ship Research Association) wall gauge, which are stylus instruments. Pneumatic instruments, used extensively in the manufacturing industry, have also been used for the characterisation of ship hull roughness (Aertssen, 1955; Aertssen, 1962), but stylus instruments have always been more prevalent. The original instrument was developed for the experiments on the 'Lucy Ashton' (Denny, 1951; Conn et al., 1953; Lackenby, 1955; Smith, 1955).

The modern version of the instrument, shown in Figure 2.14, consists of two components: the measuring head and the analyser module. A battery power pack, which is

also shown in the principle sketch in Figure 2.15 can be connected to the analyser module in case the latter's internal battery is not charged. The measuring head is a wheeled tractor, having two wheels at the leading end and one at the rear. In the standard version of the instrument, the rear wheel sends a signal to the analyser module every 50mm. In the adapted version used for the measurements done in this work, the infra-red receiver-detector system which sends the signal is installed on the front left wheel. The measuring head has a handle with which the operator propels the head over the surface, contact being kept by hand pressure. The sensing probe consists of a cantilevered bar slung under the tractor with the stylus at one end and a system of strain gauges at the other, as shown in the sketch in Figure 2.16. The stylus has an interchangeable 1.56mm diameter steel ball at its tip with a surface pressure force of about 0.147N (15gmf) when measuring the flat bottom of a hull (Byrne, 1980). An articulated skid together with a cantilever arm are associated with the probe in such a way as to remove long-wavelength curvature with a radius above 2.5m. The skid is free to move in the vertical direction. The actual quantity being measured is the difference between the stylus and the skid, so that the roughness in effect is being integrated over the width of the skid, which at its maximum is 10mm (Byrne, 1980, Thomas, 1999).

The measuring head is water-resistant and has proved robust in the difficult conditions met with in dry-dock. The measuring head is connected by a flexible lead to the analyser module. The analyser module contains the control and analysis circuitry, the output strip-printer and the operating controls.

During the traversing of the measuring head, at a speed of approximately 50mm/s, the highest peak to lowest valley perpendicular to the mean line over a 50mm interval, Rt50, is measured. The range of Rt50 which the instrument can accommodate is from 0 to 1999μm with an accuracy of ±15μm or ±5% of the measured value, whichever is the greatest. When the head has traversed the surface over about 1m, fifteen readings of Rt50 and an average, the Mean Hull Roughness (MHR) are printed out. About 100 readings spread over the entire underwater hull are recommended to give a statistically significant amount of MHR values that are averaged to obtain the overall Average Hull Roughness (AHR) of a ship (Townsin et al., 1981).

Modifications have been made in the past whereby more complex output devices connected to the instrument store digitised recordings of the profiles (Townsin, 1986; Townsin, 1987; Chuah et al., 1990) or whereby modified analysis software displays additional roughness parameters (Fitzsimmons and Ellis, 1990).

Figure 2.14. The BMT (ex-BSRA) Hull Roughness Analyser, which was used for measuring the roughness of the surfaces tested in the experiments of Chapters 3 and 5.

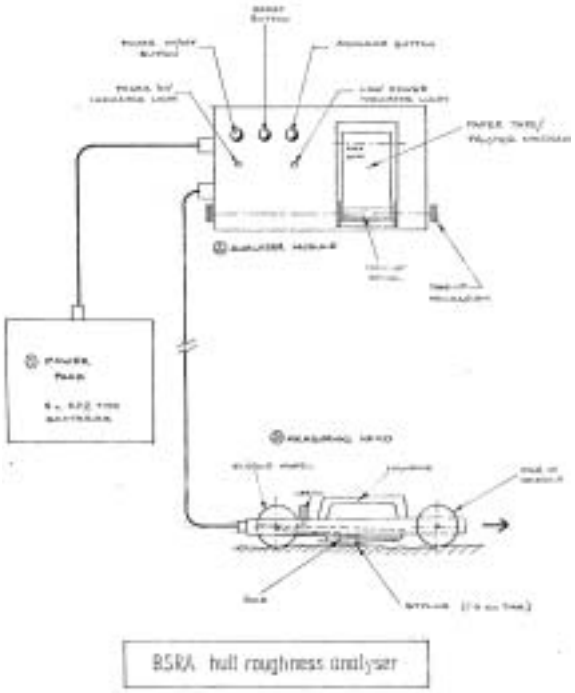

Figure 2.15. Sketch of the components of the BMT Hull Roughness Analyser (From Byrne, 1980).

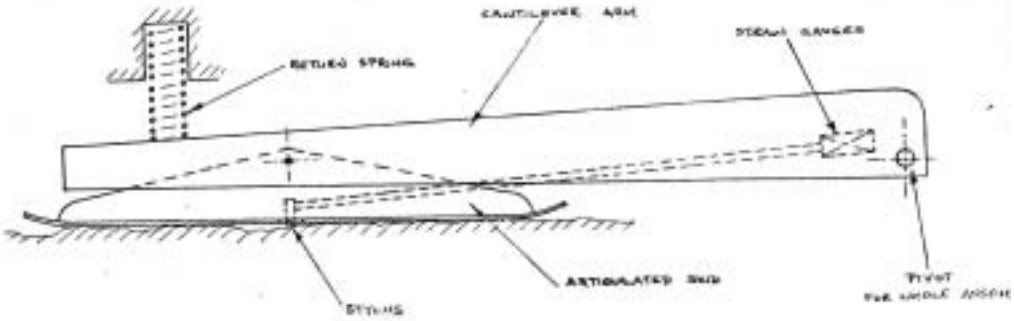

Figure 2.16. Close-up sketch of the measuring head of the BMT Hull Roughness Analyser (From Byrne, 1980).

2.6.3 The influence of roughness on ship performance

Classified by their characteristic wavelengths, the hull roughness of ships can be divided into *small-scale surface roughness* and *structural roughness*. The latter is due to imperfections in the building process such as weld beads and plate waviness (Allen and Cutland, 1956). The effect of butt welds is more important than longitudinal welds that are

aligned with the flow. Grinding off the butt welds may be economically interesting if one considers the fairly small contribution to hull roughness over the lifespan of a ship. Plate waviness, however, has a negligible contribution to the overall roughness and can probably not be improved anyway. It does play a role in paint application and can cause local overspraying.

Table 2-1. Recently measured AHR values (Data courtesy of International Coatings Ltd.)

Type	Date	DWT	LOA	B	T	Service speed	Paint system	Location	AHR	Comments
Pass./Ferry	Oct-97	142	77.32	19.5	2.15	57	Tin-free SPC	All	257	Prior to Foul Release application, pitting
							Foul Release	All	59	After Foul Release application
Pass./Ferry	Oct-00	6875	214.14	27.69	6.55	23	Foul Release		207	Foul Release after application (12/1998)
							Foul Release		205	Foul Release after 2 years service
							CDP		365	Conventional after application (12/1998)
							CDP		372	Conventional after 2 years service
Ro/ro	Jan-99	22580	199.15	32.29	11	20.5	CDP	Sides	104	
							CDP	Flats	115	
Ro/ro	Mar-99	20580	199.15	32.29	11	20.5	CDP	Sides	100	
							CDP	Flats	114	
Ro/ro	Jun-99	22580	199.1	32.26	9.5	20.2	Tin-free SPC	Sides	89	
							Tin-free SPC	Flats	96	
Ro/ro	Jul-99	22584	200	32.26	9.5	20.2	Tin-free SPC	Sides	78	
							Tin-free SPC	Flats	109	
Ro/ro	Aug-99	14927	199.1	32.3	11	20.2	TBT SPC		N/A	Newbuilding
							TBT SPC	Sides	204	Damage areas on sides
							Tin-free SPC	Sides	197	Damage areas on sides
							TBT SPC	All	138	Sides/Part of Flats
							Intersleek	All	131	Sides/Part of Flats
Ro/ro	Nov-99	22662	199.11	32.29	11.02	20.6	Ecoloflex	Sides	118	In
							Ecoloflex		187	Out
							CDP	Flats	113	In
							CDP		170	Out
Pass./Ferry	Mar-99	63	40.7	16.4	2.16	36	Substrate	Test patch	197	Prior to Foul Release application
							Foul Release	Test patch	162	After Foul Release application
Pass./Ferry	2001	700	115.25	17	2.5	38.3	Foul Release		64	After Foul Release application

The typical values of hull roughness for new ships have decreased over the decades (Townsin et al., 1986). Less than 100 μm is now generally achievable, but 70 μm is about the best practically possible. Shot-blasted and primed new steel plates have an AHR of 40-60 μm. For new ships, any excess of this is mainly due to subsequent coats of paint, resulting in a hull roughness usually between 95 and 125 μm. Thereafter during the first ten years in service, an approximately linear rate of increase occurs which is on average 20 μm/year for surfaces coated with TBT-SPCs (Townsin et al., 1986). The first quarter from the bow of the underwater hull contributes most to the overall friction drag and the contribution progressively diminishes fore to aft (Townsin et al., 1982; Kim and Lewkowicz, 1992). Table 2-1 lists some AHR values which were recently measured with the BMT Hull Roughness Analyser on the new alternatives to TBT-SPC (the names of the vessels have been omitted for reasons of confidentiality).

Apart from side effects on fouling (as mentioned in Section 2.5, fouling organisms are *thigmotactic*, i.e. they prefer rough surfaces to smooth surfaces for settlement) and hydrodynamic noise (which may affect hydro-acoustic instruments), hull roughness has a direct effect on frictional resistance. The effects of hull roughness on frictional resistance, however, are difficult to assess because it is difficult to provide a satisfactory description of the irregular roughness of typical hull surfaces and because the effect of roughness on the turbulence (and hence friction) production in the boundary layer is not entirely understood. This topic, which is further complicated at sea by the effects of slime, will be reviewed and discussed in Chapter 6 and Chapter 7.

For newly painted, moderately rough ship hulls (< 225μm), however, the use of Rt50 as a descriptive parameter of the AHR is generally regarded to provide a reasonable estimate of the drag increase (Townsin and Dey, 1990). Townsin and Dey argued that moderately rough surfaces all exhibit similar texture which would explain why a single roughness amplitude parameter such as Rt50 can account for the drag increase. One of the main objectives of this work is to investigate whether this is also the case for the surfaces coated with paint systems which have fairly recently been introduced on the market. As seen in Section 2.5, Foul Release systems have very different surface properties from toxic antifouling systems which may be expected to result in different roughness characteristics, which is investigated in Chapter 6. The drag characteristics of Foul Release and Tin-free SPC systems are studied in Chapters 3 and 5 and Chapter 7 will investigate whether there is a correlation between roughness and drag.

Several approaches are in use to correlate roughness and drag. The International Towing Tank Conference (ITTC) approach is to determine a correlation allowance, C_A, that accounts for the differences between trial results from model tests and full-scale measurements. This allowance accounts for the inadequacies in extrapolation techniques and for the roughness itself. Orginally, C_A was taken as a constant equal to 0.0004 based on the experiments carried out by Schoenherr (1932). Later, C_A was calculated by the formula given by Bowden and Davison (1974):

$$C_A \cdot 10^3 = 105(AHR/L)^{1/3} - 0.64 \qquad (2.1)$$

where AHR is the Average Hull Roughness and L is the length of the ship. Equation 2.1 was adopted by the ITTC in 1978 and is valid for ships shorter than 400 m and for roughness values below 200 μm, with restricted loading condition. The formula is used in conjunction with the ITTC extrapolation method on a form factor base:

$$C_V = (1+k)C_{F,ITTC} + C_A \tag{2.2}$$

Where C_V is the viscous resistance coefficient, 1+ k is the hull form factor and $C_{F,ITTC}$ is the total frictional resistance coefficient of a smooth plane with the same length and wetted surface as the ship and determined by the ITTC 1957 model-ship correlation line (cf. Equation 3.1). The value used before in the Schoenherr method, C_A = 0.0004, is approximately equivalent to a relative roughness AHR/L of $1 \cdot 10^{-6}$ using Equation 2.1. The problem with using the correlation factor is that it does not allow the separation of two different influences, namely roughness and extrapolation (Townsin, 1990).

A second approach, studied in this work, is to use the local skin-friction coefficient, c_f, estimated directly from the knowledge of local surface roughness parameters. Drag to roughness correlation experiments include measurements of pipe flow, tests in re-circulating water tunnels, the use of a rotor apparatus and flat plane tests. A cross-section of a hull painted surface is a broad-banded random function. There are a considerable number of well-known statistical parameters which can be used to typify such a surface (cf. Chapter 6). The purpose of selecting parameters is to choose those which can be shown to correlate with the measured drag increase of a typical painted surface. However, as mentioned, to correlate a moderately rough painted surface with drag, Rt50 was shown by Townsin and Dey (1990) to be a good descriptor of the surface which correlates with the drag increase of newly painted surfaces. As a consequence, the following approximate formula has been proposed by Townsin et al. (1984) to calculate the drag increase ΔC_F :

$$10^3 \cdot \Delta C_F = 44[(AHR/L)^{1/3} - 10(Re)^{-1/3}] + 0.125 \tag{2.3}$$

A crude formula to estimate the power savings due to hull roughness reduction is:

$$\Delta P/P \text{ (in \%)} = A \cdot (k_2^{1/3} - k_1^{1/3}) \tag{2.4}$$

where k_1 and k_2 are the AHR before and after cleaning respectively, and A is a constant factor, equal to 2.5 for single screw ships. It was used by Townsin et al. (1986) in order to estimate the direct fuel savings of decreased roughness over the decade 1976-86 of the UK fleet; the calculations showed that at the time 30 million pounds were saved per year due to better bottom maintenance.

2.7 Conclusions of the literature review and refinements of the objectives

The conclusions drawn from the literature review presented in this Chapter are:

- Antifoulings are an essential component of an economic seagoing vessel.
- At present, the most widely applied antifoulings are TBT-SPC systems but because of the toxicity of TBT, these systems will be banned from application by 2003.
- At present, Tin-free SPC and Foul Release systems are the only types of antifouling which could be satisfactory alternatives to TBT-SPCs with a lifetime of 5 years. They form the subject of this study.
- Foul Release systems have surface properties which are very different from SPC systems. They rely for their antifouling efficacy on the weak attachment and easy removal of fouling organisms. Since fouling organisms are thigmotactic (i.e. generally prefer rough surfaces to smooth surfaces), Foul Release systems need to be 'smooth' in order to be effective. How 'smoothness' can be described in terms of roughness parameters and how these characteristics differ for Foul Release surfaces from SPC systems will therefore be studied in detail in Chapter 6.
- The application of paint systems on a surface increases the drag of that surface compared to the smooth unpainted condition. Systematic data as to how much added drag is caused by the application of Foul Release and Tin-free SPC systems and how these two systems compare are not available and will be collected in Chapter 3.
- The application of paint on a surface alters the boundary-layer flow characteristics compared to when the surface is smooth, resulting in enhanced turbulence production and increased friction. The effect of paint application on the boundary-layer characteristics, however, is not entirely understood and will be studied in Chapter 5.
- Because of the different nature of Foul Release surfaces, the correlation between roughness, drag and boundary-layer characteristics according to the recommendations of the ITTC (1990) may have to be re-evaluated. This will be investigated in Chapter 7.

Chapter 3: Resistance experiments

3.1 Introduction

This chapter presents three sets of towing tank experiments which were carried out in order to directly compare the total resistance of two different paint systems: Tin-free SPC and Foul Release. The first two sets of experiments comprised friction planes while the third set involved a wave-piercing catamaran model. The experimental procedure used for these experiments is described in Section 3.2.

There is a long tradition in naval architecture of towing friction planes to investigate the surface conditions, going back to Froude (1872, 1874). The main reason for the choice of friction planes is that wave resistance is minimised and that frictional resistance makes up most of the total resistance, which is ideal to investigate the influence of the surface conditions. Section 3.3 describes the first set of experiments that have been carried out with a 2.55m long plate in the Newcastle University towing tank. In order to confirm the results of Section 3.3 and to extend the Reynolds number range, a second set of experiments was consequently carried out in the CEHIPAR (Canal de Experiencias Hidrodinamicas de El Pardo) towing tank using a 6.3m long plate, which is described in Section 3.4.

The implications of applying the paint systems on a three-dimensional body was investigated by towing a 1/35-scale wave-piercing catamaran model in the third set of experiments, which has been described in Section 3.5. A catamaran model rather than a monohull was chosen for the experiments since drag reduction of a Foul Release system in full-scale was first observed on a catamaran (Millett and Anderson, 1997). It was also thought that it was appropriate to select a model which is a suitable representative of the high-speed ferries on which Foul Release systems to date have been most applied.

3.2 Experimental procedure

The methodology used for the experiments consisted of executing three series of measurements. The first series involved testing the surface without paint, which served as the smooth reference. The following two series involved testing both coatings. Runs over a range of speeds were carried out for each series to produce a curve of the total drag coefficient, C_T, against Reynolds number, Re. The total resistance consists of the frictional resistance (C_F), the wave-making resistance (C_W) and the viscous pressure drag (C_{VP}), which is considered negligible. The differences in frictional resistance were consequently calculated by subtracting the wave resistance from the total resistance, assuming that the wave resistance is not affected by the coatings. The wave resistance was calculated by a computational fluid dynamics (CFD) software package called SHIPFLOW. The software is described in Appendix A.1 while the calculations of the wave resistance are presented in Appendix A.2.

The kinematic viscosity and density at different temperatures throughout this work were taken from van Manen and van Oossanen (1988, p. 58).

In addition to the measurement of the total resistance, the wave profile was captured by video camera for the experiments with 6.3m long plate described in Section 3.4.

In the third set of experiments out with the 1/35-scale model of a wave-piercing catamaran, which is described in Section 3.5, the sinkage and trim were also measured in addition to the measurement of the total resistance. Preparatory tests had been carried out by White (1999) with a smaller model of another wave-piercing catamaran at the Newcastle University Towing Tank.

The application conditions of the coatings were kept as near identical as possible. However, due to circumstances, the application methods and the paint systems used in the wave-piercing model experiments (Section 3.4) were quite different since spraying was not a practical option for the experiments.

Roughness measurements were taken of all surfaces with the BMT Hull Roughness Analyser, which has been described in Section 2.6.2. Sample plates were painted alongside the tested plate of the second set and the model of the third set of experiments, in order to analyse the roughness characteristics with an optical measurement system (cf. Chapter 6). However, as will be discussed later, the sample plates of the model experiments were not completely representative of the respective tested surfaces.

3.3 Experiments in the Newcastle University Towing Tank with a 2.55m long plate

The experiments reported in this Section were carried out between January and November 1998. They were partially reported in the Author's MSc Dissertation (Candries, 1998) and full details of the completed experiments can be found in Candries et al. (1998).

3.3.1 Facilities and test conditions

3.3.1.1 Towing tank and model details

The experiments were carried out in the towing tank of the Department of Marine Technology at the University of Newcastle-upon-Tyne. The tank is 40m long, 3.75m wide and 1.2m deep. A central mono-rail is used to guide the carriage and model along the tank. The water used in the tank is freshwater with a small amount (0.5kg) of copper sulphate added to eliminate growth and deter the formation of algae. Each day of operation the surface is skimmed to get rid of debris and dust.

The friction plane used for the tests was manufactured from 10 gauge aluminium plate, bonded to an aluminium framework. The keel and both ends were machined from solid aluminium. Figure 3.1 below depicts the overall dimensions of the plane which has a wetted surface equal to 5.08m^2.

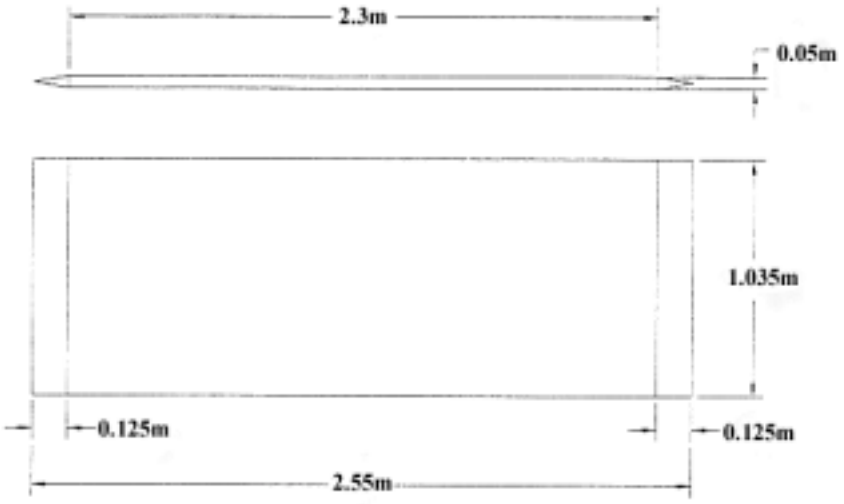

Figure 3.1 Dimensions of the flat plane

On the upper edge of the plane, fore and aft guide rollers were fitted as well as the attachment for the two load cells which measure the resistive force of the plane. Care was

taken to ensure that the plane was smooth. Figure 3.2 depicts the friction plane suspended from the towing carriage.

Figure 3.2. 2.55m long flat plate (coated with the Foul Release) suspended from the towing carriage

A trip wire of 1mm diameter was fitted at a distance of 0.125m from the leading edge of the plane for turbulence simulation.

3.3.1.2 Test methodology

As mentioned in Section 3.2, runs at various speeds were carried out for each series to produce a curve of the total drag coefficient C_T against Reynolds number Re. The upper test speed was taken as high as practicable, i.e. around 2 m/s. The water depth was 1.252m and the freeboard of the plate was 65mm. For each test series, the tank was filled to the same water level, ensuring the same freeboard and wetted surface for the plane. Apart from the automatic measurements of time, velocity and drag, measurements of the fluid drift were taken at a depth of 30mm by determining the displacement of a floating device in 30 seconds; positive values of the drift indicate a movement of the water towards the dock of the towing tank, negative towards the wavemakers.

The measured speed and total resistance were averaged from the point where the desired steady-state speed was reached until the recording where the speed dropped again. This effectively meant that for the lower speeds a very large amount of the 1200 recordings (30s)

were averaged, but for the highest speed only 80 recordings (2s) were averaged. This is demonstrated by a typical plot which displays the measurement of the highest and lowest speed selected, as shown in Figure 3.3.

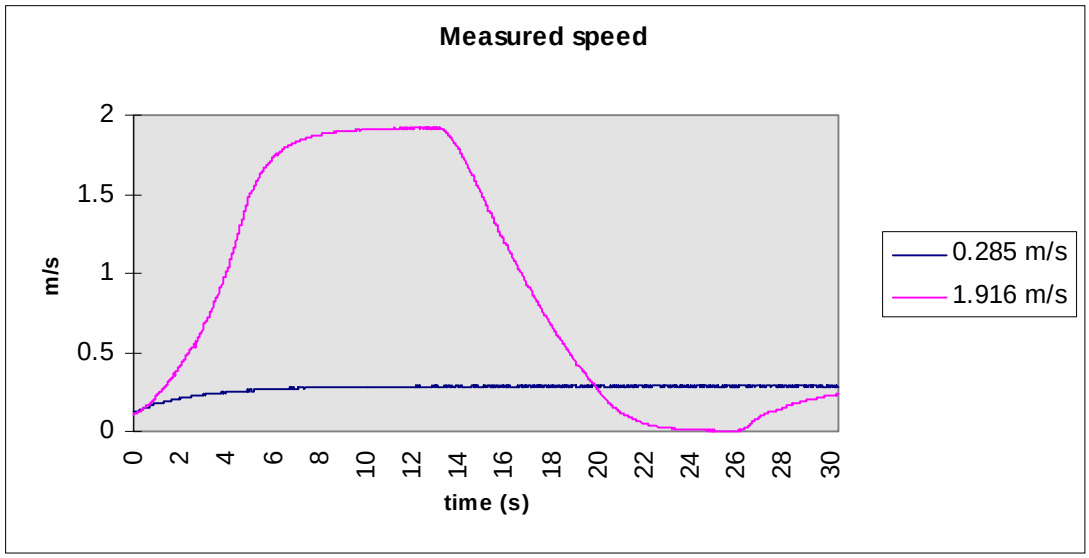

Figure 3.3. Typical records of two different speeds during a test run

From Figure 3.3, it is also clear that at the highest speed, the measured velocity does not reach a steady-state, but keeps increasing slightly over the three seconds retained for further analysis. In effect, the towing tank was not long enough to allow steady-state measurements for speeds exceeding 1.8m/s.

For the highest speed shown in Figure 3.3, the measurements between the 11th and 13th second of recording were averaged. Over this period the average velocity increases linearly from 1.914 to 1.918m/s and the average resistance from 39.399 to 42.660N. For the lowest speed, 640 recordings were averaged, this is over a period of 16s (12.325-28.325s).

As soon as the desired speed of each run was reached, 10-point averages were taken to filter the measured drag values. At each time step, these 10-point average drag values were divided by the squares of the instantaneous velocities that oscillated slightly around the desired average speed. These calculations were analysed up until the moment when the brake action was set in.

With the average speed, which was corrected by taking the drift into account, and the resistance thus measured, the Reynolds number (Re), the Froude number (Fn), the total drag coefficient (C_T) and the ITTC frictional drag coefficient ($C_{F,ITTC}$), were calculated, whereby:

$$C_{F,ITTC} = 0.075/(\log Re-2)^2 \quad (3.1)$$

It may be noted that Equation 3.1 is not a friction line, but a (smooth) model-ship correlation line that is used in naval architecture to extrapolate model results to ship scale (Townsin and Mosaad, 1985). The ITTC line is included in this work merely for illustrative purposes. What is of importance throughout this work are the differences of the coated surfaces relative to the smooth reference surface or to each other.

After the first test series which established the resistance profile of the smooth Aluminium surface, the plane was taken to International Coatings Ltd. to coat the plane with the Tin-free SPC system. After the second series of measurements with the SPC coating applied, the SPC system was removed and the plate was coated with the Foul Release silicone elastomer to perform the third test series.

3.3.1.3 Application of the two different coating schemes

Figure 3.4. Outdoor application of the second and final coat of Tin-free SPC (July 9, 1998).

Because of the dimensions of the plane, the aluminium plate had to be sprayed outdoors in good weather conditions, as shown in Figure 3.4. Waiting for these conditions delayed the application of the coatings considerably and the second test series with the SPC coating was carried out 6 months later than the first reference series with the smooth Aluminium surface.

Three coats of paint were sprayed on the plane. The top and both end tips of the plane were taped and solvent was applied on both sides. After that a vinyltar anticorrosive (called 'Intertar') was sprayed on. The following day, the plane was sprayed with the first layer of the Tin-free SPC (called 'Intersmooth 460 Ecoloflex'). The second and final coat was applied 24 hours later.

After the second test series, the plane was stripped from the Tin-free SPC by putting on a paintstripper for 30 minutes, followed by paint scraping and a solvent wash. Consequently the anticorrosive layer was applied on and the following week, the tie- and topcoat of the Foul Release scheme (called 'Intersleek') were applied.

3.3.1.4 Roughness measurements

Before applying each layer of paint, the roughness of the surface was measured with the BMT Hull Roughness Analyser, as shown in Figure 3.5. 5 measurement lanes were selected on each side of the surface at a distance 0.9, 0.7, 0.5, 0.3 and 0.1m from the bottom. The Average Hull Roughness values (in μm) of the three tested surfaces are presented in Table 3-1. For the SPC scheme, three values for each coat respectively are listed.

Figure 3.5. Measuring the roughness of the Tin-free SPC surface with the BMT Hull Roughness Analyser.

Table 3-1. Average (Hull) Roughness values for the different surfaces in microns.

Surface	Average
Aluminium	17
Anticorrosive	48
SPC Coat 1	61
SPC Coat 2	75
Foul Release	44

The histograms of the roughness distributions of the Tin-free SPC scheme are presented in Figure 3.6, which shows that the distribution becomes more broad-banded with each coat of paint.

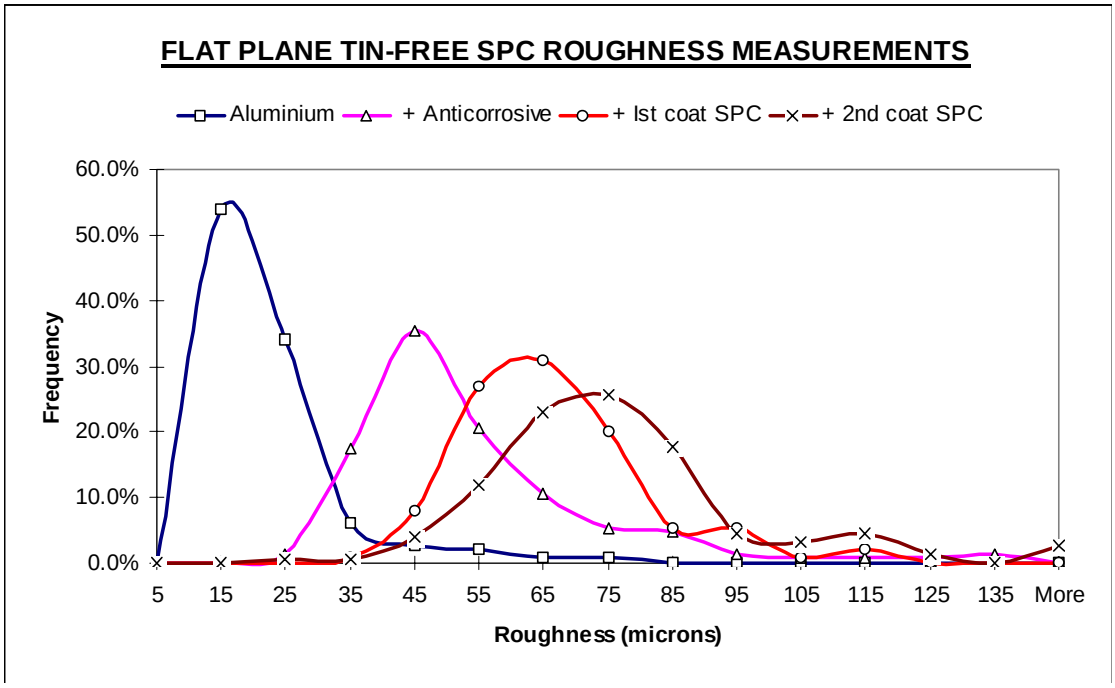

Figure 3.6. Roughness histograms for the Tin-free SPC scheme.

Prior to paint application, it had been decided that the plane should not be sprayed under laboratory conditions in order to better simulate good dock bottom conditions and this became evident in the roughness values. Nevertheless, the surface roughness values are still better than those normally found on a ship hull.

Roughness measurements of the Foul Release surface were not taken until the final tests had been completed. At first, the tank was emptied and the roughness was measured along the same lanes as mentioned above while the plane was still suspended, as shown in Figure 3.7. During these measurements, it was observed that the stylus of the measuring head stuttered over the dry silicone surface. In order to prevent this, the surface was slightly sprinkled with

water. Despite this, it was not possible to pull the measuring head over the surface at an even speed. Instead, the traverse proceeded in a series of little shocks and it was decided to apply some grease on the skid. Consequently, ten extra measurements were taken along the same lanes, but from aft to bow. Furthermore, it was thought worthwhile to take extra measurements when the plane was immersed horizontally in water. Only nine measurements were taken on each side, since weights put on the plate to keep it immersed, prevented the measurements from being taken along the same lanes as before. It was difficult to prevent the drive wheels from slipping or the entire measuring head from slipping laterally over the surface during these measurements. When the analysis of these measurements gave lower results than before, it was decided to carry out the measurements again, when the plate was horizontal but only slightly wet. The plate was brought outside and on a rainy day, ten more measurements were taken on each side. The average and mode values of each set of Foul Release roughness measurements are shown in Figure 3.8.

Figure 3.7. Measuring the Foul Release roughness of the suspended plate.

The last roughness measurements of the Foul Release surface were more consistent (i.e. they displayed a smaller standard deviation) than previous measurements. This was in accordance with the feeling that the stylus did not stutter over the surface, the drive wheels did not slip and that the traverse of the measuring head proceeded gently. Therefore, the last measurements were used for further analysis and correlation with the frictional resistance. Figure 3.9 depicts the roughness distributions of the three surfaces used for further analysis.

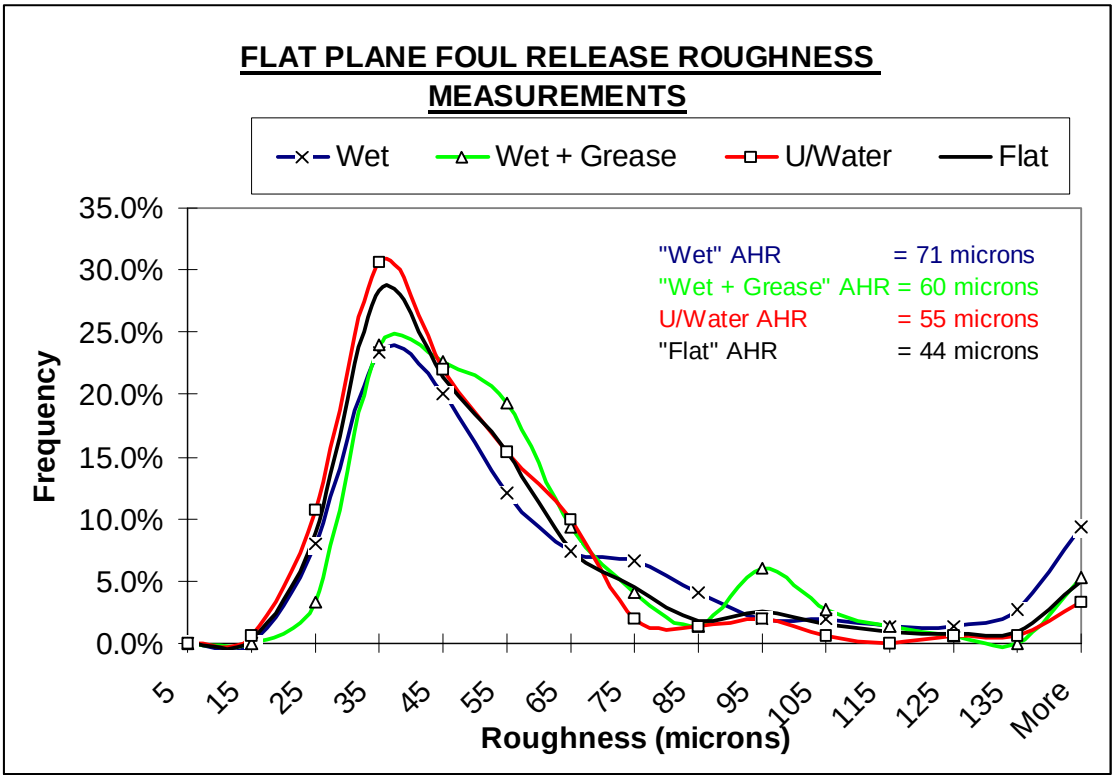

Figure 3.8. Different roughness measurements of the Foul Release surface: 'wet' (surface sprinkled, 12/10/1998), 'wet +grease' (surface sprinkled, grease on stylus, 12/10/1998), 'underwater' (surface immersed, 13-15/10/1998) and 'flat' (wet surface, 5/11/1998)

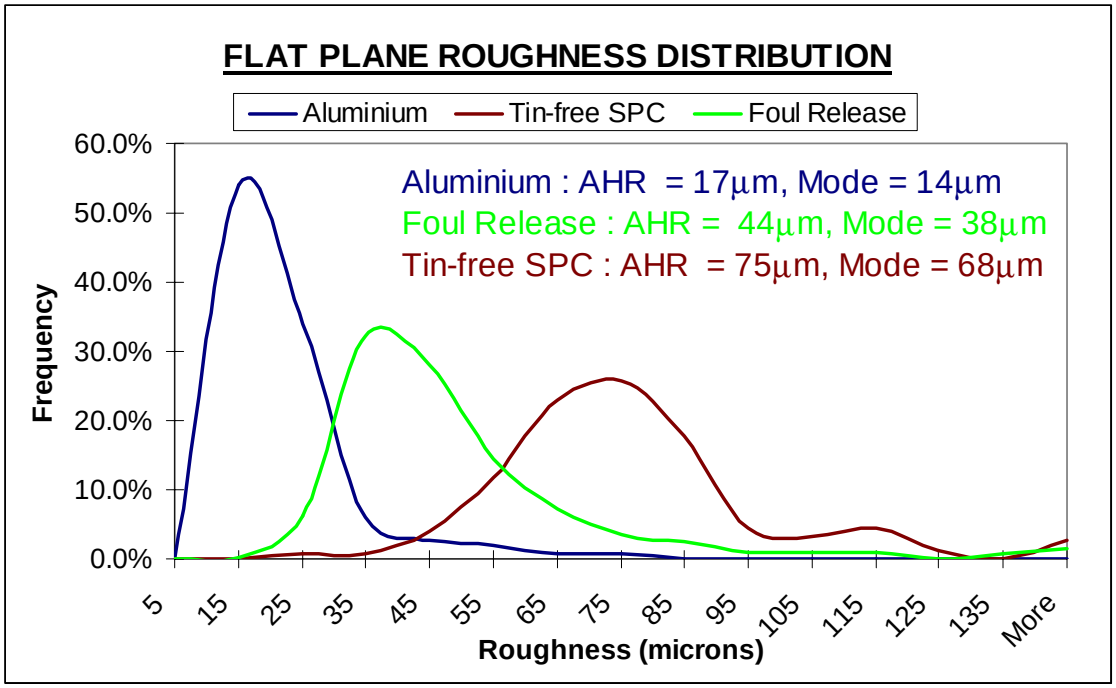

Figure 3.9. The roughness measurements of the three tested surfaces

3.3.2 Experimental results

The Aluminium surface was tested in January 1998. A total number of sixteen runs at different speeds were carried out.

Figure 3.10. The flat plane coated with the Tin-free SPC fitted to the towing carriage.

The SPC surface was tested in July 1998. A total number of twenty-eight runs at different speeds was carried out.. Figure 3.10 shows the flat plane coated with the TBT-free SPC fitted to the towing carriage.

Figure 3.11. The flat plane coated with the Foul Release fitted to the towing carriage.

The Foul Release surface was tested in October 1998. Thirty-seven runs in total were carried out, of which 35 were retained for further analysis. Figure 3.11 depicts the plane suspended fitted to the towing carriage. Figure 3.12 below depicts the plane while it is being towed (from right to left) at a speed of 1.373m/s.

Figure 3.12. The flat plane coated with the Foul Release towed at speed of 1.373m/s

Figure 3.13 shows the total resistance coefficients for the different surfaces along with the ITTC line, against Reynolds number.

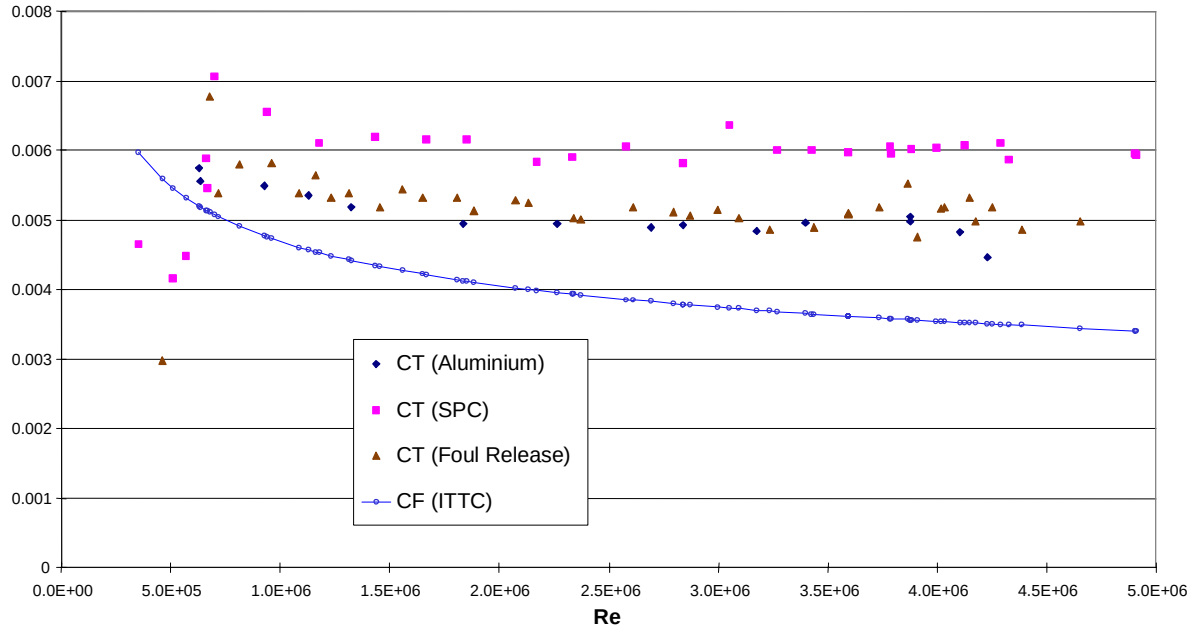

Figure 3.13. Total resistance coefficients against Reynolds number of the three tested surfaces in the Newcastle University towing tank.

Figure 3.13 shows more scatter for the Foul Release surface than for the other two surfaces. Comparison at a Reynolds number of 2.8 million shows a difference between the Aluminium and the SPC surface of 18% and between the Aluminium and the Foul Release surface of 6% (i.e. 12% difference between the two paints). At a Reynolds number of 4.1 million, these differences have increased to 27% and 13% respectively (i.e. 13% difference between the two paints).

The frictional resistance has been calculated for the measurements taken between Reynolds numbers of 2 and 4.2 million. Values below $Re = 2 \cdot 10^6$ were discarded because it was evident that there was a certain extent of laminar-turbulent transition. Above $Re = 4.2 \cdot 10^6$ (i.e. for speeds exceeding 1.8m/s), only a limited amount of recordings was available (cf. Figure 3.3) and a constant speed was not reached over this limited amount of recordings.

The computed wave-making resistance (cf. Appendix A.2) was subtracted from the total resistance to obtain the frictional resistance. The frictional resistance coefficients and the computed wave-making resistance coefficients versus Reynolds number are plotted in Figure 3.14.

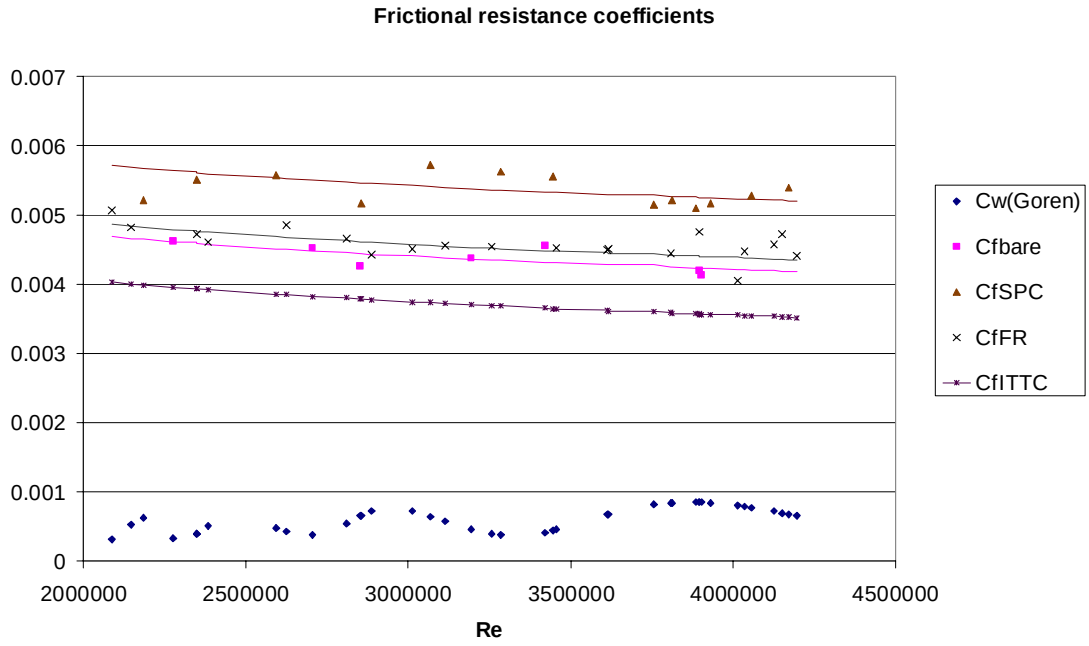

Figure 3.14. Frictional and wave-making resistance coefficients versus Reynolds number

Using the Aluminium surface as smooth reference, measurements at five separate Reynolds numbers are compared in Table 3-2.

Table 3-2. Comparison of frictional resistance coefficients

Re	Cf(bare)	Cf(SPC)	%increase	Cf(FR)	%increase	Cf(ITTC)	%increase
2.3E+06	0.004628	0.005504	18.94%	0.004725	2.10%	0.003942	-14.81%
2.9E+06	0.004266	0.005157	20.90%	0.004422	3.65%	0.003779	-11.41%
3.2E+06	0.00438	0.005624	28.41%	0.004544	3.75%	0.003695	-15.63%
3.4E+06	0.004553	0.005563	22.19%	0.004518	-0.76%	0.003652	-19.77%
3.9E+06	0.004125	0.005168	25.28%	0.004047	-1.89%	0.003558	-13.74%

It is clear from Table 3-2 and Figure 3.14, that the results are scattered. However, the SPC results lie significantly higher than the Foul Release results, while the ITTC line lies significantly below the bare plane results throughout the range of Reynolds numbers considered. Table 3-2 indicates that on average the C_F values are 22.3% larger for the SPC surface than for the Aluminium surface, whereas the C_F values of the Foul Release surface are on average 4.6% larger than the Aluminium surface.

3.4 Experiments in the CEHIPAR Towing Tank with a 6.1m long plate

The experiments reported in this Section were carried out in March 2000 and were made possible by funding under the European CEHMAR programme which promotes access of researchers to large-scale facilities. A full report of the experiments is given by Candries and Atlar (2000). An additional report in Spanish was written by Guerrero (2000).

3.4.1 Facilities and test conditions

3.4.1.1 Towing tank details

Table 3-3 and Figure 3.15 show the principal particulars of the CEHIPAR Calm Water Tank.

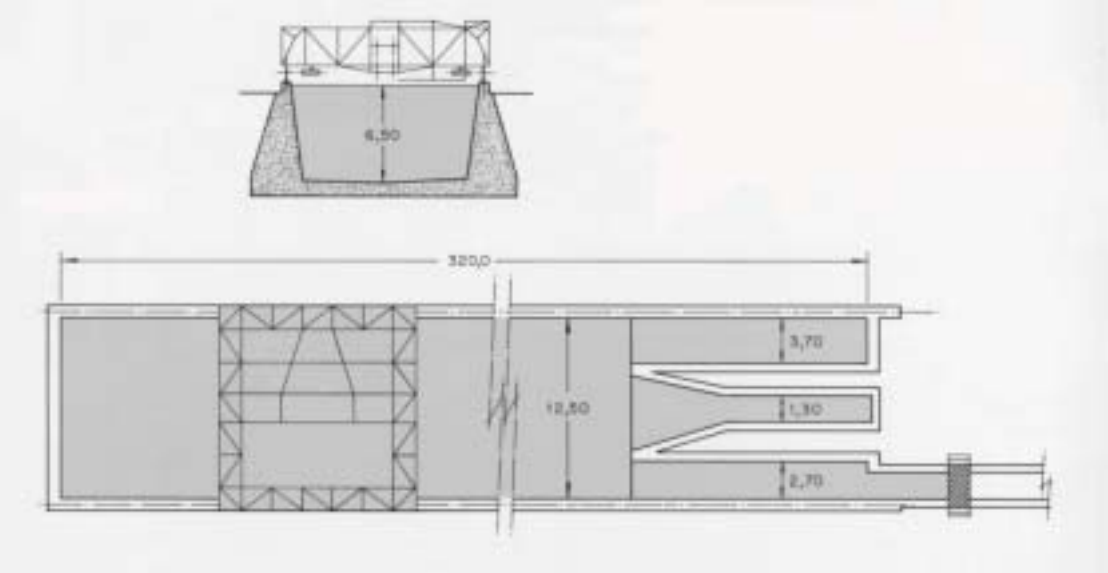

Figure 3.15. Sketch of the CEHIPAR Calm Water Tank particulars.

Table 3-3. Particulars of the CEHIPAR Calm Water Tank

Length	320m
Breadth	12.5m
Water Depth	6.5m
Maximum Carriage Speed	10m/s

Total resistance measurements were carried out up to a speed of 8m/s over a Froude Number range of 0.125 to 1 or a Reynolds Number range $1.2 \cdot 10^6$ to $4 \cdot 10^7$.

The tank has a manned carriage, as shown in Figure 3.16, that was fitted with a Kempf and Remmers dynamometer, shown in Figure 3.17, to measure the 6 force and moment components of which only the component in the longitudinal direction was recorded. The

limit of the dynamometer is 150kg, which restricted the maximum speed of the experiments to 8m/s.

Figure 3.16. Photograph of the manned carriage.

Figure 3.17. Photograph of the dynamometer.

3.4.1.2 Model details

The aluminium plate manufactured for these experiments was modelled on NSRDC friction plane model 4125, which was used for similar experiments (Todd, 1951; West, 1973). Figure 3.18 shows the main particulars of the plate used in the experiments. Two aluminium sheets of 6000mm by 1500mm by 5mm were fitted onto a wooden frame. Two 150mm long solid aluminium ends were fitted to taper the plate The wooden frame has a 2000mm by 1420mm by 80mm void space in the middle for ballasting. The plate was designed to have a total weight of 773.362kg at a draught of T = 1m.

Turbulence stimulating studs were fitted on each side at 35mm aft of the bow. The studs were 3mm in diameter and 2.5mm in height and had a vertical spacing of 25mm, in accordance with the standard recommendations of Hughes (Hughes and Allan, 1951). Vertical lines and waterlines were marked on the aluminium surface with a spacing of 315mm and 20mm respectively, as shown in Figure 3.19.

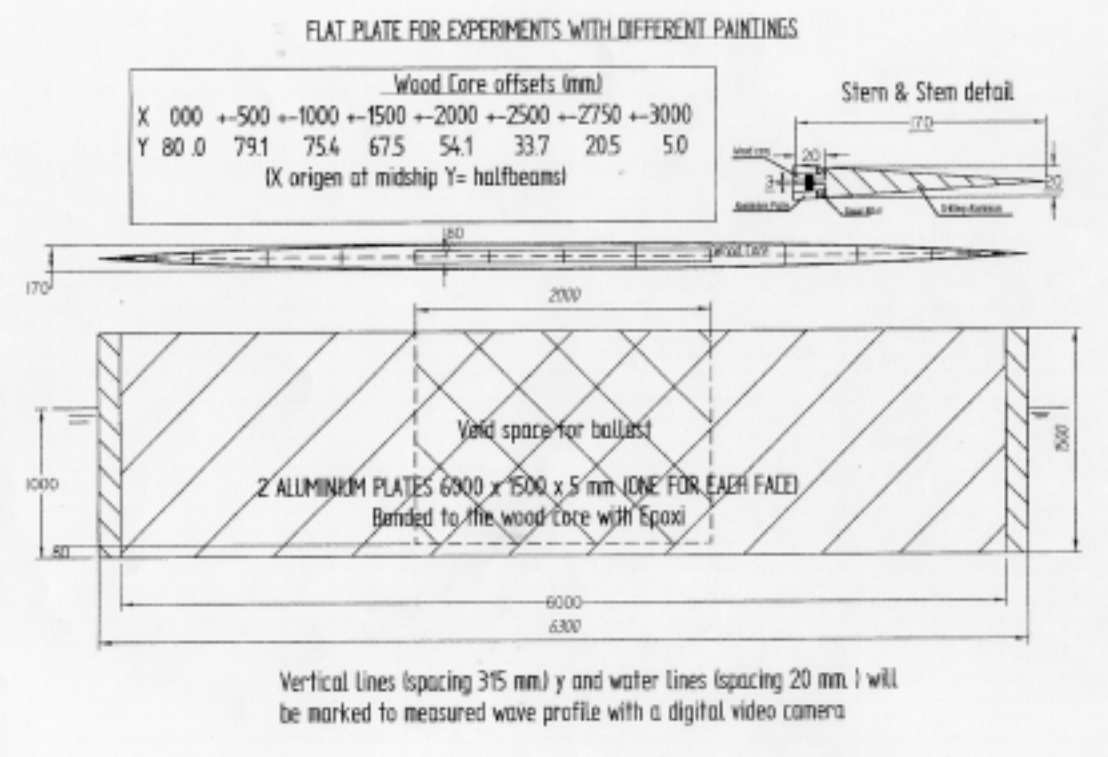

Figure 3.18. Flat plate particulars.

Table 3-4 lists the hydrostatic particulars of the plate valid for the experiments.

Table 3-4. Hydrostatic particulars of the plate.

	T = 1m
B (m)	0.17
L (m)	6.3
WPA (m^2)	0.77336
S (m^2)	13.37767
∇ (kg)	773.362
$C_P = C_B$	0.722

Figure 3.19. The flat plate, marked with vertical and waterlines, prior to first immersion.

3.4.1.3 Application of the two different coating schemes.

The paints were applied in a spraying booth with AISA-made high-pressure spraying equipment, shown in Figure 3.20.

Figure 3.20. Spraying equipment.

3.4.1.3.1 First coating scheme: Tin-free Self-Polishing Co-polymer

The first coating scheme consisted of one layer of primer with a thickness of 100µm (corresponding to a wet film thickness of 175µm), and two layers of antifouling with a thickness of 125µm for each layer.

The primer, called 'Intershield', consists of two components: a bronze base (ENA300) and a curing agent (ENA303), and was applied directly onto the clean Aluminium surface. 6 hours later, the first layer of the Tin-free Self-Polishing Co-polymer (SPC), called 'Intersmooth 360 Ecoloflex (BEA369)', was applied, as shown in Figure 3.22. The second layer of the antifouling was applied the following morning. Figure 3.23 shows the appearance of the SPC surface after testing.

Figure 3.21. Application of the primer.

Figure 3.22. Application of the first coat of Tin-free SPC.

Figure 3.23. The appearance of the SPC surface after testing: the different colour shade due to polishing of the coating under the waterline is clearly visible.

3.4.1.3.2 Second coating scheme: Foul Release system

For the second coating scheme, the surface was first cleared of the Tin-free SPC. Several methods were tried, but eventually the best procedure was to heat the surface with hot air and to gently scrape off the antifouling, as shown in Figure 3.24. However, there were several large patches where the primer came off as well, as shown in Figure 3.25. In order to get as smooth a surface as possible, the surface was sanded, shown in Figure 3.26, and vacuum cleaned. The surface after sanding is shown in Figure 3.27.

Figure 3.24. The removal of the Tin-free SPC by blowing hot air and gently scraping the surface.

Figure 3.25. Patches of exposed aluminium after removal of the Tin-free SPC.

On this surface, a flash coat of primer was applied, followed four hours later by the tiecoat of the Foul Release system. The tiecoat, called 'Intersleek 386', consists of curing agent (BXA330), a light-grey base (BXA386) and an accelerator (BXA391). Figure 3.28 shows the appearance of the tiecoat just after its application. The following day, the topcoat of the Foul Release system was applied. The topcoat, 'Intersleek 425', consists of a blue base (BXA812), a curing agent (BXA821) and an accelerator (BXA822). Figure 3.29 shows the appearance of the topcoat just after its application. Figure 3.30 shows the appearance of the plate prior to immersion.

Figure 3.26. Sanding of the surface.

Figure 3.27. The surface after sanding.

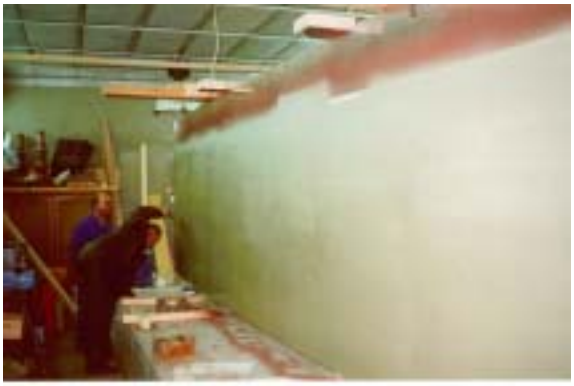

Figure 3.28. Foul Release system: tiecoat.

Figure 3.29. Foul Release system: topcoat.

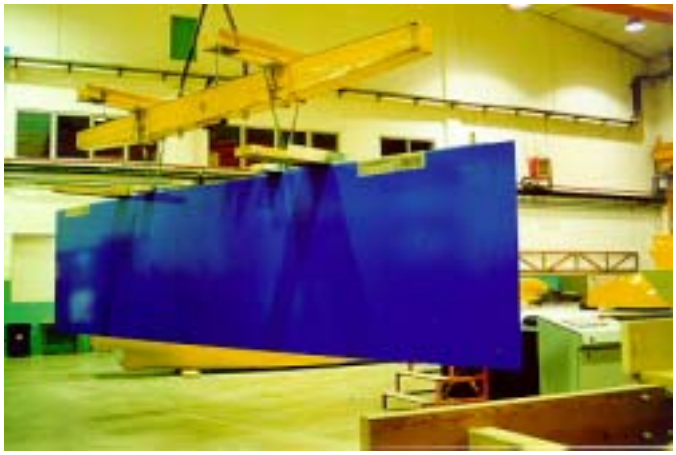

Figure 3.30. The plate coated with the Foul Release system prior to immersion.

3.4.1.4 Roughness measurements

The roughness measurements were carried out with the BMT Hull Roughness Analyser. In order to obtain steady measurements of the Foul Release surface, the surface was slightly wetted with a piece of cloth, but prior to testing it was difficult to prevent the gauge from slipping sideways. However, after testing this was not the case and the surface had to be wetted only very slightly.

Table 3-5 presents the average, mode and standard deviation of the different surfaces.

Table 3-5. Statistical roughness characteristics (in microns)

Surface	Average	Mode	Standard deviation
Clean aluminium	18	10	9.5
Aluminium after testing	42.5	40	20
SPC before testing	38.5	34	16
SPC after testing	39.5	38	16
Scraped	68	20	32
Sanded	37	22	30.5
Foul Release before	83	90	35.5
Foul Release after	62	48	24

It is clear from Table 3-8 that the Aluminium surface measured after testing was much rougher than when the surface was clean. This is explained by the fact that sand particles seemed to attach to the plate, particularly on the vertical lines which had been marked with a standard water-insoluble marker, as is shown in Figure 3.31. The roughness histograms of the clean and 'dirty' Aluminium surface are shown in Figure 3.32.

Figure 3.31. The aluminium surface after testing: sand particles around the marked line

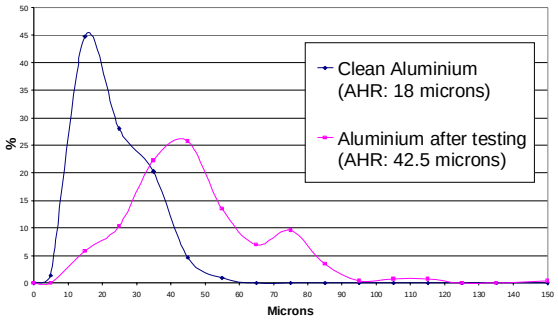

Figure 3.32. Roughness histograms: Aluminium

The application of the Tin-free SPC appeared to have been excellent and this can be seen in Figure 3.34 from the low average roughness values of the roughness histograms before and after testing. Figure 3.33 shows the surface after testing, with its typical different colour shade below the waterline due to polishing of the coating.

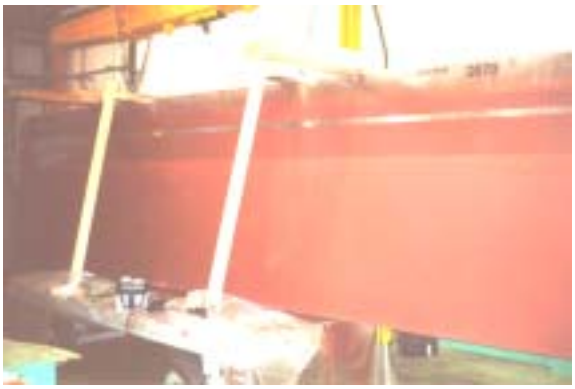

Figure 3.33. SPC surface after testing.

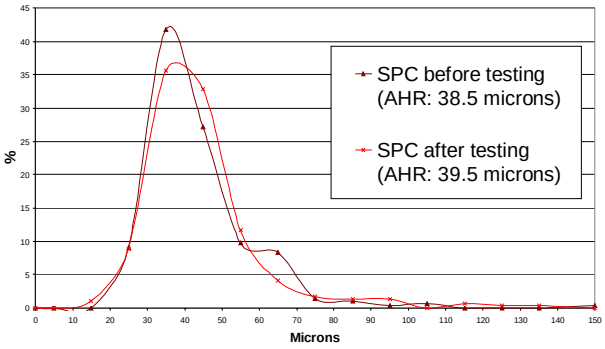

Figure 3.34. Roughness histograms: SPC.

Figure 3.35. Measuring the roughness of the scraped surface

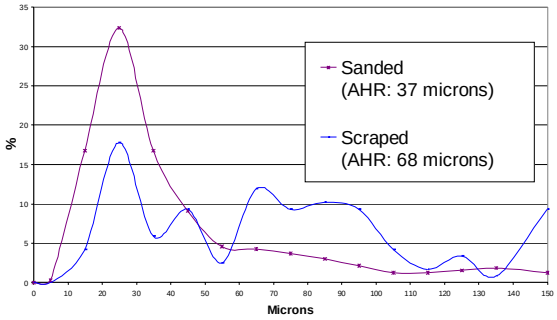

Figure 3.36. Roughness histograms: scraped and sanded surfaces.

When the SPC was scraped off, the average roughness was very high. Figure 3.35 shows the measurement of the roughness of the scraped surface, and clearly shows that the surface consisted of patches of exposed aluminium and patches of scraped (and therefore rough) primer. This had its repercussions in the roughness histogram, shown in Figure 3.36, with a low peak at 25 microns, a high plateau at 60-100 microns, and a high tail-end of very high readings which would be measured at the jump between aluminium and primer. The consequence of the sanding afterwards was that the plateau readings of the primer and the

jumps between aluminium and primer were smoothened out, as is clear from the second histogram in Figure 3.36.

The application of the Foul Release system had not been ideal. The pressure at the tip of the spray-gun was sometimes too low which caused poor atomisation of the paint. Sagging of the tiecoat had occurred a couple of times, once to a severe extent. The overall impression of the surface before testing was 'uneasy' and reminiscent of orange peel. Moreover, close inspection still revealed the difference between the patches where the aluminium had been exposed by the scraping and where the primer had adhered to the surface. This will explain the high average roughness value for the Foul Release surface prior to testing. After testing however, the surface looked much better. Figure 3.37 shows a slightly different colour shade under the waterline and a patch that was restored to its original colour by wiping with a moist piece of cloth. More importantly, the paint looked as if it had 'settled' and the orange peel appearance had disappeared. The roughness histograms of Figure 3.38 show the difference between the surface before and after testing.

Figure 3.37. Foul Release surface after testing.

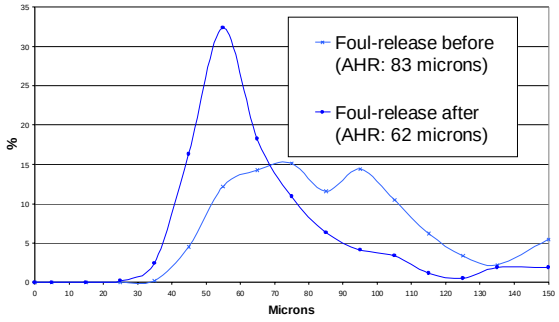

Figure 3.38. Roughness: Foul Release.

coefficient. Figure 3.40 shows the confidence levels for the measured total resistance coefficient values of the Foul Release surface, as obtained by adding 0.1N and –0.1N to the measured total resistance data. Figure 3.40 shows that at Fn = 0.2 (or U_e = 1.5m/s), the uncertainty is 2.1%, but at Fn = 0.5 (or U_e = 4m/s), the uncertainty is only 0.2%. Due to time constraints it was not possible to carry out a detailed uncertainty analysis as carried out in Chapter 5 for the boundary-layer measurements.

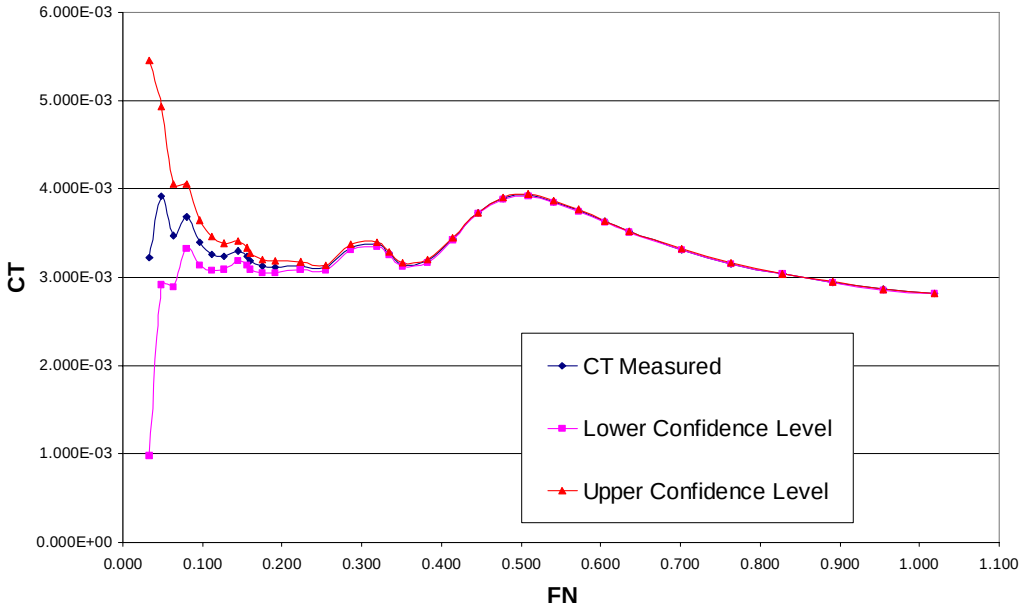

Figure 3.40. Estimated confidence levels versus Froude number of C_T (Foul Release)

A comparison of the differences of the total resistance coefficients of the two coated surfaces with the aluminium surface indicates that above a Froude number of Fn = 0.5, the Foul Release surface exhibits a drag which is on average 1.56% higher than the aluminium surface, and the SPC surface exhibits a drag which is on average 2.91% higher than the Aluminium surface.

The frictional resistance was computed by subtracting the wave-making resistance computed by the CFD programme SHIPFLOW (cf. Appendix A.2). It was found that the frictional resistance of the Aluminium surface showed excellent agreement with the Schoenherr line, which is given by the equation:

$$0.242 / \sqrt{C_F} = \log(\mathrm{Re}\, C_F) \tag{3.2}$$

Above a Froude number of 0.5, the frictional resistance of the Foul Release and the SPC surface respectively was on average 2.1 and 3.8% higher than the Aluminium surface.

3.5 Experiments in the Denny Tank with a 3.2m long wave-piercing catamaran model

The experiments were carried out between July 1999 and February 2000 by kind permission of the University of Strathclyde. Full details of the experiments are given by Candries and Atlar (2000b)

3.5.1 Facilities and test conditions

3.5.1.1 Test tank details

The experiments were carried out in the Denny tank in Dumbarton, Scotland. The tank was built in 1884 closely following Froude's tank in Torquay in size and features (Gawn, 1955), which is quite clear if one compares Figure 3.41 with Figure 3.42. After the dismantlement of the Torquay tank in the same year, the Denny tank effectively became the oldest towing tank in the world.

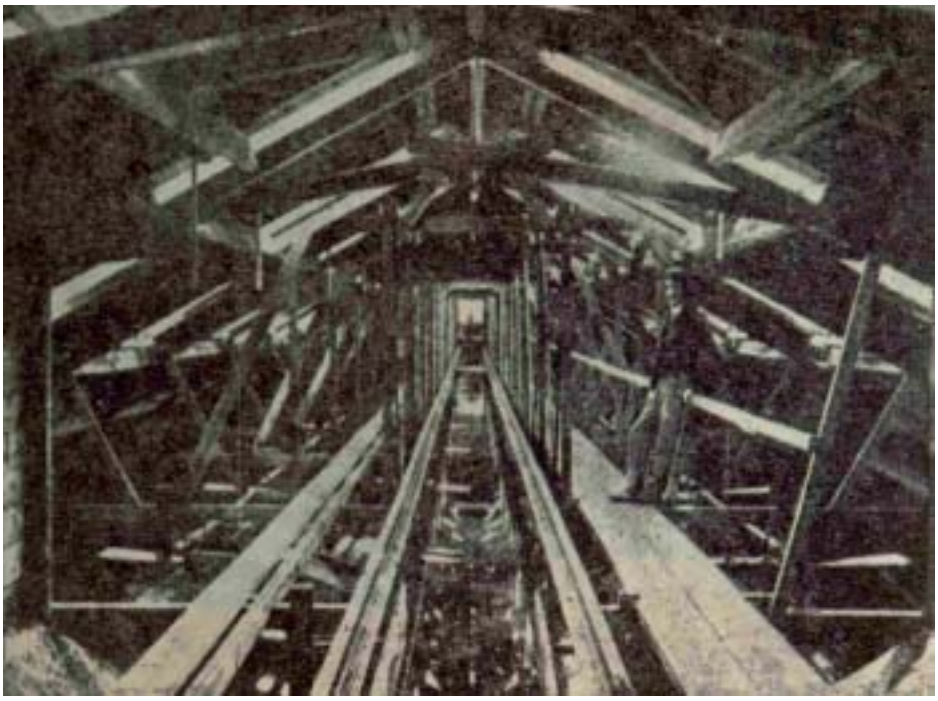

Figure 3.41. Froude's experiment tank in Torquay, photographed in 1871 (From Gawn, 1955).

The principal particulars of the Denny tank are shown in Table 3-6.

Table 3-6. Particulars of the Denny Tank

Length	65 m (max.: 93m)
Breadth	6.8m
Water Depth	2.19m
Maximum Carriage Speed	5.5m/s

Total resistance, running trim and sinkage measurements were carried out up to a speed of 4.7m/s. This corresponds to a Froude Number range of 0.1 to 0.9 or a Reynolds Number range of $1.5 \cdot 10^6$ to $11 \cdot 10^6$.

Figure 3.42. Photograph of the model attached to the carriage.

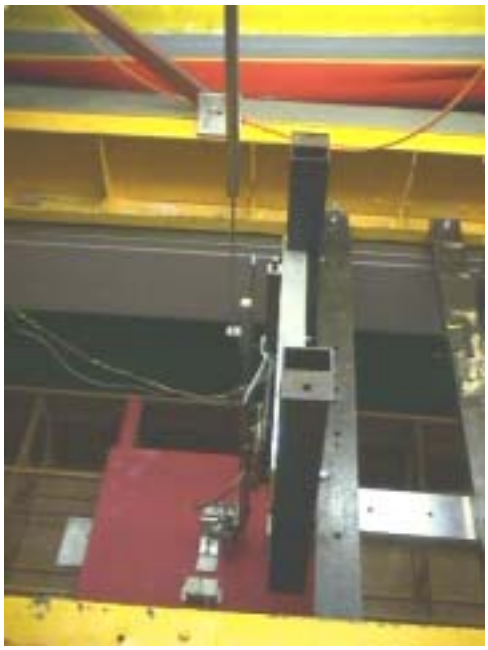

Figure 3.43. Photograph of the measuring equipment. From top to bottom: linear displacement probe, dynamometer and inclinometer.

The tank has a manned carriage which is shown in Figure 3.42. The carriage is equipped with a load cell to measure the resistance, an inclinometer to measure the running trim (positive bow up) and a linear displacement potentiometer to measure the sinkage (positive upwards), which are shown in Figure 3.43. These instruments were calibrated prior to each test series.

3.5.1.2 Model details

A 1/35-scale wave-piercing catamaran model was used for the experiments with particulars given in Table 3-7. The model was made of plywood in 1990 and it was in very good condition. It was towed at the L_{CG} position and ballasted with weights to level trim.

Table 3-7. Particulars of the wave-piercing catamaran.

	Full Scale	Model Scale
LWL	95.08m	2.717m
LCG	39.53m	1.129m
Trim	Level trim	
Surface Area	1614m^2	1.318m^2
Displacement	2000 tonnes	47.394kg

Turbulence stimulating studs, three on each side of the hull, were fitted at a position $L_{WL}/20$ or 135mm aft of the bow. The studs were 3mm in diameter and 2.5mm in height and had a spacing of 25mm. The model is shown with the studs in Figure 3.44.

Figure 3.44. Photograph of the model, positioned to level trim. The waterline is marked in green on the coated surface and the studs are put in 135mm aft of the bow.

3.5.1.3 The different coatings and painting of the model

The first series comprised the testing of the model with its original, very smooth and thin, bright-yellow epoxy gel coat. This series is further referred to as the 'original surface'.

For the second series, the model was coated with a paint of the Foul Release type. In contrast to the Foul Release paint used in the flat plate experiments (cf. Section 3.2.1.3 and 3.3.1.3), this paint, commercially known as 'Veridian', is specifically designed for yachts and is usually applied by rollers, rather than by spraying. For that reason particularly, this type of Foul Release was chosen for this set of experiments since it was not possible to spray the paint systems on the model at the premises, nor was it convenient to transport the model. The paint was applied with 150mm foam rollers in two steps: the tiecoat was applied in the morning, as shown in Figure 3.45, and the topcoat was applied 5 hours later, as shown in Figure 3.46.

Figure 3.45. Application of the Foul Release tiecoat.

Figure 3.46. Application of the topcoat

Prior to the application of the Tin-free SPC used in the third experimental series, the Foul Release paint was stripped off with the solvent 'Xylene' and the use of a paint scraper, as shown in Figure 3.47. This was a time-consuming process since the solvent did not react as desired with the Foul Release coating. Figure 3.48 shows that applying large quantities of solvent caused the coating to blister only to a small extent. The blistered coating then had to be scraped off with the scraper in a delicate manner in order to prevent damage to the surface. Consequently, the surface was gently smoothened with sandpaper. Figure 3.49 shows the condition of the surface after the stripping process.

Figure 3.47. Stripping of the Foul Release coating.

Figure 3.48. Only slight blistering of the coating occurs after application of the solvent.

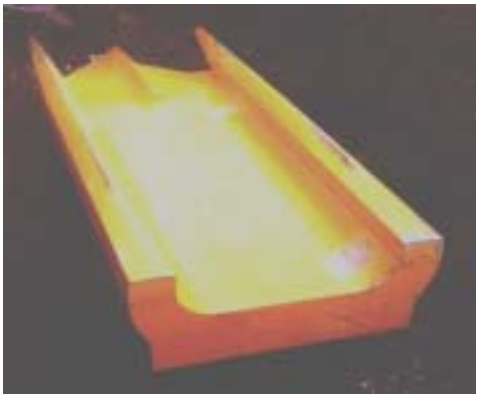

Figure 3.49. Condition after stripping off the Foul Release coating.

Figure 3.50. Condition of the model after application of the Tin-free Self-Polishing Co-polymer.

Because a similar roughness was aimed at, no primer (also omitted for the second series) and only one layer of the SPC (known as 'Intersmooth 360 Ecoloflex') was applied, using 100mm long foam rollers. The standard application scheme for the SPC requires a primer for good attachment to the surface and at least two layers of paint for satisfactory antifouling performance. However, it was considered that the attachment of the paint to the original would be strong enough for the duration of the experiments and that a similar roughness (i.e. only one coat of Tin-free SPC) would allow easier comparison of the different series. Figure 3.50 shows the condition of the model after application of the Tin-free SPC.

3.5.1.4 Roughness measurements

The roughness measurements were carried out for each different surface with the BMT Hull Roughness Analyser. The original surface was analysed both prior to the experiments and after the stripping.

The model was divided in eight different surface sections shown in Figure 3.51, which can be compared with Figure 3.52. Four runs of roughness measurements were carried out for each surface section.

In order to obtain steady measurements of the Foul Release surface, the surface was slightly wetted, but it was difficult to prevent the gauge from slipping sideways.

Figure 3.51. Sketch of the eight sections of the model surface.

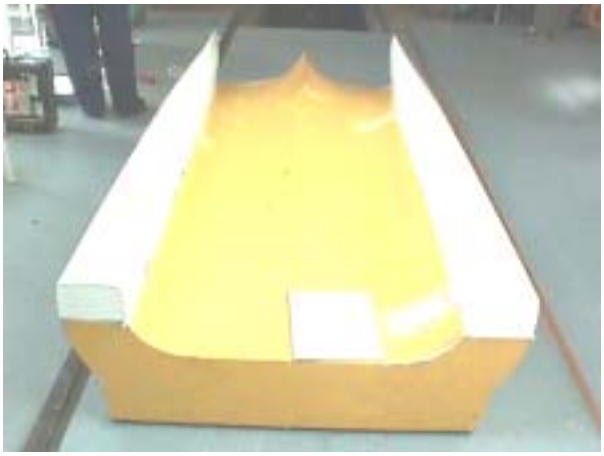

Figure 3.52. Photograph of the model coated with the Foul Release paint.

Table 3-8 presents the average hull roughness, the mode and the standard deviation of the different surfaces. Figure 3.53 shows the roughness distribution of the three tested surfaces.

Table 3-8. Statistical roughness characteristics of the different surfaces (in micron).

Surface	Average	Mode	Standard deviation
Original paint	49	17	45
Foul Release: Topcoat	64	34	39
Stripped : Orig. paint	48	32	26
SPC	66	52	25

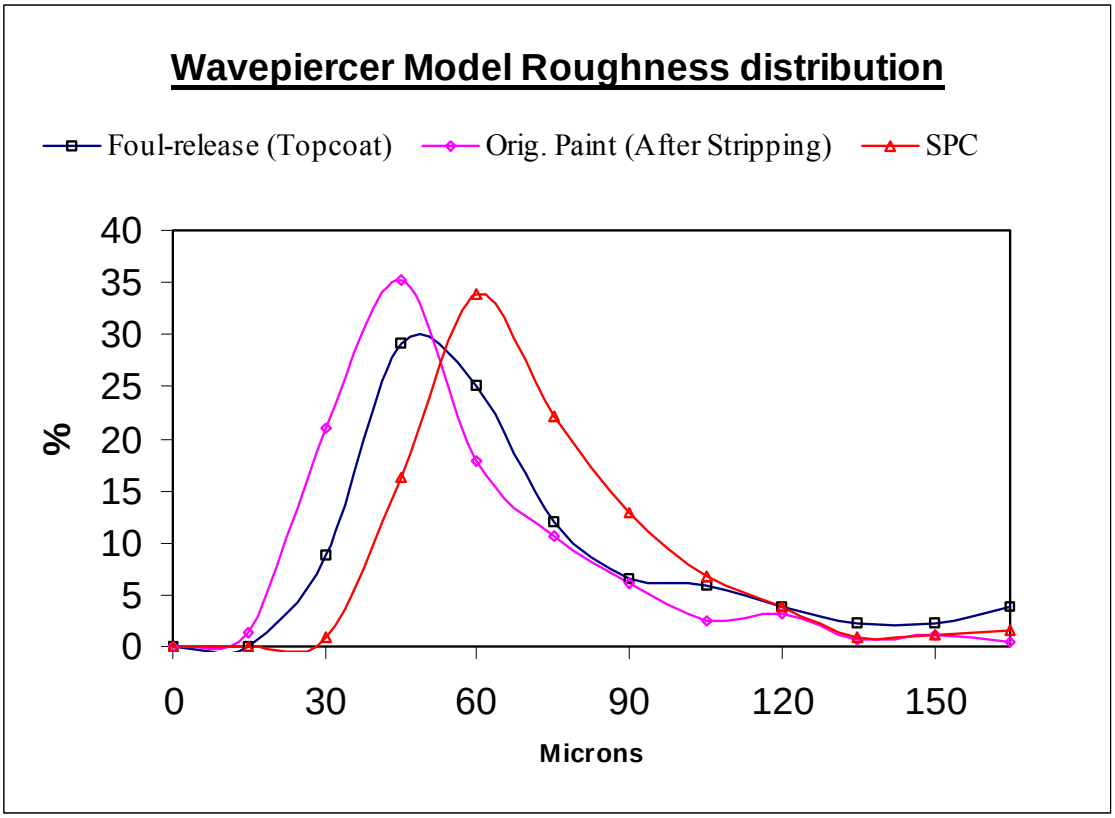

Figure 3.53. Roughness distribution of the tested model surfaces.

Table 3-8 shows that the objective of obtaining a similar Average Hull Roughness value for the coated surfaces was achieved. The AHR values effectively lie within 2 microns. However, the roughness distributions are dissimilar in that the mode of the SPC surface lies significantly higher. The similar AHR is explained by the higher percentage of high roughness values for the Foul Release distribution.

3.5.2 Experimental Results

3.5.2.1 Accuracy of the measurements

Since there were no draught marks on the model and since the exact draught was not known beforehand, the water level was determined from the displacement and the waterline length. Both corresponded well with each other. The level trim position was determined by shifting two 500g ballast weights when the model was in the water. The position of the weights was marked to assure identical position for the consequent series and the tests were carried out at identical water levels. The alignment of the model with the flow was checked by a vertical fork gripping with a horizontal pin placed on the bow of the model (cf. Figure 3.44). The position of the model in the water was checked by visual inspection of the draught marks and by an electronic leveller. Nevertheless, there was a small disagreement between the three series, notably between the left and right hull. It was estimated that the variation in draught was less than ±2mm. An investigation with the CFD tool SHIPFLOW revealed that the influence of this variation in draught was negligible (See Candries et al. (2000) for details).

The relatively small differences in force measured at the lower speeds have a significant influence on the resistance coefficients. Even though the dynamometer was calibrated at the beginning of each series, it was noticed that at the end of the first series, when the dynamometer was calibrated again, the sum of 4 weights of 1kg did not add up to 39.24N but to 42.6N. This inexplicable difference (which did not occur with the inclinometer or the displacement potentiometer) could imply that (some of) the measurements have been overestimated by up to 8.6%. The calibration of the dynamometer was not repeated after the second series but after the third series there was a much smaller difference of 0.6N. This poses some questions about the accuracy of the force measurements.

3.5.2.2 Resistance

Figure 3.54 shows the total resistance versus velocity of the three model surfaces.

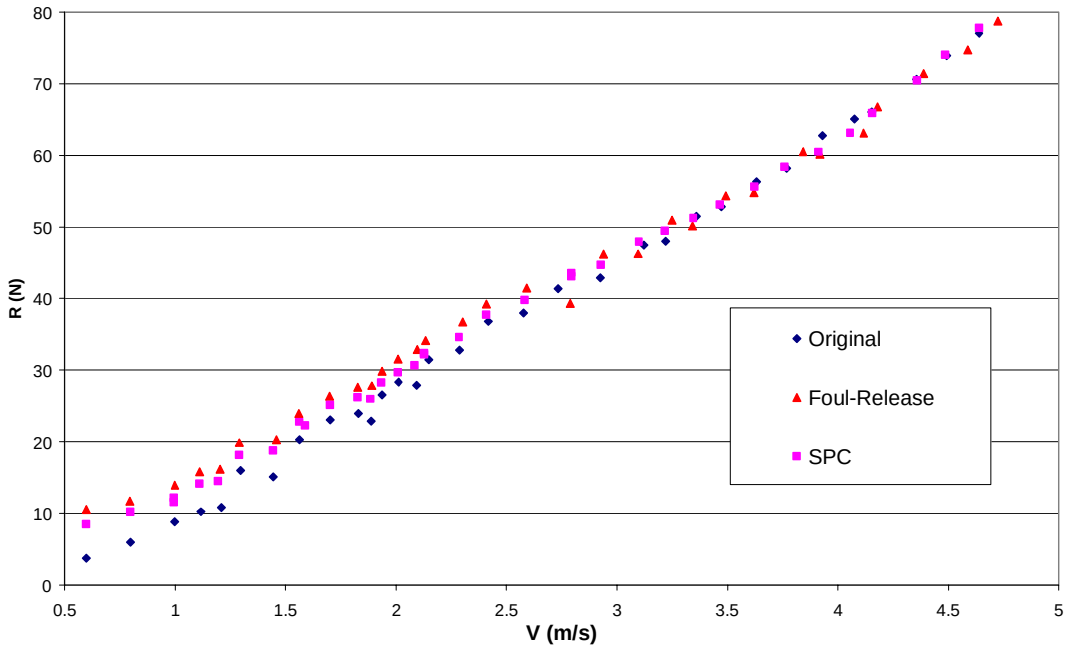

Figure 3.54. Resistance versus velocity for the three different model surfaces.

In Figure 3.55, the total resistance coefficients of the three surfaces are plotted against Reynolds number. Figure 3.55 shows that, as could be expected, the results for the original surface lie below the two rougher surfaces, but only for the lower Reynolds numbers. As the Reynolds number increases, the results for the SPC surface dip below the original surface. Overall, the total resistance coefficient of the Foul Release surface is on average 11.8% higher than the total resistance coefficient of the original surface (19.6% if the first two measurements are included). By linear interpolation, the total resistance coefficient of the SPC surface is on average 3.8% higher than the total resistance coefficient of the original surface. However, above a Reynolds number of $5 \cdot 10^6$ the difference between the two coatings and the original surface are +1.1% and –7.1% respectively.

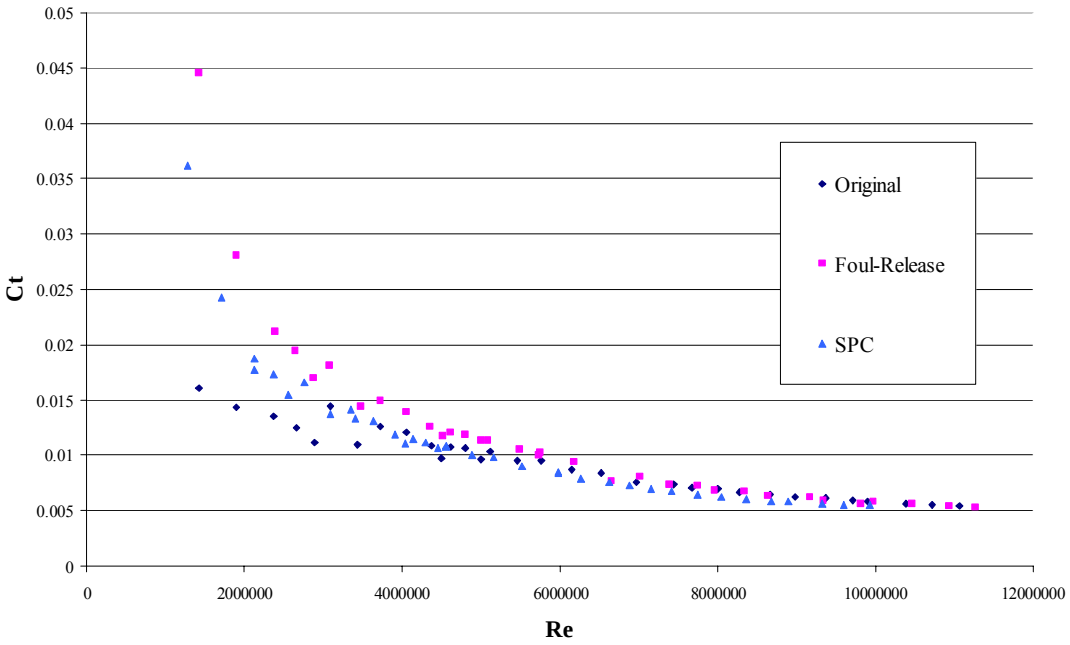

Figure 3.55. Total resistance coefficient versus Reynolds Number for the tested model surfaces.

The wave-making resistance computed by SHIPFLOW (cf. Appendix A.2) was subtracted from the total resistance to obtain the frictional resistance. Above a Reynolds number of 5 million, the linearly interpolated frictional resistance coefficient of the SPC surface is on average 9.2% lower than the original surface, and the frictional resistance coefficient of the Foul Release surface is on average 1.9% higher than the original surface. In other words, the frictional resistance coefficient of the Foul Release surface is on average 12.2% higher than the SPC surface.

3.5.2.3 Sinkage and trim

The sinkage at the centre of gravity and the running trim versus Froude number are shown in Figure 3.56 and Figure 3.57 respectively. They show relatively good comparison for the three different surfaces.

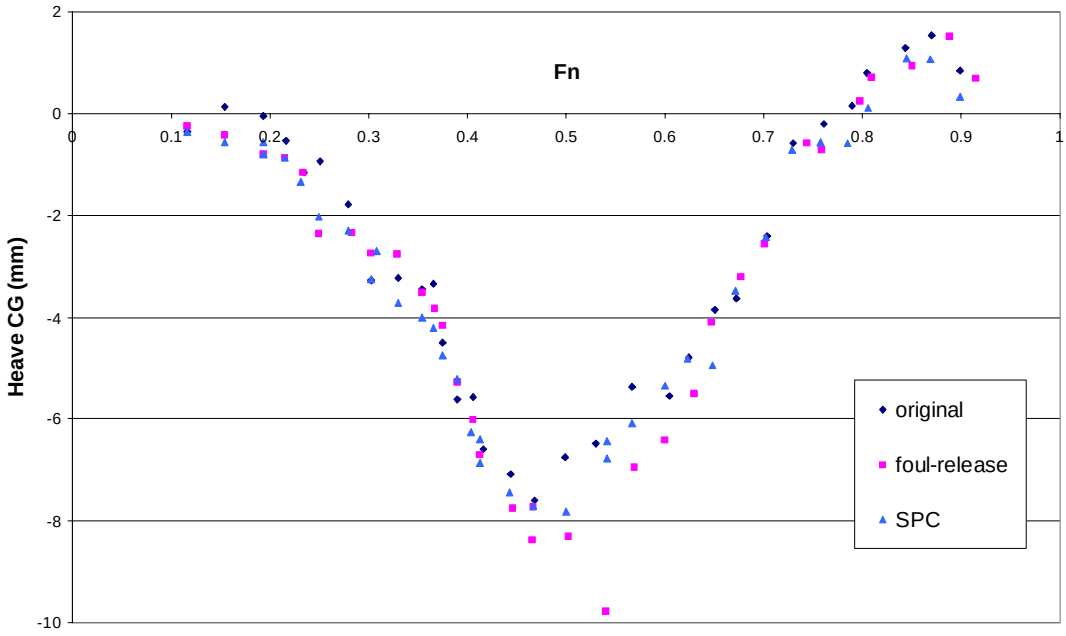

Figure 3.56. Sinkage of model versus Froude Number for the three different surfaces.

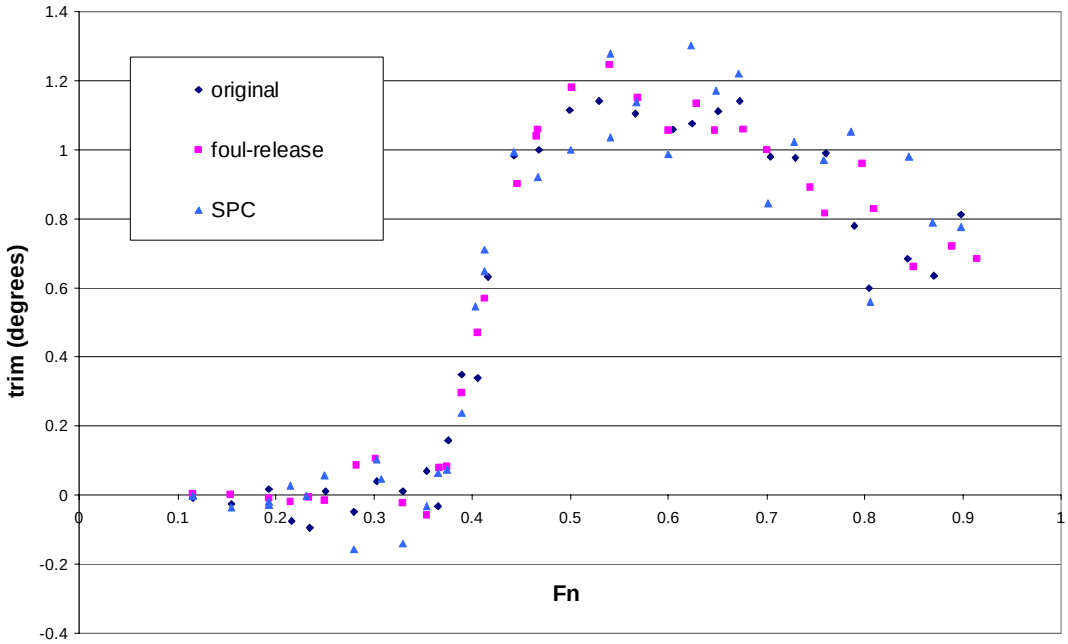

Figure 3.57. Running trim of model versus Froude Number for the three different surfaces.

3.5.2.4 Discussion of the experimental results

The resistance of the model was higher for the Foul Release surface than for the SPC surface, whereas there were no discernible differences for sinkage and running trim for the different surfaces. The fact that the Foul Release surface had higher resistance is unexpected in connection with the roughness measurements and with the previous flat plate experiments reported in the Sections 3.3 and 3.5.

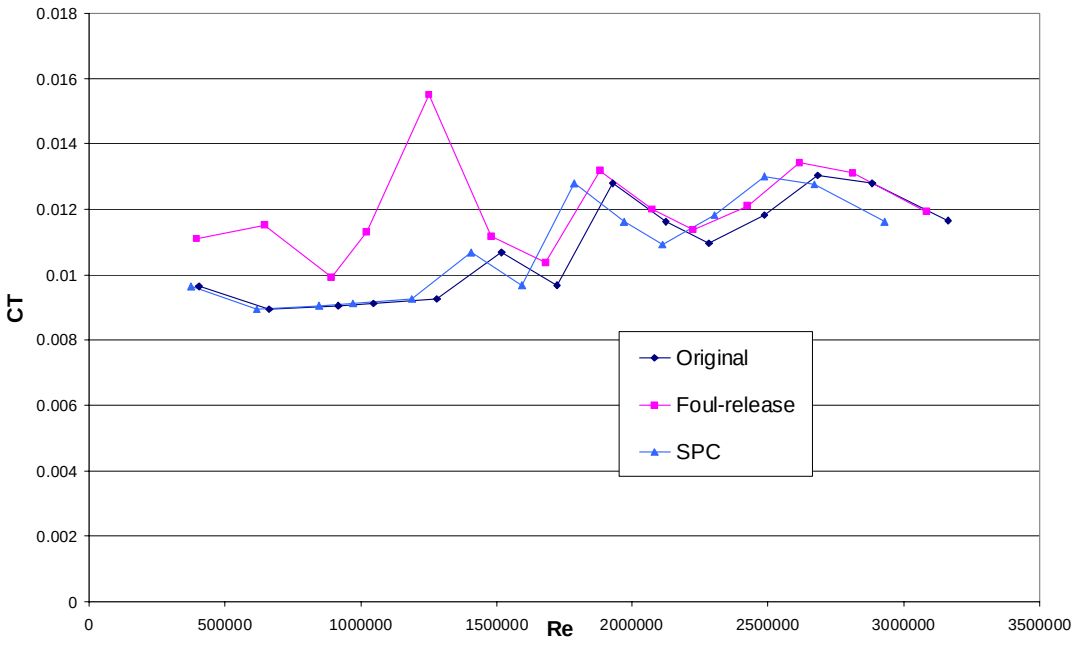

Figure 3.58. Differences in total resistance coefficient between the different surfaces from (White, 1999).

However, the preparatory tests which had been carried out with a smaller catamaran model also indicated that the drag measured for the Foul Release surface seemed higher than for the SPC surface, whereas the measured roughness was considerably lower for the Foul Release surface, 80 microns, than for the SPC surface, 150 microns (White, 1999). The 1/25-scale model of the wave-piercing catamaran Condor 9, had a waterline length of 1.6168m, a displacement of 21.09kg, a demihull beam of 0.121m, an overall beam of 0.728m, a draught of 0.0792m and a wetted surface area of 0.578m^2. Instead of studs, a trip wire was used to stimulate turbulence, and the paint systems were applied by brush. The roughness measurements reported in (White, 1999) should be treated with extreme caution as they were not taken on a flat surface and not enough measurements were taken to be statistically reliable. Figure 3.58, plotted from the data reported by White (1999), shows that on average,

the total resistance of the Foul Release surface seems higher than the original surface, whereas the SPC surface virtually coincides with the original surface. However, if measurements below Re = $2 \cdot 10^6$ are discarded as in the first set of experiments (cf. Section 3.3.2), the total resistance values no longer show clear differences for the three surfaces.

Bearing in mind the experimental uncertainties for both model tests, the importance of the pilot experiments is that they largely confirm the trends with regards to drag for a different model (albeit of the same ship type). In conjunction with the flat plate experiments, it is logical to assume that the method of application which was different for the model tests than for the flat plate tests must have influenced the drag increases of the surfaces.

Only one coat of paint was applied for both schemes aiming at comparable roughness for both paint systems, but the layer of SPC was very thin. Particularly at highly curved areas of the model, the thickness of the Foul Release paint applied by rollering was much higher (because of the different rheological characteristics and higher viscosity of the Foul Release paint), as shown in Figure 3.59. The roughness of these areas was not measurable with the stylus instrument. Spraying the Foul Release onto the model could have prevented this thickness build-up. Furthermore the choice of aiming for similar roughness was questionable, and the simulation of full-scale application schemes is much more relevant.

Rollering or brushing the Foul Release paint may not be the ideal method of application with regards to drag. This will be further investigated in Chapter 5 where a direct comparison between a sprayed and a rollered Foul Release surface will be made. The roughness characteristics of the surfaces will be investigated in Chapter 6 and an explanation for the differences observed in the model experiments will be given in Chapter 7.

Figure 3.59. Paint thickness build-up of the Foul Release system around areas of high curvature.

3.6 Conclusions of the resistance experiments

A comprehensive experimental study of the frictional resistance of a Tin-free SPC and a Foul Release surface has been made. Table 3-9 presents a summary of the findings from the three sets of experiments in terms of average roughness and the average frictional resistance increase in comparison with the respective smooth reference surfaces, along with the employed calculation method and the range of validity.

Table 3-9. Summary of the experimental results

Surface	Average Roughness (μm)	ΔC_F (compared to reference, %)
2.55m long plate		least-squares regression, 2e6 < Re < 4.2e6
Aluminium	17	
Foul Release	44	3.9
SPC	75	23.4
6.3m long plate		linear interpolation Fn > 0.5 (Re > ca. 2e7)
Clean Aluminium	18	
Foul Release	62	2.1
SPC	39	3.8
Catamaran model		linear interpolation Re > 5e6
Original surface	49	
Foul Release	64	1.9
SPC	66	-9.2

The following conclusions are made from the resistance experiments:

- The flat plate experiments showed that the sprayed Foul Release system exhibits less drag than the Tin-free SPC system. This is not surprising in the case of the first set of experiments since the measured average hull roughness was lower for the Foul Release system. However, it is surprising in the case of the second set of experiments where the average hull roughness was higher for the Foul Release system than for the Tin-free SPC system. This indicates that the added drag does not correlate with the average hull roughness measured by the BMT Hull Roughness Analyser.
- The third set of experiments with the wave-piercing catamaran model showed higher resistance for the rollered Foul Release system than for the Tin-free SPC system. It is thought that the application method of rollering the Foul Release system may

have an influence and this will be further investigated in the boundary-layer experiments presented in Chapter 5.

- Another important issue which has become clear from these experiments is the special care with which roughness measurements have to be carried out with the BMT Hull Roughness Analyser over Foul Release surfaces. If the surface is dry, it is likely that the stylus of the measuring head will stutter over the surface, resulting in unrealistically high readings. The surface has to be wetted with a piece of cloth to prevent this. However, if the surface is too wet, the measuring head very easily slips sideways which may also cause the readings to be too high. It is thought that some of the full-scale AHR readings in Table 2.1 might therefore have been overestimated. The roughness characteristics of the analysed sample plates measured with an optical measurement system will be presented in Chapter 6.

Chapter 4: A review of turbulent rough-wall boundary layers

4.1 Introduction

In this Chapter, the literature on turbulent rough-wall boundary layers is reviewed. This material will provide a basis to conduct and analyse the boundary-layer experiments reported in Chapter 5.

Section 4.2 is an introduction to the concept of the boundary layer and some boundary-layer parameters are defined. Section 4.3 presents the equations which govern the motions in the turbulent boundary-layer. Smooth-wall velocity profiles are presented in Section 4.4 and rough-wall velocity profiles are presented in Section 4.5. Structural boundary-layer characteristics are reviewed in Section 4.6. Successful boundary-layer experiments depend on the accurate measurement of the shear stress at the wall which determines the friction velocity used to scale many of the boundary-layer parameters. Several such measuring techniques have been reviewed in Section 4.7.

4.2 The turbulent boundary layer

In 1904, Ludwig Prandtl introduced the concept of the boundary layer as a thin layer near the surface where the average velocity of the fluid increases from zero at the wall to its full free-steam value. This is due to the fact that the fluid adheres to the wall (the 'no-slip' condition) and frictional forces retard the motion of the fluid in the boundary layer. Even in fluids with very small viscosities, the frictional shearing stresses $\tau = \mu \partial U / \partial y$ in the boundary layer are considerable because of the large velocity gradients of the flow, whereas outside the boundary layer they are very small (Schlichting, 1979, pp. 24-25). The net viscous force on an element of incompressible fluid is determined by the local gradients of vorticity, which form the basis of the conceptual understanding of the production of turbulence in a boundary layer. Vorticity can be produced only at a solid boundary and cannot be created or destroyed in the interior of a homogeneous fluid under normal conditions (Gad-el-Hak and Bandyopadhyay, 1994).

The thickness of the boundary layer is arbitrary because the mean velocity U reaches the free-stream-velocity U_e asymptotically. The boundary layer thickness δ is conventionally defined as the distance from the wall where the local mean velocity U becomes equal to $0.99U_e$. The turbulent boundary-layer thickness for a smooth flat plate at a distance x from the leading edge and at zero incidence is given by Schlichting (1979, p. 638) as:

$$\delta(x) = 0.37 x \, \mathrm{Re}_x^{-0.2} \tag{4.1}$$

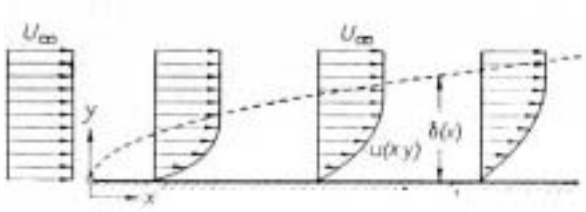

Figure 4.1. Sketch of the development of the boundary layer along a flat plate (From Schlichting, 1979).

Figure 4.1 shows the development of the boundary layer over a flat plate with zero-pressure gradient. The thickness of the boundary layer increases with the distance of the leading edge. Initially, the boundary layer will be laminar, but at a point instabilities will arise and the boundary layer will become turbulent. The transition from laminar to turbulent mainly depends on the Reynolds number, which is the ratio of inertial to viscous forces: $\mathrm{Re}_x = Ux/\nu$,

and occurs for a smooth plate at $Re_x = 3.2 \cdot 10^5$ (Schlichting, 1979, p. 41). The transition process is also dependent on surface roughness, pressure and free-stream velocity fluctuations and other factors. Surface roughness increases the apparent Reynolds number and has the effect of hastening transition. This work concentrates on fully turbulent boundary layers since the Reynolds numbers for ship hull surfaces become so large that the downstream extent of the laminar boundary layer is small compared to the length of the ship.

A boundary-layer thickness parameter which is not ill-defined like δ is the displacement thickness δ_1, which indicates the distance by which the streamlines are shifted due to the formation of the boundary layer and which is defined by:

$$\delta_1 = \int_0^\infty \left(1 - \frac{U}{U_e}\right) dy \tag{4.2}$$

Another important parameter is the momentum thickness θ, which is defined by (Monin and Yaglom, 1971, p. 51):

$$\theta = \int_0^\infty \frac{U}{U_e}\left(1 - \frac{U}{U_e}\right) dy \tag{4.3}$$

The shape factor H is defined by $H = \delta_1/\theta$.

These parameters depend on roughness and pressure gradient, unlike Clauser's boundary-layer thickness parameter Δ, which is defined by (Clauser, 1954):

$$\Delta = \int_0^\infty \frac{U_e - U}{U_\tau} dy \tag{4.4}$$

whereby U_τ is the friction velocity, which is an important scaling parameter (see infra). Another parameter is Clauser's shape parameter:

$$G = \int_0^\delta \left(\frac{U_e - U}{U_\tau}\right)^2 dy \Big/ \int_0^\delta \left(\frac{U_e - U}{U_\tau}\right) dy \tag{4.5}$$

This parameter is dependent on the Reynolds number; Gad-el-Hak and Bandyopadhyay (1994) give the relationship $G = 7.0[1\text{-}e^{-(Re\theta/425)}]$. Clauser (1954) also gives some useful relationships between the boundary-layer thicknesses

$$\begin{aligned} \delta_1 &= (c_f/2)^{0.5} \cdot \Delta \\ \theta &= (c_f/2)^{0.5} \cdot (1 - G(c_f/2)^{0.5}) \cdot \Delta \\ H &= 1/(1 - G(c_f/2)^{0.5}) \end{aligned} \tag{4.6}$$

whereby c_f is the local frictional resistance coefficient.

In fully turbulent flow, the velocity can be divided into a mean and fluctuating component, u = U + u' (similarly for v and w), which is known as the *Reynolds decomposition*. The fluctuations are 3-dimensional swirling motions over a wide frequency range and lead to mixing, momentum exchange and enhanced shear stresses and heat transfer.

Turbulence motion was long thought to be completely random and chaotic, but the turbulent phenomenology actually consists of recurring dynamical flow patterns known as 'coherent motions'. In very general terms, flow visualisation techniques have identified:

i. slow moving vortical streaks very close to the surface
ii. bursts or sweeps of rapidly moving jets of fluid a little further out in the boundary layer
iii. large eddies in the outer part of the boundary layer

The general view of the dynamics is that the low-speed streaks appear near the wall, caused by streamwise vortices. As these vortices develop they 'eject' from the surface and finally 'burst'. The bursting generates intense turbulence and appears to initiate the formation of new vortices (Kim et al., 1971; Cantwell, 1981; Robinson, 1991; Grass et al., 1991). Figure 4.2 gives a conceptual overview of the coherent structures.

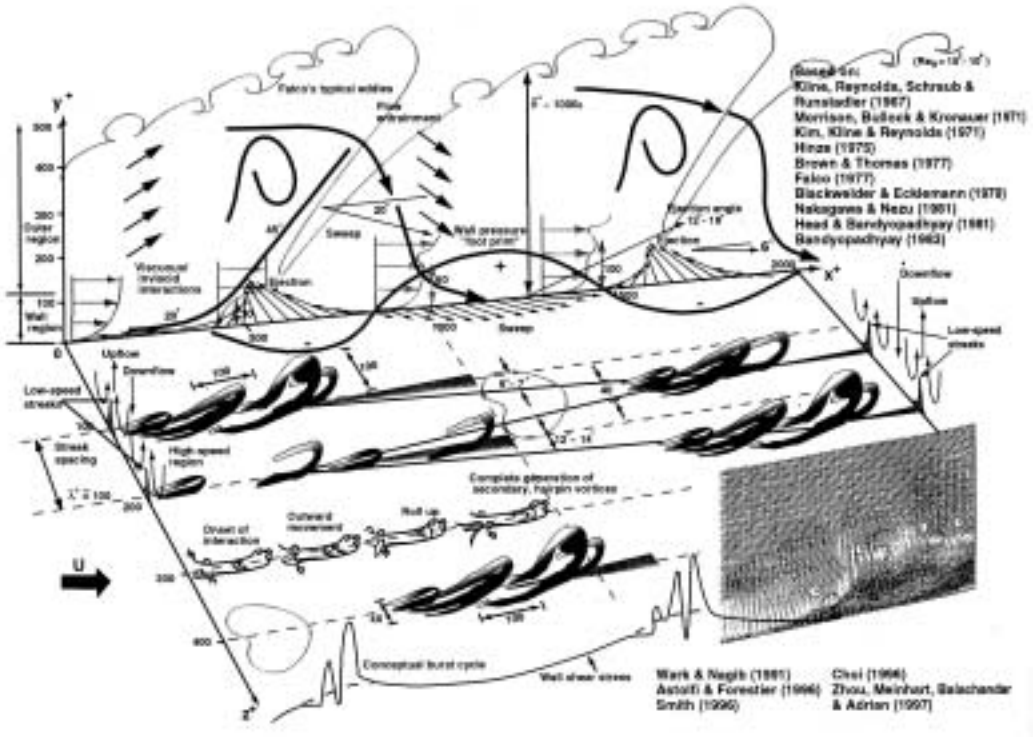

Figure 4.2. Overview of the coherent structures in the turbulent boundary layer (From Meng, 1998)

4.3 Turbulent boundary-layer equations

The fundamental physical laws of physics that govern fluid mechanics are the equation of continuity, which expresses the conservation of mass, and the dynamic Navier-Stokes equations that apply Newton's second law to a small volume of fluid and express the equation of conservation of momentum in each direction. By applying the Reynolds decomposition (i.e. splitting the velocity into a mean and fluctuating part) and averaging these four equations the Reynolds equations are obtained, in which new unknowns $\tau_{ij}^{(1)} = -\overline{\rho u_i' u_j'}$ appear. The appearance of these new unknowns, which are called the *turbulent or Reynolds stresses*, is due to the non-linearity of the equations of fluid dynamics. By considering the mean value of the momentum flux density (see Monin and Yaglom, 1971, p. 261), it becomes clear that in turbulent flows, in addition to the exchange of momentum between fluid particles due to the forces of molecular viscosity (as expressed by the viscous stress tensor), the transport of momentum from one volume of fluid to another appears, induced by the mixing caused by the velocity. In other words, the effect of turbulent mixing on the averaged motion is similar to that of an increase of viscosity. Thus the total boundary-layer shear stress τ can be divided into a viscous and turbulent (or Reynolds) shear stress component:

$$\tau = \mu \frac{\partial U}{\partial y} - \rho \overline{u'v'} \tag{4.7}$$

In near-wall turbulence, the wall shear stress τ_w is one of the most important parameters since it is directly related to the local frictional resistance coefficient:

$$c_f = \tau_w / (\tfrac{1}{2} \rho U_e^2) \tag{4.8}$$

As will be seen in Section 4.4, most of the scaling laws involve the friction velocity U_τ which is directly related to the wall shear stress τ_0 and defined by:

$$U_\tau = \sqrt{\frac{\tau_w}{\rho}} = \sqrt{\frac{c_f}{2}} U_e \tag{4.9}$$

By using the conservation of mass and the two-dimensional Navier-Stokes equations, the steady-state ($\partial U / \partial t = 0$) boundary-layer equations become:

$$\frac{\partial U}{\partial x} + \frac{\partial V}{\partial y} = 0 \tag{4.10}$$

$$U \frac{\partial U}{\partial x} + V \frac{\partial U}{\partial y} = -\frac{1}{\rho} \frac{\partial P}{\partial x} + \upsilon \frac{\partial^2 U}{\partial y^2} - \frac{\partial \overline{u'v'}}{\partial y} - \frac{\partial \overline{u'^2}}{\partial x} \tag{4.11}$$

$$\frac{1}{\rho}\frac{\partial P}{\partial y} = -\frac{\partial \overline{v'^2}}{\partial y} \tag{4.12}$$

assuming that w = 0, $\partial(\ )/\partial z = 0$, V << U, $\partial(\ )/\partial x << \partial(\ )/\partial y$, δ << x. By integrating Equation 4.12 over y and differentiating over x, followed by substitution into Equation 4.11, the two-dimensional momentum equation is obtained:

$$U\frac{\partial U}{\partial x} + V\frac{\partial U}{\partial y} = -\frac{1}{\rho}\frac{\partial P}{\partial x} + \frac{1}{\rho}\frac{\partial}{\partial y}\left[\mu\frac{\partial U}{\partial y} - \rho\overline{u'v'}\right] + \frac{\partial}{\partial x}\left[\overline{v'^2} - \overline{u'^2}\right] \tag{4.13}$$

The left-hand side of Equation 4.13 contains the convection of momentum by the mean flow. The first term on the right-hand side of the equation denotes the momentum contribution of the free-stream pressure gradient, whereas the second term is made up of the viscous and turbulent diffusion of momentum, and the third term includes the turbulent normal stresses.

The turbulent kinetic energy is given by $\overline{q^2}/2 = (\overline{u'^2} + \overline{v'^2} + \overline{w'^2})/2$ and the turbulent kinetic energy equation is given by:

$$U\frac{\partial}{\partial x}\left(\frac{\overline{q^2}}{2}\right) + V\frac{\partial}{\partial y}\left(\frac{\overline{q^2}}{2}\right) + \left(\overline{u'v'}\frac{\partial U}{\partial y}\right) + \frac{\partial}{\partial y}\left[\frac{1}{2}\overline{q^2 v'} - \frac{\overline{p'v'}}{\rho}\right] - \upsilon\frac{\partial^2\left(\overline{q^2}/2\right)}{\partial y^2} + \varepsilon = 0 \tag{4.14}$$

in which the first two terms are the mean flow convection, the third term the energy production, the fourth term is the diffusion by turbulent and pressure fluctuations, the fifth term is the viscous diffusion and the sixth term is the energy dissipation (Cebeci and Smith, 1974, pp. 97-99; Schetz, 1993, pp. 281-282). Figure 4.3 illustrates how these components change over the boundary layer.

It is very important to note that the nonlinearity of the fluid dynamics equations causes the equations to contain more unknowns than the number of equations themselves. This is the so-called *closure problem* of turbulent flows. The equations which govern the movement of the flow cannot be solved without the use of some supplementary speculative closure hypotheses. None of the various semi-empirical closure theories in use is strict and they lead to different conclusions.

In contrast, similarity laws and dimensional analysis obtain results using only general physical reasoning without any use of the dynamic equations and closure hypotheses (Yaglom, 1979).

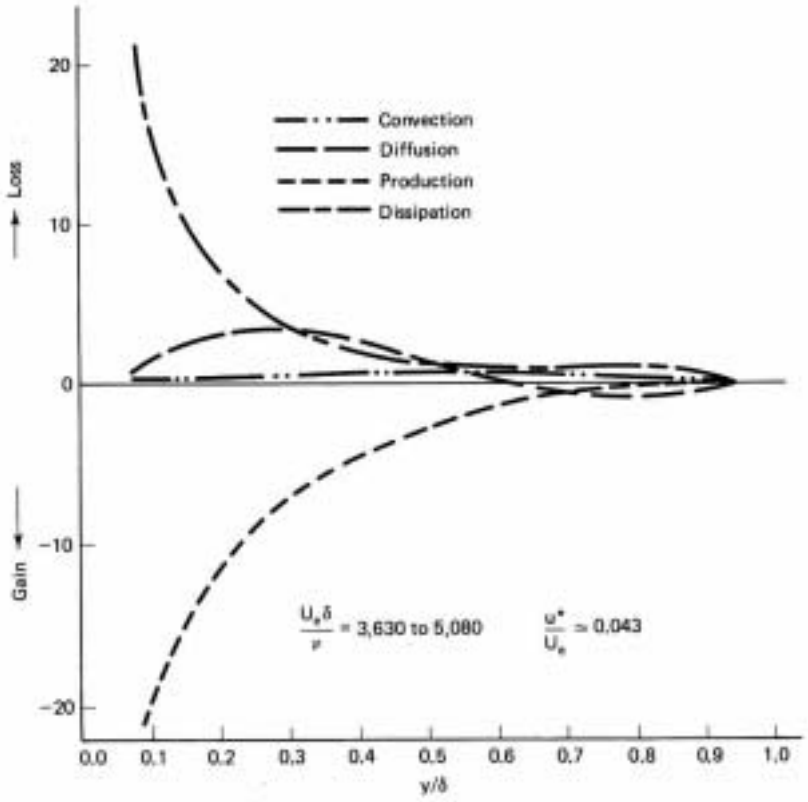

Figure 4.3. Turbulent energy balance in the boundary layer on a smooth plate (From Schetz, 1993, data from Klebanoff, 1955)

4.4 Smooth surface mean velocity profiles

On the basis of experimental data and their physical interpretation, a turbulent boundary layer is regarded approximately as a composite layer made up of inner and outer layers, based on the consideration of the relative importance of viscous and turbulent shear stress in the boundary layer. In terms of similarity laws, the motions in the inner layer are independent of the length scale δ which leads to *Prandtl's universal wall law*, and in the outer layer the relative fluid motions are independent of viscosity, which in turn leads to *von Karman's velocity defect* law (Yaglom, 1979).

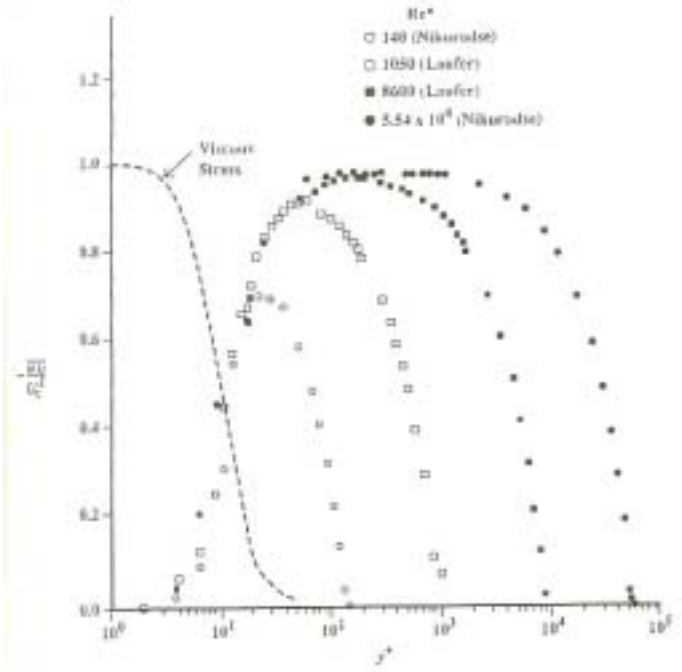

Figure 4.4. Distribution of viscous (dotted line) and turbulent shear stresses in wall-bounded flows (From Gad-el-Hak and Bandyopadhyay, 1994).

Figure 4.4 shows that close to the wall is a region where the mean viscous stress $\mu \partial U / \partial y$ dominates. The wall layer is followed by a region of approximately constant Reynolds stress. Finally, an outer layer layer is characterised by a diminishing turbulence shear stress. The extent of the first region does not depend on Reynolds number and both the viscous and the constant Reynolds stress region are similar in all wall-bounded flows.

The flow close to the wall is sensitive to the local surface conditions while in the outer region, the shearing stress is usually unaffected by them (cf. Section 4.5.1). It is therefore fundamentally impossible to describe the flow phenomena in the entire turbulent boundary

layer in terms of one single set of parameters and it is necessary to treat a turbulent boundary layer as a composite layer consisting of inner and outer regions as shown in Figure 4.5.

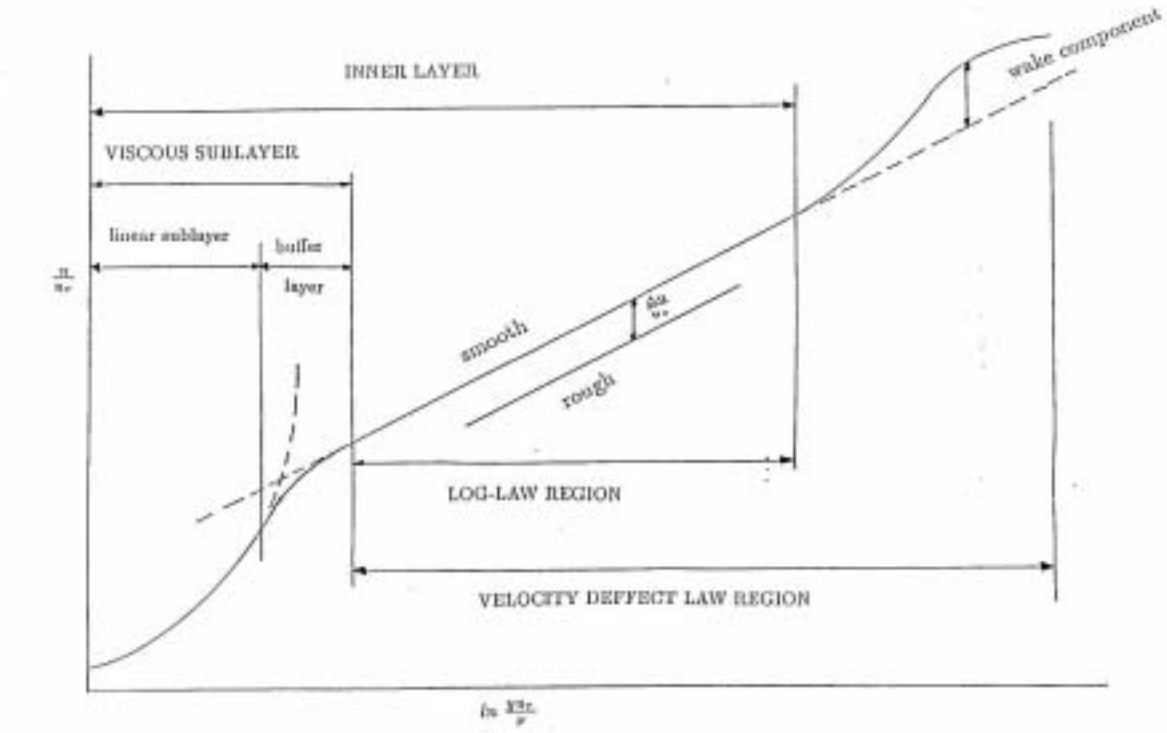

Figure 4.5. The composite picture of the turbulent boundary layer (from Dey, 1989).

The inner region of the turbulent boundary layer occupies only 10 to 20% of the entire boundary layer thickness. In this region the viscous shear stress is predominant and in a zero-pressure gradient boundary layer, the shear stress τ will equal to the shear stress at the wall τ_w across the inner layer. The friction velocity $U_\tau = (\tau_w/\rho)^{0.5}$ is introduced as a normalising quantity to express y and u in 'wall-units': $y^+ = yU_\tau/\nu$ and $u^+ = u/U_\tau$. The velocity distribution is described by the inner law or the law of the wall and is a function of shear stress, density, viscosity and distance to the wall. The region consists of the viscous sublayer and the constant stress or log-law region as indicated in Figure 4.5.

4.4.1 Viscous region

Viscosity appears to be important only up to $y^+ = 30$ and the viscous region can be subdivided into the linear sublayer and the buffer layer. The turbulent shear stress is nearly

zero which implies that the only relevant scaling quantities are the kinematic viscosity ν and the friction velocity U_τ. For hydraulically rough walls (cf. Section 4.5.2), where the average roughness height is greater than the viscous sublayer thickness, the relevant scaling parameters are the characteristic roughness height h and the friction velocity.

The linear sublayer makes up only a very small part of the boundary layer: $y^+ < 5$ or 7, and is characterised by a linear velocity profile:

$$U^+ = y^+ \tag{4.15}$$

Since the viscosity dominates, both the mean and fluctuating velocity components are impeded by the no-slip boundary condition at the wall. The shear stress at the wall τ_w increases as the free-stream velocity U_e increases, which causes the thickness of the viscous sublayer to decrease. Conversely, the thickness of the viscous sublayer increases along a zero-pressure gradient smooth plate as the shear stress decreases.

Gad-el-Hak and Bandyopadhyay (1994) give several Taylor's series expansions asymptotically estimated from considerations of the non-slip condition and continuity and dynamical equations:

$$\begin{aligned} U^+ &= y^+ - 1\cdot10^{-4}y^{+4} + 1.6\cdot10^{-6}y^{+5} + \ldots \\ u'^+ &= 0.3y^+ + c_1\, y^{+2} + \ldots \\ v'^+ &= 0.008y^{+2} + c_2\, y^{+3} + \ldots \\ -\overline{u'v'}^+ &= 4\cdot10^{-4}y^{+3} - 8\cdot10^{-6}y^{+4} + \ldots \end{aligned} \tag{4.16}$$

For $y^+ < 5$, the leading term of each of the expansions suffices, whereas the expansion with three terms for U^+ is valid up to $y^+ = 20$.

As the distance from the wall increases, a departure from the linear velocity profile is noted and the linear sublayer goes over in the buffer layer ($7 < y^+ < 30$). The buffer layer is where both the viscous stress and the turbulence shear stress are important, and where the peak production and dissipation of turbulent kinetic energy occurs (at about $y^+ = 12$). Spalding (1961) gives the following equation for the velocity profile in the buffer layer:

$$y^+ = U^+ + e^{-xC}\left[e^{xU^+} - 1 - xU^+ - \frac{\left(xU^+\right)^2}{2} - \frac{\left(xU^+\right)^3}{6}\right] \tag{4.17}$$

4.4.2 Constant Reynolds stress region (or Log-law region)

This region includes all points within -3dB of the peak Reynolds stress, and extends from $y^+ = 30$ to $y/\delta = 0.2$. In this region, viscous stresses are negligible and the momentum flux is accomplished nearly entirely by turbulence. The only relevant length scale is y itself, and the square root of the nearly constant Reynolds stress, $\sqrt{-\overline{u'v'}}_{\max}$, is the appropriate velocity scale. Therefore the mean velocity gradient can be expressed as

$$\frac{\partial U}{\partial y} \sim \sqrt{-\overline{u'v'}}_{\max} / y \tag{4.18}$$

The well-known logarithmic velocity profile follows directly from integrating Equation (4.18) and using the velocity at the edge of the viscous sublayer as a boundary condition:

$$U^+ = \frac{1}{\kappa} \ln y^+ + B \tag{4.19}$$

whereby κ is the von Karman constant and B is the smooth-wall log law constant.

Several other methods can be used to derive the logarithmic velocity profile. In order to resolve the closure problem (cf. Section 4.3), Prandtl introduced the 'mixing- length' concept,

$$\overline{u'v'} = -l^2 \left(\frac{\partial U}{\partial y} \right)^2 \tag{4.20}$$

whereby the mixing-length is proportional to the distance from the wall: $l = \kappa y$. As part of the inner layer, $\tau = \tau_0$ and in the log-law region, and the total shear stress is entirely due to the turbulent shear stress $\tau = -\rho \overline{u'v'}$, so that

$$U_\tau^2 = l^2 \left(\frac{\partial U}{\partial y} \right)^2 \qquad \text{and} \qquad \frac{\partial U^+}{\partial y^+} = \frac{1}{\kappa y^+} \tag{4.21}$$

By integration, the *log law*, Equation 4.19, is obtained again:

$$U^+ = \frac{1}{\kappa} \ln y^+ + B$$

Millikan (1939) used an asymptotic analysis that recovers the log relation by assuming the existence of a region of overlap where both the inner and outer laws are simultaneously valid, which will be presented in Section 4.4.4. All methods invariably rely on the presence of the constant-stress layer experimentally observed (Gad-el-Hak and Bandyopadhyay, 1994)

Clauser has verified the log-law over a range of pressure gradients and obtained the values κ = 0.41 and B = 4.9 (Clauser, 1956). Depending on the experiments the values for κ

and B were found to vary slightly, but by convention the Stanford Conference in 1969 has agreed on the values $\kappa = 0.41$ and $B = 5.0$.

4.4.3 Alternatives to the logarithmic velocity profile

Despite ample experimental evidence for the existence of the log law, the arguments leading to it have been questioned (Barenblatt, 1993; Barenblatt and Prostokishin, 1993; George and Castillo, 1997). From a practical point of view, a portion of the streamwise mean-velocity profile could equally well fit either a logarithmic relation or a power law of the form:

$$U^+ = c(y/\delta)^{1/n} \tag{4.22}$$

Whereby the value of the exponent 1/n will decrease as the velocity profile becomes fuller (i.e. as H decreases and Re increases). The behaviour of the exponent as Re approaches infinity is of particular interest. If it tends to zero, the log-law is recovered. However, if it tends to a non-zero constant, the log law does not strictly hold and viscous effects will persist even at infinitely large Reynolds number. Existing experimental or numerical mean-velocity data cannot readily be used to verify this, since the difference between a logarithmic relation and a power law with a large but finite n is imperceptible (Gad-el-Hak and Bandyopadhyay, 1994).

The strongest arguments in favour of a power law come from George and Castillo (1997). They assert that boundary-layer data taken at different Reynolds numbers collapse in the log region only if the shear stress is calculated from Clauser's method (see Section 4.7.6), which forces a log-law by pre-assumption. This compromises the collapse in the viscous sublayer where no adjustable constants or Reynolds number dependence should exist. Consequently, George and Castillo used measured shear stress to normalize experimental data and showed that the profiles collapsed well very close to the wall but not in the log region where discernible Reynolds number dependence was observed. Therefore, they proposed matching a new velocity-defect law with explicit Reynolds number dependence to the traditional law of the wall. The result in the matched region is a power-law velocity profile of the form:

$$\frac{U}{U_e} = C_0\left(\frac{y}{\delta}\right)^n \qquad \text{and} \qquad \frac{U}{U_\tau} = C_i\left(\frac{U_\tau y}{\nu}\right)^n \tag{4.23}$$

where the coefficients C_0 and C_i and the exponent n are Reynolds number dependent, but all are asymptotically constant. Thus, the friction coefficient is readily expressed as

$$c_f = Re^{-2n(1+n)} \tag{4.24}$$

4.4.4 Outer layer

The outer layer, when $y/\delta > 0.1$ to 0.2, is characterised by a decreasing turbulence shear stress. The *Reynolds number similarity* principle assumes that the relative fluid motions far from the wall are independent of the fluid viscosity ν (Yaglom, 1979). In other words, geometrically similar flows are expected to be dynamically similar if their Reynolds numbers are the same, and to be structurally near-similar for all Reynolds numbers which are large enough to allow fully turbulent flow (Townsend, 1956).

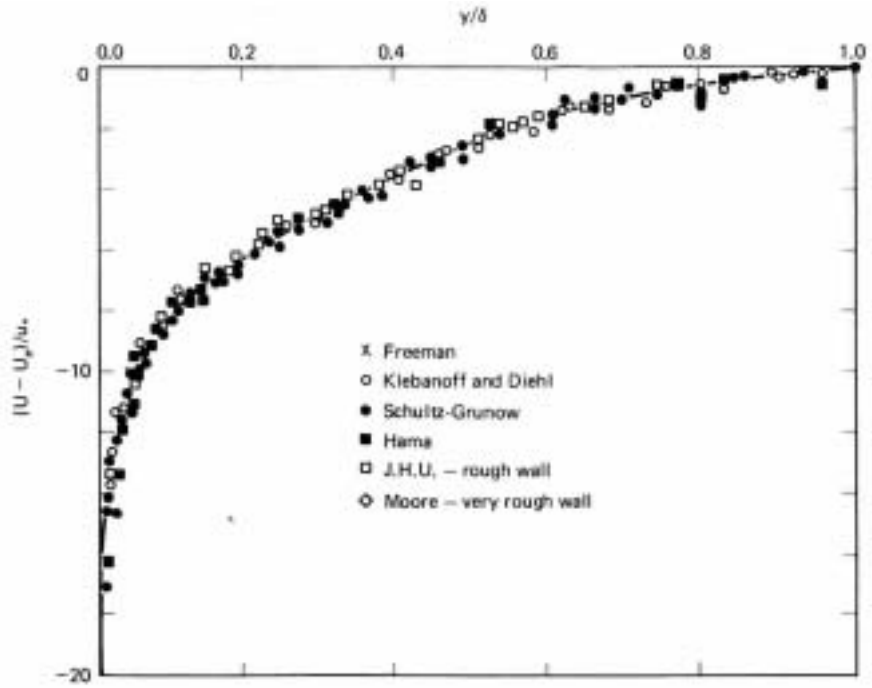

Figure 4.6. Defect law plot of turbulent velocity profiles in the outer layer for turbulent flow over smooth and rough flat plates (From Schetz, 1993; Clauser, 1956).

The turbulence normalisation by U_τ is no longer applicable, but dimensional analysis shows that the velocity profile scales with $(U_e\text{-}U)/U_\tau$ and y/δ, which can be interpreted as the velocity (momentum) defect at a distance y as the result of the wall shear stress τ_w. Thus, the *velocity defect law* can be written as:

$$\frac{U_e - U}{U_\tau} = g(\frac{y}{\delta}) \tag{4.25}$$

whereby g(y/δ) is a universal function (Schetz, 1993) . The velocity defect law is also valid for rough surfaces since it is generally regarded that roughness loses its influence away from the wall (cf. Section 4.5.1), as shown in Figure 4.6.

The log-law region forms an overlap between the inner and outer region and the log-law can therefore also be written as:

$$\frac{U_e - U}{U_\tau} = -\frac{1}{\kappa}\ln\frac{y}{\delta} + C \tag{4.26}$$

whereby C is between 2.35 and 2.5 for for a smooth plate with dP/dx = 0, and 0.65 for pipe and channel flow. It is interesting to note that Millikan (1939) obtained the log law by reasoning that abrupt changes between the inner and outer region of the boundary layer are physically impossible, and that there should be an overlap region, for which both the velocity defect law $(U-U_e)/U_\tau = g(y/\delta)$ and Prandtl's universal wall law $U/U_\tau = f(yU_\tau/\nu)$ should be valid simultaneously. Thus:

$$U/U_\tau = g(y/\delta) + U_e/U_\tau = f((y/\delta)(\delta U_\tau/\nu)) \tag{4.27}$$

Thus, a constant multiplicative factor on the argument inside the universal function function f (i.e. $\delta U_\tau/\nu$, which does not vary with y) must have the same effect as a different additive constant (U_e/U_τ) outside the function g. The logarithm is the only function that displays such a property (log(XY) = logX + logY). For the overlap region only, Equation (4.27) can therefore be written as Equation 4.19 or Equation 4.26:

$$U/U_\tau = A\ln(yU_\tau/\nu) + B \qquad \text{and} \qquad (U-U_e)/U_\tau = A\ln(y/\delta) + C$$

Coles (1956) effectively extended the range of applicability of the log-law region by introducing the law of the wake:

$$U^+ = \frac{1}{\kappa}\ln y^+ + B + \frac{2\Pi}{\kappa}\sin^2(\frac{\pi y}{2\delta}) \tag{4.28}$$

whereby the wake parameter Π according to Hama (1954) is 0.55 for low free-stream turbulence and dP/dx = 0. The wake parameter Π depends strongly on Re for small Reynolds number ($Re_\theta < 6000$) but is independent of streamwise location for equilibrium flows (Gad-el-Hak and Bandyopadhyay, 1994). The pressure gradient also has a strong effect on Π; a strong adverse pressure gradient causes a significant increase of Π. The free-stream

turbulence Tu also has a strong influence on Π, which decreases as Tu increases and can even become negative for large values of Tu.

The wake value appears to reach an asymptotic value for $Re_\theta > 6000$. Above this value of the momentum thickness Reynolds number, the inner- and outer-layer mean flows are expected to reach an asymptotic state which the turbulence quantities are also hypothesized to follow. However, recent experiments have revealed that this is not the case, since the wake component has been revealed to decrease slowly above $Re_\theta = 15000$. The question whether the mean flow ever truly achieves self-preservation is an important topic of current turbulence research (Gad-el-Hak and Bandyopadhyay, 1994).

4.5 Effect of surface roughness on boundary layers

4.5.1 Important concept in connection with rough walls

In turbulent flows, changes in Reynolds number and/or roughness, change c_f, and that influences the shape of the profile U/U_e versus y/δ, as shown in Figure 4.7.

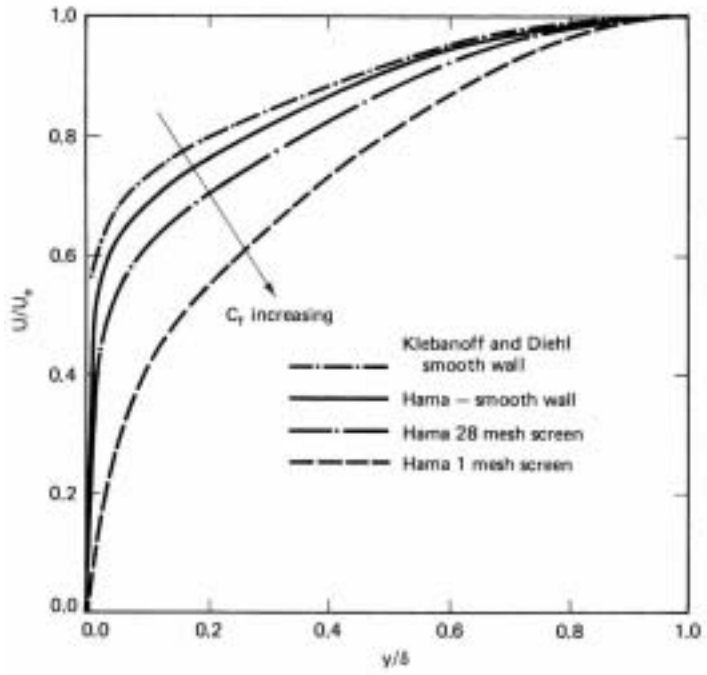

Figure 4.7. Mean velocity profiles on smooth and rough flat plates in a turbulent boundary layer (From Schetz, 1993; Clauser, 1956).

Turbulent flow over rough surfaces is a complex phenomenon because the flow is spatially heterogeneous and may be three-dimensional in the vicinity of the roughness elements.

A rough wall with protrusions with a representative average height h is now considered. Figure 4.8 presents a schematic of the rough wall. For a rough surface, y is defined as the distance from the highest peak of the rough surface profile to the point of interest. The hydrodynamical origin lies lower in between the asperities of the surfaces, so that an error-in-origin ε has to be introduced and $y+\varepsilon$ replaces y. For simplicity the addition of ε is not done in the remainder of this Section, but will be done in Section 4.7 and Chapter 5.

The term *roughness sublayer* is the counterpart of the viscous sublayer in a smooth wall turbulent boundary layer. It refers to the entire layer which is dynamically influenced by length scales associated with roughness elements and it typically extends 2-5 roughness heights from the wall. The roughness Reynolds number is defined as $h^+ = hU_\tau/\nu$. Physically it represents the ratio of a typical roughness height to the viscous length scale.

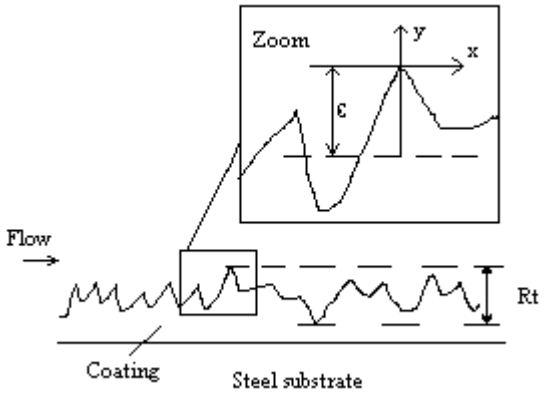

Figure 4.8. Definition sketch of the rough surfaces studied in this work.

The *Reynolds number similarity* principle assumes that the relative fluid motions far from the wall are independent of the fluid viscosity ν (Yaglom, 1979). In other words, geometrically similar flows are expected to be dynamically similar if their Reynolds numbers are the same, and to be structurally near-similar for all Reynolds numbers which are large enough to allow fully turbulent flow (Townsend, 1956). The *wall similarity hypothesis*, given by Raupach et al. (1991) states that outside the roughness (or viscous) sublayer, the turbulent motions in a boundary layer at high Reynolds number are independent of the wall roughness and the viscosity, except for the role of the wall in setting the velocity scale U_τ, the height y and the boundary-layer thickness δ. This suggests that the effects of surface roughness are confined to the immediate vicinity of the wall and that the turbulence structure over a significant portion of the boundary layer should be unchanged in spite of the substantial alterations to the surface characteristics.

With regard to the flow characteristics, there are two different types of roughness: 'h-type' (better known as 'k-type') and 'd-type'. If the roughness function ΔU^+ (see Section 4.5.3) scales on the roughness height h, the surface is said to be of 'h-type', whereas for 'd-

type' roughness, ΔU^+ scales on the pipe diameter d in pipe flow or on δ in a zero-pressure-gradient boundary layer (Raupach et al., 1991).

Classical sand grain pipe flow experiments were carried out by Nikuradse (1933) whereby the characteristic height was the sand grain size h_s. A number of rough wall turbulent boundary-layer experiments have consequently been reported (e.g. Hama, 1954; Perry et al., 1969; Antonia and Luxton, 1971, 1972; Bandyopadhyay, 1987; Perry et al., 1987, Krogstad et al., 1992). A comprehensive review of both theoretical and experimental knowledge of rough-wall turbulent boundary layers was given by Raupach et al. (1991).

4.5.2 Flow regimes over rough surfaces

Three flow regimes exist over rough surfaces and the roughness Reynolds number $h^+ = hU_\tau/\nu$ determines the degree to which the surface roughness has an effect on the flow. When the surface only consists of small imperfections that do not protrude the viscous sublayer, the surface is said to be *dynamically or hydraulically smooth*. The flow near the wall simply follows the contour of the roughness without any separation. The roughness therefore does not increase the drag, which is a function of Reynolds number only. In terms of Nikuradse's sand grain roughness, this regime arises when $h_s^+ = h_sU_\tau/\nu < 5$ (Schlichting, 1979, p. 516).

When roughness protrusions partly extend outside the viscous sublayer, they are subject to form drag and eddy shedding, which causes additional resistance, and the flow over the surface is in the *transitional or intermediate* regime. As the thickness of the sublayer decreases with the increase of the Reynolds number, the roughness effect at this stage depends on the Reynolds number as well as the surface topography. In terms of Nikuradse's sand grain roughness, this regime arises when $5 \leq h_sU_\tau/\nu \leq 70$ (Schlichting, 1979, p. 517).

In the *fully rough* regime, form drag dominates and the effect of roughness induced flow separation and eddy shedding completely overwhelms the viscous effect. At this stage the roughness effect is no longer Reynolds number dependent. In terms of Nikuradse's sand grain roughness, this regime arises when $h_sU_\tau/\nu > 70$ (Schlichting, 1979, p. 517). In this regime, the resistance is known to obey the *square law* ($R_F \sim U_e^2$) and for fully developed sand roughness, the resistance coefficients are given by (Lackenby, 1962):

$$C_F = [1.89 - 1.62\log(h_s/L)]^{-2.5} \quad \text{and} \quad c_f = [2.87 - 1.58\log(h_s/x)]^{-2.5} \qquad (4.29)$$

When h remains constant over a rough plate and assuming the flow is turbulent from the leading edge onwards, fully rough flow over the forward portion will be followed by the transitional regime and eventually the plate may become dynamically smooth as the relative roughness h/δ decreases (Schlichting, 1987, p. 652).

4.5.3 Roughness effects

Instead of $U^+ = f(y^+)$, the law of the wall for rough surfaces is replaced by $U(y) = f(y^+, h^+, \alpha, \beta, ...)$ where $\alpha, \beta, ...$are dimensionless parameters characteristic of the form of the protrusions and their distribution over the surface of the wall and where h is a characteristic linear roughness measure.

Consequently, the log law over rough walls may be written as:

$$U^+ = \frac{1}{\kappa}\ln y^+ + B_0(h^+, \alpha, \beta, ...) + \frac{2\Pi}{\kappa} w(\frac{y}{\delta}) \tag{4.30}$$

For a rough wall boundary layer, the complete velocity profile may also be written in the following form:

$$U^+ = \frac{1}{\kappa}\ln y^+ + B - \Delta U^+ + \frac{2\Pi}{\kappa} w(\frac{y}{\delta}) \tag{4.31}$$

where B is the smooth wall constant, κ is the von Karman constant, ΔU^+ is the *roughness function or velocity loss function*, Π is the Coles wake parameter and w is a universal wake function of y/δ. Consequently:

$$\Delta U^+ = B - B_0(h^+, \alpha, \beta, ...) \tag{4.32}$$

Thus, over the region of validity of the logarithmic law, the velocity, U, is augmented by ΔU. This shifts the logarithmic portion of the smooth wall curve down and to the right, and corresponds to an increase in c_f. ΔU^+ as described by Hama (1954) is one form of the roughness function. In his earlier pipe flow experiments, Nikuradse (1933) used another form of the roughness function, χ, such that in the boundary-layer overlap region:

$$U^+ = \frac{1}{\kappa}\ln\frac{y}{h} + \chi \tag{4.33}$$

whence,

$$\chi = B + \frac{1}{\kappa}\ln h^+ - \Delta U^+ \tag{4.34}$$

The effect of roughness on wall friction can therefore be isolated by means of either roughness function ΔU^+ or χ, but ΔU^+ can be determined directly from the boundary-layer velocity profile as demonstrated by Hama (1954) whereas χ depends on the introduction of a roughness measure h.

Much work has been done on the fully rough flow with respect to the behaviour of the roughness function. As mentioned, Nikuradse (1933) carried out experiments on pipes roughened by uniform sands of various sizes. In this case of homogeneous sand, the parameters α, β, ... in Equation 4.31 are the same and the roughness function depends only on h, which is taken as the average sandgrain height h_s. Nikuradse carried out his experiments for a wide range of roughness Reynolds numbers and found that χ tended towards a constant value, χ_r, for large values of $h_s^+ = h_s U_\tau / \nu > 70$. The constant roughness function χ in the fully rough flow is equal to 8.5 in the case of Nikuradse's sand. In the case of wind flow over natural vegetation, a value of $\chi \approx 5$ has been reported (Yaglom, 1979).

By implication of Equation (4.34), if χ is constant, ΔU^+ has the corresponding asymptotic form in fully rough flow over sand surfaces:

$$\Delta U^+ = \frac{1}{\kappa} \ln \frac{h_s U_\tau}{\nu} + C_0 \tag{4.35}$$

where C_0 is a constant. Hama (1954) obtained a similar relationship between ΔU^+ and h^+ for fully rough flow over uniform roughness. Hama (1954) concluded that for geometrically similar roughness, ΔU^+ is a unique function of h^+ and is directly related to the increase in surface resistance which the roughness produces, as shown in Figure 4.9. Moreover, he demonstrated that the roughness function is universal, which implies that results obtained in different types of experimental facilities can all be compared with each other.

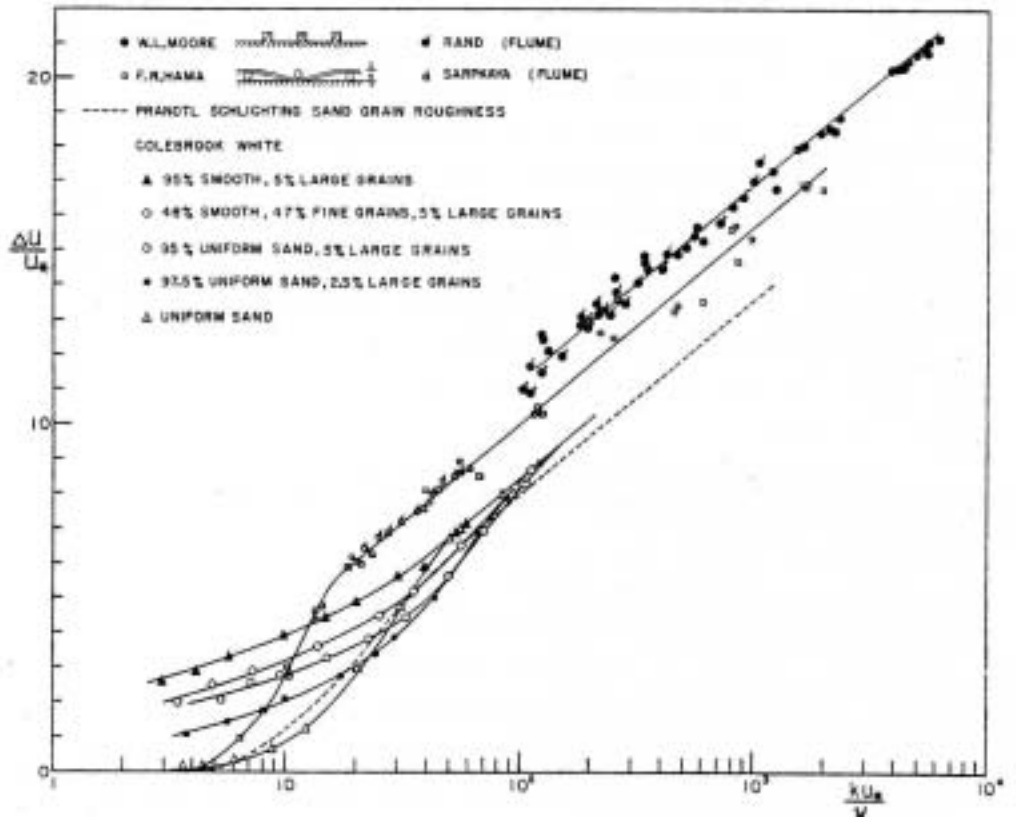

Figure 4.9. Roughness function versus roughness Reynolds number for various roughness geometries (From Clauser, 1956)

For different roughness geometries, the *roughness density* expressed by the geometric parameters α, β,... will have an influence on the roughness function. This was already noted in 1934 by Prandtl and Shlichting (Collatz, 1986) who proposed the roughness density as an additional parameter. The dependence of the roughness function on the geometric parameters in the case of fully rough flow has been studied by several researchers (Bettermann, 1966; Dvorak, 1969; Feiereisen and Acharya, 1986). Simpson (1973) used a parameter α which is the ratio of the total frontal area of the roughness normal to the flow to the total surface area. He found that C_0 in Equation 4.35 increases with increasing α, reaches a maximum and then decreases as α increases further. This result can be explained by physical reasoning. At first, when the when the frontal area and/or the density of the roughness elements increase, the total drag (and the roughness function ΔU^+) increases too. However, at one point, it is no longer possible to flow through the cavities between the roughness elements, and the flow no longer penetrates into the bottom part of the cavities. If the flow is visualised (cf. Grass, 1971, Furuya et al., 1976), stagnant regions appear clearly. Consequently, if α increases further, the

effective roughness height (and ΔU^+) will decrease (since the stagnant regions are excluded from the real flow).

In many practical applications the flow over naturally rough surfaces never reaches the fully rough condition. Moreover, engineering surfaces behave differently from sand grains and other types of uniform roughness in the transitional or intermediate region. Colebrook and White (1937) conducted experiments on surfaces of various topographies by cementing assemblies of grains to tubes. They demonstrated that the nature of the effect of surface roughness in the intermediate region depended on the geometrical characteristics of the roughness pattern such as the spacing between the sand grains and the composition of grain sizes. Colebrook (1939) concluded that the roughness function of a range of engineering surfaces in fluid flows is an asymptotic fit to both the hydraulically smooth and the fully rough. He derived a formula to describe the behaviour of engineering roughness in a pipe from the hydraulically smooth to fully rough conditions and added a quantity of experimental evidence to demonstrate the universality of the formula. The Colebrook-White roughness function is described as:

$$\Delta U^+ = \frac{1}{\kappa}\ln(1+\frac{C_1}{B_1}h^+) \tag{4.36}$$

where h is a one-dimensional characteristics measure of roughness, C_1 is a constant which depends on the chosen measure of roughness, and B_1 is another universal constant related to κ and B by $B = -1/\kappa \cdot \ln B_1 = 0.128735$. The Colebrook-White law will be studied in more detail in Chapter 7.

There is still a distinctive lack of hard experimental facts with regard to the behaviour of roughness functions for even uniformly rough surfaces. The different flow regimes are well-defined in a qualitative sense, but it is very difficult to describe the flow behaviour in the transitional regime between hydraulically smooth and fully rough flows (Musker, 1977).

It is also important to note that the Colebrook-White formula does not apply to all irregularly rough surfaces. Some artificially produced irregular surfaces exhibit Nikuradse's trend in the intermediate region (e.g. Hama's simulated paint surface, 1954).

4.6 Turbulence characteristics

4.6.1 Turbulence intensities

Benchmark experiments into the turbulent boundary-layer structure were carried out by Klebanoff (1955). He measured the three velocity components with a hot-wire in a wind tunnel with very low free-stream turbulence (Tu < 0.04% at the maximum velocity) to keep the background turbulence effects to a minimum. The boundary layer was artificially thickened with coarse sandpaper, which allowed near-wall measurements. Figure 4.10 shows the non-dimensional turbulence intensities plotted against y/δ.

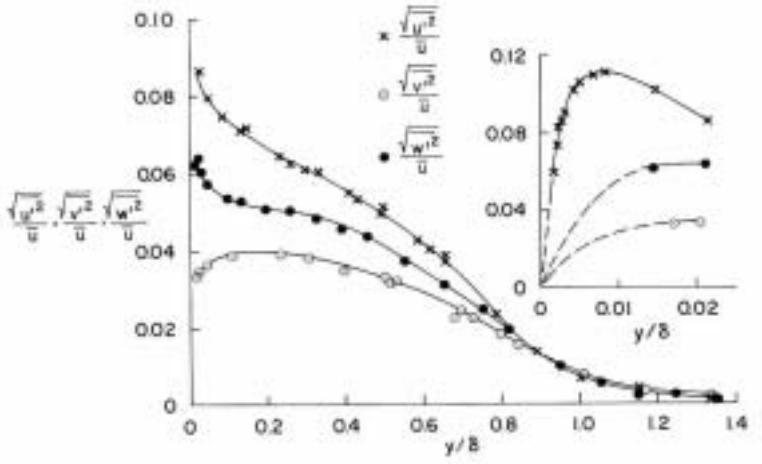

Figure 4.10. Relative turbulence intensities in the flow along a smooth plate (From Cebeci and Smith, 1974, data from Klebanoff, 1954)

Figure 4.10 shows that the axial turbulence intensity is larger than the spanwise intensity, which in turn is larger than the wall-normal intensity, which is constrained by the wall. An interesting feature is that the three components coincide for $y/\delta > 0.9$, which indicates that in the outer-layer where the velocity gradient is small, conditions of nearly isotropic turbulence are created, in contrast to the inner layer where the velocity gradient is large.

The effect of surface roughness on turbulence intensities was examined by Corrsin and Kistler (1954), who used corrugated paper in their experiments. Figure 4.11 shows that all intensities increased and the axial turbulence intensity remained higher at the outer edge which may attest to larger scale motions induced by the roughness. Antonia and Luxton

(1971) and Ligrani and Moffat (1986) also studied the effect of h-type roughness on the turbulence intensities.

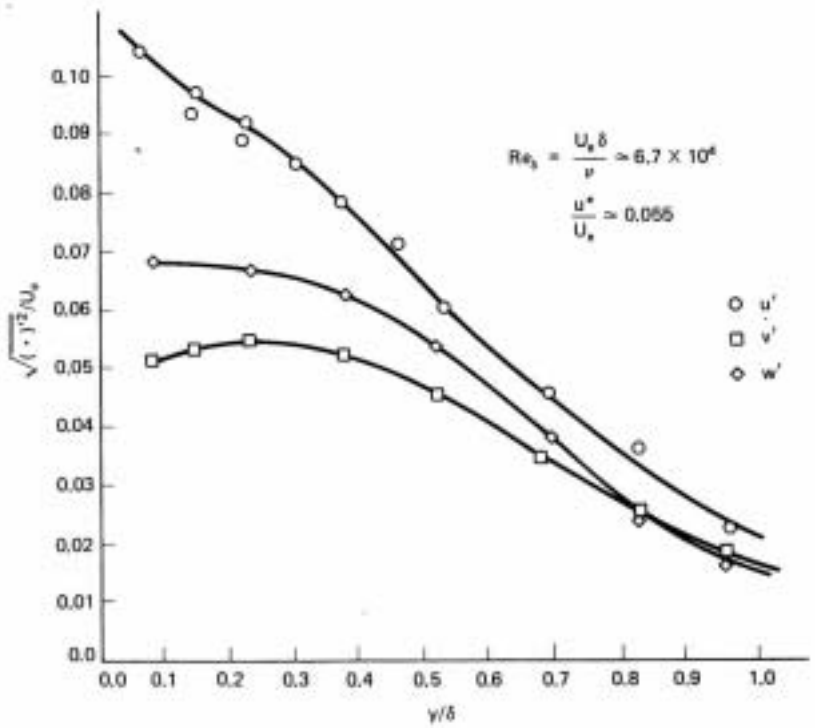

Figure 4.11. Turbulence intensity profiles for flow over a fully rough flat plate (From Schetz, 1993, data from Corrsin and Kistler, 1955)

The cross-correlation of fluctuating velocity components in the axial and wall-normal direction are necessary to find the Reynolds shear stress across the boundary layer. Figure 4.12 shows the results obtained by Klebanoff (1955) along with the turbulent kinetic energy, $K = (\overline{u'^2 + v'^2 + w'^2})/2$.

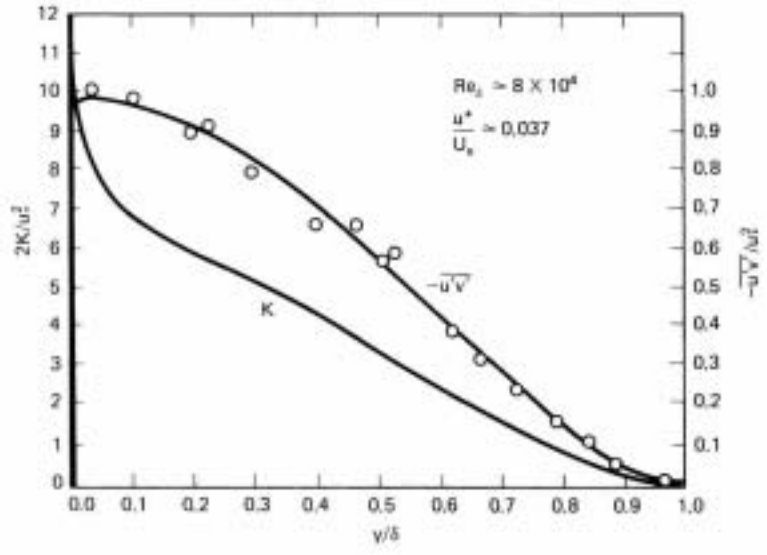

Figure 4.12. Profiles of Reynolds stress and turbulent kinetic energy in a turbulent boundary layer on a flat plate (From Schetz, 1993, data from Klebanoff, 1955).

When non-dimensionalised by the wall shear stress, the total shear stress becomes equal to $\frac{\upsilon}{U_\tau^2}\frac{\partial U}{\partial y} - \frac{\overline{u'v'}}{U_\tau^2}$. Figure 4.12 shows that the second component approaches unity and hence demonstrates the dominance of the Reynolds shear stress over the viscous shear stress in the log-law region and the outer layer (see also Figure 4.4). Klebanoff was unable to measure sufficiently into the viscous sublayer, where the Reynolds shear stress is expected to decline steeply and the viscous shear stress to rise correspondingly to keep the total shear stress constant. Other experiments have since shown the Reynolds shear stress declined steeply when y^+ became smaller than 20 (Gad-el-Hak and Bandyopadhyay, 1994).

Fewer data are available on the effect of surface roughness on the velocity cross-correlation (Ligrani and Moffat, 1986; Raupach et al., 1991 and Antonia and Luxton, 1971). Antonia and Luxton studied the effect of a step change from smooth to rough conditions and found that the Reynolds shear stress was mainly affected in the inner region. They found a good collapse of $\overline{u'v'}/U_\tau^2$ over uniform spheres provided the data were plotted against $(y+\varepsilon)/\delta$ over the entire range of different roughnesses.

4.6.2 Turbulence spectra

Turbulence spectra express the amount of energy stored in a range of eddy sizes. Wave number spectra are expressed against a wave number $k_1 = f/U$. The energy associated with an axial turbulence component that is associated with a given wave-number band is equal to $E_1(k_1)/\overline{u'^2}$ and the total amount of energy stored is equal to the integral over k_1 from zero to infinity. Figure 4.13 shows a plot of E_1 against k_1 and shows that the spectrum shifts down and to the right as the wall is approached, which signifies that more energy is present in the high wave-number range near the wall and in the low wave-number range in the outer layer. This is an illustration of the 'energy cascade' flowing from the larger scales to the smaller scales and ultimately to dissipation by the viscosity into heat (Schetz, 1993, p. 228). The effect of large-scale eddies in the outer region that extract their energy from the external stream, is therefore readily observed with turbulence spectra.

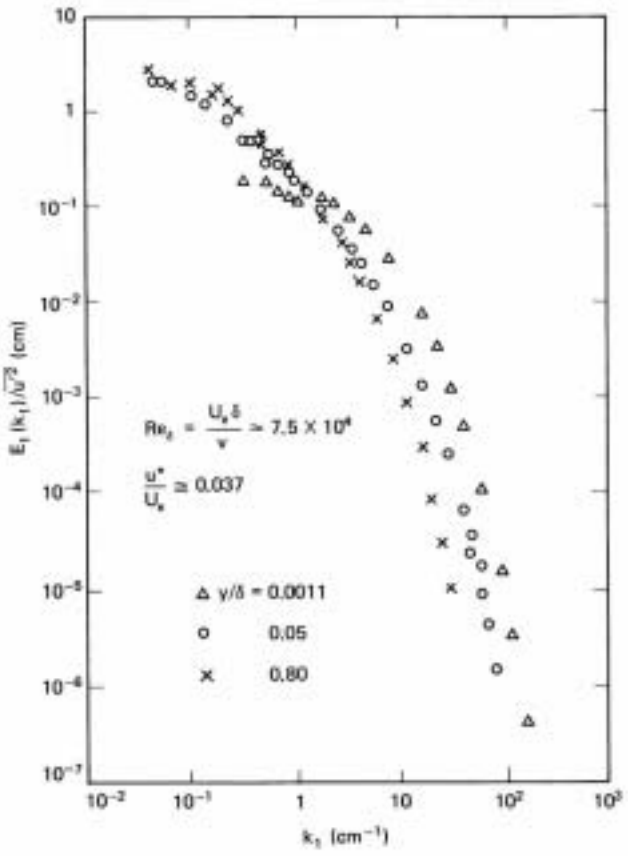

Figure 4.13. Spectra of the axial turbulence intensity in the boundary layer on a flat plate (From Schetz, 1993, data from Klebanoff, 1955).

It is also interesting to note from Figure 4.13 that at $y/\delta = 0.05$ the spectrum exhibits a range where $E_1(k_1)$ varies nearly according to k_1^{-1}, which indicates strong interaction between mean and turbulent flow (Hinze, 1977) and at this point a strong production of turbulence energy takes place (cf. Figure 4.3).

In general, three spectral ranges can be considered, corresponding to inactive, active and fine-scale eddies (in order of increasing k_1), which respectively obey outer-layer, inner-layer and Kolmogorov scaling. The spectral ranges overlap in two wavenumber intervals that are proportional to k_1^{-1} and $k_1^{-5/3}$ (which is known as the Kolmogorov law) respectively (Hinze, 1977; Perry et al., 1987; Raupach et al., 1991).

The effect of roughness on the distribution of longitudinal turbulence energy is to increase the energy contained in the larger-scale motions. Ligrani and Moffat (1986) found that in full-rough conditions over h-type roughness, a significantly higher amount of energy was contained in the low wave-number range across the entire boundary layer as compared to the smooth wall, but no significant effect was observed in the high wave-number range.

4.7 Measurement of the local frictional resistance

4.7.1 Skin friction laws

The shear stresses created by an object moving through a fluid result in skin friction, which is the force generated in the boundary layer. A *skin friction law* for smooth walls can be found by eliminating U and y by subtracting Equation 4.19 from Equation 4.26:

$$\frac{U_e}{U_\tau} = \frac{1}{\kappa}\ln\frac{\delta U_\tau}{\nu} + B + C \tag{4.37}$$

$$\Rightarrow \quad \sqrt{\frac{2}{c_f}} = \frac{1}{\kappa}\ln\left(\mathrm{Re}_\delta\sqrt{\frac{c_f}{2}}\right) + B + C \tag{4.38}$$

As mentioned, δ is ill-defined, but an equation $\delta = a_1(U_\tau/U_e)x$ may be used whereby x is the distance from the leading edge of a plate. The *von Karman skin friction law* is obtained if the constant $a_1 = 0.34$ is used. This implicit formula can be made explicit by simplifying or by fitting data.

In order to determine the frictional resistance experimentally, several methods can be used, reviewed in the following Sections.

4.7.2 Direct force measurements

This technique measures c_f directly by the use of a floating element force balance. The skin friction at the wall is allowed to act on and displace a flush mounted element, which is calibrated with respect to the force necessary for a given displacement. Output signals are given by either a linear variable differential transformer or by a bridge arrangement of strain gauges. This method has been used for example by Karlsson (1978) and by Johansson (1985) to measure the influence of roughness of ship hull surfaces on frictional resistance.

Several practical problems occur with this method such as the effect of gaps, leakage, forces due to pressure gradients and especially misalignment. Even when the floating element is only slightly misaligned with the flow, edge and normal forces can be generated that are an order of magnitude greater than the skin friction forces to be measured (Hanratty and Campbell, 1996).

An additional problem with rough walls is that the surface of the floating element should accurately mimic the surrounding environment. This is not so critical with smaller elements, but then the measured forces will be equally small.

4.7.3 Sublayer slope method

The wall shear stress can be obtained by measuring the velocity gradient at the wall (where the turbulent shear stresses are negligible, cf. Figure 4.4):

$$\tau_W = \mu \frac{\partial U}{\partial y}\Big|_{y=o} \tag{4.39}$$

In practice, it is very difficult to do this with good accuracy, since a linear gradient is only present over the viscous sublayer. Obtaining multiple accurate velocity measurements in the viscous sublayer is difficult due to the physical limits. Moreover, the viscous sublayer may not exist at all over rough boundaries. Nevertheless, if enough data can be obtained in the viscous sublayer, the sublayer slope method has proven to be very elegant and has been employed by many researchers (e.g. Tachie, 2000; Wang et al., 2000).

4.7.4 Reynolds stress method

Like the sublayer slope method, the Reynolds stress method can be explained by Figure 4.4 and relies on the observation that in the constant stress region, the total shear stress is entirely made up of the Reynolds stress, so that a plot of $-\overline{u'v'}/U_\tau^2$ versus $(y+\varepsilon)/\delta$ should approach a maximum equal to unity. As such it was used for example by Schultz (1998, 1999, 2000), and it will be used in Chapter 5.

4.7.5 Momentum methods

The basic premise of momentum methods is that c_f is the result of a deficit of momentum across the boundary layer. The von Karman integral equation for two-dimensional incompressible steady flow is:

$$\frac{d\theta}{dx} + \frac{1}{U_e}\frac{dU_\tau}{dx}(2\theta + \delta_1) = \frac{c_f}{2} \tag{4.40}$$

which simplifies for a flat plate with zero pressure gradient into: $d\theta/dx = c_f/2$. Thus, by measuring velocity profiles at several streamwise locations and calculating $d\theta/dx$, C_f can be determined. It is important that enough streamwise profiles are measured to get accurate results from momentum methods.

4.7.6 Inner layer wall similarity techniques

Clauser (1954, 1956) developed a method that is based on the fundamental notion that similarity exists over the inner region scaled on $U_\tau = \sqrt{2/c_f}$. Clauser rewrote the log-law as:

$$\frac{U}{U_e}\frac{U_e}{U_\tau} = A\log(\frac{yU_e}{\nu}) + A\log(\frac{U_\tau}{U_e}) + B \qquad (4.41)$$

whereby $A = 1/\kappa \cdot \ln(10)$. When a family of curves of U/U_e versus yU_e/ν is constructed for a range of values of c_f and the experimental data are plotted on this so-called *Clauser chart*, the data in the log-law region will coincide or be parallel to one of the c_f curves. This method has shown good agreement with other methods for smooth walls in zero pressure gradient and low Tu. The method can also be used for small pressure gradients and rough walls, but under strong adverse pressure gradients, the wake component can slip into the inner layer and the determination of c_f from the smaller log-law region may become inaccurate. For rough surfaces, the experimental data will be shifted below the smooth c_f reference lines on the Clauser chart, but the correct value will be given by using the reference line with the same slope as the experimental data.

An alternative wall similarity method using similar reasoning was proposed by Bradshaw using a reference point with co-ordinates y^+_{ref}, U^+_{ref} (Schultz, 1998). The latter method is only valid for smooth walls, but the *Clauser method* has been modified for rough walls by Perry and Joubert (1963). The problem with any wall similarity technique to determine c_f for rough walls is that the y-origin is not known a priori. The wall has asperities and one could put the origin of the velocity profile at the peak, at the bottom or in the middle of the asperities (cf. Figure 4.8). Inaccuracy in the determination of the y-origin can manifest itself as a curvature for the points in the log-law region. The origin in effect is arbitrary and one has to use an adjustment value ε to force a linear log-law. Perry and Joubert (1963) devised a simple method to determine ε. When the experimental data U/U_e are plotted versus

log(y), they will be linear or slightly curved in the log-law region, with the data in the sublayer and in the wake diverging from linearity. A faired curve can be drawn through the data in the log-law region and if this curve is for example concave up (having a positive second derivative) a positive value for ε can be added. This process is repeated until linearity is achieved over the log-law region as illustrated in Figure 4.14, taken from Perry and Li (1990).

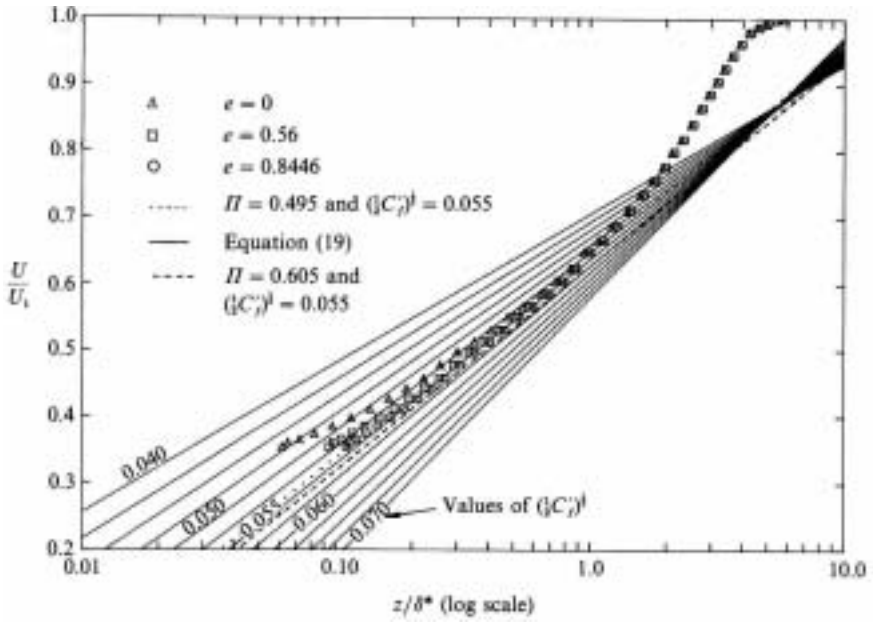

Figure 4.14. 'Modified Clauser method' to determine the skin friction over a rough wall (From Perry and Li, 1990).

The Clauser method was applied by Lewthwaite et al. (1985), using the log-law slope as variable. They measured full-scale velocity profiles with a pitot-static tube and through-hull traverse to find the change with time in frictional resistance for a ship out of dock. Schultz (1998, 2000) applied this method to study the effect of fouled surfaces on boundary-layer parameters and the increase in frictional resistance. The experimental data are plotted as U/U_e versus $\ln(yU_e/\nu)$ and a linear regression of the data points in the log-law region is calculated. The slope of this regression line is used to find c_f since $c_f = 2\kappa^2(\text{slope})^2$. Since the roughness function does not affect the slope of the regression line, this method is also valid for rough surfaces provided ε is taken into account. The modified Clauser method used in this analysis is basically an iteration technique that determines ε and U_τ by forcing the log-law slope ($1/\kappa$ for natural logarithms cf. Equation 4.19) over a selected region of the collected data.

The y-adjustment value ε in wall similarity techniques introduces another degree of freedom into the determination of c_f and hence more error can be expected for the skin friction values of rough surfaces than of smooth surfaces. An alternative is to use a different method to determine c_f and to use this value to calculate U_τ and ΔU^+ in order to minimise error. This could be done by direct force measurements or by the use of a Preston tube, which is a small pitot tube placed against the wall. Preston found in 1954 that the dynamic pressure measured by the tube is directly proportional to the wall shear stress provided the tube is placed entirely in the inner layer. A variant pitot tube with a rectangular opening is called the Stanton tube. One could also measure c_f with film gauges through which an electrical current creates a small amount heat flow which is proportional to $\tau_w^{1/3}$ (Hanratty and Campbell, 1996; Schultz, 1998).

4.7.7 Outer layer wall similarity techniques

The outer region of the boundary layer is most often studied using the velocity defect law, which relates the difference between the free-stream velocity U_e and the local velocity U to the distance from the wall. Clauser (1956) and Hama (1954) demonstrated the validity of the velocity defect law for boundary-layer flows on both smooth and rough walls, which Hama formulated in terms of U_e^+-U^+. Bandyopadhyay (1987) has suggested that the Hama formulation could be fitted to obtain a reliable estimate of U_τ, irrespective of the nature of the surface. Since the Clauser wall similarity technique matches the profile in the logarithmic region, which is thin, there is only a restricted amount of data points to work with. In contrast, the profile matching using Hama's formulation covers virtually the entire boundary layer.

It has been observed (Bandyopadhyay, 1987; Krogstad et al., 1992) that the values of the friction velocity obtained from the Hama formulation are consistently higher than by extrapolating the Reynolds stress to the wall. It has been suggested (Tachie et al, 2000) that this may be due to the strength of the wake value being too small. Krogstad et al. (1992) and Krogstad and Antonia (1994) employed a modified formulation that does not fix the value of the wake strength, Π, but rather allowed its value to be optimised:

$$w(y/\delta) = 1/2\Pi[(1+6\Pi)-(1+4\Pi)(y/\delta)](y/\delta)^2 \qquad (4.42)$$

This equation is the simplest equation satisfying the two boundary conditions (correct slope and function values) both near the wall and at the boundary-layer edge. Consequently, the values of U_τ, Π and ε in the present study were determined following an optimisation procedure similar to that outlined in Krogstad et al. (1992) and Tachie et al. (2000). The optimisation procedure was carried out by fitting Equation 4.43 to the data using Equation 4.42 for the wake function:

$$U_e^+ - U^+ = 2\Pi/\kappa[w(1) - w((y+\varepsilon)/\delta)\ ] - 1/\kappa \ln((y+\varepsilon)/\delta) \qquad (4.43)$$

In the present analysis, y was replaced by $y+\varepsilon$ in Equation 4.43. The procedure involved optimising U_τ and Π first with $\varepsilon = 0$, and when the near-wall data showed premature departure from the fit in the log-law region, a virtual origin was introduced to straighten the data. This had a limited effect on the values of U_τ and Π and one extra iteration loop generally sufficed. Compared to the Clauser method, the Hama method has a tendency to converge to larger values of ε in order to keep the correct slope in the log-law region. Occasionally, careful consideration of the near-wall measurements was taken into account so that the method converged to a more physically realistic solution by restricting the value of ε.

As will be seen in the following Chapter, the boundary-layer experiments showed that the *Hama method* gave good agreement with the Reynolds stress methods.

4.8 Keynote elements of the literature review on rough-wall boundary layers

This Chapter has presented a literature review on rough-wall boundary layers, and provides the theoretical foundations for the boundary-layer experiments in Chapter 5.

It should be mentioned that because of practical reasons the experiments from the outset were planned to be conducted in a water tunnel. Section 4.7 has therefore presented those techniques which can be applied to flat plate boundary layers. The same techniques can be used for pipe flow experiments but one additional advantage there is that the pressure drop in a fully developed pipe flow can be related directly to the wall shear stress by simple equilibrium considerations. Any regression method applied to the data (cf. Section 4.7.6 and 4.7.7) can then be devoted specifically to the problem of identifying the virtual origin error ε to provide an accurate datum for the effective position of the wall (Musker and Lewkowicz, 1978). According to Musker (1991), this is the reason why pipe flow experiments give the most reliable data for turbulent boundary layers over irregularly rough surfaces.

In the experiments described in Chapter 5, the frictional velocity will be determined using an outer layer wall similarity method (cf. Section 4.7.7, henceforth named the *Hama* method) and the Reynolds stress method (cf. Section 4.7.4). Additionally, an inner layer similarity method (cf. Section 4.7.6, henceforth named the *Clauser* method) will be applied for the smooth surface. As discussed in Section 5.2.4.4, the Clauser method as modified by Perry and Joubert (1963) was applied for the coated surfaces but not retained for further analysis.

Once the friction velocity has been determined, velocity profiles will mainly be presented in wall units (cf. Figure 4.5), but outer variables will also be used, i.e the velocities will be non-dimensionalised by the free-stream velocity U_e and the distances from the wall by the boundary-layer thickness δ. The roughness function for the different surfaces will be determined from the shift in the log-layer (cf. Section 4.5.3). Plots of the turbulence intensities and Reynolds stresses (cf. Section 4.6.1) will also be presented, in addition to plots of the spectra (cf .Section 4.6.2).

Chapter 7 will investigate whether the roughness characteristics of the coatings correlate with the drag and boundary-layer measurements. Section 4.5.3 will be used to discuss further properties of the Colebrook-White law in transitional flows and some additional remarks will be made on the coherent structures (cf. Section 4.2) in rough-wall turbulent boundary layers.

Chapter 5: Boundary-layer experiments

5.1 Introduction

This chapter describes the experiments that were carried out in order to study the boundary-layer characteristics of coated surfaces using Laser Doppler Velocimetry (LDV). LDV measures the fluid velocity by detecting the Doppler frequency shift of laser light that has been scattered by small particles moving with the fluid. A LDV set-up consists of a laser source, an optical arrangement, a photo-detector that converts light into electrical signals and a signal processor. The various components are discussed in Appendix B.

The main objectives of this investigation were:

- to examine the influence of the surface conditions generated by different marine coatings on the mean velocities and turbulence parameters at different positions from the leading edge and at different free-stream velocities
- to verify whether the boundary-layer characteristics of the surfaces correspond to rough-wall characteristics reviewed in Chapter 4
- to calculate the roughness function of the different surfaces from the measured velocity profiles.

Two sets of experiments have been carried out. The first set was carried out in the Emerson Cavitation Tunnel at the University of Newcastle-upon-Tyne. They involved 5 different surfaces: a steel reference surface (designated as STEEL), a surface coated with a Tin-free Self-Polishing Co-polymer (SPC), two surfaces coated with a Foul Release system, which was applied by spraying on the first (FR) and by rollering on the other (ROLL), and a surface partially covered with sand-roughness (SAND).

The test facilities and conditions have been described in Section 5.2.1 while the experimental procedure is presented in Section 5.2.2. The discussion of the results is presented in Section 5.2.4.

The second set of experiments was carried out in the CEHIPAR Cavitation Tunnel in order to confirm the results obtained in the first set of experiments and to study the boundary-layer effects at a higher free-stream velocity. These experiments are described in Section 5.3, which has the same structure as Section 5.2. A summary of the experiments in presented in Section 5.4. A detailed uncertainty analysis of both sets of experiments is included in Appendix C, while boundary-layer plots of the first set are given in Appendix D.

5.2 Boundary-layer experiments in the Emerson Cavitation Tunnel

The tests were carried out at the Emerson Cavitation Tunnel at the University of Newcastle-upon-Tyne, between 15 February 2000 and 1 May 2001.
The entire measurements for the mean velocity profiles, the turbulence intensity profiles, the Reynolds stress profiles and the turbulence spectra are presented in Appendix D. Full details of the experiments can be found in Candries et al. (2001).

5.2.1 Facilities and test conditions

5.2.1.1 Emerson Cavitation Tunnel

The Emerson Cavitation Tunnel has a rectangular measuring test section of 1.22m wide by 0.81m high and 3.1m long. A diagram of the tunnel is shown in Figure 1. The Kempf and Remmers propeller dynamometer shown in Figure 5.1, which is usually employed for propeller testing, was removed for the present experiments.

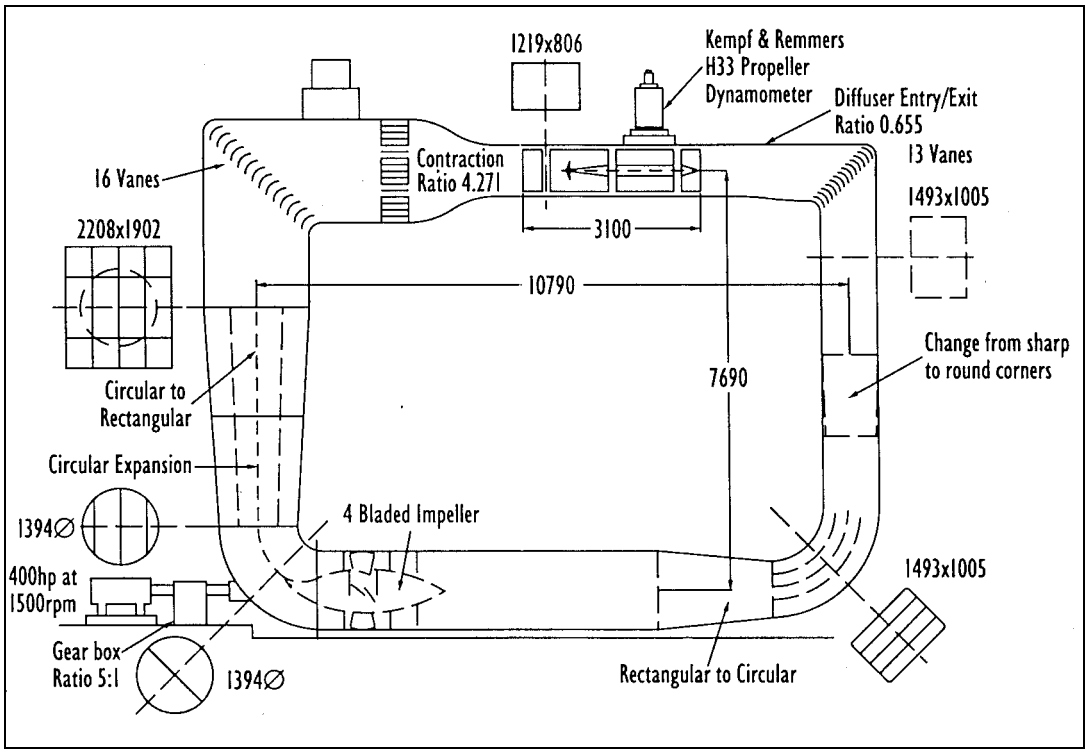

Figure 5.1. Schematic diagram of the Emerson Cavitation Tunnel

The contraction ratio is 4.271 and flow management devices include turning vanes placed in the corners and a flow straightener at the entrance to the contraction section. The resulting free-stream turbulence in the test section ranges from 2.5% to 3.5% (Atlar and Korkut, 1997).

The free-stream velocities in the test section can be adjusted from 1m/s to 8m/s. The mean velocity can be maintained constant between +1.5% and –2.5% throughout the range (Atlar and Korkut, 1997). Table 5-1 lists the main particulars of the tunnel, while a detailed description of the facility can be found in Atlar (2000).

Table 5-1. Main details of the Emerson Cavitation Tunnel

Establishment year	1949
Description of facility	Vertical plane, closed re-circulating
Test section size (LxBxH)	3.10x1.22x0.81m
Test section area	0.99m^2
Contraction ratio	4.271
Type of drive system	4 Bladed axial flow impeller with thyristor control
Main pump power	300kW
Main pump rotational speed	294rpm
Impeller diameter	1.4m
Maximum velocity	8m/s (15.5knots)

5.2.1.2 Test plate details

In order to allow the development of a fully turbulent boundary layer in the water tunnel, a test plate fixture had to be designed and constructed. The design requirements for the plate included sufficient length for boundary-layer development, an adjustable angle of attack to obtain a zero pressure gradient flow, and a large and interchangeable test section.

The boundary-layer test plate was 0.80m in height, 2m in length as two 1m long sections attached together, and 12mm thick. There is a 30mm overlap to join both sections together. A drawing of the boundary-layer test plate is shown in Figure 5.2.

The plate was constructed of mild steel and a strip of foam was attached underneath the assembled plate to prevent damage to the water tunnel window, as shown in Figure 5.3. The leading and trailing edges, each 50mm long, were tapered and the forward 300mm of the plate was covered with #40 sand grit to hasten and artificially thicken boundary-layer development, as shown in Figure 5.4. The #40grit was chosen in accordance with the boundary-layer experiments carried out by Schultz (1998).

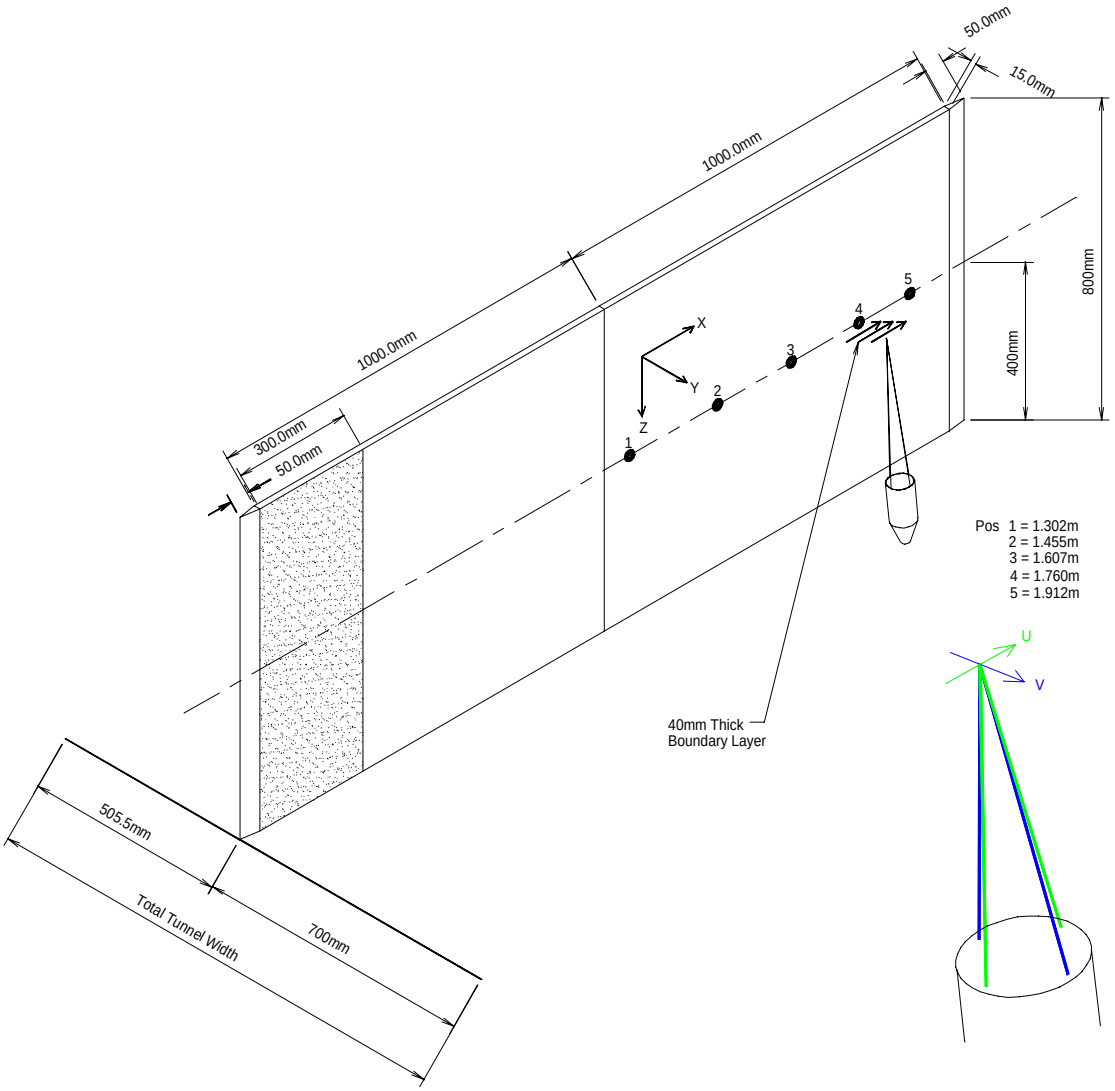

Figure 5.2. Schematic sketch of the boundary layer plate

Figure 5.3. The plate with a strip of foam at the bottom.

Figure 5.4. Leading edge of the mounted plate.

The plate was mounted 700mm from the front side of the water tunnel and was held in place with 6 corner brackets, shown in Figure 5.5, which supported the plate in pairs (top and bottom) at the front middle and end. The brackets have a certain degree of freedom until the bolts are fixed firmly, which allows adjustments to the free-stream pressure gradient.

Figure 5.5. The corner brackets at the back of the plate

Figure 5.6. The aft section of the 12mm thick plate with magnets

Six thin plates were fabricated from 3mm thick mild steel. One thin plate was used to cover the front section of the model and was partially covered with grit as mentioned. The other 5 thin plates were used as test specimens to investigate the influence of the different surfaces. The test specimens were held on the 12mm plate by 5 magnets each with a pull of 25kg, and are shown in Figure 5.6. At the edges 18 countersunk screws were employed to fix the test specimen. It was noticed that the magnets alone were not sufficient to keep the test specimens in place at higher speeds due to the suction created in the tunnel. Consequently 10 extra countersunk screws were drilled 250mm below and above the centreline.

5.2.1.3 LDV system

The velocity measurements were taken using a four-beam two-component fibre-optic DANTEC Laser Doppler Velocimetry (LDV) system, of which the principles are described in Appendix B. The LDV system consists of a laser light source, a beam separator, fibre-optic couplers, a multi-colour receiver, a signal processor, a personal computer, a fibre-optic probe and a three-axis computer-driven traverse. Figure 5.7 and Figure 5.8 show an overview of the LDV set-up. The laser beam is separated into green (λ = 514.5nm) and blue (λ = 488nm)

light. The two-component system uses a four-beam two-colour configuration arranged at perpendicular angles to each other. The optical elements include a 40MHz Bragg cell to remove directional ambiguity and a 600mm focal length lens. The measurement process, data acquisition and data processing are controlled by a software package called 'PDA Flow and Particle Software' developed by DANTEC.

The traverse allowed the position of the probe to be maintained to ±12.5μm in all directions. In order to obtain near-wall data, the probe, approaching from the bottom of the tunnel, was tilted 5º towards the plate, as shown in Figure 5.9. Theoretically, the minimum angle which would let all beams pass through was 1.814º, which is the half-angle between the beams. Correction of the measurements for this angle was incorporated in the signal processor software.

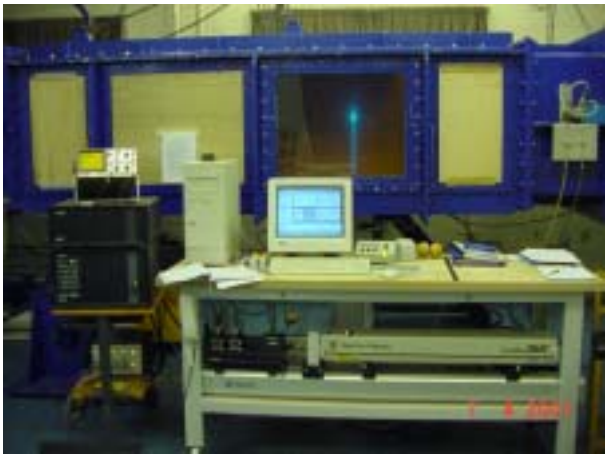

Figure 5.7. Overview of the LDV set-up

Figure 5.8. The LDV Set-up: traverse positioned underneath the tunnel

Figure 5.9. The probe was tilted 5°

Silver coated (soda lime borosilicate) glass spheres with a mean particle size of 16.3μm (ranging from 8.4-24.8μm were used for seeding the flow. About 2g (i.e. one pinchful) of seeding was put in per week.

Velocity measurements were conducted in backscatter mode over 20s or until 4096 validated samples (whichever came first) were collected per location. The measurements were transit time averaged.

The probe volume diameter was 276μm for the (blue) wall-normal channel and 291μm for the (green) streamwise channel, while the probe volume length was 8.725 and 9.199mm respectively. The probe volume contained 35 fringes spaced 7.709 and 8.128μm respectively. The frequency bandwidth for the streamwise channel was set at 1.2MHz throughout the experiments, whereas for the wall-normal channel it was set at 0.12MHz for speeds of 2 and 3m/s and at 0.4Mhz for the higher speeds. The validation and validated data rate increased from very low values near the wall to values of approximately 65-98% and 180-300Hz respectively further away from the wall.

The viscous length ν/U_τ varied from a minimum of 2.3μm for the SAND surface to a maximum of 17.1μm for the STEEL surface. The diameter of the probe volume therefore ranged from 127 viscous lengths for the SAND surface to 17 viscous lengths for the STEEL surface.

5.2.1.4 Test specimens.

As mentioned in Section 5.1, 5 different surfaces were tested: a steel surface which served as smooth reference (henceforth simply named STEEL), a surface coated with a Tin-free Self-Polishing Co-polymer (SPC), two surfaces coated with a Foul Release scheme; one of which was coated by spraying (FR) and the other was coated by rollering (ROLL). The paint systems were applied at the site of International Coatings Ltd in Felling. The sprayed systems were each applied in different spraying booths, one being specifically designated to silicone spraying jobs. The fifth surface was covered partially by sand-grit #40 (SAND).

Figure 5.10 shows the steel reference test specimen (STEEL).

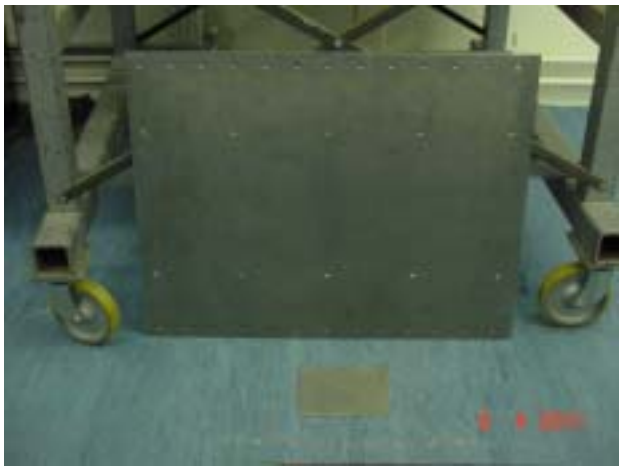

Figure 5.10. STEEL test specimen

The first coating scheme consisted of one layer of primer with a dry film thickness of 100µm and two layers of antifouling with a thickness of 125µm for each layer.

The primer (called 'Intertuf') was applied directly onto the clean steel surface. 6 hours later, the first layer of the SPC (called 'Intersmooth 360 Ecoloflex BEA369') was applied. The second layer of the antifouling was applied the following day.

Figure 5.11 and Figure 5.12 show the test specimen coated with the SPC scheme before and after immersion respectively. The characteristic change of colour due to polishing is evident.

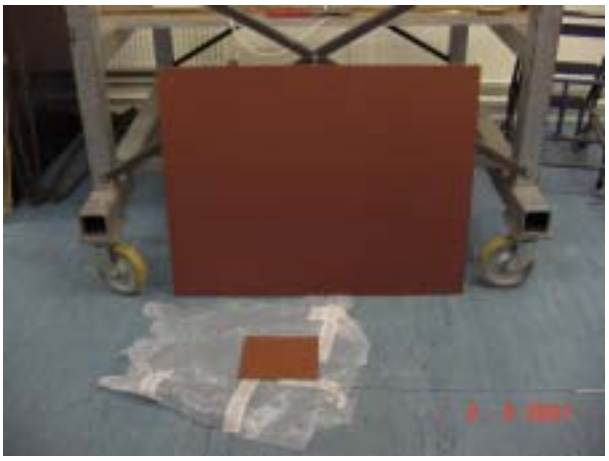

Figure 5.11. SPC test specimen before testing

Figure 5.12. SPC test specimen after testing

The second coating scheme consisted of one layer of primer (called 'Intershield') with a dry film thickness of 100µm, one layer of tiecoat (called 'Intersleek 731 BXA730/731') with

a dry film thickness of 100μm, and one topcoat (called 'Intersleek 757 BXA757/758/759') with a dry film thickness of 150μm.

Figure 5.13 shows the test specimen coated with the FR scheme.

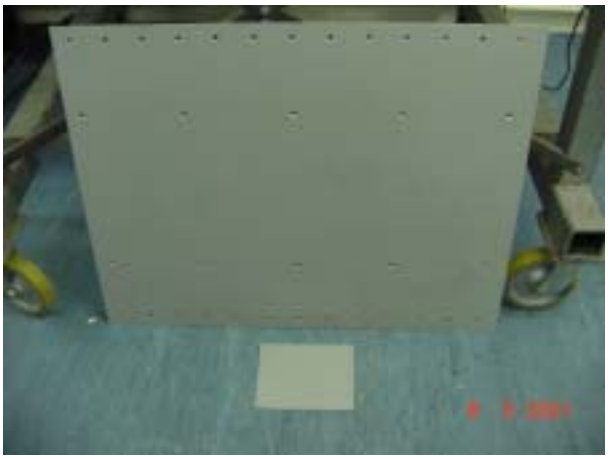

Figure 5.13. FR test specimen

Figure 5.14. ROLL test specimen

The third coating scheme was essentially the same as the second coating scheme, except that the application was done by rollering instead of spraying. Figure 5.14 shows the test specimen coated with the ROLL scheme.

In order to examine the boundary layer over a very rough surface, the fifth test specimen was partially covered with sand grit #40, over an area of 400 by 1000mm along the centreline. The grit was glued to the steel surface by varnish, in the same way as the tripping area at the leading edge of the plate. Figure 5.15 shows the SAND test specimen.

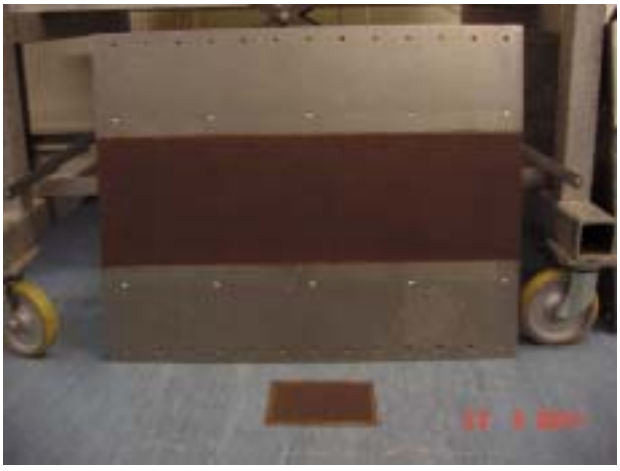

Figure 5.15. SAND test specimen

5.2.1.5 Roughness measurements

The roughness measurements were carried out with the BMT Hull Roughness Analyser described in Section 2.6.2. In order to avoid the stylus from scratching the surface, the Foul Release surfaces were slightly wetted, as shown in Figure 5.16.

Figure 5.16. The Foul Release surfaces were wetted slightly prior to the roughness measurements

Table 5-2 presents the average, mode and standard deviation of the different surfaces.

Table 5-2. Statistical roughness characteristics (in microns)

Surface	Average	Mode	Standard deviation
STEEL	22.9	14.0	10.3
SPC	68.6	68.0	17.8
FR	51.3	36.0	36.3
ROLL	59.7	40.0	25.5
SAND	727.3	702.0	100.3

It was visually observed that the sprayed Foul Release surface had some sagging around the centreline near the trailing edge of the plate, which was due to non-optimal pressure at the tip of the spray gun during application.

According to the Federation of European Producers of Abrasives (FEPA), the average sand grain size of sand grit #40 (i.e. 40 holes in a standard sized screen) is 425μm. This agrees rather well with the measured AHR value if one uses the rule of thumb given in Canham (1975) based on the measurements of Chaplin (1967): $h_s = 4.65 \cdot (AHR)^{0.7} \approx 465\mu m$, taking into account that some sand grains would lie on top of others, thus increasing the AHR.

The roughness histograms of the steel and coated surfaces are shown in Figure 5.17.

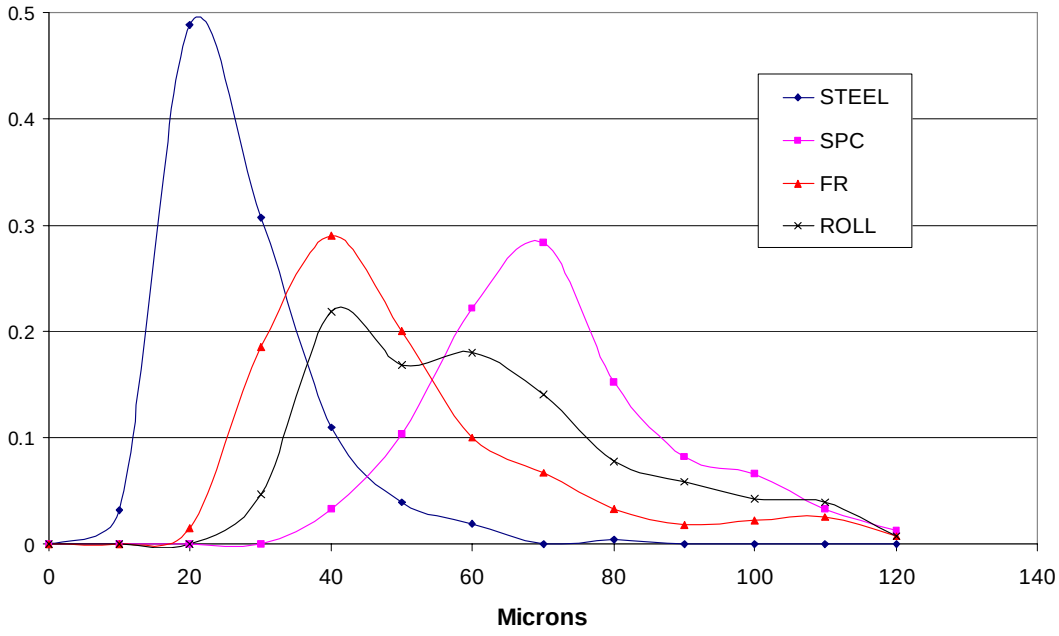

Figure 5.17. Roughness histograms of the different surfaces (excluding SAND).

Figure 5.17 does not include roughness measurements above 120µm. In the case of the Foul Release surface this exclusion of 3% of the values higher than 120µm gives a rather deceptive image since their average value was high (197µm). This explains why the average value was 51µm rather than ca. 40µm, which would be expected from looking at the histogram. Most of these very high values were caused by sagging, as mentioned. The centreline had a MHR of 70µm.

Small sample plates, shown in Figure 6.8, were coated alongside the test specimens and have been analysed with an optical measurement system for a more extensive study of the roughness characteristics (cf. Chapter 6).

5.2.2 Experimental procedure

In order to study the effect of paint on the turbulent boundary-layer structure, a baseline hydrodynamic performance of the smooth, unpainted STEEL surface was first evaluated. Subsequently, the different test specimens were tested. In order to look at boundary-layer development and the effect of Reynolds number on the flow, velocity profiles were taken at five downstream positions. The profile locations were at 1.302m, 1.4545m, 1.607m, 1.7595 and 1.912m from the leading edge (x/L = 0.620, 0.693, 0.765, 0.838 and 0.910 respectively) and the five free-stream velocities were 2m/s, 3m/s, 4m/s, 5m/s and 6m/s. The locations are referred to as POS1, POS2, POS3, POS4 and POS5 respectively. Each boundary-layer profile is identified by putting the name of the surface and the free-stream velocity value before the name of the location, e.g. FR4POS3.

Before conducting any LDV measurements, the angle of attack of the boundary-layer test plate was adjusted to give zero pressure gradient over the test plate. The lengthwise origin of the traverse was set at the beginning of the experiments and was determined by the maximum reach of the traverse (0.61m) and the farthest possible position from the leading edge, i.e. position 5 (1.91m from the leading edge) which was very near the edge of the last observation window of the tunnel. This origin of the traverse was not changed for the duration of the experiments.

The following procedure was carried out to measure the velocity profile over the different test specimens:

1. Mount the test specimen into the boundary-layer plate and fill the tunnel with water
2. Move the traverse so that the probe volume lies at the centreline height of the tunnel approximately 0.2m from the boundary-layer plate and 0.5m from the near tunnel-wall, 1.912m from the leading edge of the plate
3. Adjust the free-stream velocity until the LDV velocity readings indicate that U = 2m/s
4. Find the wall (y = 0) by receding the probe volume until the observed noise on the oscilloscope increases significantly. This will indicate that the centre of the probe volume is within about one half of the probe volume diameter of the wall. The current through the anode of the PDA receiver will now reach a maximum, often

very near its maximum allowed value of 100μA. If this value is exceeded and the overload of the anode occurs, the probe has to be moved away from the surface until the overload disappears. It was observed that this overload frequently occurred with the SPC surface, but not with the other surfaces. The exact reason is not known.

5. Recede the probe until the wall signal dominates. The measurements now should not measure a significant velocity signal. This was not always the case for the glossy Foul Release surfaces. Sometimes significant streamwise velocities were measured, which would reach a minimum and then rise steeply. The minimum indicates the position nearest to the wall. The earlier measurements were actually taken *in* the surface, the signals being distorted by reflected light.
6. Start the actual data collection using the automated traverse datafile. The system will collect for each channel 4000 coincidence samples or sample for a duration of 20s, whichever comes first, and then proceed to the next location in the traverse file. In the inner region, between 100 and 200 validated samples were picked up over 20s at a very low validation rate (ca. 0.01%). In the outer region of the boundary layer ($y >$ ca. 0.15δ), the data rate would lie between 0.18 and 0.28kHz with validation rates between ca. 75 and 99% (depending on the position and the free-stream velocity). The traverse datafile consist of four regions with different traverse stepsize. In Region 1 near the wall (consisting of approximately 90 data points) the stepsize is 0.05mm. Regions 2 and 3 have stepsizes of 0.25mm (ca. 10 data points) and 1mm (ca. 40 points) respectively. Finally a last data point was collected 200mm from the wall. At a later stage of the experiments, a near-wall region of 21 points with a stepsize of 0.0125mm was put before Region 1. This process is indicated in Figure 5.18.
7. Continue measuring until the mean axial velocity becomes invariant. One extra data point is collected 200mm from the wall.
8. Measure and record the temperature and the kinematic viscosity of the water.
9. Repeat steps 2-8 for free-stream velocities of 3, 4, 5 and 6m/s.
10. Repeat steps 2-9 for positions 1302, 1454.5, 1607 and 1759.5mm from the leading edge.

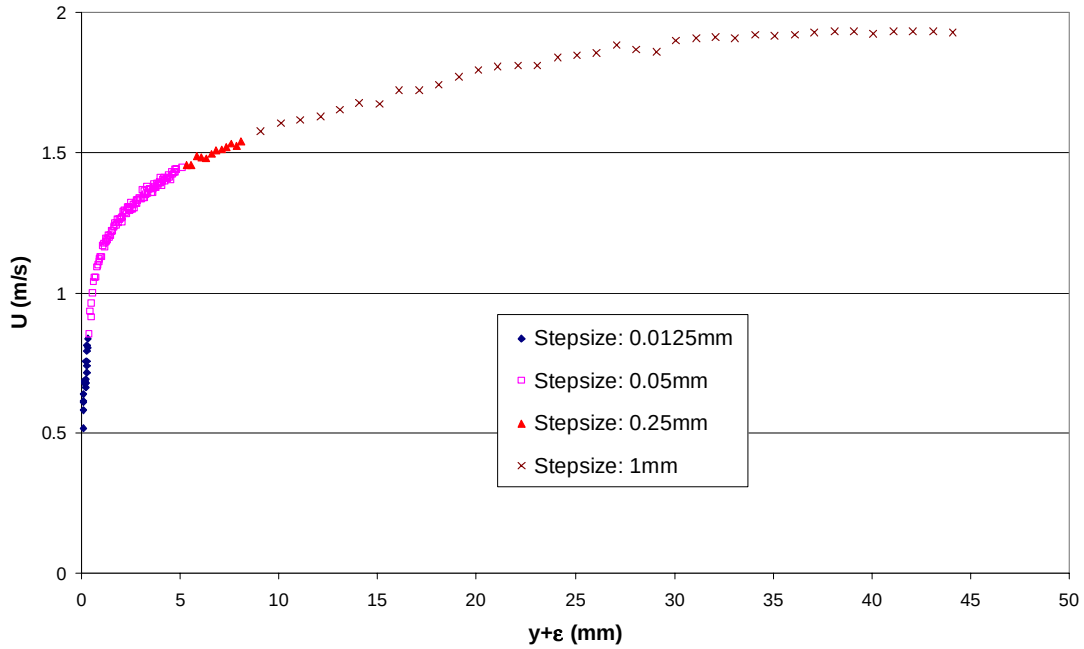

Figure 5.18. Typical boundary-layer velocity profile (STEEL2POS3) with indication of the different traverse stepsizes used during measurement (Extra data point measured at y=200mm not included).

5.2.3 Data reduction and analysis

The collected data were exported in ASCII format and were imported into Excel spreadsheets for further analysis. The data comprised of the average velocity components U and V, the turbulence intensities u'_{RMS} and v'_{RMS}, the Reynolds stress $-\overline{u'v'}$ and the number of validated samples at each collected data point. For each point (provided the local data rate was high enough), a power spectrum and autocorrelation function were exported to separate files.

All the boundary-layer parameters were calculated within the Excel spreadsheets. The boundary-layer thickness, $\delta_{0.99}$ (hereafter simply called δ), the displacement thickness δ_1 and the momentum thickness θ were computed by using a trapezoid integration method.

An accurate determination of the friction velocity U_τ is very important because of its relevance in scaling the mean velocity and turbulence quantities. The sublayer slope method (cf. Section 4.7.3) was not applied because sufficient data could not be obtained in the viscous sublayer ($y^+ < 7$) to apply the method accurately. The momentum method based on the von Karman momentum integral (cf. Section 4.7.5) was tried for the STEEL surface but this method suffered from the fluctuations observed in the momentum thickness values and was therefore found to be inaccurate.

The friction velocity of the STEEL surface was calculated by the Clauser method (C), the Hama method (H) and the Reynolds stress method (RS). The latter two methods were retained for the rough surfaces.

Firstly, the origin of the smooth STEEL wall (i.e. ε) was determined by matching the points collected in the viscous sublayer with the theoretical equation $(y+\varepsilon)^+ = U^+$. Consequently, following Lewthwaite et al. (1985) and Schultz (1998, 2000), the Clauser method was applied using the log-law slope as variable (cf. Section 4.7.6). The experimental data were plotted as U/U_e versus $\ln(yU_e/\nu)$ and a linear regression of the data points in the log-law region was calculated. The slope of this regression line is used to find U_τ since $U_\tau = \kappa \cdot (\text{slope}) \cdot U_e$. Following Schultz (1998, 1999, 2000) the lower limit of this region was set at $y^+ = 50$ and the upper limit was set at $y < 0.125\delta$ (Schultz, 1998; Lewthwaite et al., 1985). In

addition, Bradshaw's method by using reference values was checked at reference values $y^+ = 200$, $U^+ = 17.93$, which showed good agreement.

Since the roughness function does not affect the slope of the regression line, this method is also valid for rough surfaces provided ε is taken into account. Following Schultz (1998), U is plotted against $\ln(y+\varepsilon)$ and a least-squares second-order polynomial is drawn through the selected data points. Consequently, ε is varied until the quadratic term disappears and the polynomial effectively becomes linear. The slope is then calculated and U_τ adjusted. This in turn shifts the region $50 < y^+ < 0.125\delta^+$ and the calculations are iterated until convergence is achieved. Thus, the modified Clauser method used in this analysis is basically an iteration technique that determines ε and U_τ by forcing the log-law slope ($1/\kappa$ for natural logarithms cf. Equation 4.19) over a selected region of the collected data.

The Reynolds stress method (cf. Section 4.7.4) was very straightforward to apply. Despite the considerable scatter of the measured Reynolds stress peak, as shown in Appendix D, it was not difficult to make an accurate estimation from the trend displayed by the collected data points a little further away from the wall (ca. $0.04 < y/\delta < 0.09$). Measurements taken in the viscous sublayer showed a sharp decline in the Reynolds stress, indicating that the viscous shear stress becomes prominent.

The Hama method (cf. Section 4.7.7) involved optimising U_τ and Π first with $\varepsilon = 0$. When the near-wall data showed premature departure from the fit in the log-law region, a virtual origin was introduced to straighten the data. This had a limited effect on the values of U_τ and Π and one extra iteration loop generally sufficed. Figure 5.19 shows an arbitrary selection of the measured data and the respective fits as calculated with the Hama method

Following Tachie (2000), the chi-squared distribution of the fitted curve and the experimental data was computed in the region $0.1 < y/\delta < 0.99$ as a quantitative measure of the goodness-of-fit for the plots shown in Figure 5.19. It was noted that the plots gave a good representation of the experimental data at a 99.5% confidence level.

A detailed experimental uncertainty analysis has been carried out on the STEEL and the SPC surface, which is presented in Appendix C.

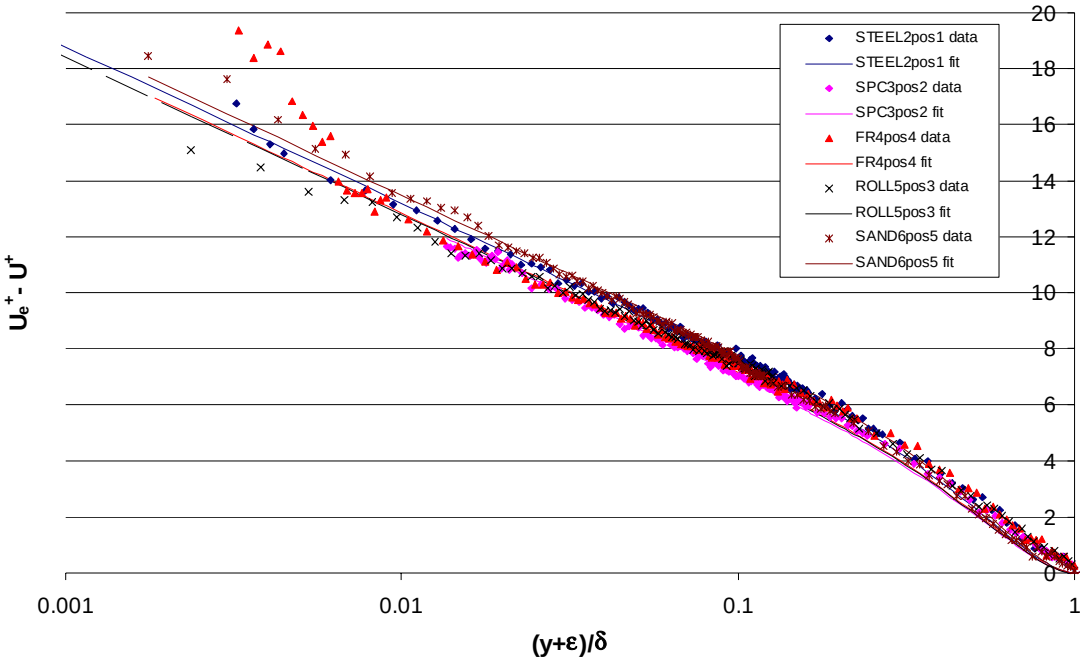

Figure 5.19. Determination of U_τ, Π and ε using Equation 5.2 to fit the data.

5.2.4 Results and discussion

5.2.4.1 Test parameters

The basic boundary-layer parameters calculated for all surfaces are shown in Table 5-3 to Table 5-7. The boundary-layer thickness δ is specified for $U = 0.99U_e$.

Table 5-3. Boundary-layer parameters of the STEEL surface

STEEL	Ue	Reθ	δ	δI	θ	H	Tu
STEEL2pos1	1.97	7.30E+03	30.25	4.20	3.11	1.35	0.0337
STEEL2pos2	1.93	7.19E+03	31.15	4.45	3.35	1.33	0.0248
STEEL2pos3	1.94	7.99E+03	36.00	4.73	3.63	1.30	0.0211
STEEL22pos4	1.92	8.34E+03	36.30	5.11	3.91	1.31	0.0349
STEEL2pos5	1.92	7.31E+03	33.80	4.65	3.43	1.36	0.0290
STEEL3pos1	3.04	1.07E+04	29.25	3.89	2.96	1.31	0.0292
STEEL3pos2	3.03	1.06E+04	31.15	4.30	3.25	1.32	0.0204
STEEL3pos3	3.05	1.23E+04	34.65	4.41	3.44	1.28	0.0186
STEEL3pos4	3.03	1.20E+04	36.25	4.74	3.55	1.33	0.0209
STEEL3pos5	3.00	1.20E+04	34.80	5.07	3.60	1.41	0.0259
STEEL4pos1	3.94	1.33E+04	28.03	3.90	2.91	1.34	0.0271
STEEL4pos2	3.95	1.49E+04	36.05	4.52	3.36	1.35	0.0172
STEEL4pos3	3.98	1.59E+04	32.80	4.46	3.40	1.31	0.0264
STEEL4pos4	4.00	1.19E+04	27.45	3.72	2.76	1.35	0.0363
STEEL45pos5	3.92	1.54E+04	35.70	4.74	3.66	1.29	0.0238
STEEL53pos1	5.08	1.50E+04	29.35	3.76	2.90	1.30	0.0255
STEEL53pos2	4.88	1.53E+04	33.70	3.47	2.79	1.24	0.0238
STEEL5pos3	5.27	2.04E+04	36.65	4.61	3.46	1.33	0.0231
STEEL5pos4	5.00	1.88E+04	36.25	4.67	3.49	1.34	0.0252
STEEL52pos5	4.96	1.93E+04	38.55	4.82	3.71	1.30	0.0256
STEEL6pos1	6.05	2.23E+04	31.90	3.94	3.09	1.27	0.0229
STEEL6pos3	6.06	2.39E+04	34.40	4.50	3.39	1.33	0.0262
STEEL6pos5	6.05	2.31E+04	36.90	4.91	3.48	1.41	0.0289

Table 5-4. Boundary-layer parameters of the SPC surface

SPC	Ue	Reθ	δ	δI	θ	H	Tu
SPC2pos1	1.93	6.95E+03	31.40	4.06	3.17	1.28	0.0194
SPC2pos2	1.93	7.91E+03	34.55	4.24	3.36	1.26	0.0184
SPC22pos3	1.93	7.63E+03	34.35	4.49	3.55	1.26	0.0184
SPC2pos4	1.93	8.22E+03	34.90	4.46	3.45	1.29	0.0246
SPC23pos5	1.92	7.36E+03	34.00	4.31	3.45	1.25	0.0252
SPC3pos1	3.03	1.06E+04	29.40	3.91	3.05	1.28	0.0216
SPC3pos2	3.05	1.19E+04	32.40	4.02	3.20	1.26	0.0274
SPC3pos3	3.00	1.25E+04	34.35	4.30	3.37	1.28	0.0207
SPC3pos4	3.05	1.28E+04	36.70	4.36	3.47	1.26	0.0268
SPC3pos5	3.02	1.26E+04	35.80	4.42	3.55	1.25	0.0244
SPC4pos1	3.98	1.42E+04	32.40	3.93	3.11	1.27	0.0157
SPC4pos2	3.98	1.58E+04	35.25	4.06	3.25	1.25	0.0231
SPC4pos3	3.96	1.52E+04	35.25	4.22	3.34	1.26	0.0258
SPC4pos4	3.99	1.79E+04	37.70	4.56	3.64	1.25	0.0240
SPC4pos5	3.93	1.62E+04	33.80	4.31	3.47	1.24	0.0266
SPC5pos1c	4.98	1.77E+04	32.00	3.85	3.06	1.26	0.0225
SPC5pos2	4.99	1.98E+04	34.25	4.06	3.25	1.25	0.0217
SPC5pos3	4.99	2.11E+04	36.10	4.32	3.46	1.25	0.0214
SPC5pos4	4.97	2.13E+04	36.70	4.40	3.51	1.26	0.0278
SPC5pos5	4.93	2.09E+04	38.00	4.46	3.60	1.24	0.0251
SPC6pos1	6.08	2.23E+04	30.60	3.91	3.12	1.26	0.0221
SPC6pos3	6.11	2.71E+04	40.10	4.75	3.77	1.26	0.0196
SPC6pos5	6.00	2.54E+04	36.85	4.29	3.47	1.24	0.0286

Table 5-5. Boundary-layer parameters of the FR surface

FR	Ue	Reθ	δ	δ1	θ	H	Tu
FR2pos1	1.95	6.06E+03	29.25	4.40	3.12	1.41	0.0224
FR2pos2	1.98	8.18E+03	35.00	4.65	3.55	1.31	0.0191
FR2pos3	1.95	7.88E+03	34.90	4.91	3.69	1.33	0.0210
FR2pos4	1.93	8.12E+03	35.00	4.75	3.66	1.30	0.0230
FR2pos5	1.95	6.92E+03	32.50	4.89	3.56	1.37	0.0289
FR3pos1	3.04	9.01E+03	29.25	4.22	2.98	1.42	0.0241
FR3pos2	3.04	1.14E+04	32.85	4.10	3.18	1.29	0.0202
FR3pos3	3.04	1.16E+04	34.75	4.52	3.50	1.29	0.0203
FR3pos4	3.04	1.27E+04	36.00	4.80	3.63	1.32	0.0246
FR3pos5	3.00	1.08E+04	34.60	4.71	3.56	1.33	0.0245
FR4pos1	4.12	1.21E+04	30.00	3.84	2.90	1.33	0.0232
FR4pos2	3.97	1.50E+04	33.85	4.22	3.18	1.33	0.0238
FR4pos3	3.97	1.43E+04	31.75	4.23	3.29	1.29	0.0239
FR4pos4	3.98	1.66E+04	34.80	4.61	3.59	1.28	0.0220
FR42pos5	3.97	1.66E+04	35.60	4.30	3.47	1.24	0.0281
FR5pos1	5.14	1.51E+04	28.85	3.78	2.88	1.31	0.0262
FR5pos2	5.00	1.93E+04	32.85	4.13	3.21	1.29	0.0234
FR5pos3	5.00	1.94E+04	36.75	4.81	3.55	1.36	0.0222
FR5pos4	4.98	2.10E+04	39.80	4.67	3.62	1.29	0.0257
FR5pos5	4.98	1.93E+04	37.75	4.58	3.54	1.29	0.0288
FR6pos1	6.20	1.82E+04	29.70	3.93	2.88	1.36	0.0259
FR6pos2	6.15	2.59E+04	35.50	4.58	3.49	1.31	0.0219
FR6pos3	6.14	2.57E+04	37.45	4.79	3.69	1.30	0.0221
FR6pos5	6.08	2.33E+04	38.60	4.58	3.57	1.28	0.0251

Table 5-6. Boundary-layer parameters of the ROLL surface

ROLL	Ue	Reθ	δ	δ1	θ	H	Tu
ROLL2pos1	1.97	6.45E+03	30.55	3.87	2.88	1.34	0.0204
ROLL2pos3	1.99	7.33E+03	29.50	4.40	3.31	1.33	0.0278
ROLL2pos5	1.95	7.85E+03	34.25	4.58	3.54	1.29	0.0321
ROLL3pos1	3.07	1.07E+04	27.70	3.96	3.02	1.31	0.0229
ROLL3pos3	3.09	1.21E+04	34.30	4.62	3.52	1.31	0.0202
ROLL3pos5	3.06	1.28E+04	37.00	4.72	3.67	1.29	0.0213
ROLL4pos1	3.93	1.34E+04	28.70	3.85	2.96	1.30	0.0258
ROLL4pos3	3.99	1.43E+04	31.30	4.39	3.24	1.36	0.0235
ROLL4pos5	3.93	1.46E+04	36.90	4.06	3.28	1.24	0.0276
ROLL5pos1	5.20	1.79E+04	30.60	3.84	2.95	1.30	0.0235
ROLL5pos3	5.13	1.97E+04	34.30	4.71	3.42	1.38	0.0251
ROLL5pos5	4.94	2.03E+04	37.10	4.72	3.58	1.32	0.0259
ROLL6pos1	6.19	2.08E+04	30.25	3.74	2.88	1.30	0.0243
ROLL6pos3	6.16	2.33E+04	35.30	4.34	3.37	1.29	0.0245
ROLL6pos5	5.95	2.61E+04	40.10	4.80	3.68	1.30	0.0255

Table 5-7. Boundary-layer parameters of the SAND surface

SAND	Ue	Reθ	δ	δ1	θ	H	Tu
SAND2pos1	1.95	7.42E+03	31.80	4.87	3.40	1.43	0.0227
SAND2pos3	1.99	9.66E+03	34.00	6.24	4.33	1.44	0.0234
SAND2pos5	1.94	1.02E+04	34.85	6.85	4.68	1.46	0.0295
SAND3pos1	3.05	1.17E+04	28.90	5.09	3.43	1.49	0.0248
SAND3pos2	3.06	1.39E+04	33.00	5.56	3.87	1.44	0.0225
SAND3pos3	3.07	1.46E+04	33.20	6.24	4.25	1.47	0.0216
SAND3pos5	3.02	1.62E+04	34.85	6.88	4.61	1.49	0.0302
SAND4pos1	3.96	1.59E+04	28.90	5.47	3.42	1.60	0.0283
SAND4pos2	3.95	1.72E+04	30.00	5.51	3.71	1.49	0.0287
SAND4pos3	3.99	1.92E+04	35.20	6.33	4.24	1.49	0.0206
SAND42pos5	4.00	2.20E+04	34.92	7.36	4.72	1.56	0.0364
SAND5pos1	4.97	1.96E+04	32.70	5.44	3.47	1.57	0.0234
SAND5pos3	5.18	2.53E+04	37.20	6.34	4.30	1.48	0.0252
SAND5pos5	5.19	2.95E+04	38.75	7.56	5.00	1.51	0.0318
SAND6pos1	6.00	2.51E+04	32.40	5.90	3.60	1.64	0.0235
SAND6pos3	6.19	3.10E+04	35.90	6.54	4.41	1.48	0.0236
SAND6pos5	6.09	3.31E+04	39.65	6.93	4.68	1.48	0.0261

Table 5-3 to Table 5-7 show that the actual measured free-stream velocity U_e varied between 1.92 and 6.20m/s. The kinematic viscosity fluctuated between $0.82 \cdot 10^{-6}$ and $1.08 \cdot 10^{-6} m^2/s$ and the momentum thickness Reynolds number Re_θ between 6060 (FR2pos1) and 33110 (SAND6pos5). The boundary-layer thickness δ varied between 27.45 (STEEL4pos4) and 40.10mm (ROLL6pos5) and the free-stream turbulence, taken at $y = \delta$, varied between 1.57 (SPC4pos1) and 3.64% (SAND4pos5) with an average free-stream turbulence of 2.46%. This is in fairly good agreement with previous measurements of the free-stream turbulence in the Emerson Cavitation Tunnel as measured by Atlar and Korkut (1997).

To determine if the differences of the parameters between the surfaces were significant within the experimental uncertainty, statistical tests were carried out. The tests consisted of two-factor ANOVAs (Analysis of Variances) with test surface and Re_x as factors. In cases where the ANOVA indicated significant differences between the different test surfaces, multiple pairwise comparisons were conducted using Tukey's test (Mason et al., 1989). The significance level for all the tests was set at $\alpha = 0.05$.

The ANOVA on the boundary-layer thickness results showed that Re_x had a significant effect, but not the test surface. The ANOVA indicated a significant effect of both Re_x and test surface on the boundary-layer displacement and momentum thicknesses. However, multiple pairwise comparisons indicated that a significant increase in δ_1 and θ only occurred for the SAND surface. The ANOVA test on the shape factor, showed that the test surface had an influence, but not the Reynolds number. Multiple pairwise comparisons indicated that a significant increase in H was observed for the SAND surface, which had an average shape factor of H = 1.51, while a significant (but small) decrease was noted for the SPC surface, which had an average shape factor of H = 1.26. The average shape factors for the other surfaces were between 1.31 and 1.33.

Based on the velocity defect law, Hama (1954, p.337) derived the following equation for H :

$$H = (1 - U_\tau / U_e \cdot I_2 / I_1) \tag{5.1}$$

whereby I_2/I_1 is a universal constant for flows without a pressure gradient. Hinze (1975, p. 633) gives a value of 6.1 for this constant, based on Hama's experimental data. This equation for H is shown in Figure 29 plotted against U_e/U_τ, along with the H values obtained presently.

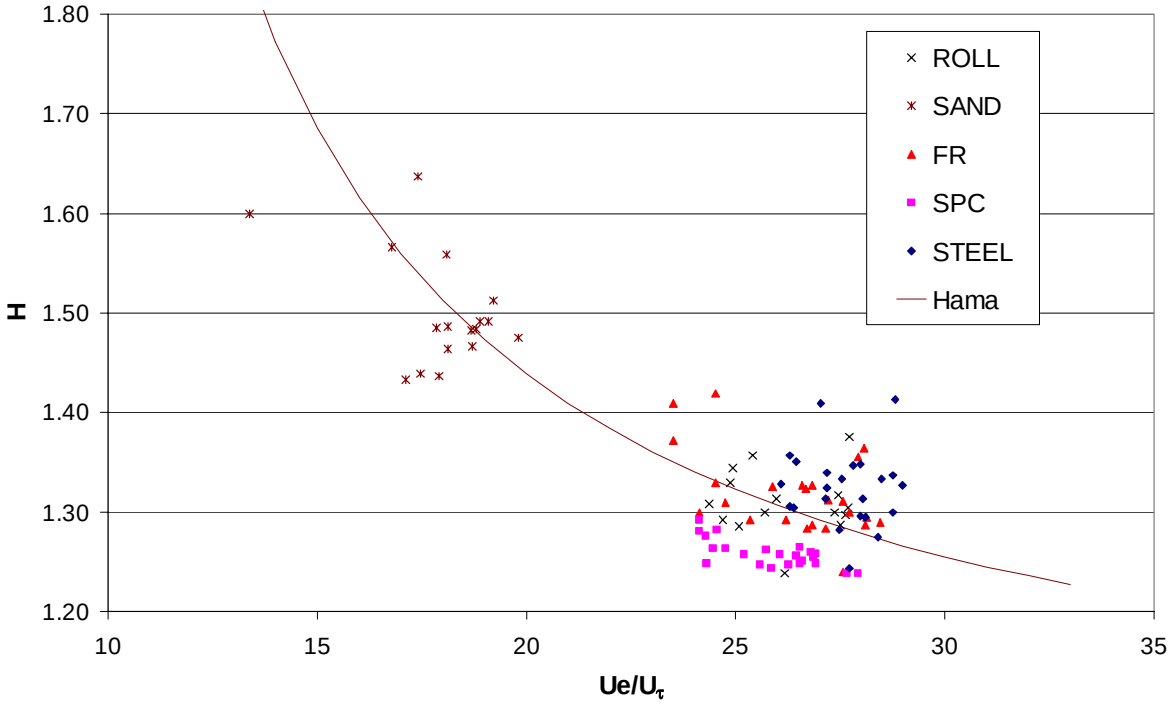

Figure 5.20. H values plotted against U_e/U_τ (uncertainty in H: ±3.17% for STEEL, ±0.58% for the rough surfaces, uncertainty in U_e/U_τ: ±1.07% and ±1.56% respectively).

It is expected that for rougher surfaces, the H values will be higher, but as is clear from Figure 5.20, this does not seem to be the case for the coated surfaces.

5.2.4.2 Mean velocity profiles in outer variables

The mean velocity profiles in outer variables are shown in Figure 5.21 for an arbitrary selection of the data (i.e. 2pos1, 3pos3, 4pos1, 5pos3 and 6pos5). The effect of roughness is to increase the drag, resulting in a less full profile. It is clear from this figure that the SAND surface exhibits by far the largest drag.

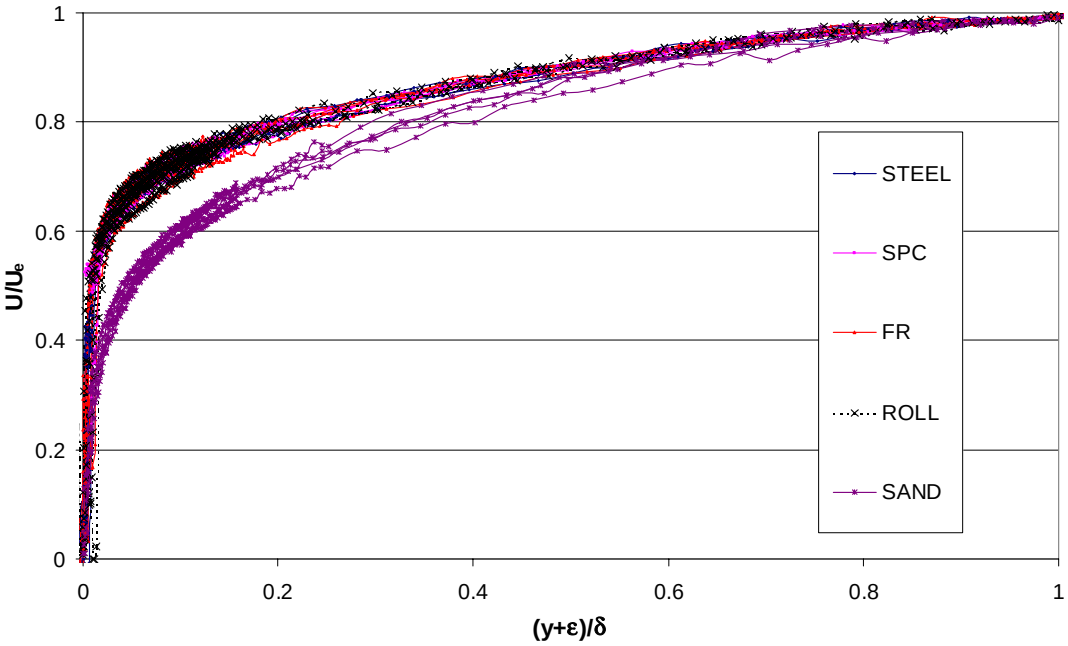

Figure 5.21. Variation of mean velocity in outer co-ordinates for the different surfaces (Uncertainty in U/U_e : ±1.7% outside the viscous sublayer for the STEEL surface, ±1.6% for the rough surfaces. The uncertainty in $(y+\varepsilon)/\delta$ varies with y and is dominated by the uncertainty in ε for the near-wall points, declining to the uncertainty in δ for the outer-layer points.

5.2.4.3 Shear velocities, wake values and mean velocity profiles in wall co-ordinates

The shear velocities, wake values and other related parameters are listed in Table 5-8 to Table 5-12. The shear velocities were calculated by three different methods for the STEEL plate: the Clauser method (C), between the Reynolds-stress method (RS) and the Hama method (H) for which good agreement was found. Only the latter two methods were retained on the coated surfaces and good agreement was found. U_τ as calculated with Hama's method was chosen to non-dimensionalise the plots in Appendix D.

Table 5-8. U_τ, Π and related parameters of the STEEL surface

STEEL	Reδ1	Uτ HAMA	Π	δ+	cf (C)	cf (H)	cf (RS)
STEEL2pos1	9856	0.0745	0.4	2683	0.002908	0.00286	0.002957
STEEL2pos2	9547	0.074	0.42	2561	0.002908	0.00294	0.003053
STEEL2pos3	10430	0.0735	0.44	3007	0.002815	0.002871	0.002899
STEEL22pos4	10899	0.073	0.45	2944	0.002723	0.002891	0.002914
STEEL2pos5	9922	0.073	0.44	2742	0.002908	0.002891	0.002917
STEEL3pos1	14069	0.112	0.4	3900	0.002687	0.002715	0.002768
STEEL3pos2	14002	0.1115	0.45	3735	0.002651	0.002708	0.002747
STEEL3pos3	15806	0.111	0.42	4525	0.002633	0.002649	0.002673
STEEL3pos4	15942	0.11	0.44	4431	0.002663	0.002636	0.002674
STEEL3pos5	16912	0.111	0.35	4292	0.002693	0.002738	0.002628
STEEL4pos1	17858	0.145	0.37	4726	0.002633	0.002709	0.002712
STEEL4pos2	20014	0.142	0.42	5733	0.002604	0.002585	0.002624
STEEL4pos3	20885	0.142	0.43	5480	0.002545	0.002546	0.00255
STEEL4pos4	16076	0.143	0.4	4244	0.002754	0.002556	0.002643
STEEL45pos5	19968	0.1395	0.43	5355	0.002545	0.002533	0.002618
STEEL53pos1	19479	0.1815	0.4	5437	0.002545	0.002553	0.00256
STEEL53pos2	18973	0.176	0.32	6642	0.002574	0.002601	0.002687
STEEL5pos3	27233	0.185	0.4	7593	0.002429	0.002465	0.002519
STEEL5pos4	25104	0.174	0.4	6782	0.002458	0.002422	0.00247
STEEL52pos5	25093	0.1725	0.4	6985	0.002401	0.002419	0.002465
STEEL6pos1	28368	0.213	0.41	8089	0.002372	0.002479	0.002477
STEEL6pos3	31691	0.209	0.45	8360	0.002429	0.002379	0.002526
STEEL6pos5	32567	0.21	0.4	8487	0.002418	0.00241	0.002449

Table 5-9. U_τ, Π and related parameters of the SPC surface

SPC	Reδ1	Uτ HAMA	Π	δ+	cf (H)	cf (RS)	ΔU+ (H)	ΔU+ (RS)
SPC2pos1	8906	0.08	0.3	2854.545	0.003436	0.003555	1.78	1.96
SPC2pos2	9988	0.078	0.34	3286.463	0.003267	0.003254	1.45	1.17
SPC22pos3	9642	0.079	0.31	3015.167	0.003341	0.003304	1.63	1.27
SPC2pos4	10623	0.08	0.33	3446.914	0.003436	0.003323	2.22	1.58
SPC23pos5	9195	0.079	0.3	2984.444	0.003386	0.00342	1.68	1.57
SPC3pos1	13603	0.1235	0.34	4173.448	0.003323	0.003372	2.43	2.38
SPC3pos2	14949	0.121	0.3	4780.976	0.003148	0.003136	1.99	1.72
SPC3pos3	15939	0.1235	0.32	5237.315	0.003389	0.003299	3.07	2.51
SPC3pos4	16146	0.117	0.3	5210.966	0.002943	0.002916	1.32	0.98
SPC3pos5	15713	0.118	0.25	4969.882	0.003053	0.003148	1.73	1.89
SPC4pos1	17981	0.15	0.34	5586.207	0.002841	0.003012	1.13	1.67
SPC4pos2	19687	0.15	0.34	6448.171	0.002841	0.002937	1.35	1.57
SPC4pos3	19188	0.154	0.34	6239.655	0.003025	0.00287	2.11	1.20
SPC4pos4	22443	0.15	0.3	6981.481	0.002827	0.002809	1.62	1.31
SPC4pos5	20187	0.152	0.25	6116.19	0.002992	0.002897	2.10	1.45
SPC5pos1c	22293	0.185	0.34	6883.721	0.00276	0.00287	1.28	1.58
SPC5pos2	24696	0.1855	0.31	7748.018	0.002764	0.002959	1.55	2.23
SPC5pos3	26296	0.19	0.35	8364.634	0.0029	0.002766	2.35	1.49
SPC5pos4	26697	0.185	0.3	8279.878	0.002771	0.002764	1.78	1.52
SPC5pos5	25844	0.178	0.3	7957.647	0.002613	0.002889	0.90	2.03
SPC6pos1	27994	0.23	0.34	8280	0.002862	0.002781	2.33	1.73
SPC6pos3	34132	0.228	0.34	10756.24	0.002785	0.002618	2.47	1.40
SPC6pos5	31416	0.215	0.3	9661.89	0.002568	0.002735	1.15	1.79

Table 5-10. U_τ, Π and related parameters of the FR surface.

FR	Reδ1	Uτ HAMA	Π	δ+	cf (H)	cf (RS)	ΔU+ (H)	ΔU+ (RS)
FR2pos1	8539	0.083	0.3	2418.704	0.003623	0.003649	2.31	2.16
FR2pos2	10703	0.08	0.29	3255.814	0.003265	0.003227	1.61	1.24
FR2pos3	10478	0.0795	0.3	3037.607	0.003324	0.00314	1.78	0.85
FR2pos4	10541	0.08	0.34	3218.391	0.003436	0.003163	2.20	0.95
FR2pos5	9491	0.083	0.3	2687.449	0.003623	0.003135	2.57	0.58
FR3pos1	12791	0.124	0.3	3613.486	0.003328	0.003261	2.29	1.82
FR3pos2	14680	0.116	0.32	4483.059	0.002912	0.003267	0.95	2.18
FR3pos3	15029	0.12	0.32	4565.36	0.003116	0.00306	1.88	1.42
FR3pos4	16766	0.114	0.33	4717.241	0.002813	0.002894	0.82	0.97
FR3pos5	14278	0.116	0.36	4054.141	0.00299	0.003024	1.22	1.14
FR4pos1	15989	0.155	0.3	4696.97	0.002831	0.002915	0.79	0.95
FR4pos2	19954	0.148	0.33	5964.048	0.00278	0.002989	1.10	1.83
FR4pos3	18390	0.148	0.33	5144.515	0.00278	0.00289	0.89	1.18
FR4pos4	21347	0.149	0.33	6029.302	0.002803	0.00284	1.38	1.33
FR42pos5	20576	0.144	0.33	6176.386	0.002631	0.002659	0.43	0.35
FR5pos1	19872	0.189	0.3	5569.612	0.002704	0.002786	0.72	0.89
FR5pos2	24883	0.178	0.35	7044.94	0.002535	0.002735	0.38	1.21
FR5pos3	26328	0.179	0.34	7201.938	0.002563	0.002739	0.68	1.37
FR5pos4	27039	0.175	0.33	8098.837	0.00247	0.002708	0.22	1.28
FR5pos5	24956	0.177	0.32	7315.251	0.002526	0.002681	0.34	0.94
FR6pos1	24881	0.221	0.33	6704.494	0.002541	0.002733	0.42	1.19
FR6pos2	33905	0.223	0.33	9537.952	0.00263	0.002679	1.67	1.70
FR6pos3	33419	0.2215	0.35	9426.335	0.002603	0.00259	1.49	1.20
FR6pos5	29935	0.224	0.31	9297.204	0.002715	0.002665	1.79	1.31

Table 5-11. U_τ, Π and related parameters of the ROLL surface.

ROLL	Reδ1	Uτ HAMA	Π	δ+	cf (H)	cf (RS)	ΔU+ (H)	ΔU+ (RS)
ROLL2pos1	8672	0.079	0.3	2742.557	0.003216	0.003456	0.90	1.55
ROLL2pos3	9734	0.08	0.34	2622.222	0.003232	0.003262	1.25	1.14
ROLL2pos5	10147	0.079	0.3	3074.716	0.003283	0.003414	1.55	1.80
ROLL3pos1	13962	0.126	0.34	4011.724	0.003369	0.003187	2.66	1.75
ROLL3pos3	15852	0.119	0.32	4535.222	0.002966	0.002881	1.38	0.77
ROLL3pos5	16403	0.122	0.3	5129.545	0.003179	0.003254	2.35	2.41
ROLL4pos1	17404	0.153	0.34	5047.241	0.003031	0.003169	1.89	2.23
ROLL4pos3	19457	0.157	0.28	5460.111	0.003097	0.002945	2.44	1.57
ROLL4pos5	18123	0.15	0.26	6289.773	0.002921	0.00307	1.51	1.93
ROLL5pos1	23206	0.19	0.34	6760.465	0.00267	0.002732	0.93	1.01
ROLL5pos3	27094	0.185	0.32	7129.775	0.002606	0.002707	0.98	1.28
ROLL5pos5	26777	0.18	0.3	7675.862	0.002655	0.002741	1.21	1.42
ROLL6pos1	26923	0.224	0.34	7879.07	0.002619	0.002762	1.04	1.53
ROLL6pos3	30005	0.224	0.32	8884.494	0.002645	0.002687	1.44	1.43
ROLL6pos5	33996	0.215	0.3	10263.69	0.002611	0.002705	1.58	1.83

Table 5-12. U_τ, Π and related parameters of the SAND surface.

SAND	Reδ1	Uτ HAMA	Π	δ+	cf (H)	cf (RS)	ΔU+ (H)	ΔU+ (RS)
SAND2pos1	10625	0.114	0.15	4059.938	0.006836	0.006103	9.24	8.02
SAND2pos3	13904	0.114	0.4	4340.814	0.006563	0.005838	9.56	8.28
SAND2pos5	14878	0.107	0.36	4176.13	0.006084	0.006347	9.06	9.21
SAND3pos1	17399	0.171	0.38	5534.538	0.006287	0.006103	9.74	9.25
SAND3pos2	20032	0.171	0.38	6638.824	0.006173	0.005784	9.93	9.11
SAND3pos3	21439	0.164	0.42	6097.747	0.005707	0.005762	9.38	9.24
SAND3pos5	24161	0.16	0.44	6483.721	0.005614	0.005505	9.52	9.11
SAND4pos1	25477	0.296	0.22	10064	0.00663	0.0067	11.16	11.03
SAND4pos2	25621	0.218	0.4	7694.118	0.006092	0.006004	10.43	10.07
SAND4pos3	28691	0.209	0.52	8360	0.005488	0.00556	9.74	9.64
SAND42pos5	34255	0.221	0.44	8973.628	0.006105	0.006332	11.17	11.27
SAND5pos1	30738	0.296	0.22	10999.09	0.007094	0.006987	12.21	11.86
SAND5pos3	37303	0.2615	0.45	11054.32	0.005097	0.005415	9.68	10.04
SAND5pos5	44567	0.27	0.46	11889.2	0.005413	0.005254	10.71	10.19
SAND6pos1	41150	0.345	0.28	12997.67	0.006613	0.006172	12.34	11.50
SAND6pos3	46020	0.3295	0.44	13442.1	0.005667	0.005239	11.22	10.25
SAND6pos5	49093	0.326	0.46	15030.12	0.005731	0.005765	11.49	11.32

Table 5-8 to Table 5-12 show that the optimised wake values Π obtained from the present analysis are always significantly lower than the value of 0.55 that Hama (1954) used. The values are similar for the three coated surfaces (ca. 0.31-0.33 on average), and around 0.4 on average for SAND and STEEL. The SAND surface exhibited more variation in that significantly lower values for Π were measured at position 1, 1.302 from the leading edge, compared to the other positions. Overall, it was not possible to see any trend of the wake values versus Reynolds number.

Appendix D.1 contains the mean velocity profiles in wall co-ordinates of the different surfaces, along with the smooth wall log-law using the Stanford Conference values for the slope and intercept (Equation 5.2) and the equation valid in the linear sublayer (Equation 5.3):

$$U^+ = 5.62\log(y+\varepsilon)^+ + 5.0 \tag{5.2}$$

$$U^+ = (y+\varepsilon)^+ \tag{5.3}$$

Figures D1 to D15 compare the mean velocity profiles of the different surfaces at a specific location and a specific speed.

It is evident from this set of Figures that whereas the STEEL surface is invariably the smoothest and the SAND surface the roughest, the coated surfaces do not possess a fixed hierarchy. However, in 9 out of the 15 plots, the FR surface is the smoothest whereby the sequence FR-ROLL-SPC dominates (6 out of 9). In 6 plots the ROLL surface is the smoothest and only in one plot the SPC surface is the smoothest. One possible explanation for this could be the heterogeneous nature of the coated and SAND surface (as opposed to the geometrical rough surfaces such as wires and meshes investigated before in literature). If this is the case, one should see a variation of the roughness function with the location from the leading edge.

Figures D16 to D25 show the effect of the streamwise location of the profiles at 3m/s and 5m/s. As expected from theory, the STEEL profiles collapse within the experimental uncertainty, as shown in Figures D16 and D21, and so do the FR profiles at 5m/s as shown in Figure D23. The other figures do indicate that the streamwise location has an influence on the profiles, which is significant according to the experimental uncertainty analysis.

Figures D26 to D33 investigate the influence of the free-stream velocity on the profiles at positions 1 and 5, 1.302 and 1.912m respectively from the leading edge. As shown in Figures D26 and D27, the STEEL profiles collapse within the experimental uncertainty. The other figures indicate that the free-stream velocity also has a significant influence on the profiles.

5.2.4.4 Skin friction coefficients

The frictional resistance coefficients of the STEEL surface are shown in Table 5-8 and in Figure 5.22, which shows the frictional resistance coefficients plotted against the displacement thickness Reynolds number $Re_{\delta 1}$. On average, c_f calculated with the Reynolds stress method was 2% higher than c_f calculated with the Clauser method, and 1.6% higher than c_f calculated with the Hama method. Figure 5.22 also shows the frictional resistance values as calculated with the equation given in Monin and Yaglom (1971, Vol. 1,p. 322):

$$\frac{1}{\sqrt{c_f}} = \frac{1}{\kappa\sqrt{2}} \ln(\mathrm{Re}_{\delta 1}) + B_4 \qquad (5.4)$$

This equation is based on Thompson's theoretical reasoning, similar to Coles' law of the wake (1956), whereby the constants κ and B_4 were empirically determined as 0.4 and 2.6 respectively.

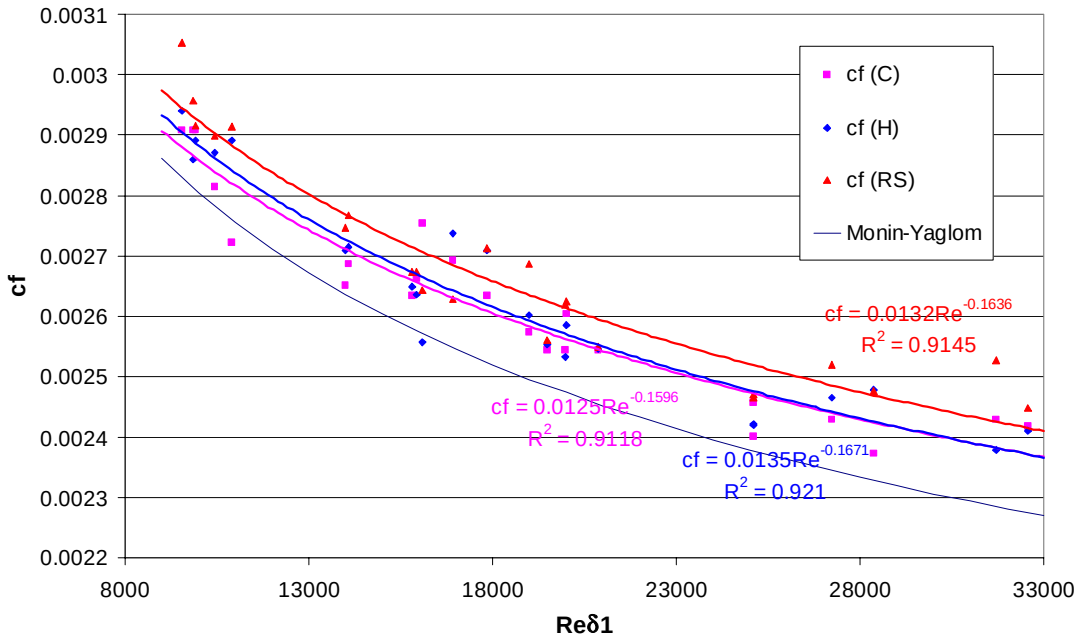

Figure 5.22. STEEL surface frictional resistance coefficients calculated with three different methods (uncertainties in c_f: ±3.61% for the Reynolds stress method, ±1.91% for the Hama method, ±1.16% for the Clauser method)

Figure 5.22 shows that c_f obtained from the Reynolds stress method is on average 5.4% higher than the c_f values predicted by equation (5.4). For the Hama and Clauser methods, the increase is 3.7% and 3.3% respectively.

Figure 5.23 shows the frictional resistance coefficients for the STEEL and painted surfaces, calculated with the Hama and Reynolds stress method. The modified Clauser method was consistently applied, but has not been included here. The results were not acceptable for the painted surfaces and showed much more variance than the other methods for the SAND surfaces. It is not clear why the modified Clauser method performed so badly, but it was observed that the virtual origin determined by the iteration method could differ very much from the virtual origin obtained with the Hama method. It is thought that the iteration method as incorporated within the spreadsheets needs modification. Most likely, the linear least-squares regression lines of U versus $\log(y+\varepsilon)$ and U/U_e versus $\ln((y+\varepsilon)U_e/\nu)$ of the selected data points put too much emphasis on the end-points. Especially the position of the first two or three selected data points has significant repercussions on the values of ε and the slope of U/U_e versus $\ln((y+\varepsilon)U_e/\nu)$ used to determine U_τ. While this adjustment is a prerequisite, the iteration method thus often converged towards unrealistic values for ε and U_τ. It is thought that the computation of non-linear least-squares regression lines would converge to results that are physically acceptable. Therefore, the following analysis concentrates on the results obtained with the Hama and Reynolds stress methods.

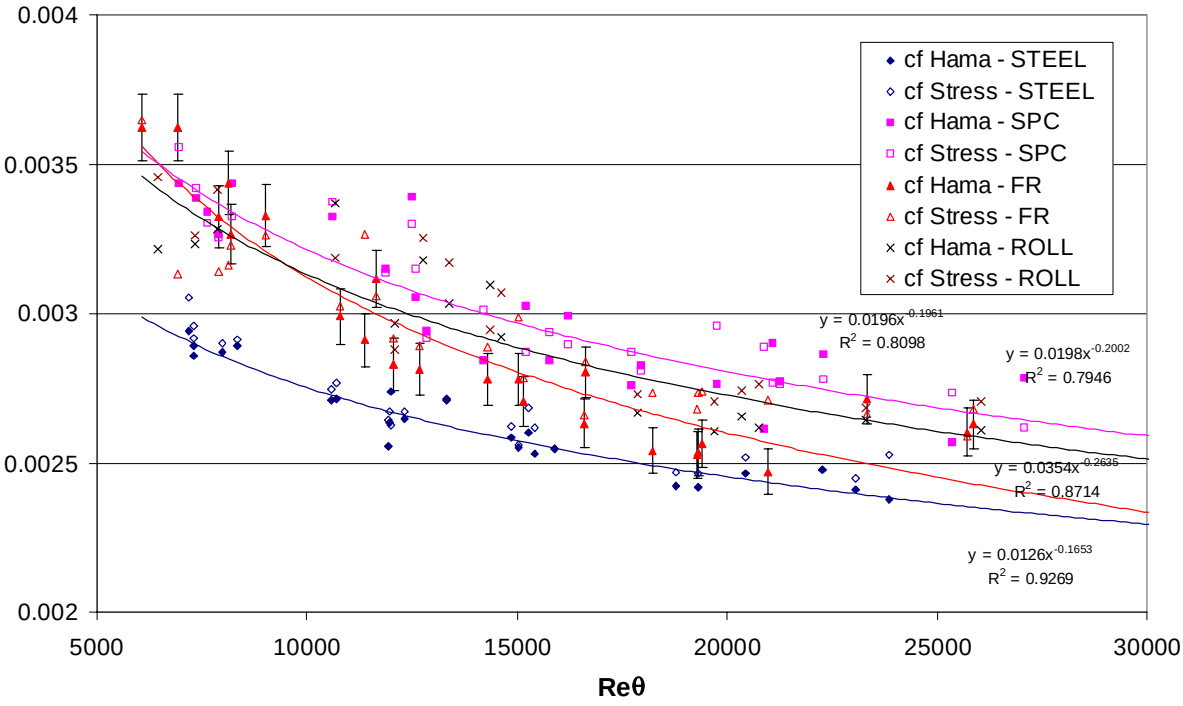

Figure 5.23. The frictional resistance coefficients of the STEEL and coated surfaces as obtained with the Hama and Reynolds stress methods (uncertainties in c_f: ±2.4% for the Reynolds stress method, ±3.1% for the Hama method – error bars of the Hama method are indicated for the FR series).

Figure 5.23 presents the skin friction coefficients of the different surfaces (bar SAND) plotted against Re_θ along with least-squares regression lines for the values obtained with the Hama method. Figure 5.23 shows that the tested surfaces had significantly increased c_f values compared to the smooth STEEL surface. Statistically, the uncertainties in c_f are comparable for the smooth and coated surfaces, but Figure 5.23 indicates slightly more scatter for the coated surfaces than the uncertainty analysis (indicated by the error bars for the FR (H) series) would predict. This may be due to the heterogeneous nature of the surfaces and its influence on local flow conditions.

The ANOVA tests carried out on the test parameters in Section 6.1 indicated that the measurements at a specific position and free-stream velocity were conducted at significantly different Reynolds numbers mainly due to significant temperature fluctuations of the water in the tunnel. ANOVA analysis essentially presumes that the results belong to the same statistical population and tests whether this assumption is valid. Since we know that the results of the different surfaces do not belong to the same population with respect to the Reynolds number, one cannot compare the ensembles of results of the different surfaces with ANOVA analysis to determine whether the differences in c_f for the different (coated) surfaces are significant because c_f is highly dependent of the Reynolds number.

The least-squares regression lines in Figure 5.23 are merely indicative for the selected results, and due to the scatter of the results should not be used for any extrapolation purposes. Whereas the power-trendlines of the STEEL, ROLL and SPC surface run fairly parallel, the descent of the FR surface trendline is steeper, despite the higher c_f values at the highest Reynolds numbers. However, the trendlines indicate that overall, the c_f values of the FR surface are lower than the values of the ROLL surface, which in turn are overall lower than the c_f values of the SPC surface. If one looks for a least-squares regression line for the FR surface which runs parallel to the other coated surfaces (i.e. of the form: constant $\cdot$ $Re_\theta^{-0.2}$, one can find the average differences in c_f between the surfaces. If one carries out the regression analysis with this constraint, one obtains a value of 0.0194 for the constant in the FR trendline, 0.0198 for the constant in the ROLL trendline, 0.0203 for the constant in the SPC trendline and 0.175 for the constant in the STEEL trendline. In other words, the c_f values for the SPC surface resulting from this rather crude analysis would be 4.6% higher than for the FR surface, 2.5% higher than for the ROLL surface, and 16.0% higher than for the STEEL surface. These results are merely indicative in view of the relatively low R^2 correlation values of the trendlines, which are 0.814, 0.828, 0.774 and 0.900 respectively. The R^2 correlation

values are defined as 1-SSE/SST, whereby SSE = $\sum (Y_i - \hat{Y}_i)^2$ and SST = $\sum Y_i^2 - \left(\sum Y_i\right)^2 / n$; and whereby n is the number of data points Y_i at X_i and $\hat{Y}_i$ is the least-squares estimate at X_i.

5.2.4.5 Roughness functions

Additional power trendlines have been included in Figure 5.22, with their respective equations and R^2 values, which were in excess of 0.9 for each different method. These trendlines could be used for interpolation of the STEEL c_f values in order to calculate ΔU^+ at the respective $Re_{\delta 1}$ of the measurements of each different surface, in accordance with Granville's recommendations (Granville, 1987). However, rather than using a power trendline for c_f versus $Re_{\delta 1}$, Monin and Yaglom (1971) used a logarthmic trendline for $1/\sqrt{c_f}$ versus $Re_{\delta 1}$. Figure 5.24 shows the trendlines obtained for the STEEL c_f values when this approach is followed and indicates that the R^2 correlation values are now slightly higher.

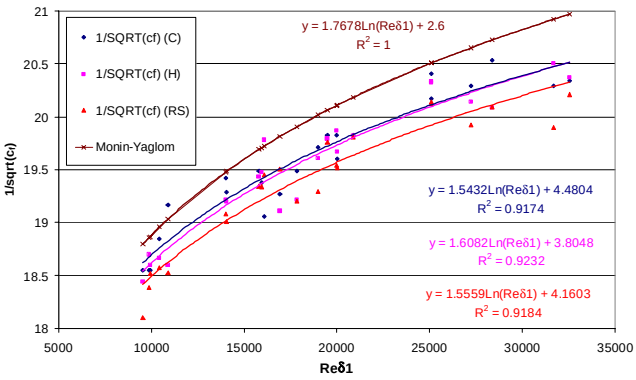

Figure 5.24. Least squares regression lines for the STEEL skin friction coefficients.

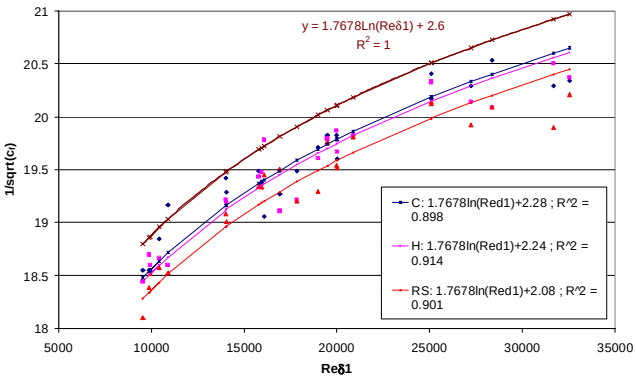

Figure 5.25. Least squares regression lines for the STEEL skin friction coefficients with the constraint of using the von Karman constant.

However, bearing in mind the iterative method which was used to derive U_τ, it is more satisfactory to constrain the von Karman constant κ to 0.41 since this value was also used in the analysis of the measurements (cf. Section 3), thus varying only the constant B_4 to obtain the best correlation. Figure 5.25 shows the resulting trendlines with this additional constraint, along with the respective equations and R^2 values.

The roughness function for the different surfaces are therefore calculated as:

$$\Delta U^+ = \left(\sqrt{2/c_{f,STEEL}}\right) - \left(\sqrt{2/c_f}\right) \tag{5.5}$$

The roughness function has to be evaluated at the same $Re_{\delta 1}$ values (Granville, 1987) so that using the trendlines from Figure 5.25, Equation 5.5 becomes:

$$\Delta U^+ = \left(\sqrt{2}(1.7247\ln(Re_{\delta 1}) + B_4)\right) - \left(\sqrt{2/c_f}\right) \tag{5.6}$$

The obtained values, listed in Table 5-9 to Table 5-12, on average do not vary much with $Re_{\delta 1}$ (except for SAND where there is a rising trend of ΔU^+ with increasing $Re_{\delta 1}$) particularly for the Reynolds stress method, but overall the values fluctuate considerably. Table 5-13 presents the average values for the roughness functions, with the standard deviations in between brackets.

Table 5-13. Average roughness functions for the different surfaces and analysis methods.

	Hama	Reynolds-Stress
SPC	1.80 (±0.53)	1.65 (±0.38)
FR	1.25 (±0.71)	1.25 (±0.44)
ROLL	1.54 (±0.56)	1.58 (±0.44)
SAND	10.39 (±1.04)	9.96 (±1.13)

Since the values do not vary much with $Re_{\delta 1}$, a relatively small difference in the Re_x (and $Re_{\delta 1}$) range as is the case for the coated surfaces due to temperature fluctuations of the tunnel water, is not expected to jeopardise ANOVA analysis. Two-factor ANOVA analysis was applied to investigate whether the differences between the coated surfaces were significant. The analysis confirmed that Re_x did not have a significant effect on ΔU^+ and indicated that the test surface had a significant effect, both for the Reynolds stress and for the Hama method. Multiple pairwise comparisons using Tukey's test (Mason et al., 1989) with a significance level set at $\alpha = 0.05$ (95% confidence), indicated that there was a significant difference between the FR surface and the SPC surface for the results obtained with the Hama method. Multiple pairwise comparisons of the results obtained with the Reynolds stress method indicated that in addition to a significant difference between the FR surface and the SPC surface, there was also a significant difference between the FR surface and the ROLL surface, but not between the ROLL surface and the SPC surface.

If one takes the approximation of h_s (cf. Section 5.2.1.5), h_s^+ is approximately 60 at 2m/s and larger than 85 for all the other SAND measurements, thus indicating that the latter

have been taken in the fully rough region. Nikuradse's roughness function χ is then constant (cf. Section 4.5.3) and can be calculated with Equation 4.34. It was found that χ is indeed fairly constant over the tested Reynolds number range and approximately equal to 7.08.

5.2.4.6 Turbulence intensities and Reynolds stresses

Figures of the turbulence intensities (strictly speaking, the variances of the turbulence intensities (Raupach et al., 1991)), $\sqrt{\overline{u'^2}}/U_\tau$ and $\sqrt{\overline{v'^2}}/U_\tau$, and the turbulent shear stresses, $\overline{-u'v'}/U_\tau^2$, are presented in Appendix D, Sections D.2 and D.3 respectively. These Figures use the friction velocity and the boundary layer thickness as the normalising scales.

Figures D34 to D48 compare the turbulence intensities of all surfaces at a specific location and free-stream velocity. Except for Figures D34 and D35, where the streamwise intensities of the STEEL surface are higher than for the other surfaces, the figures seem to indicate that the turbulence intensities of all surfaces collapse within the experimental uncertainty. The near-wall region ($y^+ < 30$) has to be considered with great precaution in view of the large uncertainties derived in Appendix C. The peak values are higher than reported elsewhere (e.g. Raupach et al., 1991) and it is believed that these were influenced by velocity bias of the near-wall measurements (cf. Appendix B.2). At first sight there seems to be a significant decrease in the outer layer of the turbulence intensities over some of the SAND surface measurements. However, the data collapse again when the plots are expressed in either inner or outer variables.

Figure 5.26 and Figure 5.27 show the comparative turbulence intensity profiles at 4pos3 in inner and outer variables respectively. When expressed in inner variables, the data collapse within experimental uncertainty. When expressed in outer variables, which is the recommended scaling according to George and Castillo (1997), the data collapse from $y+\varepsilon > 0.7\delta$, but the effect of increasing roughness clearly shows up for the SAND surface. Nevertheless, even when expressed in outer variables, the effect of increasing roughness on the turbulence intensities over the coated surfaces remains unclear within the experimental uncertainty. Kutlar and Lewkowicz (1990) noted in a wind tunnel an increase in the wall-normal and spanwise turbulence intensities, but not in the streamwise intensities, when a coarse surface was compared against a coated surface (for which the roughness function was lower). Krogstad et al. (1992) also observed a significant increase in the wall-normal

intensities over mesh roughness. They concluded that the major effect of this type of roughness was to tilt the large-scale flow structures towards the wall-normal direction, leading to a higher degree of isotropy. Musker (1990) observed increases both in the streamwise and in the wall-normal intensities over coated surfaces when compared against a smooth surface. Schultz and Swain (1999) and Gangadharan et al. (2001) also found increases in both components over fouled surfaces, although there was a large degree of variability in the results due to the nature of the biofilm. In a comparison of two different types of roughness (streamwise rods and a mesh screen) for which ΔU^+ was the same, Antonia and Krogstad (2001) measured significant differences between the wall-normal intensities, and a smaller difference in the streamwise intensities. The differences in the wall-normal intensities persisted throughout the boundary layer in contradiction to the wall similarity hypothesis. This was also noted by Tachie et al. (2000) in channel flow experiments with three different types of roughness (perforated plate, sand grain and wire mesh). The effect of roughness on the outer layer is also indicated by an increase in the wake parameter (Krogstad et al., 1992; Tachie et al., 2000). Such a trend for the turbulence intensities and the wake parameter (which decreased slightly for the coated surfaces, but by an amount which is much lower than the 2.5 to 5-fold increase noted by Tachie et al.) was not observed here, thus indicating that the wall similarity hypothesis is valid for the present experiments.

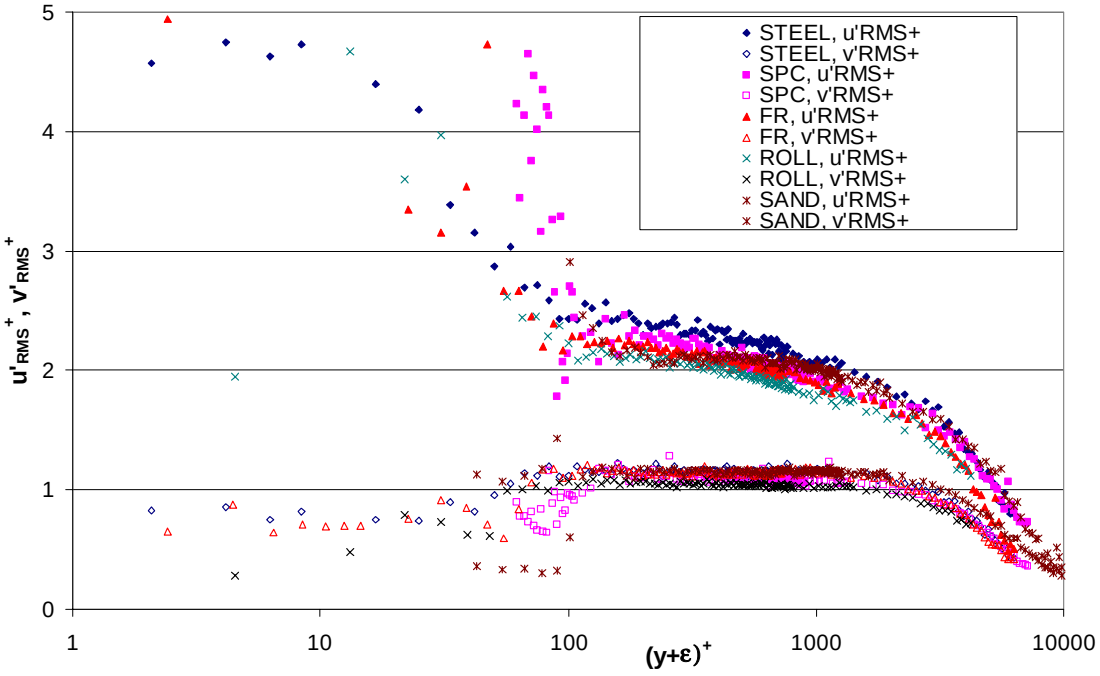

Figure 5.26. Turbulence intensity profiles at 4pos3 expressed in inner variables (uncertainties for the rough surfaces and for $(y+\varepsilon)^+ > 30$: u'_{RMS}: ±4.66%, v'_{RMS}: ±4.00%).

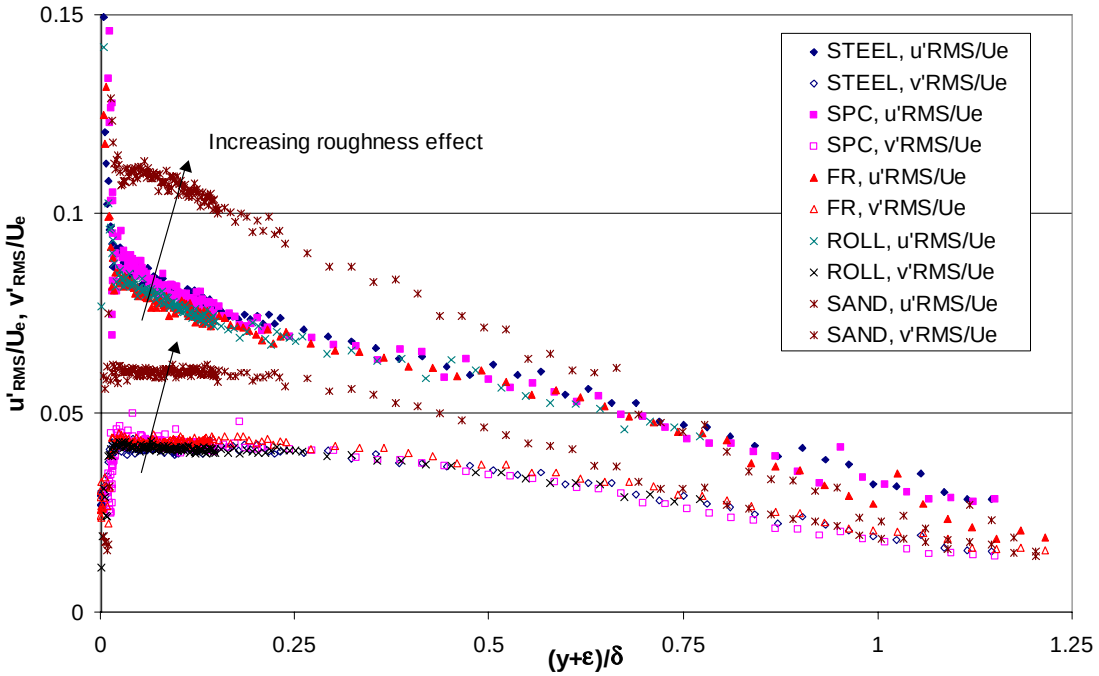

Figure 5.27. Turbulence intensity profiles at 4pos3 expressed in outer variables (uncertainties for the rough surfaces and for $(y+\varepsilon)/\delta > 0.02$: u'_{RMS}/U_e: ±4.54%, v'_{RMS}/U_e: ±3.85%).

Figure 5.27 also shows that over the region $0.02 < (y+\varepsilon)/\delta < 0.11$, the SAND surface displays a flat 'hump' in the streamwise turbulence intensity. According to Ligrani anf Moffat (1986), such 'humps' are characteristic for fully rough surfaces and they are regions where the production of longitudinal turbulence energy is important. This is in accordance with the observations made on the roughness function of the SAND surface.

Figures D49 to D56 in Appendix D.2 show the turbulence intensities for each different surface at positions 1 and 5 with changing free-stream velocity. It is difficult to tell from the experimental uncertainty, but there seems to be a weak Reynolds number dependence, which is mentioned in Raupach et al. (1991). At $(y+\varepsilon)/\delta = 0.1$, these authors give values for $\sqrt{\overline{u'^2}}/U_\tau$ of 2.1±0.2 and for $\sqrt{\overline{v'^2}}/U_\tau$ of 1.1±0.1. In the present analysis, the former values generally lie between 1.9 and 2.35 (i.e. 2.35 for the STEEL surface in Figure B1, in the majority of cases the values lie between 1.9 and 2.2), and the wall-normal turbulence intensities lie between 1 and 1.2, which is in good agreement with Raupach et al. (1991).

When expressed in inner variables, the effect of increasing Reynolds number is clearly observable in the outer layer. When expressed in outer variables, the effect of increasing Reynolds number can be distinguished in the log law region for the streamwise intensities, but

not for the wall-normal intensities, as is evident from Figure 5.28 and Figure 5.29 which display the results for the STEEL surface at position 1.

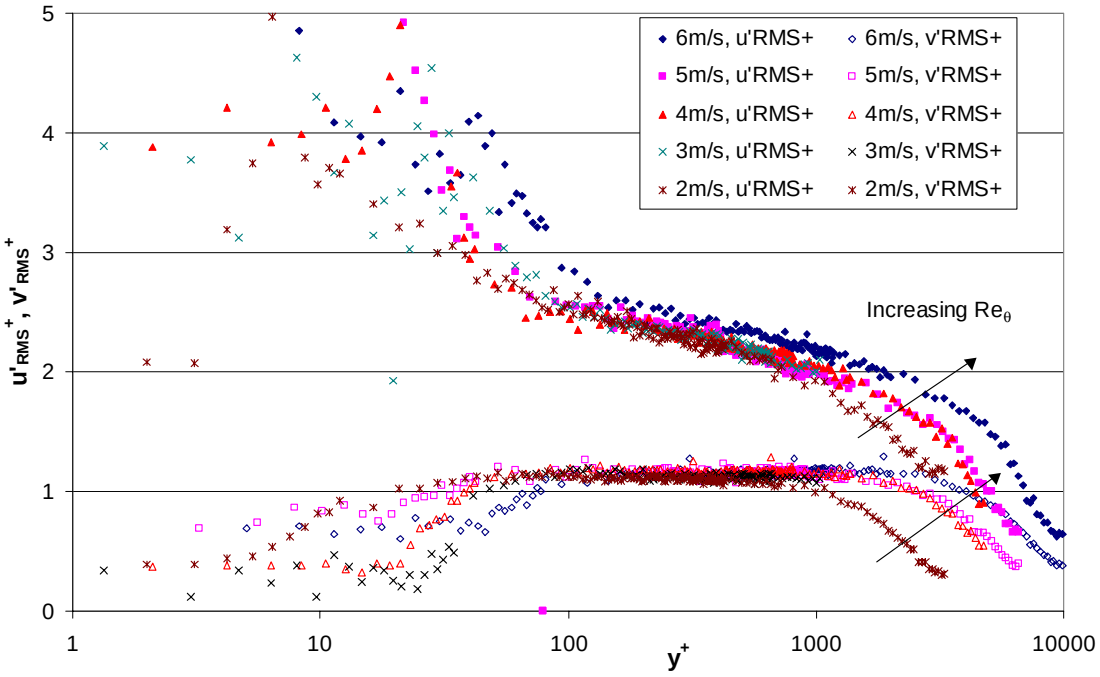

Figure 5.28. Turbulence intensity profiles of the STEEL surface at position 1 expressed in inner variables (uncertainties for $(y+\varepsilon)^+ > 30$: u'_{RMS}: ±4.54%, v'_{RMS}: ±3.85%).

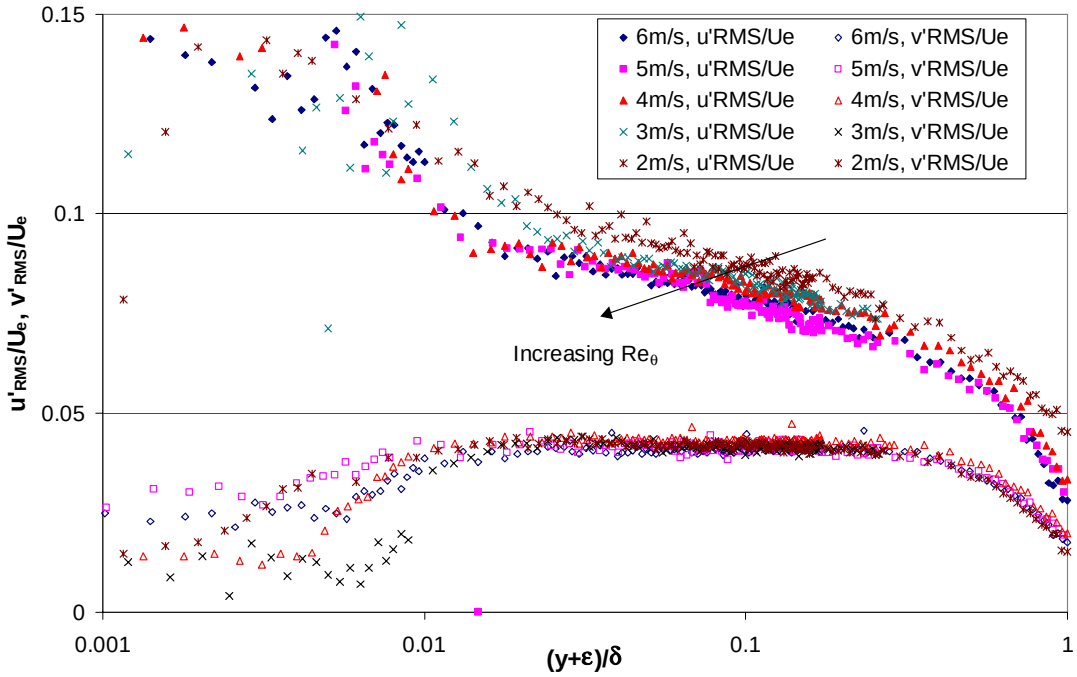

Figure 5.29. Turbulence intensity profiles of the STEEL surface at position 1 expressed in outer variables (uncertainties for $(y+\varepsilon)/\delta > 0.02$: u'_{RMS}: ±4.53%, v'_{RMS}: ±3.84%).

Figures D57 to D71 compare the turbulent shear stresses of the different surfaces at a specific location and free-stream velocity. The near-wall measurements are a direct indication of the agreement between the Hama method and the Reynolds stress method. The Reynolds shear stresses (non-dimensionalised by U_τ^2) seem to collapse for all the surfaces, except for SAND at position 1, where the shear stresses decay more rapidly in the outer layer. This may be the influence of the change from smooth to rough, which according to Antonia and Luxton (1971) may extend over a length ~ 10δ. At streamwise positions further away from the leading edge, all profiles collapse within the experimental uncertainty. Ligrani and Moffat (1986) also noticed no influence of roughness on the Reynolds shear stresses in zero-pressure gradient boundary layer over a flat plate. Similarly, Grass (1971) observed no differences in open channel flow experiments. Krogstad et al. (1992) and Tachie (2000) found a moderate increase in the Reynolds shear stresses over mesh roughness, which was further evidence that the wall similarity hypothesis did not hold for this type of surface.

Overall, the Appendices D.2 and D.3 indicate that self-preservation of the boundary layer for the different surfaces has been reached, which supports the wall similarity hypothesis and justifies the use of similarity techniques to determine the friction velocity.

5.2.4.7 Spectra

Power Spectral Density Functions were computed from the raw data samples using a Fast Fourier Transform (FFT). A Hanning filter with a filter width of 0.1 was applied to smooth the results. 512 spectral samples were taken with a maximum frequency of 1024Hz. This value was chosen so that it would not be significantly higher than the mean data-rate and hence avoid unreliable results. In general, energy contained at frequencies higher than the maximum frequency may distort results due to aliasing and as the maximum frequency is approached, flattening of the power spectrum will be evident. For these experiments, a more serious problem is the attenuation of the estimated power spectrum with f^2 above the cut-off frequency. The cut-off frequency is determined by the sample-and-hold technique used by the software prior to the FFT analysis, which effectively acts as a low-pass bandwidth filter, and is equal to $n_{mean}/2\pi$, whereby n_{mean} is the mean data rate. For these experiments, the mean data rate at best was on the order of 180-300Hz, so that attenuation of the spectrum is expected above frequencies of 30-50Hz, which explains why the spectra at higher frequencies do not follow the expected pattern. In other words, the mean data rate was not as high as one would desire, especially close to the wall. Initially, the data rate was even much lower. Triggering the bursts on the weaker v-component signal improved matters significantly, but within the present experimental set-up, no better data-rate was achieved than with the present settings.

Frequency spectra were obtained for both velocity components. The spectra were normalised by u'^2_{RMS} and v'^2_{RMS} respectively and transformed into wavenumber spectra by applying (Reynolds, 1974, pp. 80-103) $k = \omega/U$ and $E(k) = U \cdot E(\omega) = U/(2\pi) \cdot E(f)$. Unfortunately, the software cannot compute spectra of the turbulent shear stresses.

Appendix D.4 presents the wavenumber spectra at positions 1, 3 and 5 for speeds of 2, 4 and 6m/s and for $y/\delta = 0.05$ and 0.8. Along with the spectra for the 5 different surfaces, lines with slopes k^{-1} and $k^{-5/3}$ were included (cf. Section 4.6.2).

Overall, it is difficult to draw any conclusions regarding differences between the surfaces. It seems that the FR spectra lie closer to the STEEL spectra than the SPC surface, and the ROLL spectra lie closer to the SAND spectra. This would indicate that the wavelengths of the vortices which make up the turbulent boundary (in a simplified conceptual context) are generally smaller over the FR surface than over the SPC or ROLL surface. However, it is felt that the bias due to the low average data rate is a major problem and prevents any definite observations.

5.2.4.8 Integral length scales

Turbulent flows are characterised by the superposition of eddies of different length scales interacting in non-linear processes. The Reynolds decomposition into mean and fluctuating velocities is insufficient and complementary information is required to study the spatial structures in the boundary layer. This can be done by the evaluation of some characteristic length scales (Belmabrouk, 2000). For two measurements in a turbulent flow, measured by a time difference τ, the longitudinal correlation coefficient, $\rho_u(\tau)$ is defined by:

$$\rho_u(\tau) = \frac{\overline{u'(t)u'(t+\tau)}}{\overline{u'^2}} \tag{5.7}$$

where u'(t) represents the instantaneous longitudinal velocity measured at a time t. Taylor's hypothesis states that the sequence of changes in u' at a fixed point is due to the passage of a 'rigid' turbulent eddy past that point. This simplified model becomes less accurate as u' increases in relation to U. Taylor's hypothesis can be used to deduce space correlations from time correlations (Reynolds, 1974). A longitudinal integral *length* scale can then be defined in terms of the correlation coefficient:

$$L_u = U\int_0^\infty \rho(\tau)d\tau \tag{5.8}$$

The longitudinal integral length scale is a measure of the size of the largest energy-containing eddies (Hinze, 1977) and is expected to scale with the boundary-layer thickness away from the wall, indicating that the largest eddies at the edge of the boundary layer are of the order of δ itself. The wall-normal integral length scale is similarly defined and calculated. The eddies in the turbulent boundary layer are very elongated, which is indicated by the fact that the longitudinal integral length scale is several times larger than the wall-normal integral length-scale (Reynolds, 1974).

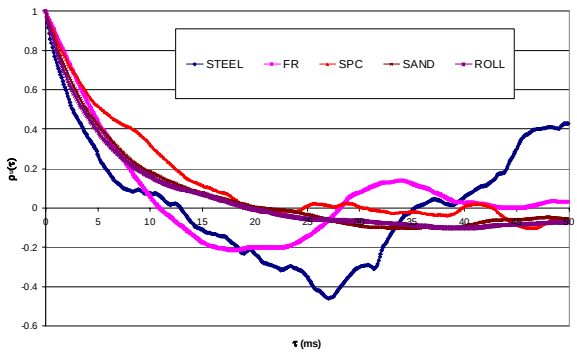

Figure 5.30. Longitudinal autocorrelation functions at y/δ = 0.08 (3POS3).

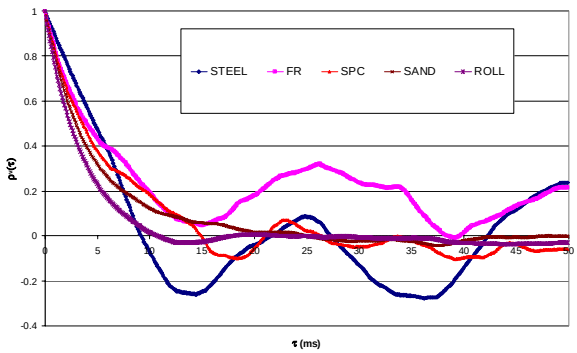

Figure 5.31. Wall-normal autocorrelation functions at y/δ = 0.08 (3POS3).

The integral length scales have been calculated from the stored autocorrelation functions. The autocorrelation functions were computed from the raw data samples using a Fast Fourier Transform (FFT). 512 data were calculated for a maximum time delay of τ = 50ms. A set of longitudinal and wall-normal autocorrelation functions for 3POS3 at y/δ = 0.08 are shown in Figure 5.30 and Figure 5.31 respectively. Figure 5.32 to Figure 5.35 show the longitudinal and wall-normal integral length scales for two different free-stream speeds (3 and 5m/s) plotted against distance from the wall.

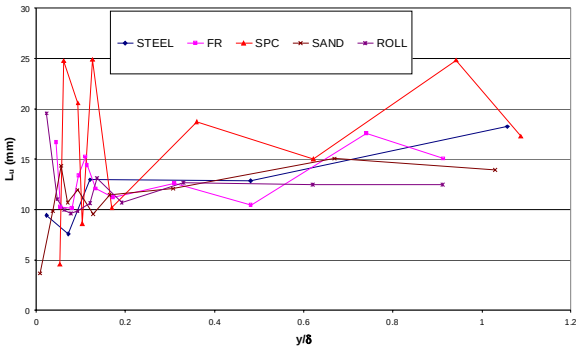

Figure 5.32. Longitudinal integral length scales at 3POS3.

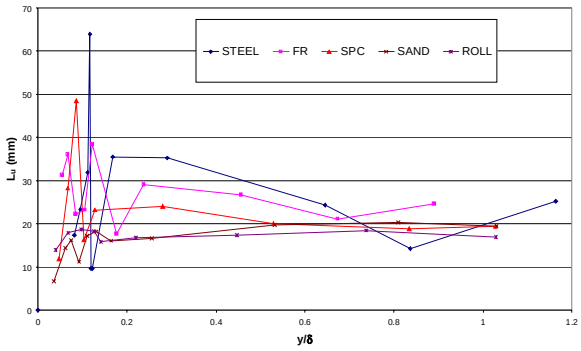

Figure 5.33. Longitudinal integral length scale at 5POS3.

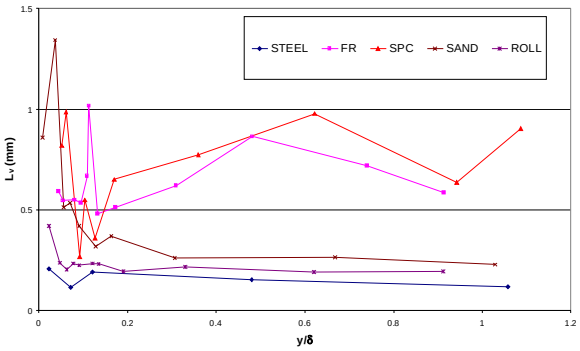

Figure 5.34. Wall-normal integral length scale at 3POS3.

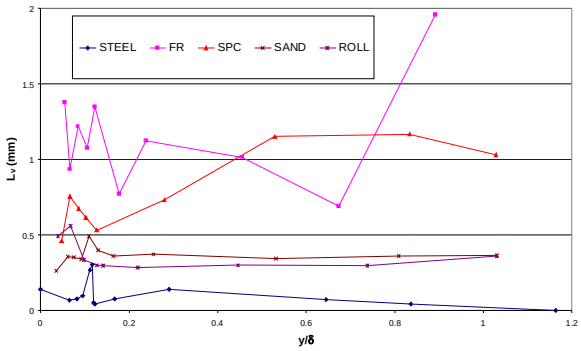

Figure 5.35. Wall-normal integral length scale at 5POS3.

Figure 5.32 to Figure 5.35 show that the integral length scales increase with the free-stream velocity, as is expected. Musker (1977, 1990) found from pipe flow experiments that the longitudinal integral length scale near the wall (i.e. $(y+\varepsilon)/R$ = 0.02 and 0.08) increased over rough surfaces. At the pipe centre-line however, surface roughness had little effect on the integral length scale, in accordance with the wall similarity hypothesis. Such a trend is not

readily observed here. In the outer layer, however, the longitudinal integral length scale is approximately constant and seems to converge for all surfaces. Bogard and Thole (1998) state that L_u is equal to approximately 0.4δ across much of the boundary layer, which is in fairly good agreement with the present data.

The integral length scale can also be derived from the wavenumber spectra (since the autocorrelation functions and PSDF are interrelated) and can be defined as:

$$L_u = \frac{E_u(k)_{k\to 0}}{4\overline{u'^2}} \tag{5.9}$$

and likewise for L_v. This allows a simple quantification of the integral length scales from the wavenumber spectra plotted in Appendix D.4 and discussed in the previous section. In the following analysis the values of the PSDF at the lowest measured wavenumber have been used to calculate the integral length scales. This is likely to slightly underpredict the length scales since the PSDF have not yet flattened out entirely over the low wavenumber range. Figure 5.36 to Figure 5.39 compare the integral length scales for the different surfaces.

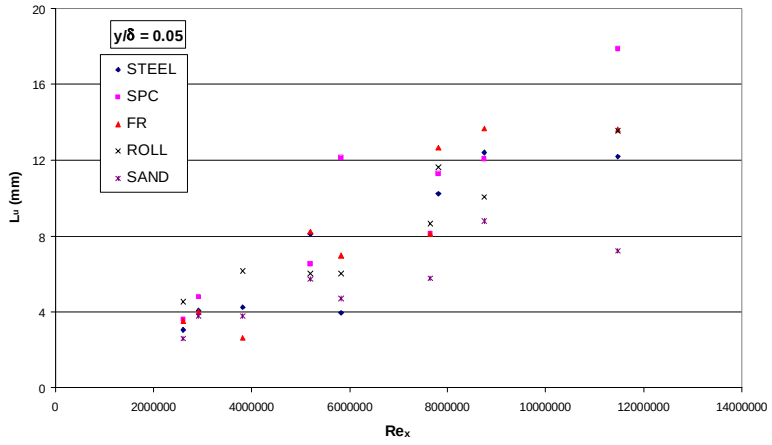

Figure 5.36. Longitudinal integral length scale at y/δ = 0.05.

Figure 5.36 to Figure 5.39 clearly show the effect of increasing Reynolds numbers on the integral length scales. The longitudinal length scales are comparable for the different surfaces and the values at y/δ = 0.8 compare relatively well with the predictions determined from the autocorrelation functions, shown in Figure 5.32 and Figure 5.33. The wall-normal integral length scales also confirm the trends observed in Figure 5.45 and Figure 5.46 and show that L_v (rather surprisingly) is significantly higher for FR and SPC , whereas ROLL and SAND lie closer to the STEEL values, for which the rate of increase with Re_x is much lower.

Given the SAND values, the measured integral length scales therefore seem not to increase with roughness in the present analysis.

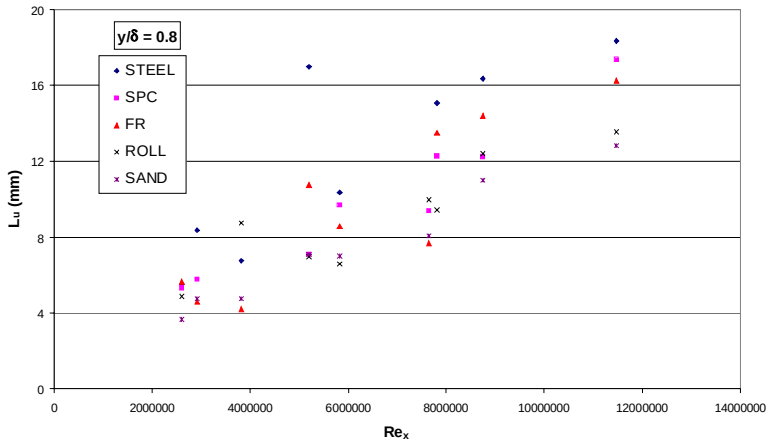

Figure 5.37. Longitudinal integral length scale at y/δ = 0.8.

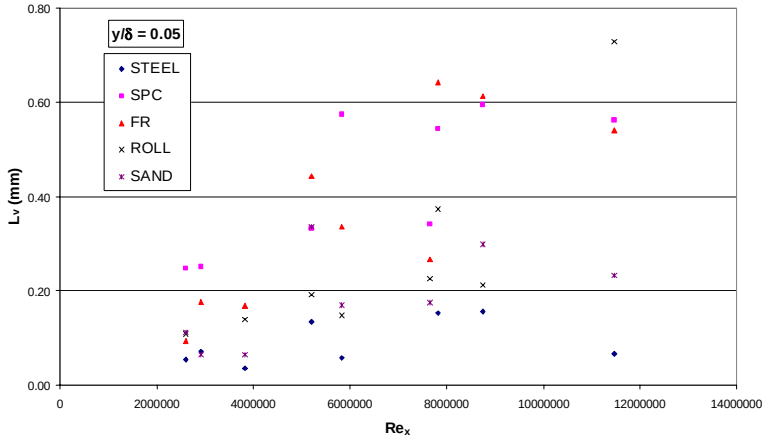

Figure 5.38. Wall-normal integral length scale at at y/δ = 0.05.

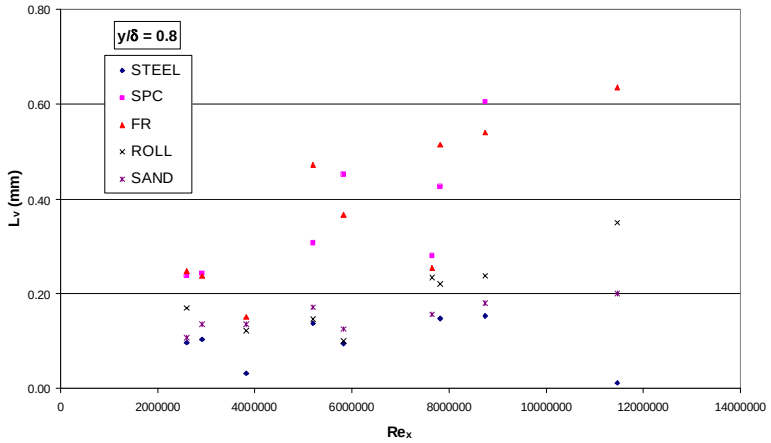

Figure 5.39. Wall-normal integral length scale at at y/δ = 0.8.

5.3 Boundary-layer experiments carried out in the CEHIPAR Cavitation Tunnel

The experiments were carried out in June 2001 and were made possible through funding from the European Community's CEHMAR programme, which promotes access to large-scale facilities for researchers. Full details of the experiments can be found in Candries and Atlar (2001).

5.3.1 Facilities and test conditions

5.3.1.1 CEHIPAR Cavitation Tunnel

The CEHIPAR Cavitation Tunnel has a parallel test section which is 0.9m in width and height and 4.7m long. A diagram of the tunnel is shown in Figure 5.40 while an overall view is shown in Figure 5.41. Table 5-14 lists the main particulars of the tunnel.

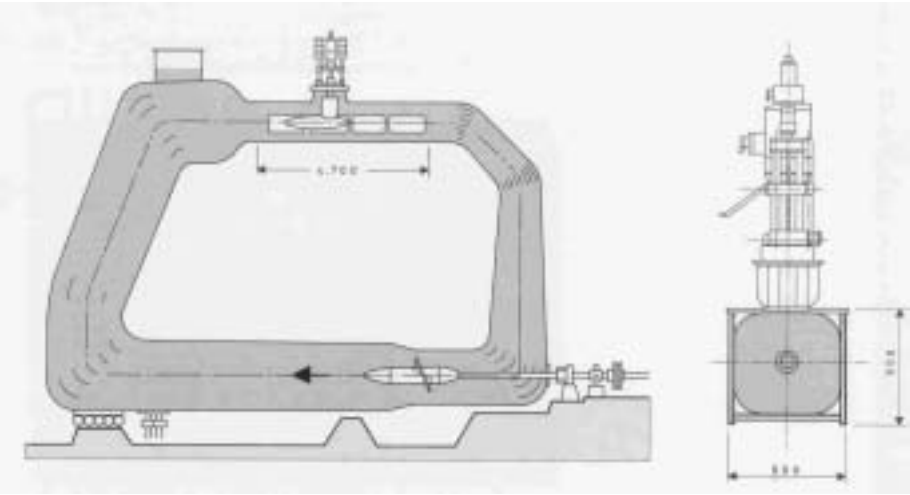

Figure 5.40. Schematic diagram of the CEHIPAR Cavitation Tunnel

Table 5-14. Main details of the CEHIPAR Cavitation Tunnel

Establishment year	1950 (Werkspoor NV, Amsterdam)
Description of facility	Vertical plane, closed re-circulating
Test section size (LxBxH)	4.10x0.9x0.9m
Test section area	0.745m^2
Contraction ratio	1:6
Type of drive system	C. C. Motor driving Propeller Pump Ward-Leonard Control system
Main pump power	220kW
Cavitation number range	0.32-130
Max. and min. abs. pressures	1.6kg/cm^2 –0.2 kg/cm^2
Maximum velocity	11m/s (7.9m/s for the present set-up)

Figure 5.41. View of the CEHIPAR Cavitation Tunnel

5.3.1.2 Test plate details

The boundary-layer test plate was closely modelled on the plate used in Section 5.2, but was wider in order to cover the entire section of the CEHIPAR water tunnel. The plate was 0.895m in width, 2m long consisting of two sections of 0.99m in length attached to each other and 12mm thick. There is a 20mm overlap to join both test plates together.

The plate was constructed of mild steel and mounted horizontally in the tunnel, as shown in Figure 5.43 and Figure 5.44. The leading and trailing edges, each 50mm long, were tapered and the forward 300mm of the plate was covered with #40 grit to hasten and artificially thicken boundary-layer development. The sand grit at the leading can be interpreted as a virtual extension of the plate (Ligrani and Moffat, 1983). In the constant stress region, the shape factor H is expected to be constant for each surface and the boundary-layer parameters display a linear behaviour with x. Following Bandyopadhyay (1987), the virtual x-origin can then simply be determined as shown in Figure 5.42.

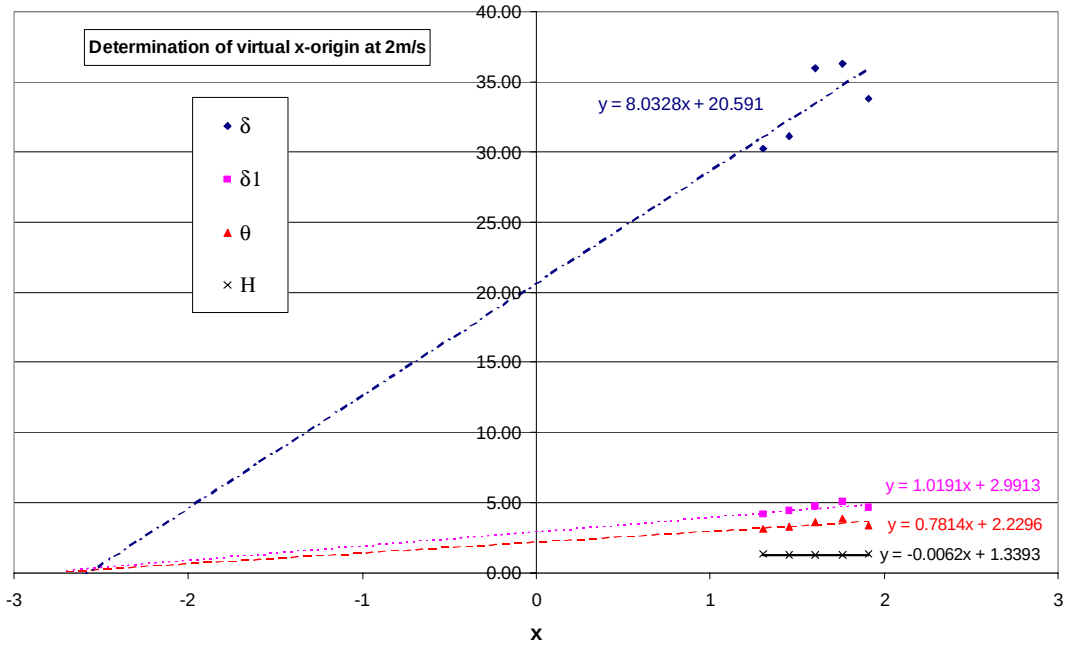

Figure 5.42. Determination of the virtual x-origin for the STEEL surface at 2m/s.

Averages have been taken for each surface over the entire speed range by extrapolating the three boundary-layer thicknesses. The averages for each surface are shown in Table 5-15.

Table 5-15. Average value of the virtual origin .

x- origin	STEEL	SPC	FR	ROLL	SAND	CSPC	CFR
δ	-2.1	-3.02	-1.853	-1.09	-1.925	-0.25	-0.23
δ1	-1.47	-3.86	-2.92	-2.03	-0.5	-2.73	-0.404
θ	-2	-3.24	-1.94	-1.685	-0.37	-2.46	-0.17
H	0.0658x+1.2193	1.30-0.0298x	1.4563-0.0864x	1.3685x-0.0364	1.5879x-0.0549	1.3669x-0.0199	1.4015x-0.0856

Figure 5.43. The front section of the plate.

Figure 5.44. The aft section of the plate.

The plate was mounted 0.45m from the bottom of the water tunnel and was held in place with 6 supports 0.21m in length, , which supported the plate in pairs at the front, middle and end. The plate was supported over 120mm at the beginning and end by two pairs of bolts each, and over 210mm in the middle by four bolts. The supports have a certain degree of freedom until the bolts are fixed firmly, which allows adjustments to the free-stream pressure gradient.

Four thin plates were fabricated from 3mm thick mild steel. One thin plate was used to cover the front section of the model and was partially covered with grit as mentioned. The other 3 thin plates were used as test specimens to investigate the influence of the surface condition and were replaced for each different surface condition. The test specimens were held on the 12mm plate by 5 magnets each. At the edges countersunk screws were employed to fix the test specimen, as shown in Figure 5.45.

Figure 5.45. The CFR test plate is being mounted on the supporting plate by countersunk screws.

5.3.1.3 LDV system

The velocity measurements were taken using a four-beam two-component fibre-optic Laser Doppler Velocimetry (LDV) system. As explained in Appendix B, the system consists of a laser light source, a beam separator, fibre-optic couplers, a multi-colour receiver, a signal processor, a personal computer, a fibre-optic probe and a three-axis traverse. The laser light source was an INNOVA 70 Series Ion Laser System with a maximum power of 5W emitting beams with a diameter of 1.5mm via Dantec 60x24 Manipulators. The signals were processed with a Dantec 58 N 10 PDA Signal Processor and analysed with Dantec PDA Flow and Particle Software, version 1.40.000124, on a Digital Celebris GL5166 PC.

Figure 5.46 and Figure 5.47 show an overview of the LDV set-up.

Figure 5.46. Overview of the LDV set-up

Figure 5.47. Overview of the LDV set-up

The traverse allowed the position of the probe to be maintained to ±50μm in all directions. The probe, approaching from the front of the tunnel, was tilted 2.9º clockwise, which was taken into account for the measurements. Theoretically, the minimum angle which would let all beams pass through was 1.814º, which is the half-angle between the beams.

Silver coated (soda lime borosilicate) glass spheres with a mean particle size of 16.3μm (ranging from 8.4-24.8μm were used as seeding of the flow. About 20g of seeding was put in gradually over the first week, and in the second week, about 3g of seeding was put in every two days.

Velocity measurements were conducted in backscatter mode over 20s or until 4096 validated samples (whichever came first) were collected per location. In practice, the data rate was not high enough to collect 4096 validated samples. The measurements were transit time averaged. The probe volume diameter was 276μm for the (blue) wall-normal channel and 291μm for the (green) streamwise channel, while the probe volume length was 8.725 and 9.199mm respectively. The probe volume contained 35 fringes spaced 7.709 and 8.128μm respectively. The frequency bandwidth for the streamwise channel was set at 4MHz throughout the experiments, whereas for the wall-normal channel it was set at 0.4MHz. The

validation and validated data rate increased from very low values near the wall to values of approximately 65-80% and 35Hz respectively further away from the wall. Conducting the experiments in single-component mode, or without any tilt of the probe did not have a significant effect on the data rate. There are several possibilities as to why the data rate was so low. The most likely explanation is poor coincidence of both channels and non-optimal alignment of the optics.

The system was set up with a 600mm focal length lens and a signal to noise ratio for the collected data of –3dB. The viscous length ν/U_τ varied between 2.7 and 7.3μm; the diameter of the probe volume therefore ranged between 40 and 108 viscous lengths.

5.3.1.4 Test specimens.

Three different surfaces were tested: a steel surface which served as smooth reference (henceforth simply named CSTEEL), a surface coated with a tin-free self-polishing co-polymer (CSPC), and one surface coated with a Foul Release (CFR). The paint systems were applied in situ at the spraying booth of CEHIPAR. The spraying equipment is shown in Figure 5.48. Small sample plates were painted alongside the large test plates in order to analyse them for their roughness characteristics with an optical measurement system (cf. Chapter 6). The application was carried out by the sprayer of CEHIPAR, Orencio Lozano, and the application was supervised by a representative of International Coatings Ltd, Sabino Quirros.

Figure 5.48. Spraying equipment

Figure 5.49. CSTEEL Test Specimen

Figure 5.49 shows the CSTEEL test specimen. Upon immersion in the tunnel, the CSTEEL plates (front and aft) quickly started to corrode as shown in Figure 5.44, so that by the time the experiments could start, the roughness had already significantly increased. The surface could therefore not serve as the smooth reference surface, instead of which the STEEL surface described in Section 5.2.1.4 was used in order to calculate the roughness function.

The SPC coating scheme consisted of one coat of primer with a dry film thickness of 100µm and two coats of antifouling with a thickness of 125µm for each coat. The primer, (called Intertuf JVA203 Bronze), was applied onto the steel surface, which had been cleaned with solvent as shown in Figure 5.50. The first coat of the Tin-free SPC (called Intersmooth 360 Ecoloflex BEA369 Red) was applied the following day. The second coat of the antifouling was applied one day later. The final look of the CSPC plate is shown in Figure 5.51.

Figure 5.50. Preparation of the sample plates

Figure 5.51. Final look of the CSPC scheme with sample plates front left showing the build-up of the SPC scheme

Figure 5.52 shows the test specimen coated with the CSPC scheme after immersion The characteristic change of colour due to polishing is evident when one compares with the sample plate which had not been immersed.

Figure 5.52. CSPC test specimen after testing. Sample plate was not immersed.

The Foul Release coating scheme consisted of one layer of primer with a dry film thickness of 100µm, one layer of tiecoat with a dry film thickness of 100µm, and one topcoat with a dry film thickness of 150µm.

The primer (called Intershield ENA300/303 Bronze) was applied in the morning, as shown in Figure 5.53. The tiecoat is a 2-pack version (called Intersleek 731 BXA730/731 Gray) and was applied 6 hours later. The topcoat (called Intersleek 757 BXA757/758/759 Gray) was applied the following day, as shown in Figure 5.54.

Figure 5.53. Application of the CFR Primer

Figure 5.54. Application of the CFR topcoat.

Figure 5.55 shows the final look of the test specimen coated with the CFR scheme.

Figure 5.55. Final look of the CFR scheme

5.3.1.5 Roughness measurements

The roughness measurements were carried out with the BMT Hull Roughness Analyser (cf. Section 2.6.2), as shown in Figure 5.56.

Figure 5.56. Roughness measurement with the BMT Hull Roughness Analyser after testing

Table 5-16 presents the average, mode and standard deviation of the different surfaces.

Table 5-16. Statistical roughness characteristics (in microns)

Surface	Average	Mode	Standard deviation
CSTEEL (before)	20.6	16	6.4
CSTEEL (after, rusted)	77.6	54	34.2
CSPC (before)	27.4	28	5.9
CSPC (after)	29.8	26	9.2
CFR (before)	49.4	46	17.7

The CSTEEL and CFR measurements before testing compare well with the values measured in Section 5.2.1.5. The CSPC scheme was applied extremely well and very low roughness values were recorded.

The roughness histograms of the steel and coated surfaces are shown in Figure 5.57.

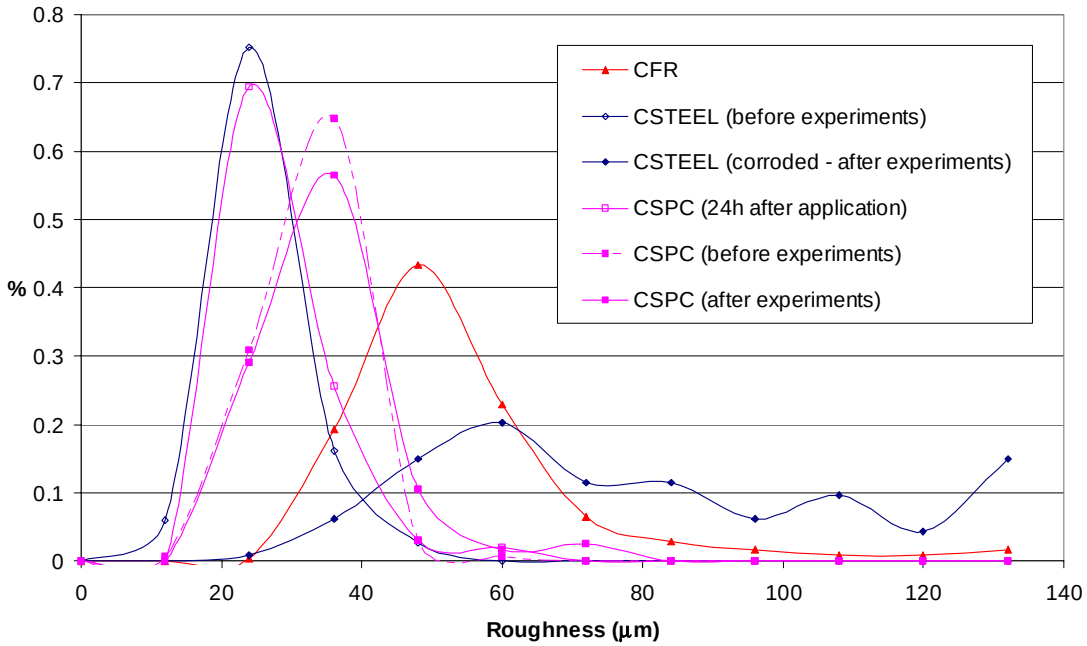

Figure 5.57. Roughness histograms of the different surfaces.

As mentioned, small sample plates were painted alongside the test specimens and have been analysed with an optical measurement system for a more extensive study of the roughness characteristics (cf. Chapter 6).

5.3.2 Experimental procedure

In order to study the effect of paint on the turbulent boundary-layer structure, a baseline hydrodynamic performance of the corroded CSTEEL surface was first evaluated. Subsequently, the different test specimens were tested. In order to look at boundary-layer development and the effect of Reynolds number on the flow, velocity profiles were taken at three downstream positions. The profile locations were at 1.4545m, 1.607m and 1.7595 from the leading edge, referred to as POS2, POS3 and POS4 respectively, and the three free-stream velocities were 3.2m/s, 5.3m/s and 7.5m/s (referred to as 3, 5 and 7 in Tables and Figures). Before conducting any LDV measurements, the angle of attack of the boundary-layer test plate was adjusted to give zero pressure gradient over the test plate.

The following procedure was carried out to measure the velocity profile over the different test specimens (cf. Section 5.2.2):

1. Adjust the free-stream velocity to 5m/s
2. Find the wall (y = 0) by receding the probe volume until the observed noise on the oscilloscope increases significantly. This will indicate that the centre of the probe volume is within about one half of the probe volume diameter of the wall. The current through the anode of the PDA receiver will now reach a maximum
3. Recede the probe until the wall signal dominates. The measurements now should not measure a significant velocity signal. The minimum velocity indicates the position nearest to the wall, the earlier measurements were actually taken *in* the surface, the signals being distorted by reflected light.
4. Start the actual data collection using the automated traverse datafile. The system will collect for each channel 4000 coincidence samples or sample for 20s, whichever comes first, and then proceed to the next location in the traverse file. In general, between 100 and 200 validated samples were picked up over 20s at a low validation rate (ca. 10%), but in the outer region of the boundary layer (y > ca. 0.15δ), the data rate would lie between 0.015 and 0.04kHz with a validation rates between ca. 50 and 80% (depending on the position and the free-stream velocity). The traverse datafile consist of four regions with different traverse stepsize with the smallest stepsize, 0.1mm, in the region near the wall (consisting of approximately 25 data points).

Regions 2 and 3 have stepsizes of 0.25mm (ca. 20 data points) and 1mm (ca. 40 points) respectively. Finally a last data point was collected at 0.8m from the wall.

5. Continue measuring until the mean axial velocity becomes invariant. One extra data point is collected 80mm from the wall.
6. Measure and record the temperature and the kinematic viscosity of the water.
7. Repeat steps 1-6 for positions 1454.5 and 1759.5mm from the leading edge

5.3.3 Data reduction and analysis

The data reduction and analysis were identical to the procedure described in Section 5.2.3. Spectra and autocorrelation functions were not obtained because the data-rate was too low.

Figure 5.58 shows an arbitrary selection of the measured data and the respective fits calculated with the Hama method, which can be compared with Figure 5.19.

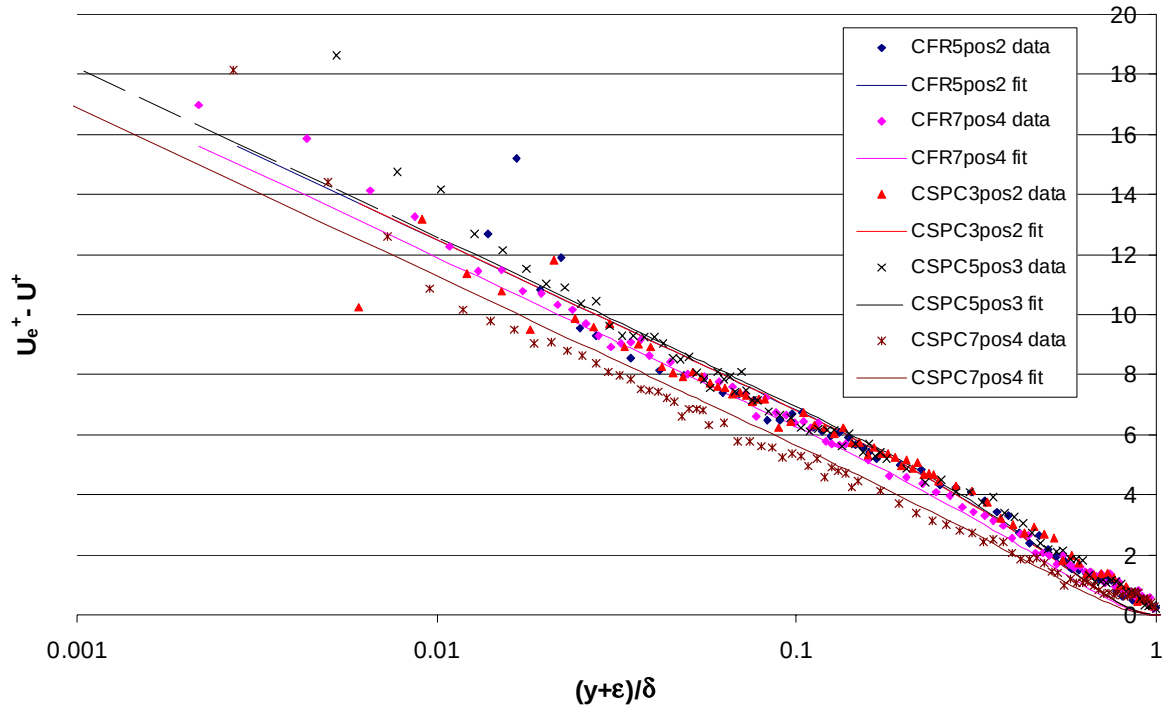

Figure 5.58. Determination of U_τ, Π and ε using Equation 6.2 to fit the data.

5.3.4 Results and discussion

5.3.4.1 Test parameters

The basic boundary-layer parameters calculated for all surfaces are shown in Table 5-17 to Table 5-19. The boundary-layer thickness δ is specified for $U = 0.99U_e$.

Table 5-17. Boundary-layer parameters of the CSTEEL surface

STEEL	Ue	Reθ	δ	δ1	θ	H	Tu
STEEL5pos2	5.10	2.19E+04	36.50	4.75	3.61	1.31	0.0363
STEEL5pos4	5.18	2.42E+04	44.00	5.33	3.92	1.36	0.0317
STEEL7pos4	7.08	3.61E+04	45.00	5.75	4.28	1.34	0.0397

Table 5-18. Boundary-layer parameters of the CSPC surface

CSPC	Ue	Reθ	δ	δ1	θ	H	Tu
CSPC3pos2	3.20	1.27E+04	33.00	4.27	3.37	1.27	0.0523
CSPC3pos3	3.21	1.27E+04	33.00	4.45	3.37	1.32	0.0550
CSPC3pos4	3.20	1.30E+04	33.50	4.48	3.46	1.29	0.0583
CSPC5pos2	5.19	2.14E+04	37.50	4.66	3.43	1.36	0.0393
CSPC5pos3	5.31	2.29E+04	40.00	5.10	3.75	1.36	0.0361
CSPC5pos4	5.35	2.48E+04	49.00	5.30	3.99	1.33	0.0313
CSPC7pos2	7.54	3.02E+04	37.00	4.20	3.04	1.38	0.0373
CSPC7pos3	7.50	2.57E+04	39.50	3.81	2.85	1.34	0.0408
CSPC7pos4	7.53	3.00E+04	44.00	4.30	3.14	1.37	0.0419

Table 5-19. Boundary-layer parameters of the CFR surface

CFR	Ue	Reθ	δ	δ1	θ	H	Tu
CFR3pos2	3.25	1.61E+04	40.70	5.10	3.80	1.34	0.0602
CFR3pos3	3.34	1.51E+04	39.80	4.71	3.80	1.24	0.0778
CFR3pos4	3.38	1.66E+04	44.00	4.86	3.88	1.25	0.0761
CFR5pos2	5.35	2.16E+04	36.00	4.20	3.19	1.32	0.0431
CFR5pos3	5.28	2.40E+04	43.50	4.56	3.86	1.18	0.0371
CFR5pos4	5.34	2.56E+04	46.50	5.27	4.07	1.30	0.0335
CFR7pos2	7.59	2.99E+04	39.10	3.87	3.11	1.24	0.0353
CFR7pos3	7.55	2.73E+04	39.10	3.70	3.00	1.23	0.0281
CFR7pos4	7.62	3.61E+04	46.00	5.13	4.03	1.27	0.0315

Table 5-17 to Table 5-19 show that the actual measured free-stream velocity U_e varied between 3.20 and 7.62m/s. The kinematic viscosity fluctuated between 0.76 and $0.87 \cdot 10^{-6} m^2/s$ and the momentum thickness Reynolds number Re_θ between 12686 and 36104. The boundary-layer thickness δ varied between 33 and 49mm and the free-stream turbulence, taken at $y = \delta$, varied 2.81 and 7.78% with an average free-stream turbulence of 4.39%.

The shape parameter H is plotted against U_e/U_τ in Figure 5.59, which can be compared with Figure 5.20.

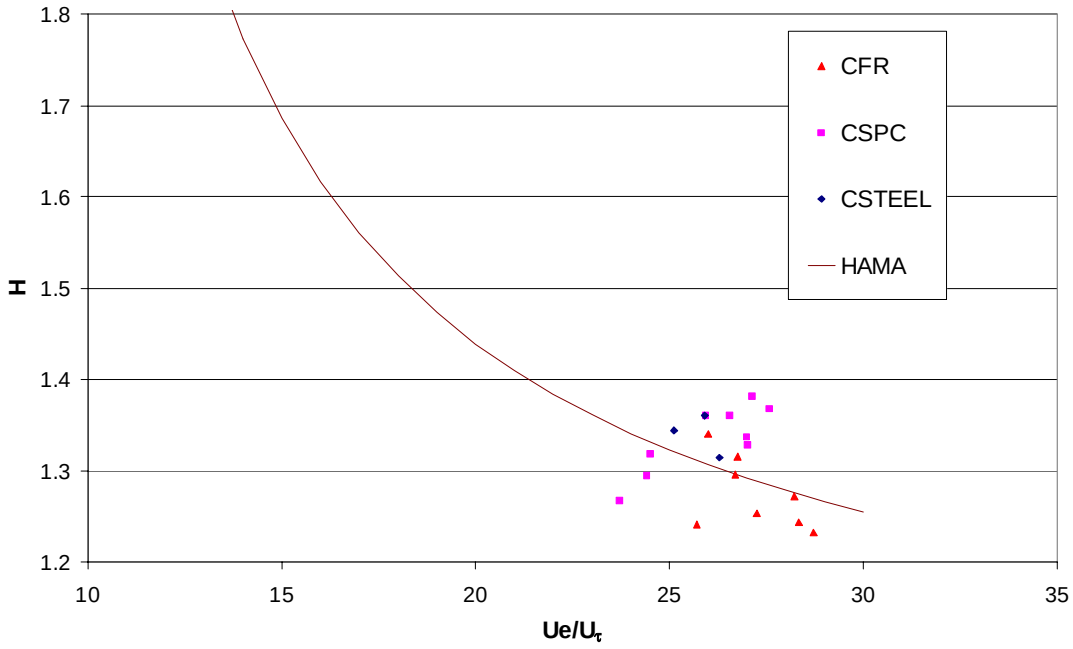

Figure 5.59. H values plotted against U_e/U_τ (uncertainty in H: ±9.2%, uncertainty in U_e/U_τ: ±4.9%).

5.3.4.2 Mean velocity profiles in outer variables

The mean velocity profiles in outer variables are shown in Figure 5.60. As mentioned, the effect of roughness is to increase the drag, resulting in a less full profile (cf. Figure 4.7). It is clear from this figure that the CSTEEL surface exhibits the largest drag, due to the fact that it had rusted very quickly upon immersion (in the Emerson Cavitation Tunnel in Section 5.2, a rust inhibitor is constantly present in the flow), increasing its roughness considerably (cf. Table 5-16). Antonia and Luxton (1971, 1972) have shown that boundary layers adjust more slowly to a change 'from rough to smooth' than vice versa, but this effect is presently not expected to have played a role on the measurements in view of the relatively smaller changes in roughness and because the measurements were taken quite far (> 10δ) from the change in roughness.

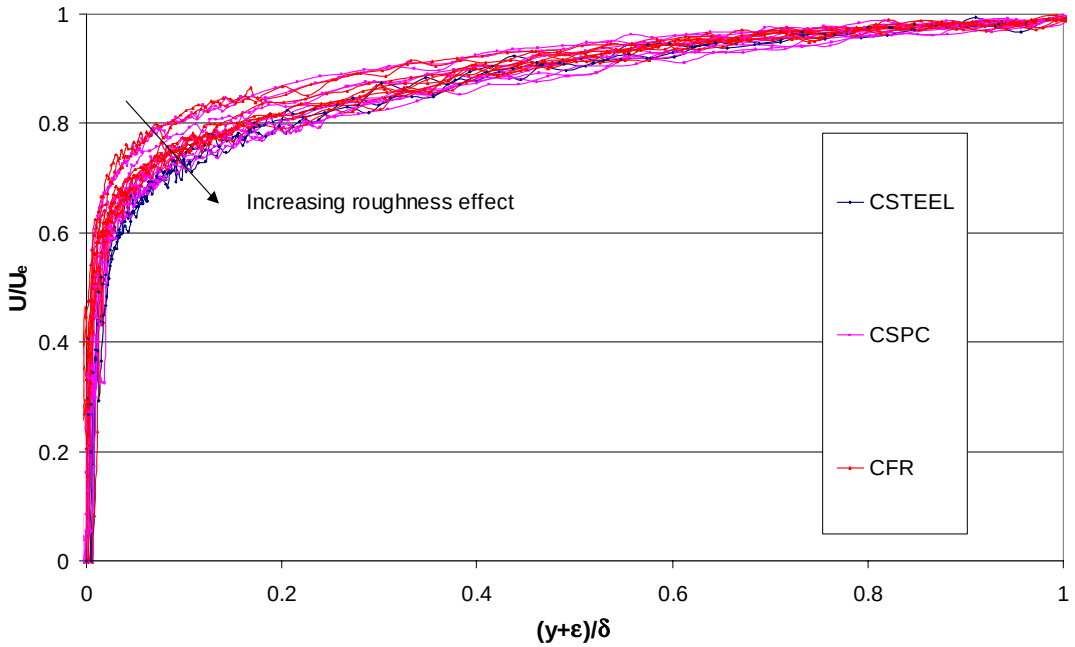

Figure 5.60. Variation of mean velocity in outer co-ordinates for the different surfaces (Uncertainty in U/U_e : ±5.6% outside the buffer layer. The uncertainty in $(y+\varepsilon)/\delta$ varies with y and is dominated by the uncertainty in ε for the near-wall points, declining to the uncertainty in δ for the outer-layer points.

5.3.4.3 Shear velocities, wake values and mean velocity profiles in wall co-ordinates

The shear velocities, wake values and other related parameters are listed in Table 5-20 to Table 5-22. The shear velocities were calculated by three different methods, but, as in Section 5.2.4, the results clearly indicated that the modified Clauser method (C) was unreliable for the coated surfaces. Good agreement was found between the Reynolds-stress method (RS) and the Hama method (H). U_τ as calculated with Hama's method was chosen to non-dimensionalise the boundary-layer parameters.

Table 5-20. U_τ, Π and related parameters of the CSTEEL surface

STEEL	Reδ1	Uτ HAMA	Π	cf (H)	cf (RS)	ΔU+ (H)	ΔU+ (RS)
STEEL5pos2	28825	0.194	0.38	0.002894	0.003069	2.55	3.09
STEEL5pos4	32872	0.2	0.28	0.002981	0.003025	3.27	3.23
STEEL7pos4	48493	0.282	0.28	0.003173	0.003151	5.03	4.72

Table 5-21. U_τ, Π and related parameters of the CSPC surface

CSPC	Reδ1	Uτ HAMA	Π	cf (H)	cf (RS)	ΔU+ (H)	ΔU+ (RS)
CSPC3pos2	16079	0.135	0.26	0.00356	0.003773	3.68	4.13
CSPC3pos3	16788	0.131	0.26	0.003331	0.003351	2.99	2.83
CSPC3pos4	16877	0.131	0.21	0.003352	0.003353	3.08	2.85
CSPC5pos2	29149	0.2	0.26	0.00297	0.003037	2.92	2.98
CSPC5pos3	31128	0.2	0.28	0.002837	0.002848	2.48	2.31
CSPC5pos4	32957	0.198	0.28	0.002739	0.002753	2.16	2.00
CSPC7pos2	41666	0.278	0.11	0.002719	0.002955	2.64	3.52
CSPC7pos3	34413	0.278	0.06	0.002748	0.002836	2.31	2.50
CSPC7pos4	41006	0.273	0.01	0.002629	0.002697	2.14	2.27

Table 5-22. U_τ, Π and related parameters of the CFR surface.

CFR	Reδ1	Uτ HAMA	Π	cf (H)	cf (RS)	ΔU+ (H)	ΔU+ (RS)
CFR3pos2	21526	0.125	0.26	0.002959	0.00324	2.11	3.04
CFR3pos3	18746	0.13	0.26	0.00303	0.002975	2.07	1.61
CFR3pos4	20793	0.124	0.26	0.002692	0.002713	0.77	0.65
CFR5pos2	28419	0.2	0.26	0.002795	0.002879	2.06	2.22
CFR5pos3	28325	0.198	0.28	0.002813	0.002838	2.13	2.02
CFR5pos4	33129	0.2	0.26	0.002805	0.002946	2.49	2.91
CFR7pos2	37171	0.268	0.06	0.002494	0.002606	1.16	1.55
CFR7pos3	33618	0.263	0.06	0.002427	0.002461	0.52	0.49
CFR7pos4	45946	0.27	0.14	0.002511	0.002531	1.78	1.67

Table 5-20 to Table 5-22 show that the optimised wake values Π obtained from the present analysis are always significantly lower than the value of 0.55 that Hama (1954) used. The values are similar for the two coated surfaces. Significantly lower values were recorded for the measurements at 7.5m/s, probably because of bending of the plate at this velocity which also would have affected the determination of the error in origin ε. The three flathead screws around the centre-line at the aft and front of the test plate were not present for the CSTEEL surface and it was observed that significant bending of the plate occurred at 7.5m/s due to a Venturi effect in the tunnel section. The presence of the pair of three screws fore and aft did not prevent the mid of the coated test specimens from bending a little thus causing a favourable pressure gradient, which in turn is known to lower the wake values (cf. Section 4.4.4). This would explain the difference not observed over the CSTEEL surface. However, there is no solid proof of this speculation. The wake values are also highly susceptible to the free-stream values, Π decreasing when Tu increases. This would explain why the wake values for the coatings were lower than those measured presented in Section 5.2.4.1, where the recorded free-stream turbulence values were lower. Tu was actually lower at the higher speeds when expressed in percentage, but the actual values $\sqrt{(\overline{u'^2}+\overline{v'^2})/2}$ would have been higher, which might also explain why the wake values were lower at 7.5m/s.

Figure 5.61 and Figure 5.62 show the mean velocity profiles in wall co-ordinates of the different surfaces, along with the smooth wall log-law using the Stanford Conference values for the slope and intercept and the equation valid in the linear sublayer (given by Equations 5.2 and 5.3 respectively).

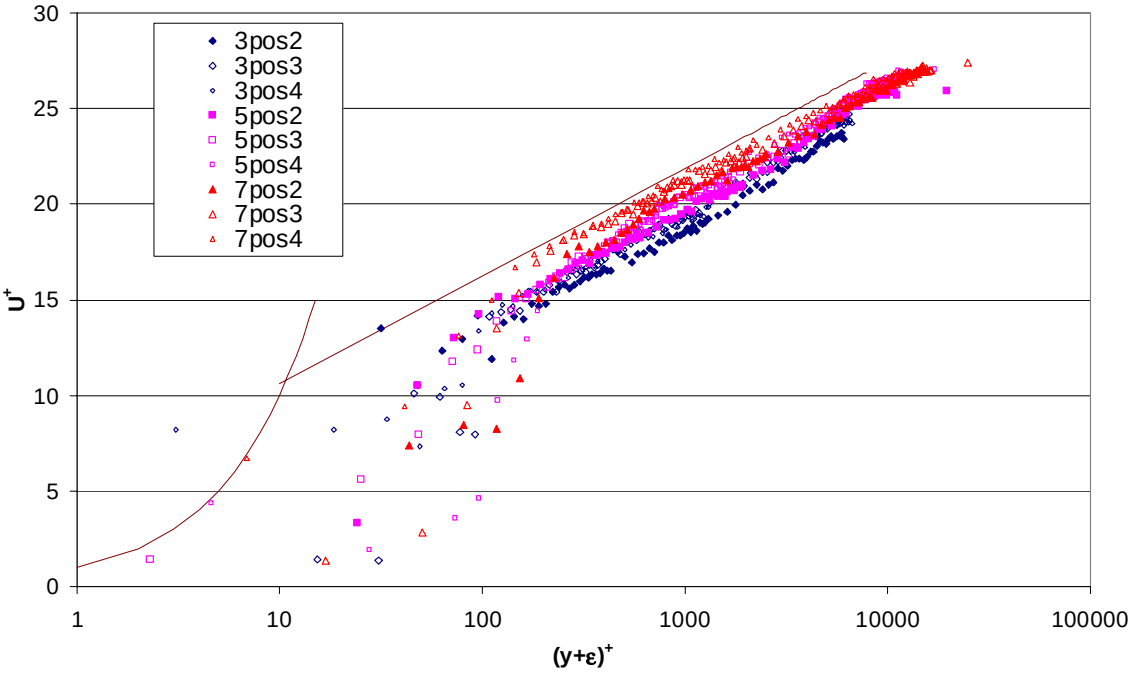

Figure 5.61. Velocity profiles in wall co-ordinates for the CSPC surface. Uncertainty in U^+: ±6.2%.

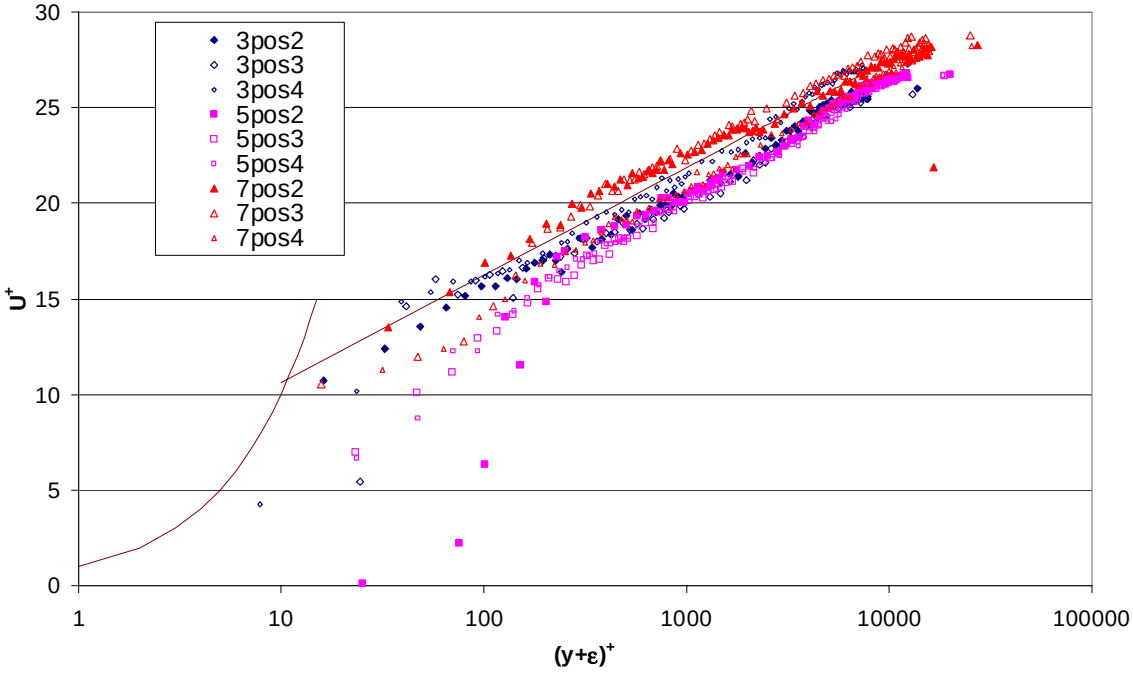

Figure 5.62. Velocity profiles in wall co-ordinates for the CFR surface. Uncertainty in U^+: ±6.2%.

Figure 5.61 shows a marked Reynolds number dependence of the CSPC surface, whereby the log-law region approaches Equation 5.5 as the Reynolds number increases, i.e. the roughness function seems to decrease with increasing Reynolds number. Figure 5.62 shows that there is also seems to be some Reynolds number dependence for the CFR surface, but there is not a clear trend as is the case for CSPC surface.

Figure 5.63 to Figure 5.65 compare the profiles of both surfaces at the three separate velocities. The profiles collapse fairly well for each surface at the respective speeds. The difference between the CFR and CSPC profiles are clearest at 3.2 and 7.5m/s, the distinction is harder to make at 5.3m/s.

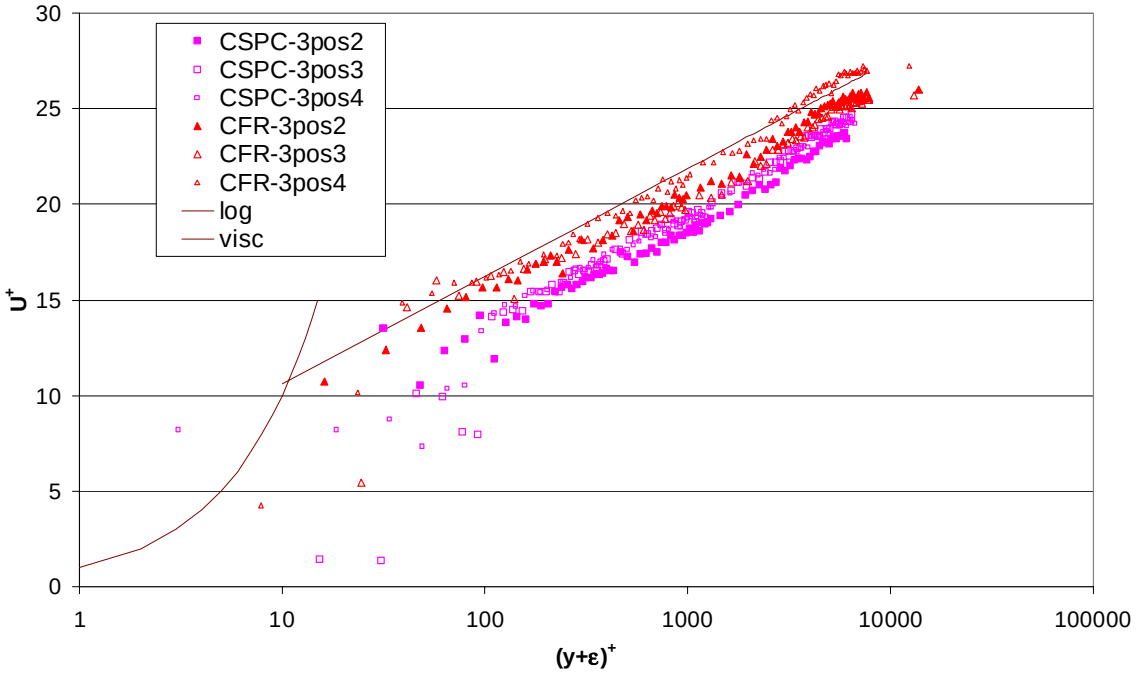

Figure 5.63. Velocity profiles in wall co-ordinates for both surfaces at 3.2m/s. Uncertainty in U^+: ±6.2%.

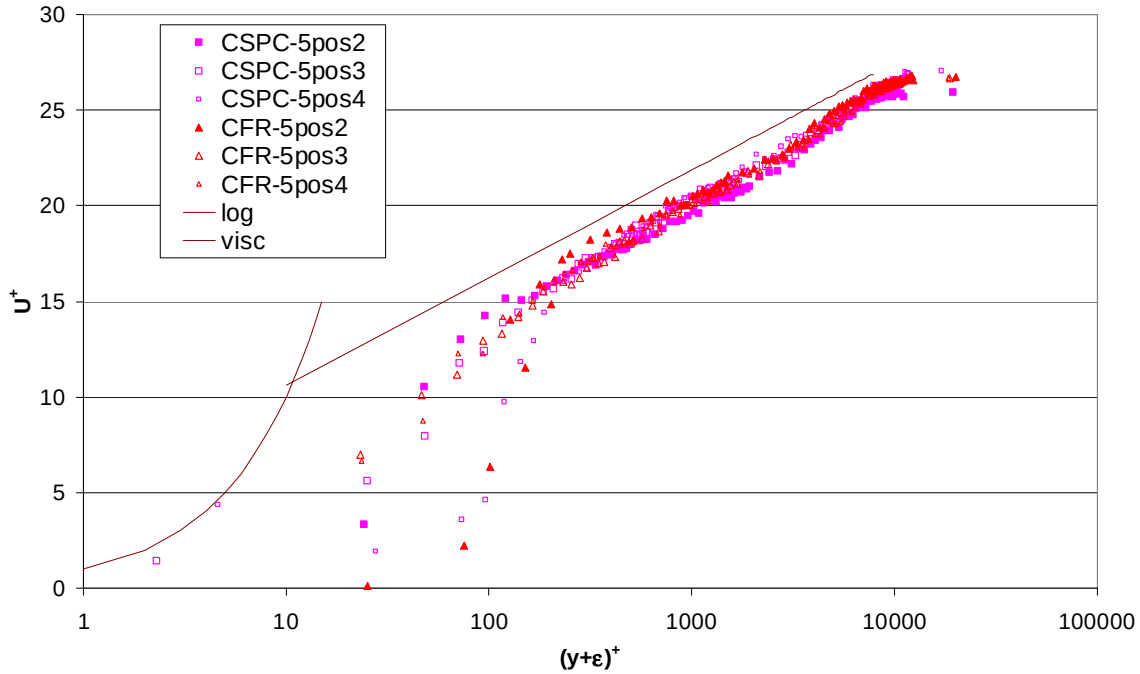

Figure 5.64. Velocity profiles in wall co-ordinates for both surfaces at 5.3m/s. Uncertainty in U^+: ±6.2%.

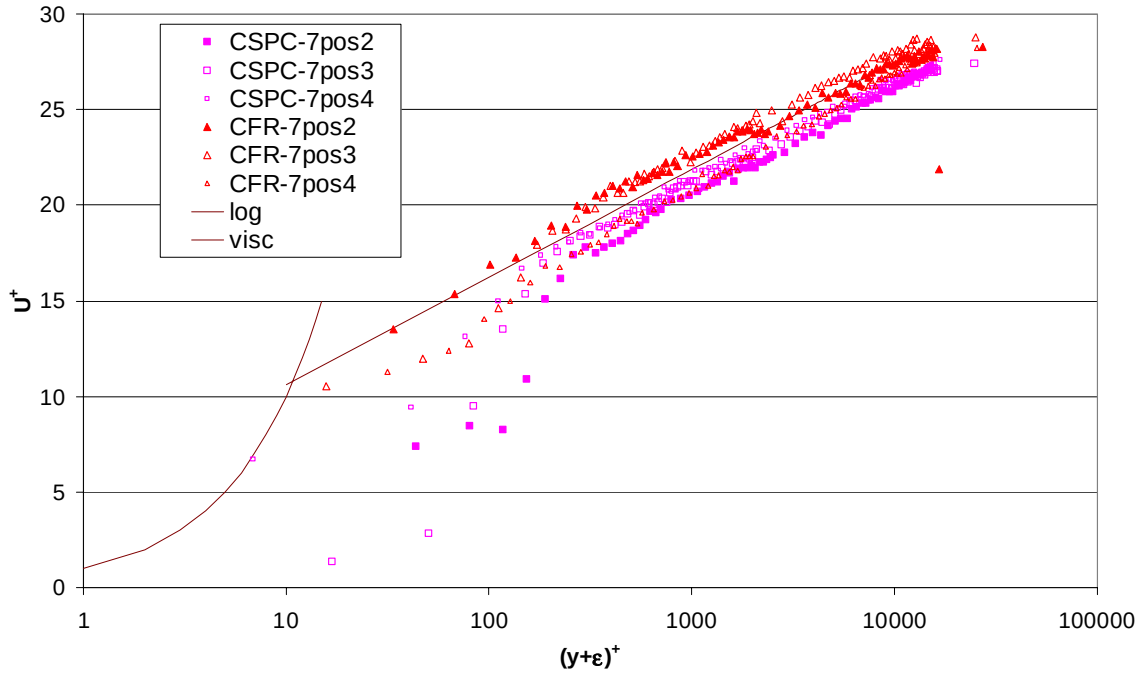

Figure 5.65. Velocity profiles in wall co-ordinates for both surfaces at 7.5m/s. Uncertainty in U^+: ±6.2%.

Reynolds number similarity (cf. Section 4.5.1) implies that the curves in Figure 5.61 and Figure 5.62 should collapse, but some Reynolds number dependence of the profiles is evident. Antonia and Luxton (1972) investigated the self-preservation of the boundary layer

by looking at the defect law plots. Figure 5.66 and Figure 5.67 show these plots for the CSPC and the CFR surface respectively. Self-preservation of the boundary layer is evident at 3.2 and 5.3m/s. The shift observed at 7.5m/s is likely due to the bending of the plate mentioned above, rather than the invalidity of the Reynolds number similarity hypothesis. This is supported by the fact that the measurements at 7.5m/s alone also seem self-preserving.

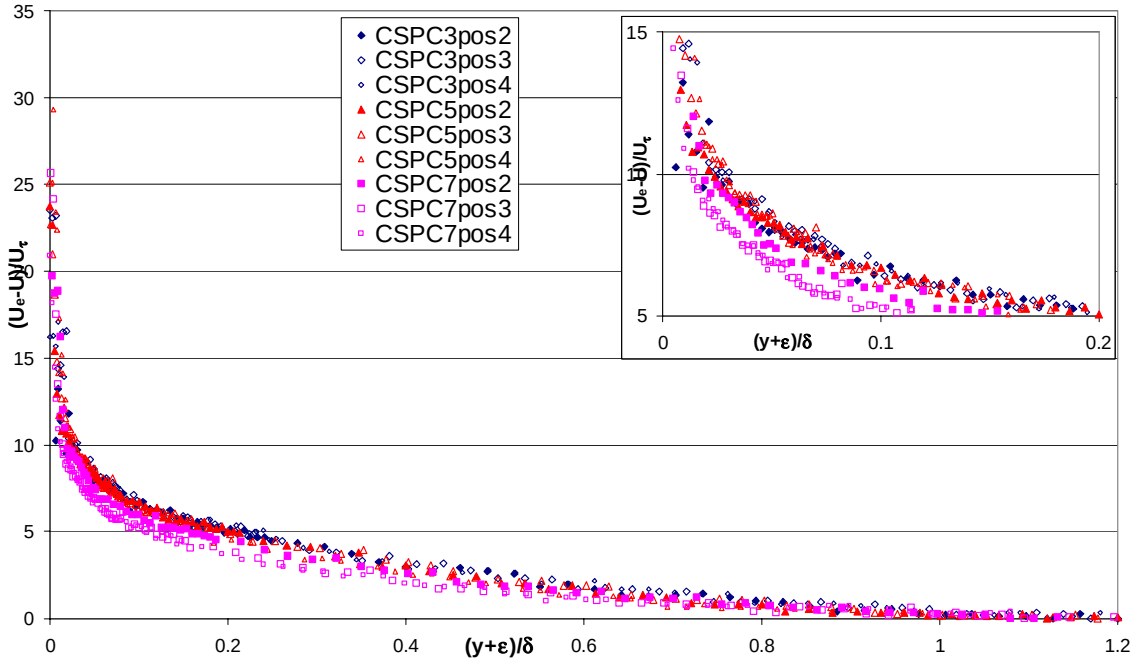

Figure 5.66. Defect law plot for the measurements over the CSPC surface. Uncertainty in U_e^+-U^+: ±7.9%.

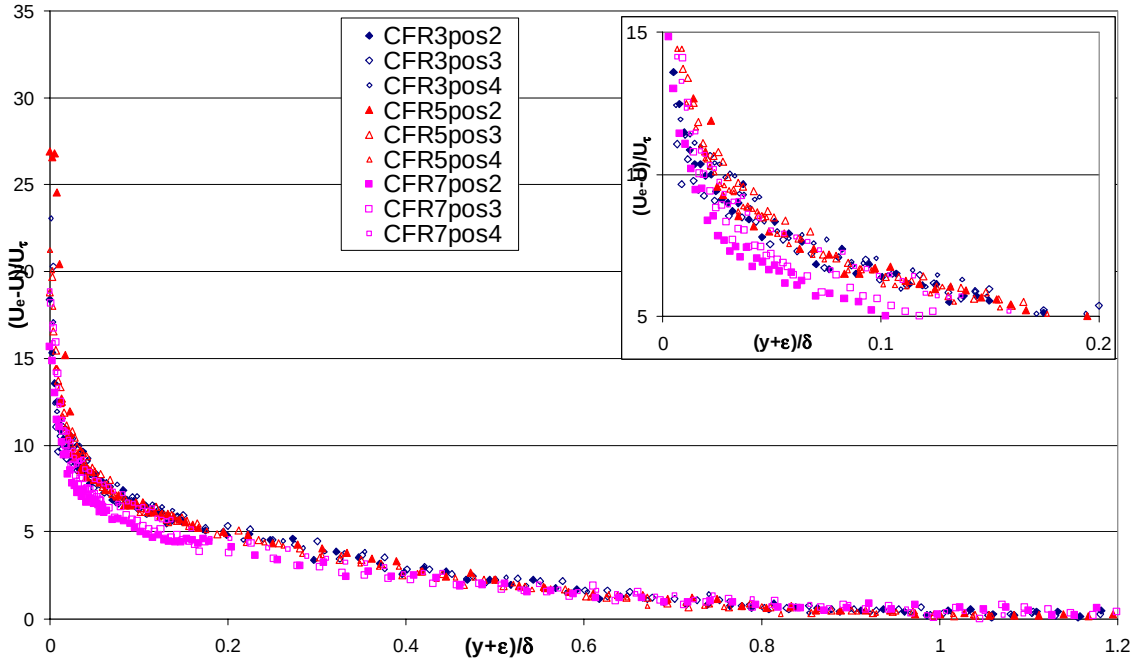

Figure 5.67. Defect law plot for the measurements over the CFR surface. Uncertainty in U_e^+-U^+: ±7.9%.

5.3.4.4 Skin friction coefficients

The frictional resistance coefficients of the STEEL surface as measured in the Emerson Cavitation Tunnel have been used as the smooth reference surface (Candries et al., 2001).

Table 5-20 to Table 5-22 show the frictional resistance characteristics of the different rough surfaces. Figure 5.68 presents the skin friction coefficients of the different surfaces plotted against $Re_{\delta 1}$ along with least-squares regression lines for the values obtained with the Hama method.

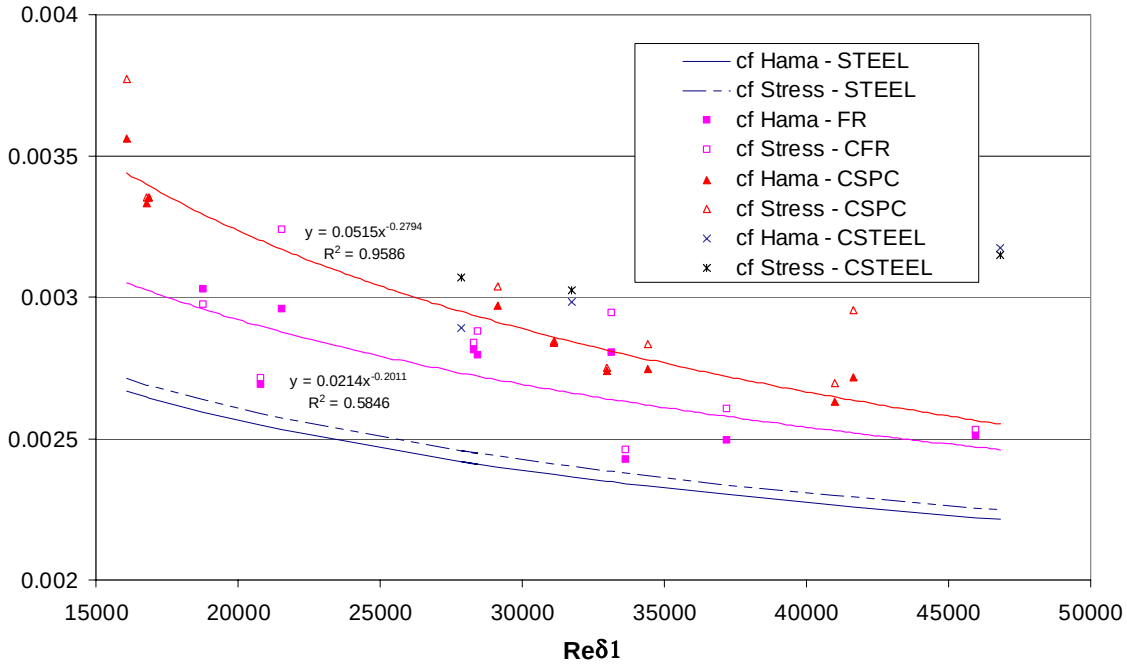

Figure 5.68. The frictional resistance coefficients of the STEEL and presently tested surfaces as obtained with the Hama and Reynolds stress methods (uncertainties in c_f: ±4.8% for the Reynolds stress method, ±6.7% for the Hama method).

Figure 5.68 shows that all the tested surfaces had significantly increased c_f values compared to the smooth STEEL surface.

The least-squares regression lines in Figure 5.68 are merely indicative for the selected results, and due to the scatter of the results should not be used for any extrapolation purposes. Whereas the power-trendlines of the CFR surface run fairly parallel with the STEEL reference surface, the descent of the CSPC surface trendline is steeper in agreement with the

observations made of the Reynolds number dependency of the velocity profiles. Except for CFR5pos4, all measurements of c_f over the CFR surface fall below the CSPC surface.

In order to obtain an idea of the percentual differences in c_f the same method as in Section 5.2.4.4 has been used. A power trendline that represents the STEEL surface well is $0.0144 \cdot Re_{\delta 1}^{-0.1745}$. Similar trendlines have been computed with least-squares regression analysis keeping the exponent constant, but varying the multiplicative factor. Thus factors of 0.0163 and 0.0177 gave the best correlation for the CFR and the CSPC surface (but the R^2 values were low: 0.58 and 0.82 respectively, indicating that this is a fairly crude indication). Hence a difference of 14.6% is observed between the CFR and the STEEL surface and 22.9% between the CSPC surface and the STEEL surface. In other words, this analysis indicates that the c_f values of the CSPC surface are 8.6% higher than for the CFR surface. A difference of 4.6% between the SPC and the FR surface was calculated in Section 5.2.4.4. However, presently the uncertainty in c_f is larger and the R^2 values are lower so that the estimate itself is also cruder. It is felt that the fact that the whole first metre from the leading edge was rough due to corrosion, rather than only the 0.3m from the leading edge covered with sand grit, also might have had an influence, possibly enhancing the differences.

5.3.4.5 Roughness functions

The STEEL trendlines obtained in Section 5.2.4.5 (Figure 5.25) were used for interpolation of the STEEL c_f values in order to calculate ΔU^+ at the respective $Re_{\delta 1}$ of the measurements of each different surface, in accordance with Granville's recommendations (Granville, 1987). The obtained values, listed in Table 5-20 to Table 5-22, seem fairly constant with $Re_{\delta 1}$. At lower Reynolds numbers, the roughness function for the CSPC surface was higher than average. Since the values do not seem to depend too heavily on $Re_{\delta 1}$, two-factor ANOVA analysis was applied to investigate whether the differences between the coated surfaces were significant with 95% confidence. The analysis confirmed that Re_x did not have a significant effect and indicated that there was a significant difference in ΔU^+ between CFR and CSPC, both for the Reynolds stress and for the Hama method. On average, ΔU^+ was 2.71 for the CSPC surface and 1.68 for the CFR surface.

5.3.4.6 Turbulence intensities and Reynolds stresses

Figure 5.69 to Figure 5.72 show the turbulence intensities, $\sqrt{\overline{u'^2}}/U_\tau$ and $\sqrt{\overline{v'^2}}/U_\tau$, and the turbulent shear stresses, $\overline{-u'v'}/U_\tau^2$, for both surfaces respectively.

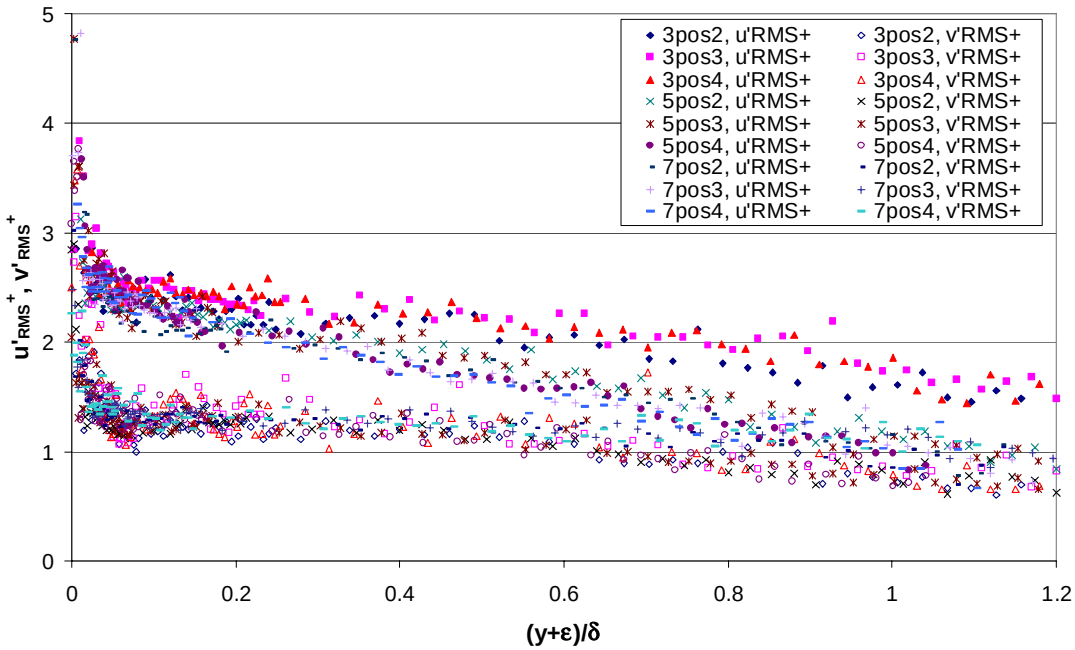

Figure 5.69. Turbulence intensity profiles for the CSPC surface. Uncertainty in u'_{RMS}^{+}: ±29.6%, uncertainty in v'_{RMS}^{+}: ±30.2%.

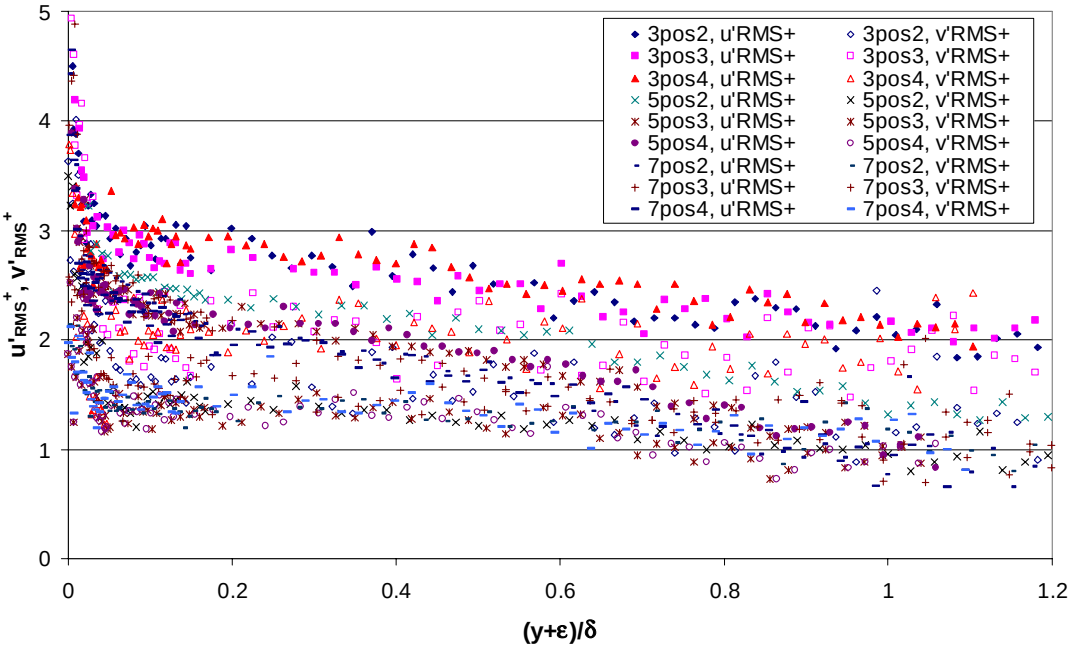

Figure 5.70. Turbulence intensity profiles for the CFR surface. Uncertainty in u'_{RMS}^{+}: ±29.6%, uncertainty in v'_{RMS}^{+}: ±30.2%.

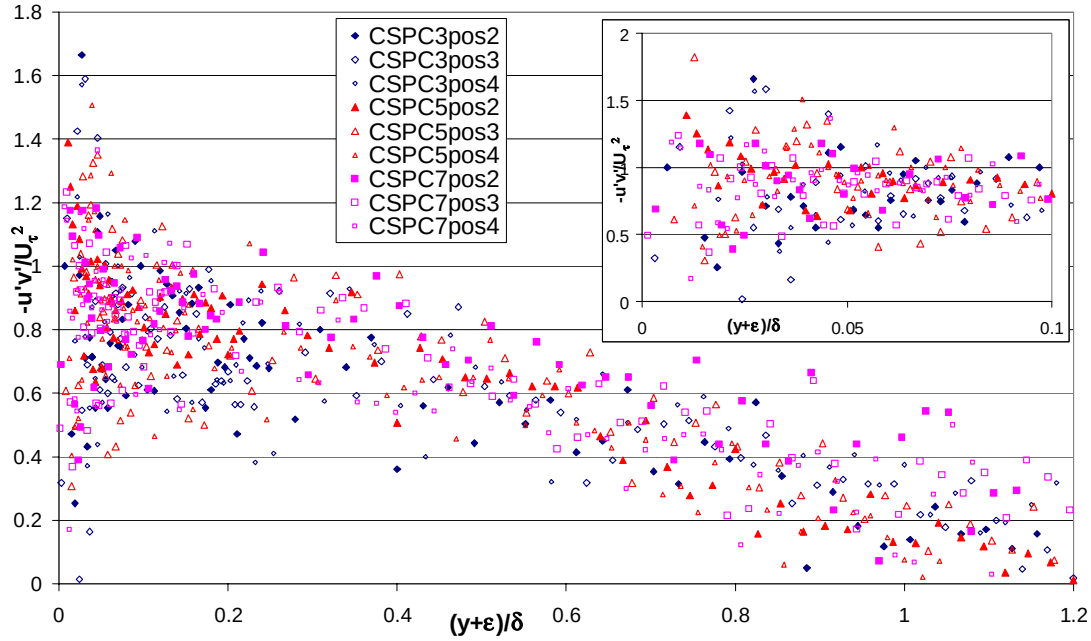

Figure 5.71. Reynolds stress profiles for the CSPC surface. Uncertainty in $-u'v'/U_\tau^2$: ±144.3%.

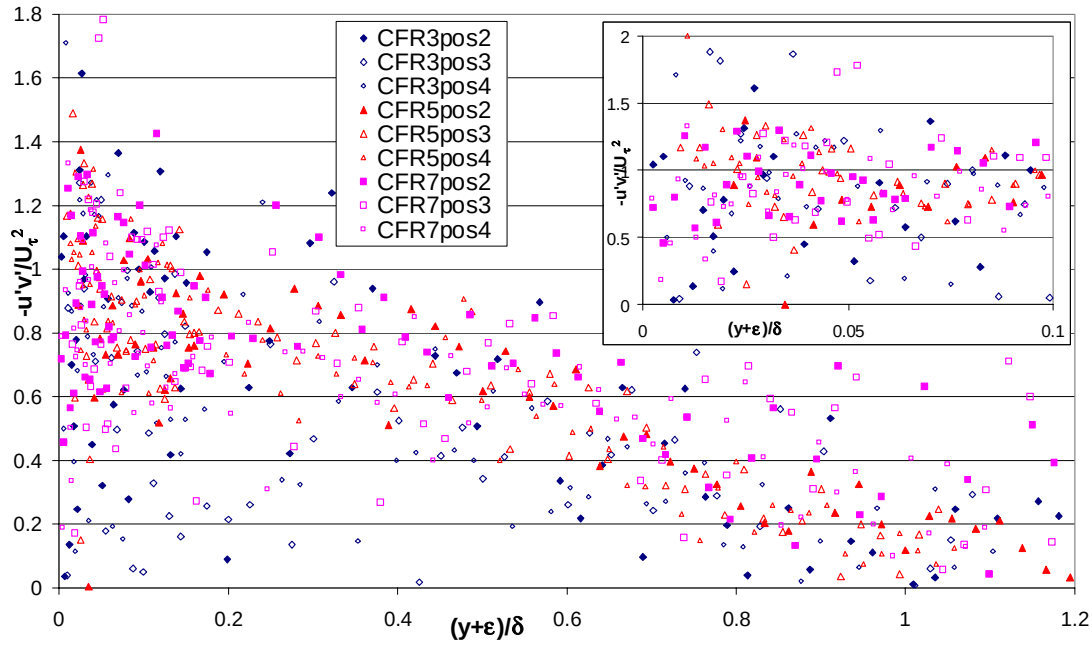

Figure 5.72. Reynolds stress profiles for the CFR surface. Uncertainty in $-u'v'/U_\tau^2$: ±144.3%.

Figure 5.69 and Figure 5.70 show the turbulence intensities of the CSPC and the CFR surface respectively. Figure 5.69 shows that the streamwise turbulence intensity is higher in the outer layer for U_e = 3.2m/s. Figure 5.70 shows that at this speed, both intensities are higher over the entire boundary layer for the CFR surface. This is most likely due to the poor

data rate and the frequency bandwidth not being optimal during the measurements. The other measurements collapse fairly well.

It is interesting to compare these measurements with the measurements taken in the Emerson Cavitation Tunnel (cf. Section 5.2.4.6). Figure 5.73 compares the turbulence intensity profiles expressed in outer variables at 5pos3. Despite the large (but arguably very stringent) uncertainties on the CEHIPAR measurements, the higher drag increases observed on CFR and CSPC seem to confirm the observations made in Section 5.2.4.6 regarding the effect of increasing roughness on the turbulence intensities. Because of the higher free-stream turbulence levels (3.7% as opposed to ca. 2.3%), the turbulence intensities over the CFR and CSPSC surface decay more slowly and remain higher in the outer layer.

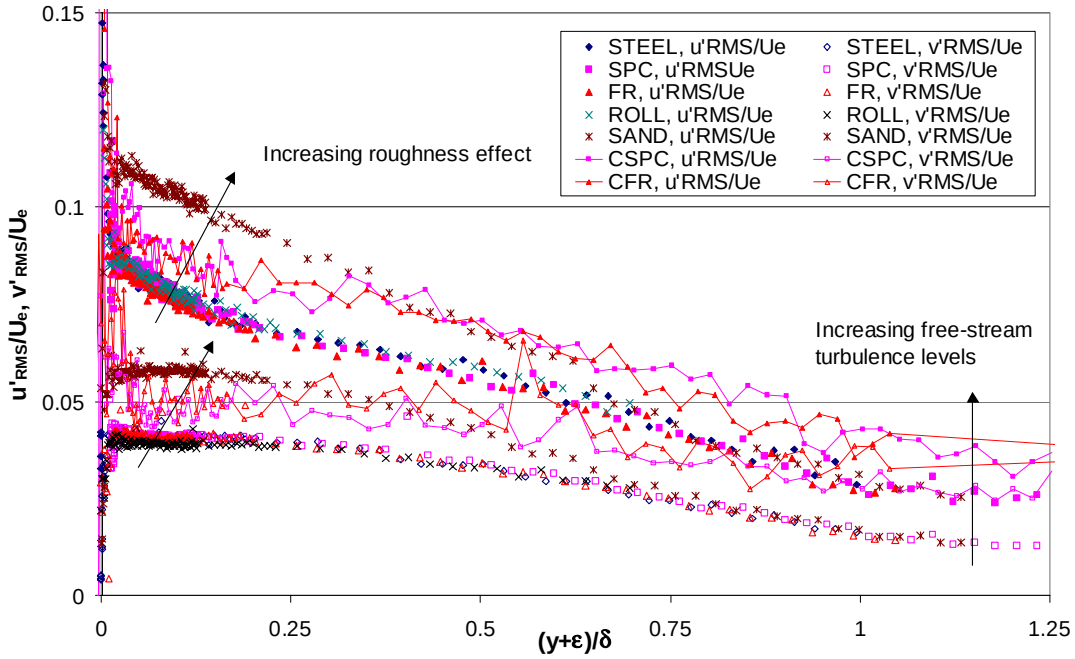

Figure 5.73. Comparative turbulence intensity profiles expressed in outer variables at 5POS3.

Figure 5.71 and Figure 5.72 show the Reynolds stresses for the CSPC and the CFR surface respectively. The Reynolds stress is effectively the parameter most sensitive and difficult to measure and is therefore the most stringent indication of the quality of the data. Figure 5.71 shows that the data rate over the CSPC surface is high enough to obtain clear plots. Figure 5.72 shows that the data rate was poorer over the CFR surface. Fewer validated samples result in increased scatter of the plots. Nevertheless, the data rate was high enough to obtain reliable plots and to employ the Reynolds stress method. The large scatter explains the very high uncertainty values. However, in practice, the 'overall' uncertainty is much lower than the analysis makes out. Several validated data points are always measured in the region

where the normalised Reynolds stress is expected to reach unity. Thus, while the uncertainty for one particular wall-normal position is extremely high, there are still sufficient data points available to determine U_τ with accuracy and confidence. This explains why the uncertainty listed in Appendix C.2 for U_τ is much lower at only ±4.3%.

5.4 Summary of the boundary-layer experiments

To the Author's knowledge, this is the first systematic investigation reported in the open literature on the boundary-layer characteristics of surfaces coated with Tin-free SPC and Foul Release systems using LDV equipment in a water tunnel. The following general conclusions are made:

- The coatings generally did not have a significant effect on the boundary-layer parameters such as δ, θ, δ_1 and H.
- The frictional resistance was significantly increased by the coatings. Overall the increase was less for the FR surface than for the ROLL surface, which in turn caused less friction increase than the SPC increase. It was estimated that c_f was increased by 10.9% by coating the STEEL surface with the FR coating, by 13.1% for the ROLL coating and by 16% for the SPC coating. In other words, the SPC coating gave a 4.6% increase over the FR coating. The c_f values of the CSPC surface were 8.6% higher than for the CFR surface.
- Multiple pairwise comparison of the roughness function of the different surfaces showed a significant difference within the experimental uncertainty between the FR and the SPC surface for the measurements analysed with the Hama method. Additionally, a significant difference was noted between the FR and the ROLL surface for the measurements analysed with the Reynolds stress method, whereas no significant difference was found between the ROLL and the SPC surface. This demonstrates the importance of the application method of the same coating system and confirms the suppositions made after the experiments carried out with the wave-piercing catamaran model (cf. Section 3.5). There was also a significant difference in ΔU^+ between CFR and CSPC, both for the Reynolds stress and for the Hama method.
- Self-preservation of the boundary layer was reached over all the surfaces in the Emerson Cavitation Tunnel as is clear from the mean velocity, Re-stress and turbulence intensity profiles. There was some Reynolds number dependency for the measurements in the CEHIPAR Cavitation Tunnel, but it is likely that these measurements were influenced by slight bending of the test plates. The self-preservation of the boundary layer supports the wall similarity hypothesis and justifies the use of similarity techniques to calculate the friction velocity.

- The average data-rate during the experiments was not high enough in order to obtain unbiased spectra (and no spectra at all in the CEHIPAR Cavitation Tunnel). Presently the average data-rate was on the order of 10^{-1}kHz, which should have been an order of magnitude larger. Nevertheless, at the lower wavenumber end, the spectra did allow to determine the integral length scales, in good agreement with the values obtained from the autocorrelation functions. The integral length scales did not show a clear trend in structural flow differences between the surfaces.

A summary of both the resistance and boundary-layer experiments is presented in Table 5-23. The relationship between a set of (h, ΔU^+) and (Re, C_F) is discussed in Section 7.8.

Table 5-23. Summary of the experimental results.

Resistance experiments	**Average Roughness (μm)**	**ΔC_F (compared to reference, %)**	**ΔU^+ (on average)**
2.55m long plate		least-squares regression, 2e6 < Re < 4.2e6	cf. Section 7.3
Aluminium	17		
Sprayed Foul Release	44	3.9	0.20
Sprayed SPC	75	23.4	2.17
6.3m long plate		linear interpolation Fn > 0.5 (Re > ca. 2e7)	cf. Section 2.3
Clean Aluminium	18		
Sprayed Foul Release	62	2.1	0.21
Sprayed SPC	39	3.8	0.62
Catamaran model		linear interpolation Re > 5e6	
Original surface	49		
Rollered Foul Release	64	1.9	
Rollered SPC	66	-9.2	
Boundary-layer experiments	**Average Roughness (μm)**	**Δc_f (compared to reference, %)**	**ΔU^+ (on average)**
Vertical Plate (Newcastle)			
Steel	23		
Sprayed Foul Release	51	10.9	1.25
Rollered Foul Release	60	13.1	1.54
Sprayed SPC	69	16	1.80
Sand grit	727		
Horizontal Plate (CEHIPAR)			
Sprayed Foul Release	50	14.6	1.68
Sprayed SPC	30	22.9	2.71

Chapter 6: Roughness characterisation

6.1 Introduction

In this Chapter the roughness characteristics of sample plates painted alongside the surfaces used in the experiments described in Chapter 3 and Chapter 5 are analysed using an optical measurement system. In general, roughness measurements are either taken by stylus instruments or by optical techniques. Instead of using a stylus instrument, it was decided to use the UBM optical measurement system available at International Coatings Ltd. for the detailed roughness analysis. The main reason was that it is a non-contact instrument, which was thought to be more suitable for the Foul Release surface.

Within the framework of this analysis, the background and detailed objectives of this Chapter are described in sections 6.1.1 and 6.1.2.

A multitude of roughness parameters is used in literature and the parameters used for the present analysis are reviewed and described in Section 6.2. The optical measurement system and the associated measurement procedure are presented in Section 6.3. The analysis and characterisation of roughness parameters is subject to several factors such as the selection of bandwidth limits and filtering. The identification and influence of these factors is described in Section 6.4, leading up to the analysis methodology which was eventually established to analyse the roughness measurements.

The actual analysis of the measurements is presented in Section 6.5. The characteristics of the different coatings are compared with each other in Section 6.5.1, with the AHR measured with the BMT Hull Roughness Analyser in Section 6.5.5, and with published characteristics in Section 6.5.3.

A summary of the findings is given in Section 6.6. Appendix E gives additional information on the UBM roughness analysis software and contains plots of the analysed roughness profiles.

6.1.1 Background

Townsin and Dey (1990) have shown that the frictional resistance of a newly painted ship surface correlates well with the average highest-peak-to-lowest-valley height, Rt50,

measured by the BMT Hull Roughness Analyser, which has been described in Section 2.6.2. The paints that were analysed by Townsin and Dey were all toxic antifoulings. Since then, Foul Release coatings have been introduced as an alternative to these paint systems. As explained in Chapter 2, Foul Release systems inherently rely on an ultra-smooth surface to minimise the adhesion of fouling organisms. The chemical formulation of toxic antifoulings is aimed at a steady release of toxins throughout the paint's lifetime, whereas the Foul Release system is formulated to have a high mobility of di-methyl groups around the siloxane polymeric backbone, thus exhibiting a low surface energy. It is therefore likely that the surface characteristics of a Foul Release coating are substantially different from those of toxic antifoulings.

Chapter 3 has described the resistance experiments which have been carried out to measure and compare both the frictional resistance and the average hull roughness (AHR) of surfaces coated with a Tin-free self-polishing co-polymer (SPC) and a Foul Release system. In the case of the 6.3m long plate (Section 3.3), the frictional resistance was lower for the Foul Release system than for the SPC system, while the AHR of the Foul Release system was higher than the SPC system, due to poor surface preparation. This immediately indicated that the AHR of a Foul Release coating measured by the BMT Hull Roughness Analyser, does not correlate with the frictional resistance, suggesting that other parameters associated with the texture of the coated surface may be involved.

This Chapter will therefore not only compare the roughness amplitude parameters of painted surfaces, but also the texture characteristics, reviewed in Section 6.2. A comprehensive set of coated sample plates has been analysed for this purpose with an UBM optical measurement system.

Much of the work presented in this Chapter was inspired by the work of the Ship Performance Group active in the 1980s under the supervision of Dr. Townsin, particularly the key publications of Byrne (1980), Medhurst (1989) and Dey (1989), which have been essential literature to understand the problems associated with ship hull roughness.

Byrne (1980) undertook the systematic measurement of hull roughness with the BMT (then BSRA) Hull Roughness Analyser. His work provided valuable insight into the nature of hull roughness, the wide variety encountered and the profundity of the difficulties associated with the characterisation.

Medhurst (1989) modified the Hull Roughness Analyser to include the measurement of parameters other than just the highest-peak-to-lowest-valley height and developed a software analysis package to systematically compute a whole series of parameters and thus characterise the metrology of the painted surfaces.

Dey (1989) analysed a whole series of surfaces with Medhurst's software analysis package and established various correlations between the different parameters. He carried out rotor experiments with a series of surfaces and correlated the measured drag with various combinations of the roughness parameters.

Two excellent works on roughness complement these publications and they have formed the backbone of the literature review, namely Thomas (1982 and 1999) and Whitehouse (1994).

6.1.2 Objectives

Within the framework of the background given above, the objectives of this Chapter are:

- to review the literature on the subject of surface profilometry with particular attention to ship hull roughness characteristics (Section 6.2)
- to analyse the data collected in Chapters 3 and 5 and to investigate the influence of factors such as the bandwidth limits (long wavelength cut-off length and sampling interval) and filtering on the roughness parameters (Section E.2 and 6.4.1)
- to establish a procedure to measure the roughness characteristics of different coated surfaces (Section 6.4.2)
- to look for differences in roughness characteristics between a Foul Release and a SPC surface and to investigate the influence of the Foul Release application method on the roughness characteristics by comparing a rollered and sprayed Foul Release panel (Section 6.5.1)
- to compare the measurements, where possible, with published data, in particular with those published by Dey (1989), which is the most comprehensive published set of data on marine coatings characteristics (Section 6.5.3)

6.2 Literature review: the characterisation of rough surfaces

Surface roughness is a three-dimensional problem for which two principal planes have to be considered: at right angles to the surface, and in the plane of the surface. The former can be characterised by a set of height parameters, whereas the texture in the plane of the surface can be characterised by a set of wavelength parameters. In the case of a painted ship hull, the surface topography is made up of wavelengths ranging from a few microns to several metres, classified into three regimes: surface roughness, waviness and error of form and the latter two are often regarded together as 'stuctural roughness' (Lackenby, 1962). The division is quite arbitrary and there is no generally agreed wavelength that divides roughness from waviness (Thomas, 1999, pp. 116-117). The effect of structural roughness, while very serious in the past has become much less significant firstly when welding replaced riveting (Allan and Cutland, 1956) and secondly with the advent of more advanced welding technology which resulted in a better finish of the weld seams.

Most investigations of the problem of flow over rough surfaces have been concerned with regular roughness made up of either graded sand or wires of different sizes or shapes. Characterisation of these surfaces is usually made by just a single dimension parameter: the height of the roughness elements. This has also been applied to the irregular roughness of a ship hull surface. For the last 50 years, the roughness of the ship hull surfaces has mainly been measured using the BMT Hull Roughness Analyser and its predecessors, which have been described in Section 2.6.2. Beside stylus instruments, pneumatic instruments, used extensively in the manufacturing industry, have also been used for the characterisation of ship hull roughness (Aertssen, 1955; Aertssen, 1962), but stylus instruments have always been more prevalent. The original instrument was developed for the experiments on the 'Lucy Ashton' (Denny, 1951; Conn et al., 1953; Lackenby, 1955; Smith, 1955) which were mentioned in Chapter 1. The AHR as an average of Rt50 readings, has been the universally accepted single roughness parameter for the characterisation of ship hull surfaces (ITTC, 1990).

However, it has been realised that the use of a single roughness parameter gives an incomplete representation of the concept of roughness, because two surfaces with the same value of height or amplitude parameter like Rt50 may have quite different textures as shown in Figure 6.1. At least one additional parameter is necessary to describe the texture.

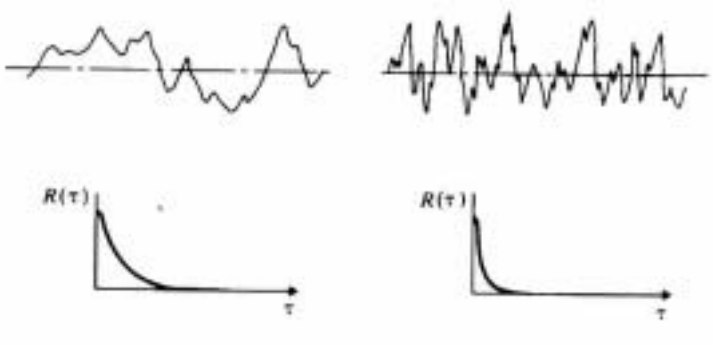

Figure 6.1. Two surfaces with the same amplitude parameters but with different textures, and their respective autocorrelation functions. The surface left exhibits an 'open' texture, right a 'closed' texture (From Thomas, 1999, p. 151).

A variety of height and texture parameters have been proposed and used in the literature. A surface cannot be said to possess a certain average roughness or slope without further qualification. Height parameters are sensitive to the long wavelength cut-off, whilst texture parameters are sensitive to the short wavelength cut-off. The width of the wavelength spectrum is fixed by the measurement instrument. Obviously, the wavelengths longer than the traverse length of the instrument cannot be measured, and the longest wavelength that can reliably be measured, the long wavelength cut-off or *cut-off length*, will only be a fraction of the traverse length. On the other hand, the short wavelength cut-off according to the Nyquist sampling theorem is equal to twice the sampling interval (Thomas, 1999, pp.115-117). The values for the long and short wavelength cut-offs must be specified in order to define the roughness parameters irrespective of height or texture.

Another major difficulty on real surfaces is that the measured values of roughness parameters are subject to large variations due to random sampling. Thomas (1999, p. 133) reports a calibration uncertainty in the UK for the parameter Ra of 4%. By comparison, a typical calibration uncertainty for the length of a gauge block is only 0.001%. Extreme-value parameters like Rt inherently have even larger calibration uncertainties.

In what follows, a brief description of the roughness parameters used in this Chapter will be described. The Reader is referred to Section 6.4.2 for the mathematical formulae used to calculate these parameters.

6.2.1 Amplitude parameters

The amplitude parameters can be subdivided into extreme-value parameters, average parameters and properties of the height distribution.

6.2.1.1 Extreme-value parameters

Rt Vertical separation of the highest peak and lowest valley of the filtered profile

Rz Vertical separation of the average of the 5 highest peaks and the average of the 5 lowest valleys within the assessment length (=RzISO)

Peaks and valleys are here defined as profile sections between two consecutive intersections with the centre line.

6.2.1.2 Average parameters

Rq Root Mean Square (RMS) roughness

Ra Arithmetic average of the absolute values of all points of the profile, also known as the centre-line average roughness

Thomas (1999, p. 139) points out that for many surfaces, it is possible to use Ra and Rq interchangeably, as they are correlated and the inherent statistical variation in all roughness measurements, is of the same order for these parameters.

6.2.1.3 Height distribution parameters

The probability density, p(z), of the distributions of heights z, may be characterised by its central moments (of order n):

$$\mu_n = \int_{-\infty}^{\infty} z^n p(z) dz \tag{6.1}$$

The second moment, μ_2, is the variance and describes the excursions of the distribution from the mean roughness. The parent deviation, σ, is the square root of μ_2 and is formally identical to Rq. The third central moment μ_3 is the *skewness* and is normalised as $Sk = \mu_3/Rq^3$. It is a measure of the asymmetry of the distribution. Most surfaces tend to be at least slightly negatively skewed, because peaks are more easily removed than valleys (Thomas, 1999, p. 143). The fourth moment μ_4 is the *kurtosis*, normalised as $Ku = \mu_4/Rq^4$ and describes the

overall shape of the distribution. Distributions which have a sharper central peak and longer tails are called leptokurtic.

6.2.2 Texture parameters

6.2.2.1 Spacing parameters

The high spot count, *De*, is the number of peaks per unit length of a profile and its reciprocal *S* is the mean distance between local peaks. A *local peak* is defined as a point where the height difference to the next minima is at least 1% of the Rt value. Thomas (1999, pp. 151-152) defines De as the reciprocal of *Sm*, which is the average distance between two mean line crossings. Dey (1989, p. 235) and Medhurst (1989) define De as the number of extrema per unit length, whereby an extrema is encountered when $|z_{i-1}| < z_i > |z_{i+1}|$. The agreement with Thomas' definition of De is fairly good.

The number of zero crossings with the mean line is defined as *Dz*, and is equal to two times *D* divided by the cut-off length L_c.

6.2.2.2 Hybrid parameters

Hybrid parameters incorporate both height and spacing information, and are usually derived from the differentials of the profile. *Δa* is the mean absolute slope, and can be converted into degrees to obtain the mean absolute slope angle *Sa* over the cut-off length of the surface profile while *Sq* is the RMS slope angle of the profile (cf. Ra and Rq). As the value of the sampling interval increases, the value of the average slope will logically decrease. Different values for surfaces with similar height parameters will have a different texture and will produce different hydrodynamic drags (Dey, 1989, p. 234).

The average wavelength, *λa*, is the average measure of spatial wavelength variations and is defined as $2\pi Ra/\Delta a$ (Whitehouse, 1994)

6.2.2.3 Spectral parameters

Another way of looking at the texture of a surface is by computing its random-process functions, notably its *autocorrelation function* (ACF) and its *power spectral density function* (PSDF). The *autocovariance function* (ACVF) of a function z(x) is mathematically defined as:

$$R(\tau) = \int_{-\infty}^{\infty} z(x)z(x+\tau)dx \tag{6.2}$$

For a profile z(x) of length L, R(τ) can be numerically approached by:

$$R(\tau) = \frac{1}{L-\tau}\int_{0}^{L-\tau} z(x)z(x+\tau)dx \tag{6.3}$$

where z(x) and z(x+τ) are pairs of height separated by a delay τ. This is normalised as the ACF: ρ(τ)=R(τ)/R(0) where R(0) is equal to the variance Rq^2 of the height distribution. The *correlation length* τ_c is then defined as the length over which the ACF decays from 1 to an arbitrary value, but usually taken as 0.5 or 1/e, i.e. $\tau_{0.5}$ and $\tau_{1/e}$.

The ACVF and the ACF are very sensitive to periodic components of the surface profile and will detect these even when they are obscured by random components. If the surface profile is entirely random, the ACF will decay asymptotically to zero at a rate which depends on the open-ness of the texture, and will thus distinguish between the two surfaces shown in Figure 6.1 (Thomas, 1999, p. 153). This rate of decay can be characterised by the correlation length and a greater correlation length indicates a more open texture of the surface.

The function corresponding to the ACF in the frequency (or wavelength) domain is the *power spectral density function* (PSDF), which is defined as the Fourier transform of the ACVF:

$$P(\omega) = \frac{1}{2\pi}\int_{-\infty}^{\infty} R(\tau)e^{-i\omega\tau}d\tau \qquad \text{or} \qquad G(\omega/2\pi) = 4\int_{-\infty}^{\infty} R(\tau)\cos(\omega\tau)d\tau \tag{6.4}$$

where ω is the wave number, 2π/λ and λ is the wavelength. Hence the inverse relationship is:

$$R(\tau) = \int_{-\infty}^{\infty} P(\omega)e^{i\omega\tau}d\omega \tag{6.5}$$

so that R(0) = Rq^2 is equal to the area under the PSDF. The spectral moments of order n are defined as:

$$m_n = \int_{-\infty}^{\infty} \omega^n P(\omega)d\omega \tag{6.6}$$

so that the variance of the height distribution, Rq^2, is equal to the zeroth spectral moment m_0. The second and fourth spectral moment are the variances of the slope and curvature distribution respectively.

An alternative to the PSDF is the *structure function*:

$$S(\tau) = \frac{1}{L-\tau} \int_0^{L-\tau} [z(x) - z(x+\tau)]^2 \, dx \tag{6.7}$$

which is related to the ACF by the relationship: $S(\tau) = 2Rq^2[1-\rho(\tau)]$ and which tends asymptotically to a value of $2Rq^2$ as τ approaches infinity.

An important texture parameter is the *bandwidth parameter*, α, which is defined as $\alpha = m_0 m_4 / m_2^2$. Longuet-Higgins (1957) has demonstrated that the first three even spectral moments are related to De and Dz and hence α can also be calculated as $(De/Dz)^2$ provided the sample contains more than 1000 measurements. Two other methods to calculate α are to determine the derivatives at the origin of the autocorrelation function or to measure the variance of the distribution of profile heights, slopes and curvatures.

The most important problem with all the parameters discussed so far is that none of them is intrinsic to the geometry of the surface in the sense that both amplitude and texture parameters are sensitive to low-pass and high-pass filtering of the measuring instrument, i.e. to the sampling interval and the cut-off length. For example, a parameter like the correlation length has been shown to increase as the cut-off length increases (Thomas, 1999, p. 161), so that, despite its fundamental theoretical significance, it has not been used much for practical characterisation.

6.2.2.4 Fractal parameters

It has been observed that some surfaces have a particular property called *fractal behaviour*. Fractal geometry was founded by Mandelbrot (1967) when he showed that for decreasing unit of measurement, the length of a natural coastline does not converge but increases monotonically. On plotting the length L as a function of the unit of measurement ε, he found a simple relationship of the form $L \sim \varepsilon^{1-FD}$ and he concluded that FD associated with every coastline is the dimension of the coastline. Mandelbrot (1977) describes the occurrence of fractal behaviour in other examples from nature such snowflakes and clouds. Fractal behaviour implies that the geometry, regular or random, exhibits *self-similarity*, over all ranges of scale, as sketched in Figure 6.2. These surfaces can be characterised by a *fractal dimension*, *FD*, which is not Euclidean. Thus, a snowflake is not two-dimensional, but has a fractal dimension just over unity. The fractal dimension of a profile can only have values

between 1 and 2, whereby 1 corresponds to a straight line, while 2 is an infinitely rough profile that fills in the whole plane of the surface (Whitehouse, 1994, p. 96-97).

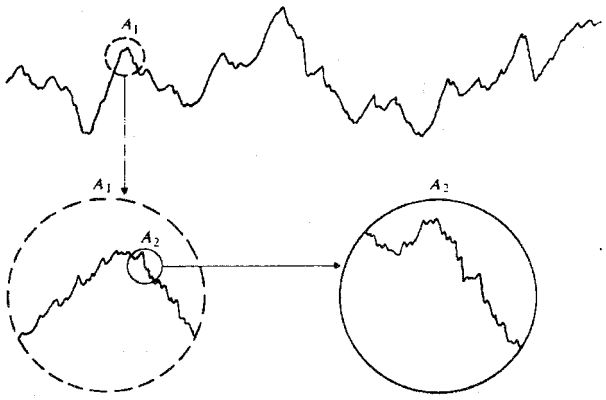

Figure 6.2. Self-similarity of surface profiles (From Thomas, 1999, p. 164).

Fractal behaviour has now found numerous applications in characterising and describing disordered phenomena in science and engineering. The particular relevance of fractal behaviour to rough surfaces is that self-similarity implies that any roughness parameter should be independent of the scale of sampling. The profiles of rough surfaces turn out to be s*elf-affine* which is self-similar but only when scaled in one direction. When the profiles of rough surfaces are repeatedly magnified, more and more details keep appearing (Thomas, 1982). A self-affine surface requires an additional parameter to the fractal dimension to define them. This *scaling factor* with dimensions of length is also called the *topothesy* (Sayles and Thomas, 1978)

One frequently used model for a roughness profile z(x) is the Weierstrass-Mandelbrot function which is continuous and non-differentiable (Majumdar and Bhushan, 1990; Ganti and Bhushan, 1995). The self-affine nature of this function is displayed by the power spectrum of the function which provides the amplitude of the roughness at all scales and which is given by:

$$P(\omega) = G^{2FD-2} / \omega^{(5-2FD)} \tag{6.8}$$

whereby G is the scaling factor (in m) and the ω is the wavenumber (in m^{-1}). Thus the Fractal Dimension is related to the slope of the spectrum on a log-log plot and the constant G determines the location of the surface along the power axis and is a characteristic length scale of the surface (Majumdar and Bhushan, 1990). From Equation 6.8 the spectral moments can be derived (Whitehouse, 1994; Wu, 2000):

$$m_0 = \frac{G^{2(FD-1)}}{4-2FD}\left(\frac{1}{\omega_L{}^{4-2FD}} - \frac{1}{\omega_h{}^{4-2FD}}\right) \tag{6.9}$$

$$m_2 = \frac{G^{2(FD-1)}}{2FD-2}\left(\omega_h{}^{2FD-2} - \omega_L{}^{2FD-2}\right) \tag{6.10}$$

$$m_4 = \frac{G^{2(FD-1)}}{2FD}\left(\omega_h{}^{2FD} - \omega_L{}^{2FD}\right) \tag{6.11}$$

whereby ω_L and ω_h are the lower and higher bandwidth limits, i.e. ω_h is equal to the reciprocal of the sampling interval (or the short cut-off wavelength) and ω_L is equal to the reciprocal of the long cut-off wavelength (if ω is expressed in 1/m). Since $\alpha = m_0 m_4 / m_2^2$ and assuming $\omega_h >> \omega_L$ the following relationship is derived:

$$\alpha = \frac{m_0 m_4}{m_2^2} = \frac{(FD-1)^2}{FD(2-FD)}\left(\frac{\omega_h}{\omega_L}\right)^{(4-2FD)} \tag{6.12}$$

The bandwidth parameter calculated via the fractal approach will be denoted by $\alpha(2)$ and Figure 6.3 shows how it varies with FD for the bandwidth limits selected for the present analysis.

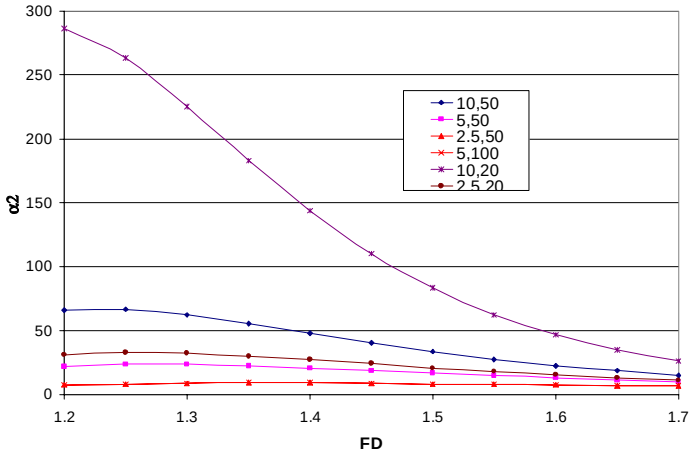

Figure 6.3. Plot of $\alpha(2)$ in function of FD for selected bandwidth limits.

Equation 6.12 again demonstrates the dependence of α on the bandwidth limits determined by the instrument. Moreover, it follows from Equations 6.9 and 6.10 that:

$$m_0{}^{0.5} (= Rq) \sim \omega_L{}^{FD-2} \tag{6.13}$$

$$m_2{}^{0.5} (= Sq) \sim \omega_h{}^{FD-1} \tag{6.14}$$

An alternative way to calculate the fractal parameters is to compute the structure function. It can be shown that for a fractal profile:

$$S(\tau) = \Lambda^{2FD-2}\tau^{2(2-FD)} \tag{6.15}$$

whereby Λ is the topothesy which can be related to G (see Wu, 2000). Hence, by plotting the logarithm of the structure function against the logarithm of τ (interpreted as the sample interval), a straight line should result whose slope allows the calculation of FD and whose intercept at unity gives Λ, as shown in Figure 6.4 (Thomas, 1999, p. 164; Whitehouse, 1994, p. 97).

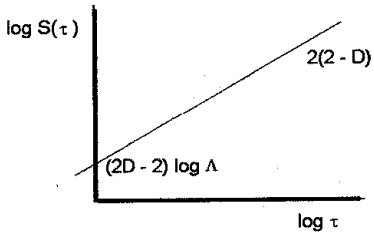

Figure 6.4. Determination of fractal properties (From Thomas, 1999, p. 165).

Not all surfaces display fractal behaviour (Whitehouse, 2001). It depends on how a surface is formed and how surface processing may change the roughness structure. Majumdar and Bhushan (1990) argue that a surface is either formed by fracture of a solid, by deposition of materials or by solidification of a liquid. These are natural and random processes which produce fractal surfaces. The fractal dimension is then an intrinsic roughness parameter valid for all scales and independent of the characteristics of the measurement instrument. However, when a surface is processed, the surface is sometimes fractal and sometimes not. When the processing technique is random and unbiased in direction at the length scales considered, the spectra of the surface are seen to be fractal. Stainless steel is an example of this since grinding produces an isotropic surface with fractal behaviour at the length scales of roughness measurement even though grinding is an anisotropic process at macroscales. Whitehouse (1994) and Thomas (1999) note that the fractal behaviour of man-made surfaces is restricted to smaller wavelengths and cannot extend over an infinite range of wavelengths. They point out that the fractal approach is an interesting alternative to the spectral approach whereby the emphasis is put on the order of the power. Majumdar and Bhushan (1990) also note that in all cases, fractal and non-fractal, the spectra of the profiles follow power laws.

6.3 Equipment and measurement procedure

6.3.1 The UBM microfocus measurement system

The roughness characteristics were measured with an optical measurement system, commercially known as the UBM Microfocus Measurement System (see also Thomas, 1999, p. 41 and Whitehouse, 1994, Section 4.3.3) which is shown in Figure 6.6.

Figure 6.5. Photograph of the optical measurement system, used to analyse the sample coated plates.

As mentioned in Section 6.1, a non-contact instrument was thought to be more suitable for the roughness analysis of the Foul Release system. Foul Release surfaces are elastomeric and therefore they easily yield elastically under the load of a stylus instrument. However, Thomas (1999, p. 28) reports that no significant differences are found if roughness measurements are taken below the glass transition temperature of elastomeric surfaces (i.e. when they are no more compliant than steel). Nevertheless, roughness measurements taken with the BMT Hull Roughness Analyser stylus instrument require slight wetting of the Foul Release surface in order to prevent the stylus stuttering over the surface or making small scratches in the coating. However, excessive wetting results in the drive wheels slipping. The use of stylus instruments on Foul Release surfaces therefore requires quite some skill and judgement, so it was thought that a non-contact measurement instrument would be more objective and suitable for the present analysis.

The working principle of the system is explained with the diagram shown in Figure 6.6.

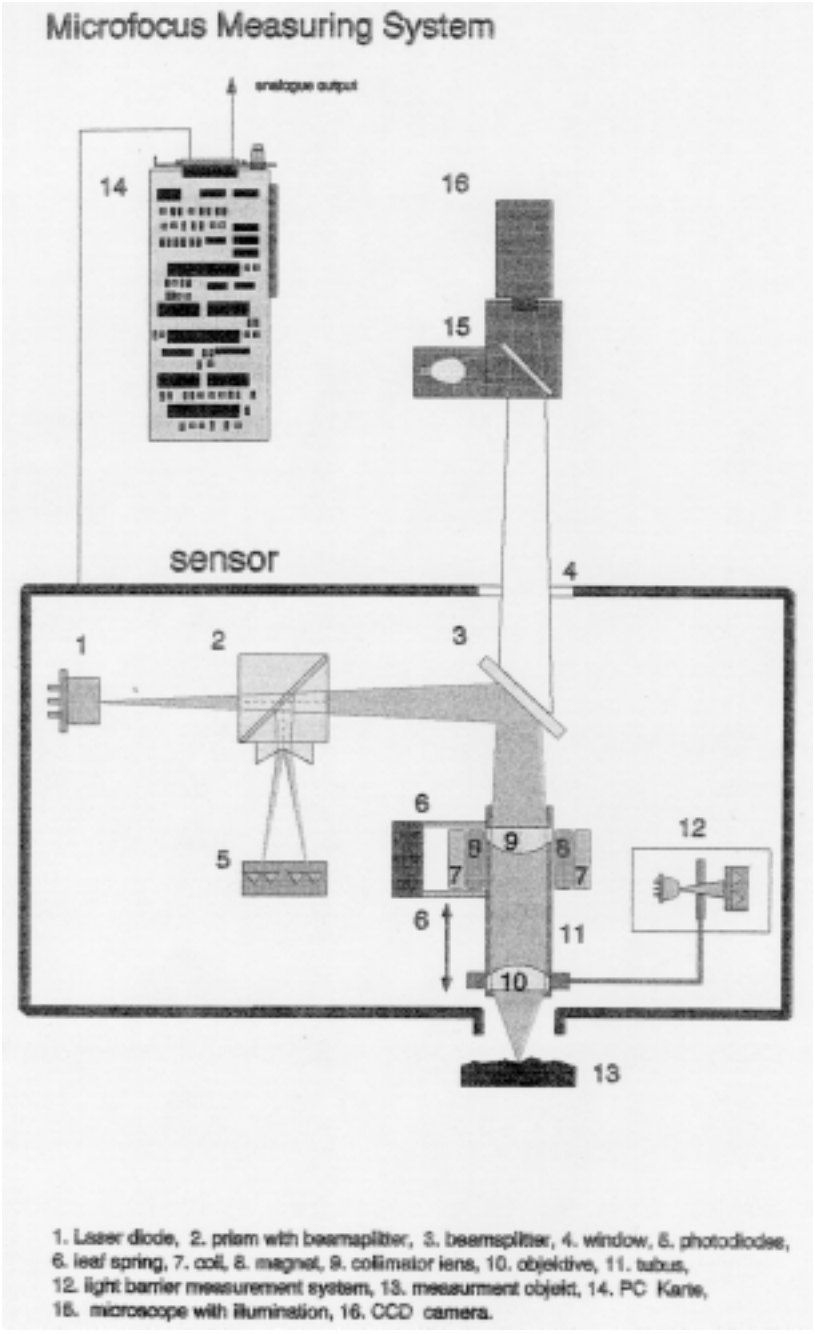

Figure 6.6. Diagram of the UBM Microfocus Measuring System used for the present analysis (From UBM User Manual)

The working principle, as explained here, is edited from the provided user manual. Infrared light from a semiconductor laser (1), with an output of 3mW, is focused to a spot by an objective lens (10). The spot diameter and sensor stand off are determined by the lens: the greater the numerical aperture, the smaller the beam diameter in the focus and the working distance. The light reflected by the object surface is directed by a beam splitter (3), through a prism (2), and is imaged as a pair of spots onto an arrangement of photodiodes (5). This is done in such a manner that when the objective lens is precisely at its focal distance from the

surface, both diodes are illuminated equally. If the distance between object surface and objective lens then changes by some amount, dA, the imaged focus point is shifted and the illumination of the photodiodes becomes unequal. This unequal illumination generates a focus error signal by means of a differential amplifier. To ensure exact measurements both the spot diameter and its light distribution across this diameter must be kept constant, which the sensors achieve by moving the objective lens as the lens/surface distance changes. A control circuit monitors the focus error signal and moves the objective lens accordingly (12). This lens movement is accomplished by a coil and magnet arrangement. The sensor is thus a null instrument because it is always set to the zero crossing of its characteristic.

The control circuitry can only function after the surface has been 'captured' by the sensor. This is achieved by sweeping the objective lens about its nominal stand off distance in a search run. When the lens focus position is within some distance of the surface, called the 'capture distance', the control is engaged and measurement can begin. The capture distance is a function of the object surface reflectivity. The control, therefore, cannot function at the beginning of a measurement procedure if the object surface/objective lens separation is more than this capture distance. When the capture distance condition is met approximately, the control engages and the full measuring range is established.

The measured data are stored on a PC (14) and analysed by the provided software. The software calculates a number of parameters, the definitions of which are given in Appendix E.

6.3.2 Description of the sample plates

Three different types of coatings were investigated: a Foul Release system applied by rollering, a Foul Release system applied by spraying, and a SPC coating scheme. Of the latter two types, 5 different surfaces were analysed and of the former type, 3 different surfaces. The surfaces were subdivided into the 5 series of experiments during which they were prepared.

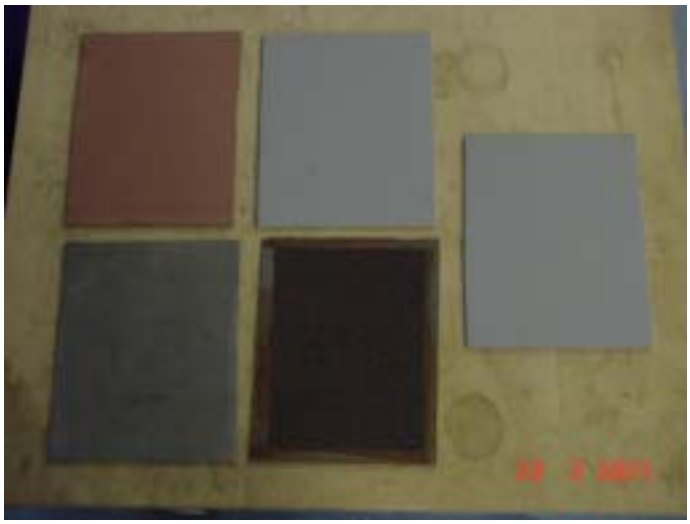

Figure 6.7. Sample plates (20cm by 25cm). Clockwise from bottom left: STEEL, SPC, FR, ROLL and SAND.

The most extensively studied series (no prefix) and the 'C-series' were prepared for the water tunnel experiments which have been set up to compare the boundary-layer velocity characteristics of flat plates fitted with different test surfaces by means of Laser Doppler Velocimetry (LDV), described in Chapter 5. Sample plates, made of mild steel and measuring 250mm by 200mm, were painted alongside the test plates and their surface characteristics as measured with the optical measurement. The plates, shown in Figure 6.7, are given the names STEEL, FR, SPC, ROLL and SAND for the first set of water tunnel tests (in conjunction with Section 5.2), and CFR and CSPC for the second set of tests at CEHIPAR (cf. Section 5.3). The sample plates of the first set of tests were immersed alongside the large coated test specimens and were analysed before and after testing. The measurements of the sample plates done after testing are known as the 'series-T' STEELT, FRT, SPCT and ROLLT (a suffix rather than a prefix has been used to indicate that they are from the same set of experiments). Unfortunately, the surface covered with sand grit (SAND) could not be analysed with the optical measurement system, which is restricted to a range of ±500μm. Measurements done with the BMT Hull Roughness Analyser of the SAND test specimen have shown that the AHR was 721 μm, with individual measurements of Rt50 exceeding 1200μm.

The 'SP-series' consists of 3 aluminium (250mm by 200mm) sample aluminium plates, which were painted alongside the 6.3m long aluminium plate used in the towing experiments (cf. Section 3.3): SPFR (Foul Release) and SPSPC (Tin-free SPC). Unfortunately, because of application problems and time constraints, the surface characteristics of the SPFR panels were not representative of the actual plate used in the experiments. As mentioned in Chapter 3,

Section 3.1, there had been some problems stripping off the SPC and it was not possible to obtain a satisfactorily smooth substrate for the Foul Release within the experimental time frame. In effect, the Foul Release was applied on an uneven surface, which had its repercussions on the final average hull roughness. Since it had been anticipated that the SPC could be stripped off easily exposing a smooth aluminium surface, the samples which were meant to represent the Foul Release surface were left unpainted, i.e. they were not painted with SPC and then stripped. Consequently, the final average roughness of the Foul Release on these sample plates was smoother than on the actual tested plate, and it was felt that the panels were not entirely representative of the tested surface.

Complementary to the Author's experimental work, rotor experiments were carried out by Pazouki (2001) using coated cylinders. The PVC cylinders were cut lengthwise after testing into 20mm wide strips. These measurements make up the 'R-series' and are given the names: RFR, RSPC and RROLL. These surfaces were visibly rougher due to sagging and problems with the application on the curved PVC substrate. Unlike the other sample plates, the roughness profiles come from surfaces which had been directly evaluated.

An summarising overview of the analysed sample plates is given in Table 6-1.

Table 6-1. Overview of the sample plates.

Name	Surface	Experimental Facility
SPC FR ROLL	SPC sprayed Foul Release sprayed Foul Release rollered	Emerson Cavitation Tunnel (before immersion)
SPCT FRT ROLLT	SPC sprayed Foul Release sprayed Foul Release rollered	Emerson Cavitation Tunnel (after immersion)
CSPC CFR	SPC sprayed Foul Release sprayed	CEHIPAR Cavitation Tunnel
SPSPC SPFR	SPC sprayed Foul Release sprayed	CEHIPAR Calm Water Tank
RSPC RFR RROLL	SPC sprayed Foul Release sprayed Foul Release rollered	Rotating Drum

6.3.3 Measurement procedure

The sample plates were put under the optical measurement system and six measurements were taken for each surface. According to the recommendations made by Medhurst (1989, 1990) an ensemble of 3 longitudinal and 3 transversal measurements taken at

a spacing of 20mm is statistically sufficient and allows the verification that the surface is isotropic.

The maximum evaluation length of the optical measurement system is 100mm. In order to compare with the published data, the sampling interval, which is equal to half the short wavelength cut-off length and which has a direct influence on the parameters (cf. Section 6.2), was taken as 50µm (or 20 samples/mm).

The measurements are characterised by specifying the cut-off length in mm and the sampling interval in µm respectively, e.g. 5&50.

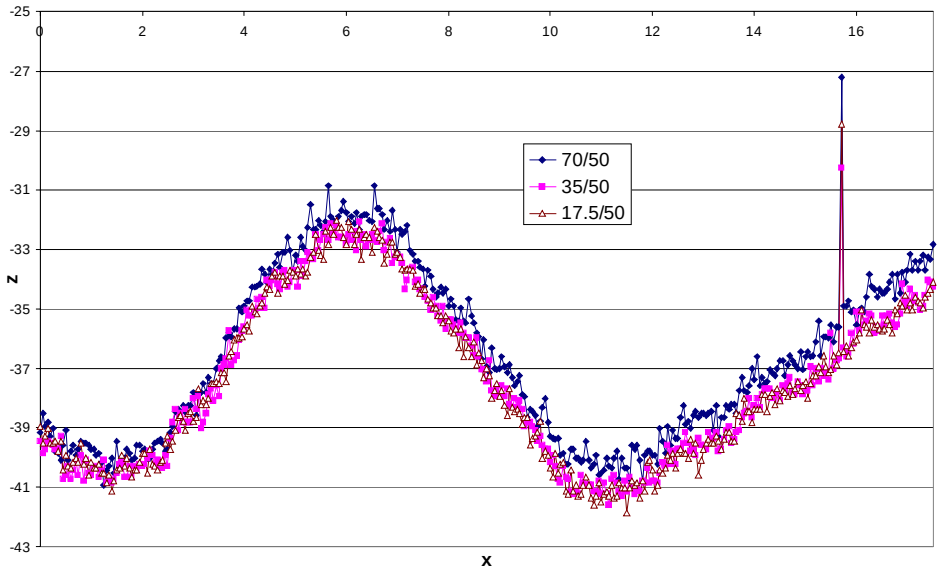

Figure 6.8. Repeatability of three different measurements over a 17.5mm long traverse

In order to guarantee perfect re-alignment of the traverse mechanism, the measurements in each direction were carried out uninterrupted for each surface. Figure 6.8 shows the repeatability of the measurements for three relocated measurements.

Each (unfiltered) measurement was stored on disk in ASCII format for subsequent analysis.

6.4 Analysis methodology

6.4.1 Filtering procedure

Before commencing the calculation of the roughness parameters of the stored profiles, the levelling or filtering procedure is considered. The procedure, which is necessary to separate the waviness of the sample plates from the actual roughness, has a profound influence on the roughness parameters. Whitehouse (1994, pp.20-45) gives a good description of the four filtering methods most used: straight lines, polynomials, low-pass filters and envelopes (see also Thomas, 1999, Chapter 6). A least-squares regression line was used to calculate the parameters in the pre-analysis with the UBM software given in Appendix E.2, where some details of the influence of this choice on the roughness parameters is also given.

Dey (1989), Medhurst (1989) and Byrne (1980) all used a low-pass filter which is a moving average 'boxcar method' for which the output is described by:

$$\overline{z}_i = z_i - \frac{1}{2M+1}\sum_{j=i-M}^{i+M} z_j$$

Medhurst (1990) recommends that the width of the window is set to $0.8L_c$, whereby L_c is the cut-off length and the width of window is equal to $\frac{2M+1}{N}L_c$, N being the number of ordinates over the cut-off length. Thus, the width of the window changes for selected cut-off lengths; e.g. for a sampling interval of 50μm, the width of the window for a cut-off length of 10mm would be 8mm, implying a 161-point moving average. However, as Byrne (1980) points out, if the smoothing length $(2M+1)\delta x$ is too long, the output of the filter contains only general trend or curvature. Byrne used a compromise between the relationship $2M+1 = \frac{L_c}{\delta x}$ and $2M+1 < L/12$, whereby L is the record or evaluation length. An 161-point moving-average window is larger than $L/12 = 116\delta x$ (whereby L = 70mm) and as Figure 6.9 shows, is not a satisfactory filter. It should be mentioned that a 161-part moving average can be applied when the evaluation length is increased to the maximum 100mm. However, because the effective wavelength cut-off for the present surfaces was estimated to lie between 2.5 and 5mm (cf. Section 7.3), the measurements were not repeated to calculate the parameters for Lc = 10mm. Figure 6.9 also shows a 41-point and 81-point moving average filter which is satisfactory for L_c = 2.5 and 5mm respectively.

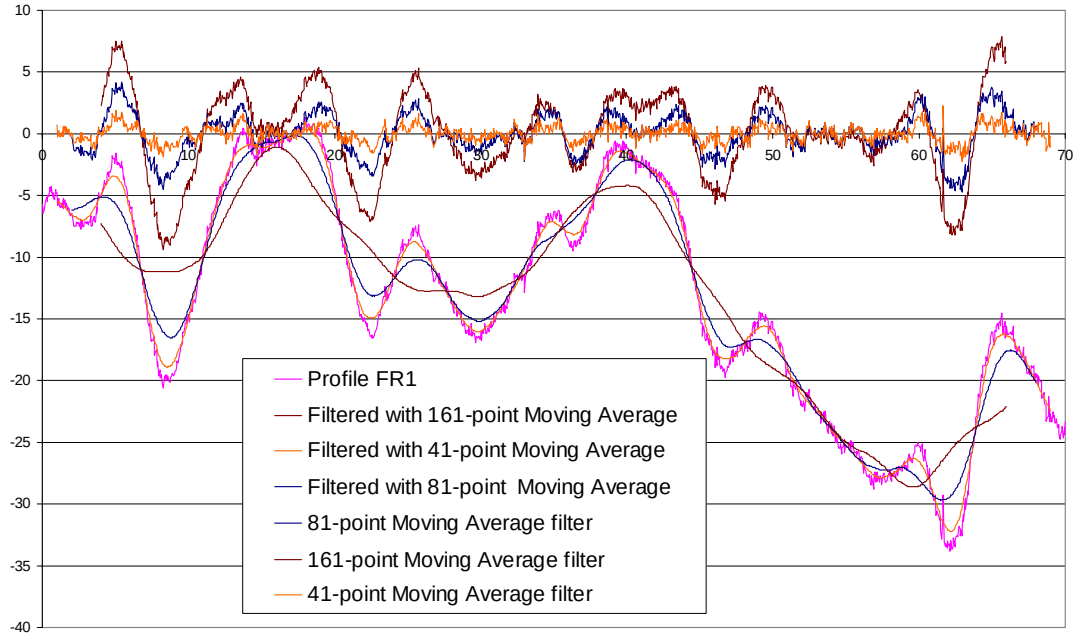

Figure 6.9. Comparison of different filters for a sample profile.

6.4.2 Analysis methodology

In order to compare roughness measurements with the data published by Dey (1989), the present data were filtered using a 41-point and 81-point moving average for cut-off lengths of 2.5 and 5mm respectively. The roughness parameters were then calculated according to the definitions given by Dey (1989) and Medhurst (1989).

The following analysis methodology was used to calculate the roughness parameters of all surfaces:

1. Six roughness profiles are measured over an evaluation length L = 70mm for each surface, three transverse and three lengthwise. The unfiltered data are saved as an ASCII file.
2. The UBM software is used to level the data with a 16^{th} order polynomial and to compute the roughness parameters in order to obtain a value of the Fractal Dimension FD.
3. The ASCII file is read into an Excel spreadsheet file. The data are levelled by a 41-point and 81-point boxcar moving average filter for the bandwidth limits 2.5/50 and 5/50 respectively. A filtered evaluation length of L = 50mm, consisting of 1001

samples, is analysed with both filters, subdivided in 20 and 10 intervals of cut-off length L_c = 2.5 and 5mm respectively.

4. The following parameters are calculated in the spreadsheets:

- Ra (in μm), the average of the average distance from the mean line over the respective intervals, which corresponds to the average of the average absolute height over the intervals
- Rq (in μm), the average of the standard deviations over the respective intervals
- Rt (in μm), the average of the distances between the highest peak and lowest trough over the respective intervals
- Sk and Ku are calculated using the discrete form of the equations for the skewness and kurtosis: $Sk = \frac{1}{N\sigma^3}\sum_{i=1}^{N} z_i^3$ and $Ku = \frac{1}{N\sigma^4}\sum_{i=1}^{N} z_i^4$ for each interval and then averaged
- Sa (in degrees), the mean absolute slope angle, is mathematically defined over the cut-off length as: $Sa = Tan^{-1}\left(\frac{1}{L_c}\int_0^{L_c}\left|\frac{dz}{dx}\right|dx\right)$. In its discrete form Sa is calculated as $Sa = \tan^{-1}\left(\frac{1}{N\delta x}\sum_{i=1}^{N}\dot{z}_i\right)$ whereby δx is the sampling interval and $\dot{z}_i$ is the first derivative of the profile height at the ith point, which is calculated using the seven-point Stirling formula: $\dot{z}_i = \frac{1}{60\delta x}\left(z_{i+3} - 9z_{i+2} + 45z_{i+1} - 45z_{i-1} + 9z_{i-2} - z_{i-3}\right)$. Thus, averaged over the intervals, the mean absolute slope angle was multiplied by 180/π to convert from radians into degrees.
- The average wavelength λa (in mm) can easily be calculated as $\lambda a = 2\pi Ra/\Delta a$. Δa is the mean absolute slope as defined by Whitehouse (1994): $\Delta a = \frac{1}{L_c}\int_0^{L_c}\left|\frac{dz}{dx}\right|dx$, i.e. Sa without performing the inverse tangent operation (which is negligible because of the small angles involved) and the conversion from radians into degrees.
- m_2(var) (in rad^2) is the average over the intervals of the average variance of the slope distribution and corresponds to Dey's (1989) $\sigma_{Sa}^2 = \frac{1}{N\delta x}\sum_{i=1}^{N}\dot{z}_i^2$.

- m_4(var) (in rad^4/μm^2)is the average over the intervals of the average variance of the curvature distribution, calculated by: $m_4(\text{var}) = \frac{1}{N\delta x}\sum_{i=1}^{N} \ddot{z}_i^2 = \sigma_c^2$ (Dey, 1989).

  The second derivative at the ith point was calculated using the seven-point Stirling formula (Whitehouse, 1994, p.215):

  $$\ddot{z}_i = \frac{1}{1860\delta x^2}\left(2z_{i+3} - 27z_{i+2} + 270z_{i+1} - 490z_i + 270z_{i-1} - 27z_{i-2} + 2z_{i-3}\right)$$

- De (in mm^{-1}), the density of extrema, was calculated as De = (#extrema)/(N·δx) whereby an extrema is encountered when: $|z_{i-1}| < z_i < |z_{i+1}|$
- Similarly, the density of zero-crossings, Dz (in mm^{-1}), is calculated as De = (#zero-crossings)/(N·δx) whereby a zero-crossing occurs when z_i and z_{i+1} are of opposite sign
- $\alpha(1) = De^2/Dz^2$ (Longuet-Higgins, 1957)
- $\alpha(3) = m_0(\text{var})\, m_4(\text{var})/\, m_2^2(\text{var})$ whereby $m_0(\text{var}) = Rq^2$

5. The roughness parameters are calculated for both sets of levelled data and averaged for the six roughness profiles (cf .Tables)
6. In addition, the levelled data are put in a Labview "Virtual Instrument" which calculates the power spectrum via a Fast Fourier Transformation, the spectral moments, the autocorrelation function and the correlation length for the selected profiles, so that the additional parameters are tabulated:

- m_0 (in μm^2)
- m_2 (in rad^2)
- m_4 (in rad^4/μm^2)
- $\alpha = m_0 m_4/m_2^2$
- $\tau_{0.5}$ (in mm)
- $\tau_{1/e}$ (in mm)
- R(0), the value of the autocorrelation function at $\tau = 0$, and theoretically equal to $m_0 = Rq^2$

6.5 Analysis of the different surfaces.

6.5.1 Analysis and comparison of the roughness parameters

The roughness parameters for each coating are presented in Table 6-2 to Table 6-4. The Tables are subdivided in four parts according to their type and calculation method. The definitions used for the calculations and the dimensions of the parameters have been mentioned in Section 6.4.2. Plots of each analysed roughness profile are shown in Appendix E.2 where they are sorted according to series and surface type

Table 6-2. Roughness parameters of the measured (Sprayed) Foul Release surfaces

	FR		FRT		CFR		SPFR		RFR			
Average	5&50	2.5&50	5&50	2.5&50	5&50	2.5&50	5&50	2.5&50	5&50	2.5&50		
Ra	1.03	0.51	1.08	0.57	3.40	1.26	0.39	0.28	3.28	1.92	Directly calculated from filtered roughness profiles	Excel spreadsheets
Rq	1.15	0.59	1.29	0.76	3.91	1.32	0.47	0.39	4.20	2.47		
Rt	4.89	2.68	6.76	3.97	13.80	4.94	3.22	2.26	18.85	10.71		
Sk	0.17	1.37	1.52	6.14	-0.01	0.56	5.70	10.10	4.82	12.68		
Ku	6.63	22.39	17.37	86.94	4.19	12.62	132.69	263.79	67.12	243.30		
Sa	0.36	0.36	0.44	0.44	0.46	0.39	0.32	0.32	0.81	0.77		
λa	1.03	0.52	0.90	0.47	2.60	1.16	0.43	0.31	1.57	0.95		
m2 (var)	7.87E-05	7.71E-05	2.08E-04	2.10E-04	1.52E-04	1.23E-04	9.59E-05	9.57E-05	1.32E-03	1.33E-03		
De	9.82	9.75	9.72	9.64	9.99	9.96	9.56	9.27	10.03	9.90		
Dz	2.51	5.12	2.67	4.98	0.91	2.23	6.13	8.82	1.50	2.51		
α(1)	16.18	3.79	15.58	3.92	139.00	21.13	2.48	1.12	53.11	17.28		
m4 (var)	2.90E-07	2.90E-07	6.60E-07	6.61E-07	4.04E-07	4.07E-07	3.65E-07	3.64E-07	1.77E-06	1.80E-06		
α(3)	66.90	17.79	32.81	10.50	281.28	53.58	10.42	7.14	86.04	29.59		
FD	1.29	1.31	1.31	1.31	1.13	1.13	1.41	1.42	1.23	1.23	Fractal	UBM
α(2)	23.75	9.00	23.51	9.03	15.05	4.48	20.43	8.96	23.23	7.94		
τ0.5	0.740	0.199	0.580	0.095	0.766	0.603	0.109	0.028	0.431	0.268	Correlation	Labview
τ1/e	0.909	0.320	0.785	0.136	0.877	0.715	0.293	0.035	0.526	0.339		
R(0)	1.74	0.51	2.11	0.83	19.36	2.80	0.33	0.22	26.28	13.95		
m0	1.70	0.43	1.88	0.80	18.20	3.68	0.29	0.18	26.23	13.92	Power spectra	
m2	1.43E-04	1.39E-04	3.46E-04	4.45E-04	1.39E-03	9.96E-04	2.01E-04	2.00E-04	2.07E-03	2.02E-03		
m4	3.16E-07	3.12E-07	7.05E-07	9.46E-07	2.74E-06	1.88E-06	4.53E-07	4.52E-07	2.74E-06	2.69E-06		
α	30.77	8.32	15.51	4.83	91.25	21.90	4.11	2.09	34.83	11.58		
h	7.02E-03	4.36E-04	7.62E-03	1.56E-03	7.42E-01	3.66E-02	2.24E-04	9.96E-05	1.22E+00	4.35E-01		

Table 6-3. Roughness parameters of the measured Rollered Foul Release surfaces

	ROLL		ROLLT		RROLL			
Average	5&50	2.5&50	5&50	2.5&50	5&50	2.5&50		
Ra	2.57	1.11	2.03	0.87	7.24	4.00	Directly calculated from filtered roughness profiles	Excel spreadsheets
Rq	3.03	1.26	2.36	1.05	8.62	4.69		
Rt	12.01	5.03	9.73	4.64	33.14	17.68		
Sk	3.92	13.77	3.98	10.81	-0.16	0.00		
Ku	41.19	215.86	53.53	166.02	6.07	10.41		
Sa	0.46	0.43	0.45	0.43	1.28	1.10		
λa	1.95	0.87	1.56	0.71	2.03	1.32		
m2 (var)	2.88E-04	2.63E-04	1.81E-04	1.63E-04	1.65E-03	1.49E-03		
De	9.88	9.89	9.85	9.72	10.25	10.17		
Dz	1.24	3.45	1.86	4.43	0.99	1.47		
α(1)	99.45	11.17	34.90	5.22	111.14	48.84		
m4 (var)	3.27E-07	3.25E-07	3.87E-07	3.89E-07	2.90E-06	2.91E-06		
α(3)	134.19	24.42	97.14	20.54	89.10	32.50		
FD	1.18	1.21	1.19	1.19	1.16	1.16	Fractal	UBM
α(2)	20.47	7.46	21.03	6.89	18.89	5.91		
τ0.5	0.676	0.378	0.708	0.256	0.507	0.343	Correlation	Labview
τ1/e	0.797	0.455	0.850	0.344	0.588	0.408		
R(0)	22.97	8.73	15.89	4.38	88.81	28.99		
m0	22.92	8.68	15.84	4.45	88.72	28.96	Power spectra	
m2	3.86E-04	3.50E-04	3.28E-04	2.75E-04	2.80E-03	2.59E-03		
m4	3.80E-07	3.62E-07	5.24E-07	4.86E-07	4.32E-06	4.29E-06		
α	79.22	22.11	53.36	17.23	51.23	20.05		
h	8.64E-01	1.67E-01	8.28E-01	9.29E-02	1.39E+01	1.48E+00		

Table 6-4. Roughness parameters of the measured Tin-free SPC surfaces

	SPC		SPCT		CSPC		SPSPC		RSPC			
Average	5&50	2.5&50	5&50	2.5&50	5&50	2.5&50	5&50	2.5&50	5&50	2.5&50		
Ra	3.64	3.41	3.66	3.39	2.48	2.33	4.57	4.38	3.24	2.71	Directly calculated from filtered roughness profiles	Excel spreadsheets
Rq	4.57	4.22	4.77	4.33	3.10	2.92	5.69	5.41	4.04	3.38		
Rt	22.24	17.98	24.88	19.42	15.57	13.14	27.38	23.24	19.61	14.86		
Sk	0.60	0.40	2.18	1.89	0.18	0.10	0.04	0.04	0.35	0.15		
Ku	7.85	6.36	18.40	17.45	3.48	3.28	3.07	3.13	4.39	5.59		
Sa	2.82	2.82	2.99	2.99	2.44	2.44	3.35	3.35	2.21	2.20		
λa	0.47	0.44	0.44	0.41	0.37	0.34	0.49	0.47	0.53	0.44		
m2 (var)	3.87E-03	3.87E-03	4.60E-03	4.62E-03	2.87E-03	2.88E-03	5.42E-03	5.44E-03	2.43E-03	2.43E-03		
De	9.65	9.69	9.72	9.66	9.52	9.62	9.77	9.83	9.57	9.56		
Dz	5.49	5.65	5.67	6.38	6.64	7.28	4.73	5.01	4.42	5.31		
α(1)	3.12	2.95	3.07	2.32	2.06	1.75	4.34	3.90	4.87	3.32		
m4 (var)	8.45E-06	8.46E-06	9.68E-06	9.65E-06	7.55E-06	7.54E-06	1.11E-05	1.11E-05	5.26E-06	5.27E-06		
α(3)	12.25	10.35	10.52	8.57	8.77	7.73	12.18	10.97	14.57	10.27		
FD	1.60	1.60	1.58	1.58	1.66	1.66	1.57	1.57	1.57	1.57	Fractal	UBM
α(2)	12.86	7.39	13.58	7.57	11.11	6.91	13.92	7.67	14.09	7.67		
τ0.5	0.118	0.092	0.114	0.088	0.051	0.044	0.106	0.094	0.135	0.084	Correlation	Labview
τ1/e	0.161	0.125	0.159	0.122	0.074	0.058	0.145	0.122	0.195	0.112		
R(0)	22.72	19.42	26.61	22.91	9.78	8.59	32.82	30.00	17.06	12.03		
m0	22.69	19.39	26.57	22.87	10.01	8.57	32.78	29.96	17.04	12.02	Power spectra	
m2	7.22E-03	7.25E-03	8.32E-03	8.34E-03	6.23E-03	5.89E-03	9.77E-03	9.79E-03	4.51E-03	4.51E-03		
m4	1.28E-05	1.29E-05	1.45E-05	1.45E-05	1.23E-05	1.15E-05	1.68E-05	1.68E-05	7.98E-06	7.98E-06		
α	5.72	4.84	5.52	4.70	3.20	2.86	5.75	5.24	6.63	4.68		
h	9.41E-01	6.83E-01	1.36E+00	1.02E+00	1.98E-01	1.44E-01	1.85E+00	1.55E+00	5.26E-01	2.61E-01		

Of the sprayed Foul Release surfaces, SPFR surface is the 'smoothest' (a general denomination which implies lower values for the amplitude parameters) and RFR the roughest. Of the SPC surfaces, the CSPC surface is the smoothest and RSPC the roughest. The roughness parameters of the Foul Release surfaces show more variation than the SPC surfaces.

It is clear that in terms of the amplitude parameters, the sprayed Foul Release surfaces are generally much better than the rollered Foul Release or SPC surfaces, which between themselves are of the same order.

If one compares both types of Foul Release application, one notices that the slope and particularly the curvature parameters agree well, as do the correlation lengths and fractal dimension. This indicates that the application method does not significantly change the texture of the surface. Typical plots of the autocorrelation function and of the power spectrum are shown for both a sprayed and rollered Foul Release surface in Figure 6.10 and Figure 6.11. The correlation lengths $\tau_{1/e}$ lie between 0.5 and 1mm for both sets of surfaces, except for SPFR which is clearly an extremely well applied (sample) surface. Figure 6.10 shows that the autocorrelation function of a Foul Release surface typically is an exponential modulated by a sinusoid, indicating the important contribution of long wavelengths in the profile. This is confirmed by the power spectra plots in Figure 6.11, which show that the spectra decay very rapidly with wavenumber. The maximum wavenumber shown in the abscissa is ω_h = 62.83rad/mm which is equal to $2\pi/\lambda_N$, whereby λ_N is the Nyquist wavelength which is equal

to twice the sampling interval 50µm. The plots shows that for both surfaces wavenumbers larger than 4rad/mm (or wavelengths < 1.57mm) contribute less than 10% (15-20% in the case of the 2.5&50 bandwidth limits) of the total power. Clearly, long wavelengths are dominant in a typical Foul Release profile.

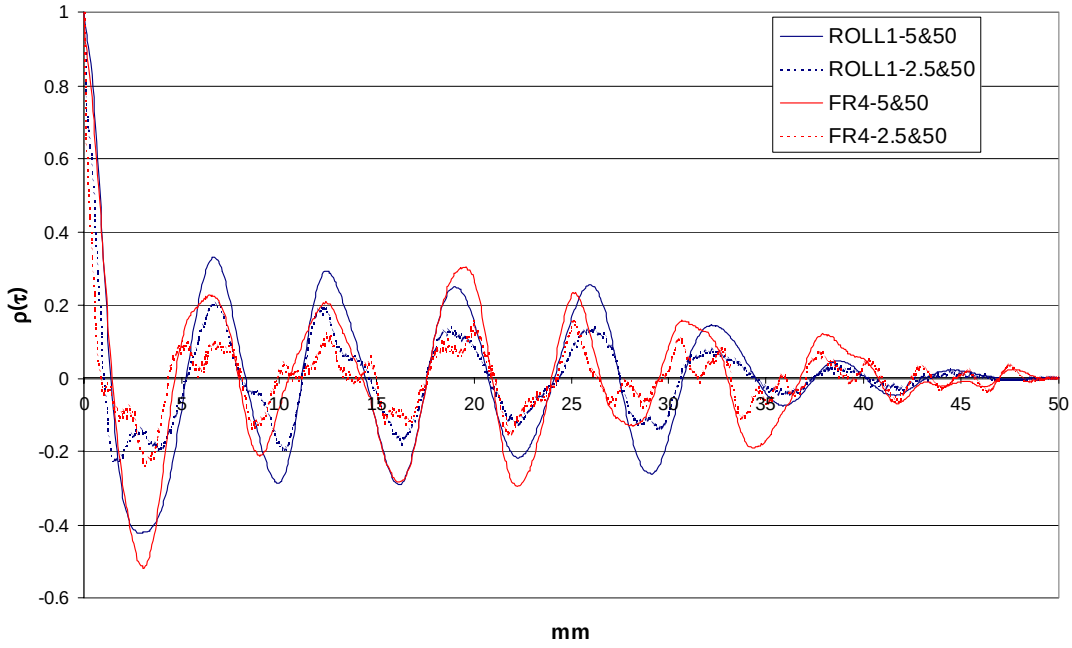

Figure 6.10. Autocorrelation functions for two typical Foul Release profiles, applied both by rollering and by spraying.

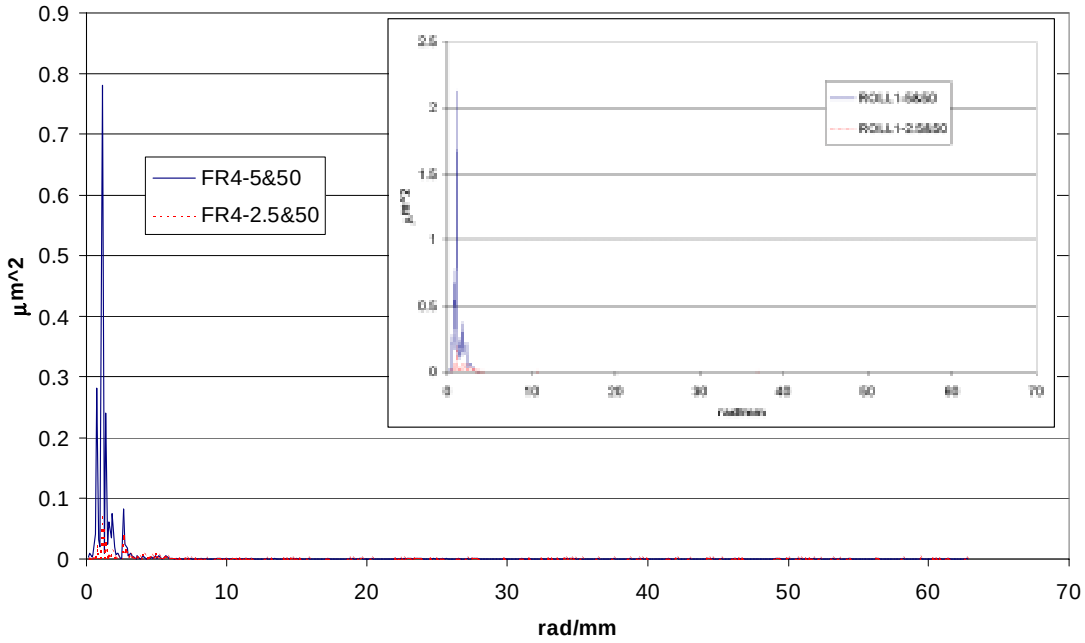

Figure 6.11. Power spectra for a typical sprayed Foul Release profile for bandwidth limits 5/50 and 2.5/50. The inset shows the power spectra for a typical rollered Foul Release profile.

The roughness amplitudes however, do significantly depend on the application method and it is clear that the rollered Foul Release surface is much more leptokurtic. If one looks at the roughness profiles in Appendix 6, one notices that large peaks occur much more frequently on the rollered Foul Release surfaces. It is expected that this greater number of high peaks present on a rollered Foul Release will engender higher drag.

Whereas the SPC surface displays comparable amplitude parameters to the rollered Foul Release surfaces, its texture is significantly different from it. Not only is the fractal dimension, on the order of 1.57-1.67, much higher than the fractal dimensions of the Foul Release surfaces, between 1.1 and 1.3 (SPFR is not considered typical in this respect), so are the mean absolute slopes angles, which typically differ by a factor 5 to 10.

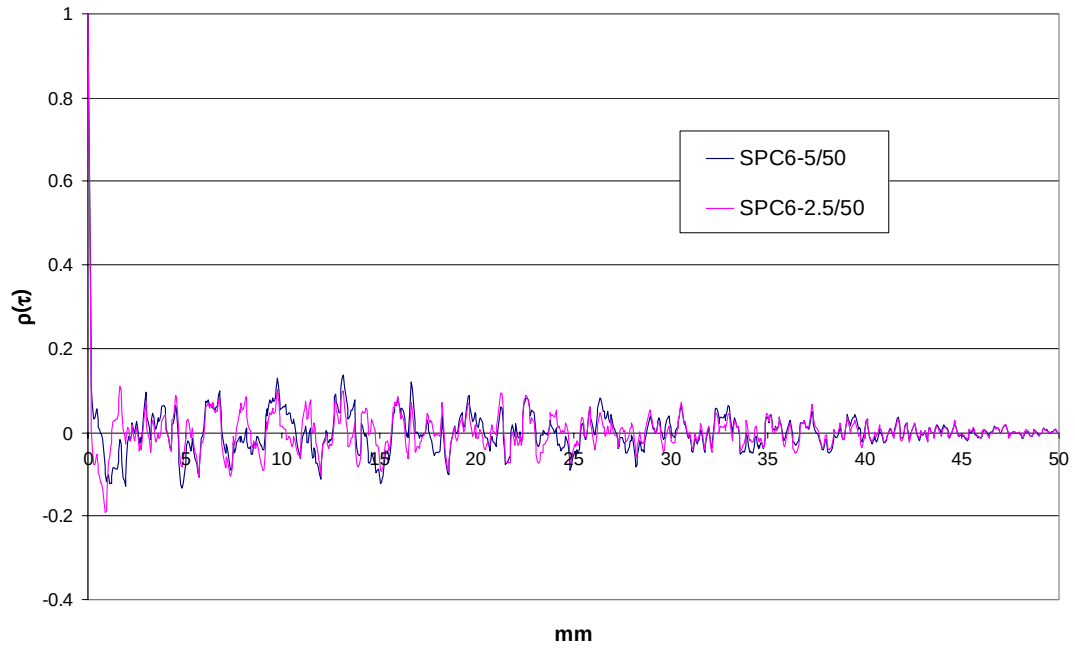

Figure 6.12. Autocorrelation function for a typical SPC profile.

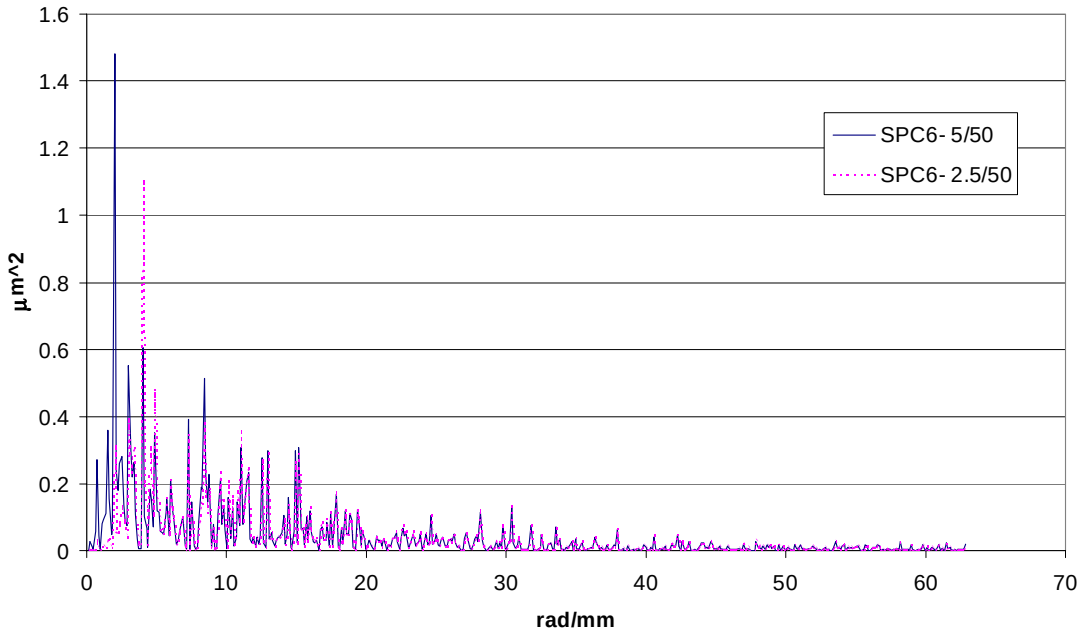

Figure 6.13. Power spectra for a typical SPC profile.

The differences in texture become even clearer when one looks at the autocorrelation function and the power spectra, which are shown for a typical SPC profile in Figure 6.12 and

Figure 6.13 respectively. Compared with Figure 6.10 and Figure 6.11, short wavelengths are clearly more important for the SPC surface, and long wavelengths no longer dominate the roughness profile. This is also clear in parameters like the density of zero-crossings Dz, and the average wavelength λa.

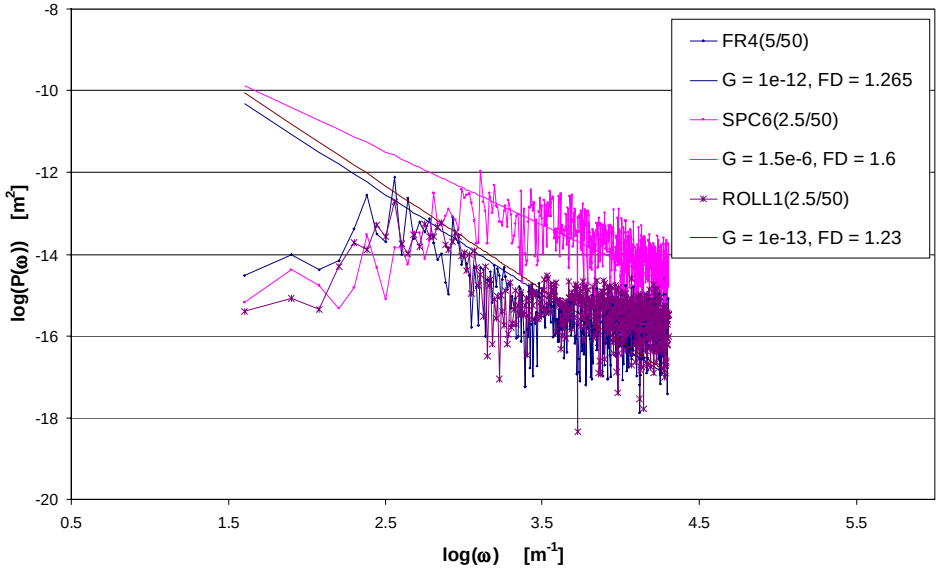

Figure 6.14. Spectral profiles for the same surfaces in log-log co-ordinates.

Figure 6.11 and

Figure 6.13 can be re-plotted in log-log co-ordinates in order to determine the Fractal Dimension and the topothesy G using Equation 6.8. Figure 6.14 shows the re-plots for the same surfaces, along with G and FD determined using Equation 6.8 for each surface. The SPC surface follows the power law well, but the Foul Release surfaces exhibit some deviation towards the higher frequencies. According to Thomas (1999) and Majumdar and Bhushan (1990) some surfaces exhibit multifractal behaviour where there are distinct spectral regions with different Fractal Dimensions for each region. There seems no particular reason why Foul Release surfaces would exhibit multifractal behaviour. Indeed, this behaviour does not seem to be typical for the Foul Release surface, sometimes it occurs and sometimes not. Note that all surfaces exhibit deviation from the power law for the lowest frequencies. Only 501 spectral samples were calculated from the 1001 of the roughness profile and obtaining more spectral samples could enhance the accuracy of the calculations. Additionally, extending the bandwidth limits would give a larger frequency which is rather restricted here to evaluate Equation 6.8. Determining the Fractal Dimension directly from the slope observed in Figure 6.14 would be difficult and inaccurate. The Fractal Dimensions used in Figure 6.14 were those obtained from the UBM roughness analysis software by the method explained in Appendix E.1. They seem to represent the correct slopes in Figure 6.14 fairly well. The topothesy is several orders of magnitude smaller for the Foul Release surfaces than for the SPC surfaces. Since the Fractal Dimension does not change much for one type of material (i.e. Foul Release and SPC), the topothesy will generally increase as the roughness amplitude parameters increase. However, a small change in the Fractal Dimension has a large effect on the topothesy. It is crudely estimated from Equations 6.9-6.11 that the topothesy is of the order 10^{-13}-10^{-12}m for the Foul Release surfaces and of the order 10^{-7}-10^{-6}m for the SPC surface (for comparison, Majumdar and Bhushan (1990) obtained for a stainless steel sample FD = 1.5 and G = $0.98 \cdot 10^{-10}$m, suggesting that the STEEL sample analysed in Appendix E.2 is rougher than theirs).

6.5.2 Build-up of the coating schemes

Two extra sample plates, shown in Figure 6.15 and Figure 6.16, were painted in such a way that the build-up of the coating scheme could be analysed with respect to the roughness characteristics.

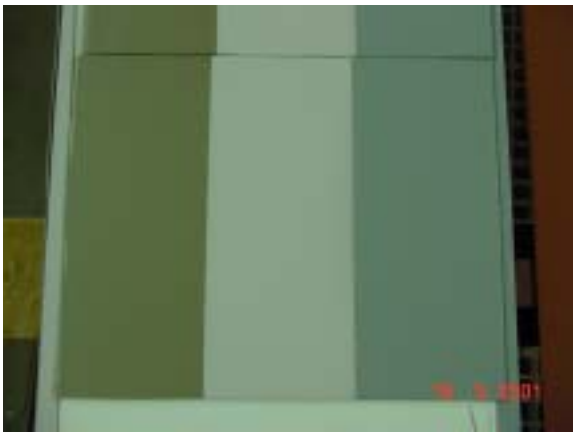

Figure 6.15. Composition of the CFR scheme: (from left to right) primer, primer + tiecoat, primer + tiecoat + topcoat = final scheme

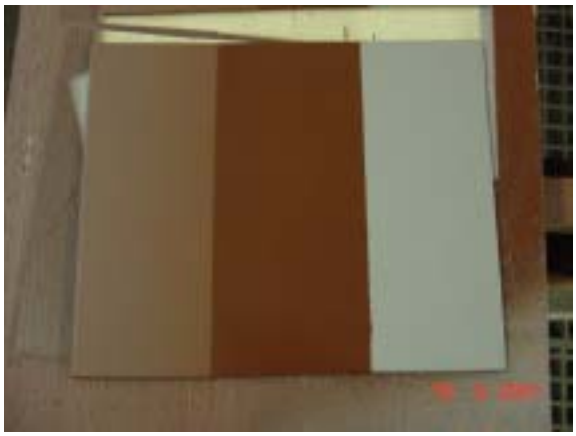

Figure 6.16. Composition of the CSPC scheme: (from right to left): primer, primer + 1 coat of SPC, primer + 2 coats of SPC = final scheme

Table 6-5 and Table 6-6 show the analysed roughness characteristics for both coating schemes. In addition, the profiles are plotted graphically in Appendix E.3.

Table 6-5. Roughness characteristics for the different coats of the CFR scheme

CFR	Primer		Primer+Tiecoat		Primer+Tie+Topcoat	
Average	5&50	2.5&50	5&50	2.5&50	5&50	2.5&50
Ra	3.05	2.15	2.95	1.66	3.40	1.26
Rq	3.80	2.70	3.54	1.98	3.91	1.32
Rt	17.60	11.99	15.10	8.34	13.80	4.94
Sk	1.73	2.95	0.20	0.31	-0.01	0.56
Ku	21.73	39.45	4.23	4.83	4.19	12.62
Sa	1.94	1.94	0.90	0.86	0.46	0.39
λa	0.57	0.40	0.55	0.40	45.43	20.24
m2 (var)	1.94E-03	1.92E-03	4.52E-04	4.21E-04	1.52E-04	1.23E-04
De	9.79	9.79	9.73	9.53	9.99	9.96
Dz	4.41	6.63	2.55	3.73	0.91	2.23
α(1)	4.93	2.19	21.65	7.39	139.00	21.13
m4 (var)	5.64E-06	5.62E-06	1.00E-06	1.00E-06	4.04E-07	4.07E-07
α(3)	22.07	11.29	66.08	23.24	281.28	53.58
FD	1.58	1.58	1.26	1.26	1.13	1.13
α(2)	13.51	7.56	23.67	8.45	15.05	4.48

Table 6-6. Roughness characteristics for the different coats of the CSPC scheme

CSPC	Primer		Primer+1coat		Primer+2coats	
Average	5&50	2.5&50	5&50	2.5&50	5&50	2.5&50
Ra	3.14	2.31	1.68	1.23	2.48	2.33
Rq	3.87	2.88	2.11	1.53	3.10	2.92
Rt	18.32	12.77	9.95	6.66	15.57	13.14
Sk	0.36	0.51	0.90	1.43	0.18	0.10
Ku	4.06	5.78	9.86	14.15	3.48	3.28
Sa	2.18	2.17	0.90	0.89	2.44	2.44
λa	0.52	0.38	0.54	0.38	6.38	6.00
m2 (var)	2.34E-03	2.32E-03	4.19E-04	4.16E-04	2.87E-03	2.88E-03
De	9.70	9.61	9.81	9.87	9.52	9.62
Dz	4.81	6.99	3.64	4.94	6.64	7.28
α(1)	4.12	1.89	7.59	4.00	2.06	1.75
m4 (var)	7.53E-06	7.51E-06	9.75E-07	9.80E-07	7.55E-06	7.54E-06
α(3)	20.79	11.54	24.86	13.39	8.77	7.73
FD	1.59	1.59	1.53	1.53	1.66	1.66
α(2)	13.27	7.50	15.39	8.04	11.11	6.91

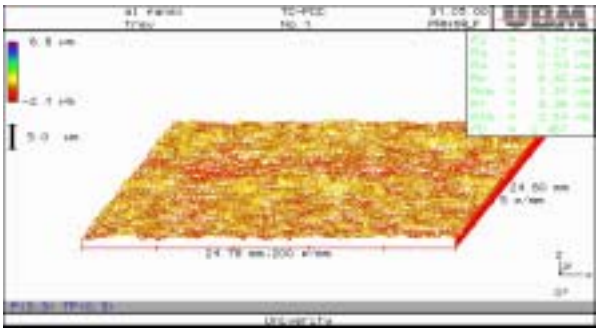

Figure 6.17. Surface profilogram of (SP) Aluminium

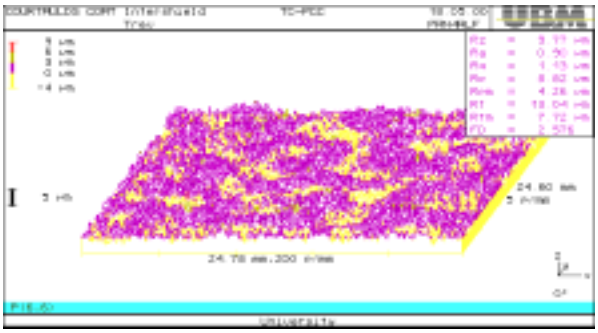

Figure 6.18. Surface profilogram of (SP) Primer

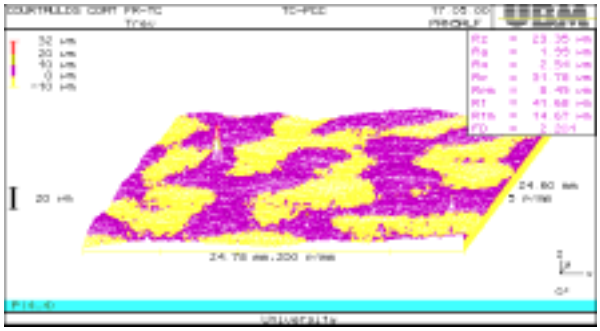

Figure 6.19. Surface profilogram of (SP) Primer + FR Tiecoat

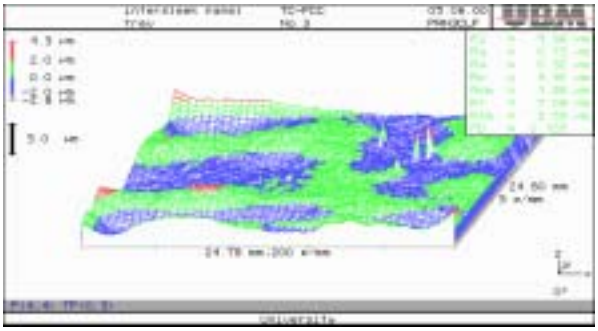

Figure 6.20. Surface profilogram of SPFR

Some striking differences are revealed between the two schemes. The Foul Release scheme starts with a relatively rough anticorrosive primer, but the amplitude parameters are decreased by each subsequent coat. The tiecoat brings the mean absolute slope angle down from 1.94° to 0.90°, which is further brought down to the typical values of the final Foul Release scheme of about 0.39°. A similar trend occurs for the fractal dimension FD, which

decreases from 1.58 to 1.26 and then to 1.13. This indicates the very good spreading characteristics of the silicone elastomer. The tiecoat alone is already quite effectively levelling out the sharp characteristics of the anticorrosive primer, the character of which in terms of roughness is not unlike the SPC.

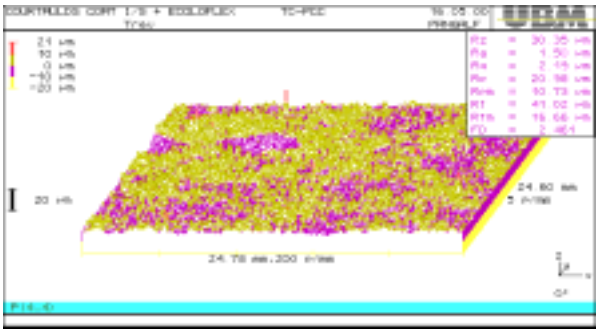

Figure 6.21. Surface profilogram of (SP) Primer + 1 coat of SPC

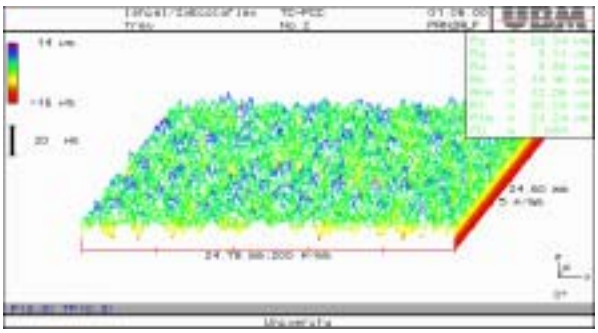

Figure 6.22. Surface profilogram of SPSPC.

Rather surprisingly, this also occurs when a first coat of Tin-free SPC is applied over the anticorrosive primer. The primers for both schemes were different, but in terms of roughness characteristics very similar (e.g. Ra, Rt, Sa, FD). However, the anticorrosive primer is relatively rough so that it is likely that the SPC gets a good 'grip' on this surface resulting in a 'very smooth' application of the SPC coating: the peaks are levelled out, Sa has decreased and the amplitude parameters have become significantly lower. However, the fractal dimension does not come down by much, indicating that the short-wavelength roughness is still prominent, whereas this was largely taken out by the tiecoat (compare the respective Figures E.18 and E.19 in Appendix E.3). This interpretation is also supported by the roughness histograms in Figure 3.6, where the first coat of SPC is applied on a smoother primer. The SPC coat cannot improve on this, the 'grip' is less good and the amplitude parameters will logically increase. The main observation, however, is that the second coat of SPC always increases the amplitude parameters and the mean absolute slope angle.

One should bear in mind that this represents best practice for a SPC application, whereas the Foul Release application was good, but not excellent (cf. SPFR , FR). Thus, it is interesting to see that both schemes have approximately the same average wavelength λa, but by relatively different contributions. The CSPC scheme has a very low average amplitude Ra and a low mean absolute slope angle Sa for a SPC paint, but much higher than the Sa values typical for a Foul Release scheme. The CFR scheme has a higher Ra, but the same λa because of the lower Sa.

Figure 6.17 to Figure 6.22 show surface profilograms of sample plates of the SP-series, where both antifouling schemes were applied on the same primer. It is clear that the same observations apply.

6.5.3 Comparison with the surfaces analysed by Dey (1989)

The results for the SPC surfaces were compared with the characteristics of the different painted surfaces tabulated in Dey's thesis. Unfortunately, Dey does not give much information on the actual paints that were used in the analysis. In reading through his Tables 3.2 to 3.34 (Dey, 1989), one notices immediately the enormous variations between the different surfaces, as it was the purpose of his analysis to investigate a very wide range of rough hull surfaces. It is interesting to compare the surfaces SK1, SK2 and SK3, which investigate the effect good to careless application can have on the roughness parameters. The same can be said of the series PL.

Table 6-7 presents a selection of the parameters (Ra, Rq, Rt, Sa, $\tau_{1/e}$, $\sqrt{m_0}$, $\sqrt{m_2}$, $\sqrt{m_4}$ and α) of all the reported surfaces at 5&50, in addition with the surfaces analysed presently.

It is obvious from the low values for the amplitude parameters that all the surfaces analysed presently are 'very smooth'. Even though they are smoother, the SPC surfaces compare in many respects well with Dey's surface SK1 (Dey, 1989, Table 3.3) described as "good finish as a result of very high quality spraying". They also compares reasonably well with surface PL2 (Dey, 1989, Table 3.12) which was originally analysed by Walderhaug (1986), and with the "Anticorrosive" surface (Dey, 1989, Table 3.20), originally tested by Todd (1951).

In comparing the Foul Release surfaces with Dey's analysed surfaces, good agreement in many ways is observed with Todd's "Cold-Plastic" surface (Dey, 1989, Table 3.19). In terms of amplitude parameters, they are 'smoother' than the mentioned "Anticorrosive" surface, which in turn agreed quite well with the present surface.

Table 6-7. Summarised comparison of the different surfaces.

Surface (5/50)	Ra (μm)	Rq (μm)	Rt (μm)	Sa (degrees)	τ1/e (mm)	m0^0.5 (μm)	m2^0.5 (rad)	m4^0.5 (rad^2/μm)	α	
SK	13.07	17.03	45.7	1.73	0.63	1.77E+01	1.21E-01	4.84E-03	38.56	Dey (1989)
SK1	6.34	7.96	32.83	2.39	0.43	8.19E+00	7.48E-02	3.11E-03	20.22	
SK2	18.05	23.2	64.69	2.32	0.63	2.39E+01	1.66E-01	6.71E-03	35.95	
SK3	29.94	38.54	115.84	4.33	0.58	3.92E+01	2.31E-01	9.01E-03	45.36	
JOHANSON	9.92	12.92	38.38	1.43	0.53	1.33E+01	8.49E-02	3.30E-03	37.63	
R550	45.91	59.38	209.68	11.29	0.45	6.01E+01	4.02E-01	1.42E-02	27.97	
R420	27.24	35.01	113.83	4.51	0.55	3.55E+01	2.55E-01	1.03E-02	34.24	
R345	31.88	41.95	140.97	5.16	0.51	4.26E+01	2.87E-01	1.22E-02	38.04	
R253	14.87	20.02	73.08	3.34	0.44	2.03E+01	1.56E-01	5.77E-03	23.48	
R173	15.77	19.95	72.97	3.63	0.49	2.03E+01	1.54E-01	6.64E-03	32.62	
PL2	10.05	12.56	41.56	1.8	0.43	1.26E+01	7.75E-02	2.79E-03	34.24	
PL3	12.9	16.8	52.04	2.17	0.48	1.69E+01	9.00E-02	3.21E-03	44.71	
PL4	20.95	25.92	79.95	2.72	0.57	2.59E+01	1.28E-01	4.70E-03	55.88	
PL5	12.37	15.91	48.26	2.08	0.46	1.59E+01	1.04E-01	3.91E-03	32.87	
PL6	23.45	29.77	95.75	4.26	0.52	2.98E+01	1.82E-01	6.81E-03	37.9	
PL7	67.18	83.1	259.75	12.18	0.42	8.32E+01	5.79E-01	2.14E-02	28.71	
ZINC-CHROMATE	3.62	4.79	20.95	1.42	0.21	5.20E+00	4.47E-02	1.34E-03	10.25	
COLD-PLASTIC	5.58	7.1	23.27	0.96	0.5	7.21E+00	4.58E-02	1.70E-03	35.47	
ANTICORROSIVE	8.49	10.89	46.29	3.28	0.22	1.12E+01	1.02E-01	3.24E-03	11.73	
HOT-PLASTIC	46.03	59.01	199.03	8.39	0.43	6.28E+01	4.24E-01	1.53E-02	29.18	
SIEW-S1	15.27	19.3	67.99	3.04	0.46	1.95E+01	1.10E-01	3.66E-03	34.31	
SIEW-S2	20.03	25.47	74.93	2.7	0.67	2.57E+01	1.32E-01	4.86E-03	53.7	
SIEW-S3	22.12	28.13	83.84	2.96	0.6	2.87E+01	1.83E-01	7.15E-03	41.72	
SIEW-S4	20.51	26.25	76.82	2.82	0.58	2.63E+01	1.68E-01	6.54E-03	40.92	
SIEW-S5	16.28	20.34	63.64	2.44	0.57	2.08E+01	1.05E-01	3.82E-03	50.75	
SIEW-S6	21.07	26.07	75.48	2.87	0.55	2.64E+01	1.74E-01	6.77E-03	39.72	
RS-LIM	141.69	174.59	710.68	44.43	0.19	1.75E+02	1.92E+00	6.80E-02	10.4	
RWS-LIM	225.91	277.78	1023.7	49.38	0.49	2.78E+02	2.33E+00	8.40E-02	18.54	
RW-LIM	166.89	196.56	501.04	17.41	0.68	1.97E+02	1.41E+00	5.74E-02	31.96	
SARABCHI-A	83.53	113.7	379.64	16.28	0.5	1.21E+02	8.47E-01	3.17E-02	26.61	
SARABCHI-B	69.47	93.45	271.79	10.14	0.62	9.68E+01	5.76E-01	2.19E-02	40.83	
SARABCHI-B	57.5	76.52	202.44	7.21	0.62	7.94E+01	4.75E-01	1.84E-02	41.5	
R550*	26.09	33.19	110.02	5.65	0.61	3.37E+01	2.84E-01	1.14E-02	25.63	
FR	1.03	1.15	4.89	0.36	0.91	1.30E+00	1.20E-02	5.62E-04	30.77	Present analysis
FRT	1.08	1.29	6.76	0.44	0.79	1.37E+00	1.86E-02	8.40E-04	15.51	
CFR	3.4	3.91	13.8	0.46	0.88	4.27E+00	3.73E-02	1.66E-03	91.25	
SPFR	0.39	0.47	3.22	0.32	0.29	5.39E-01	1.42E-02	6.73E-04	4.11	
RFR	3.28	4.2	18.85	0.81	0.53	5.12E+00	4.55E-02	1.66E-03	34.83	
ROLL	2.57	3.03	12.01	0.46	0.8	4.79E+00	1.96E-02	6.16E-04	79.22	
ROLLT	2.03	2.36	9.73	0.45	0.85	3.98E+00	1.81E-02	7.24E-04	53.36	
RROLL	7.24	8.62	33.14	1.28	0.59	9.42E+00	5.29E-02	2.08E-03	51.23	
SPC	3.64	4.57	22.24	2.82	0.16	4.76E+00	8.50E-02	3.58E-03	5.72	
SPCT	3.66	4.77	24.88	2.99	0.16	5.15E+00	9.12E-02	3.81E-03	5.52	
CSPC	2.48	3.1	15.57	2.44	0.07	3.16E+00	7.89E-02	3.51E-03	3.2	
SPSPC	4.57	5.69	27.38	3.35	0.15	5.73E+00	9.88E-02	4.10E-03	5.75	
RSPC	3.24	4.04	19.61	2.21	0.2	4.13E+00	6.72E-02	2.82E-03	6.63	

6.5.4 Correlation of the roughness parameters

A multitude of roughness parameters is used in the literature. Several of these parameters are related to each other. In this Section, possible correlations between the parameters are examined using both Dey's data and the data from the surfaces analysed presently, as listed in Table 6-7. A linear correlation table for a selection of the parameters of the 46 different surfaces listed in Table 6-7 is shown in Table 6-8 for bandwidth limits 5&50.

Table 6-8. Correlation table for the 9 selected roughness parameters of Table 6-7.

R	Ra	Rq	Rt	Sa	τ1/e	m0^0.5	m2^0.5	m4^0.5	α
Ra	1.000	0.999	0.981	0.924	0.005	0.998	0.982	0.988	-0.113
Rq	0.999	1.000	0.983	0.927	0.004	1.000	0.981	0.987	-0.112
Rt	0.981	0.983	1.000	0.976	-0.056	0.982	0.993	0.989	-0.153
Sa	0.924	0.927	0.976	1.000	-0.162	0.925	0.975	0.960	-0.231
τ1/e	0.005	0.004	-0.056	-0.162	1.000	0.008	-0.062	-0.039	0.774
m0^0.5	0.998	1.000	0.982	0.925	0.008	1.000	0.980	0.986	-0.109
m2^0.5	0.982	0.981	0.993	0.975	-0.062	0.980	1.000	0.998	-0.170
m4^0.5	0.988	0.987	0.989	0.960	-0.039	0.986	0.998	1.000	-0.157
α	-0.113	-0.112	-0.153	-0.231	0.774	-0.109	-0.170	-0.157	1.000

Table 6-8 shows that the amplitude parameters are highly correlated to each other. Figure 6.23 shows the correlation between Ra and Rq on a log-log scale (so that the correlation is even better than on a linear scale). Theoretically, the ratio Ra/Rq is $2^{3/2}\pi$ (= ca. 0.9) for a sinusoid and $(2/\pi)^{0.5}$ (= ca. 0.8) for a Gaussian distribution (Thomas, 1999, p. 139). In practice a value of 0.8 is used, which is satisfactory here.

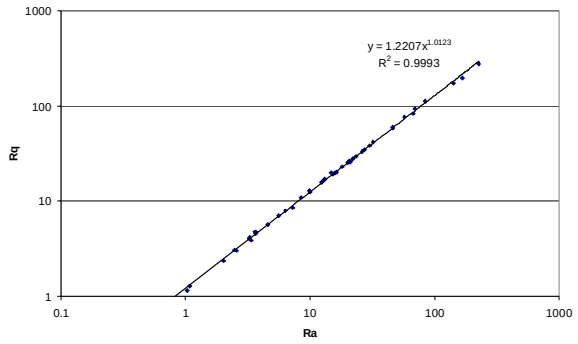

Figure 6.23. Correlation between Ra and Rq.

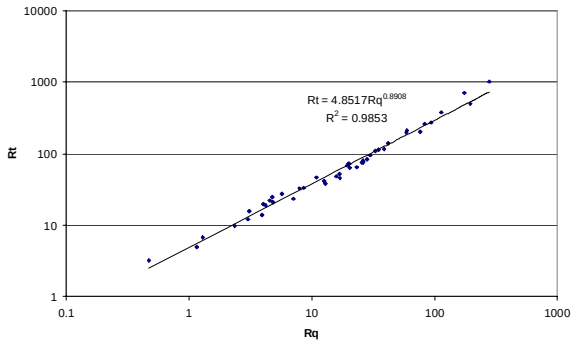

Figure 6.24. Correlation between Rq and Rt

Figure 6.24 shows the correlation between Rq and Rt, also on a log-log scale, which gives a better correlation than a linear relationship. A second order polynomial on a log-log scale would give an even better correlation coefficient, but the value of the correlation equations is relative, as Dey (1989) has shown that the relationships depend on the bandwidth limits.

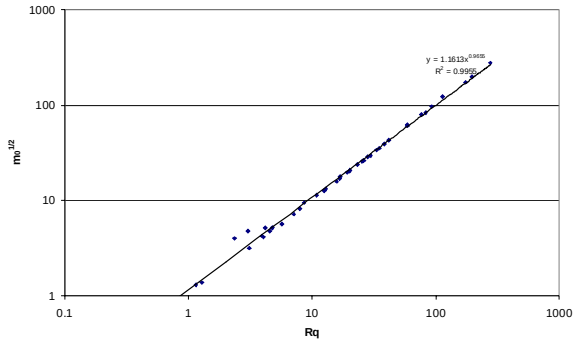

Figure 6.25. Correlation of Rq and $m_0^{1/2}$.

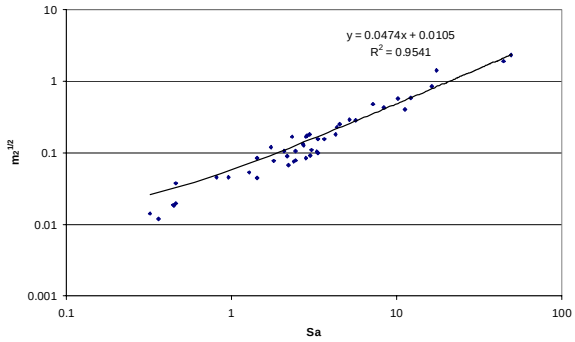

Figure 6.26. Correlation of Sa and $m_2^{1/2}$

The correlation of the spectral moments with the statistical parameters is also good. Figure 6.25 shows the correlation between Rq and m01/2 on a log-log scale. The zeroth spectral moment is very slightly larger than the square of the RMS roughness value Rq. Figure 6.26 shows the correlation between Sa and $m_2^{1/2}$. The second spectral moment m_2 is in theory equal to the variance of the slopes, $m_2(var)$, or the square of the RMS slope. Dey established from his correlation analysis a relationship between the RMS slope *angle* Sq (in degrees) and $m_2^{1/2}$: $Sq = 44.8 \cdot m_2^{1/2}$. If in the present analysis $m_2(var)^{1/2}$ is converted into degrees to obtain Sq, the correlation factor with m_2 is equal to 41.16, in very good agreement with Dey. Just like Ra and Rq, Sa is highly correlated to Sq, and consequently, Sa is also highly correlated with $m_2^{1/2}$, as Figure 6.26 shows.

The correlation lengths $\tau_{0.5}$ and $\tau_{1/e}$ are also correlated to each other. Dey found the relationship $\tau_{0.5} = 0.765\ \tau_{1/e}$, whereas for the present results the correlation factor is 0.757, again in very good agreement.

More surprisingly, Table 6-8 shows that there also is a good correlation of Sa and the higher-order spectral moments with the amplitude parameters, and also of the spectral moments with each other.

Figure 6.27 shows the correlation of Sa with Rt on a log-log scale, and indicates that the Foul Release surfaces are the lowest of the entire range of surfaces.

On the other hand, the bandwidth parameter α does not correlate with any of the other parameters excluding the correlation length with which there is a weak correlation, as shown in Figure 6.28.

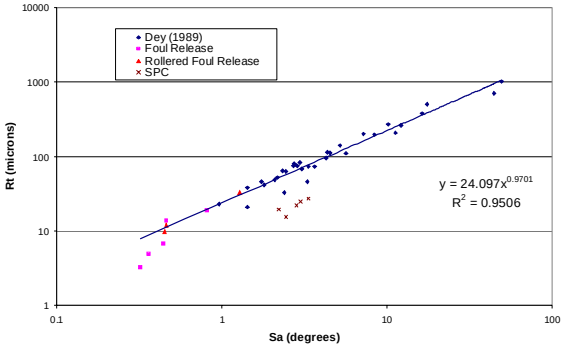

Figure 6.27. Correlation of Sa with Rt.

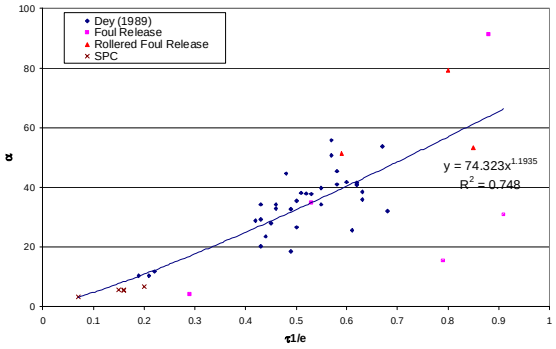

Figure 6.28. Correlation of $\tau_{1/e}$ with α.

The good correlation between several of the parameters indicate that one can replace the use of one parameter by another correlated parameter. In particular, the correlations imply that Equation 6.13, which allows the calculation of Rq for different cut-off lengths using the Fractal Dimension, can be extended and can be used for all amplitude parameters.

6.5.5 Comparison of the extrapolated Rt50 with the Average Hull Roughness

The data presented in Table 6-2 to Table 6-4 measured with the optical measurement system can be compared with the Average Hull Roughness measured with the BMT Hull Roughness Analyser (cf. Chapters 3 and 5). If one wishes to compare the filtered data listed in Table 6-2 to Table 6-4, one could extrapolate the 5&50 or 2.5&50 measurements by multiplying with the square root of the ratio of the cut-off lengths (i.e. 10 or 20) as Thomas suggested as a rule of thumb. However, Whitehouse (1994, p. 99) gives a more accurate scale factor which takes the fractal dimension FD (and so the character of the surface) into account: $Rq \sim L_c^{2\text{-}FD}$ which follows directly from Equation 6.13. In Section 6.5.4, a good correlation was found between Rt and Rq (cf. Figure 6.28), so that $Rt \sim L_c^{0.89(2\text{-}FD)}$. Because of the differences in the Fractal Dimension, the amplitude parameters of the Foul Release surfaces

are expected to increase more rapidly with the cut-off length ($Rq \sim L_c^{0.8}$) than those of the SPC surface (for which the exponent is ca. 0.4-0.5).

Table 6-9 compares the extrapolations made from the Rt values calculated from the UBM measurements (i.e. $Rt50 = Rt(5)\cdot 10^{2-FD}$ and $Rt50 = Rt(2.5)\cdot 20^{2-FD}$, neglecting the exponential factor 0.89) with the Average Hull Roughness (AHR) values as measured with the BMT Hull Roughness Analyser.

The comparison of the results listed in Table 6-9 at first sight seem to reveal several discrepancies but they can be explained after careful consideration of the respective surface conditions (as summarised in the table under the caption 'observations'). The large FR surface exhibited some severe sagging along the centre-line, thus rendering its AHR significantly higher than its mode value of 36μm. Several Rt50 values were actually measured in the 20-30μm range and the sample plate was clearly more representative of this. It was noted that the measurements with the BMT Hull Roughness Analyser over the CFR surface proceeded with some difficulty. Initially, the recorded values were in the region of the extrapolated UBM Rt values. The surface was consequently wetted a bit more than usual to prevent the needle of the gauge stuttering over the surface and this brought the values down significantly. However, if the surface is too wet (and when it is difficult to prevent the drive wheels slipping or the gauge from swinging sideways) the AHR value may become too low. The SPFR sample surface was clearly not representative of the tested surface (cf. Section 3.2.3). In view of all the application problems with the SPFR surface, it is quite ironic that these UBM values are actually the lowest of the entire range. Both the extrapolated values of Rt for RFR and RROLL seem to agree with visual observation, testimonial of the problems with the application over the curved cylinder surfaces. The RSPC surface was visibly better and, except for SPSPC, the SPC measurements are consistent, with CSPC clearly being the best SPC application of the range.

Table 6-9. Comparison of the extrapolated Rt values with the measured AHR.

Surface	UBM		BMT	Observations
FR	5&50 2.5&50	25.10 21.44	51.32	Sagging around the centreline of the tested plate explains higher BMT values
FRT	5&50 2.5&50	33.14 31.33	N/A	
CFR	5&50 2.5&50	103.21 67.80	49.4	Quite difficult to obtain measurements with BMT
SPFR	5&50 2.5&50	12.52 12.87	(83) 62	Sample plates not representative of tested plate
RFR	5&50 2.5&50	109.83 107.57	N/A	Extrapolations seem acceptable according to visual observations
ROLL	5&50 2.5&50	79.36 53.66	59.67	Good agreement
ROLLT	5&50 2.5&50	63.15 52.56	N/A	
RROLL	5&50 2.5&50	228.63 218.14	N/A	Values seem high but application on cylinders was difficult and the surface was visibly "wavy"
SPC	5&50 2.5&50	55.87 59.58	68.56	Good agreement
SPCT	5&50 2.5&50	65.55 68.33	67.4	Excellent agreement
CSPC	5&50 2.5&50	34.30 36.70	29.77	Good agreement
SPSPC	5&50 2.5&50	73.69 84.27	38.5	UBM Extrapolation seems overestimated
RSPC	5&50 2.5&50	53.35 53.89	N/A	Application on cylinder was visibly good

Overall it is thought that the agreement with both roughness measurement methods is quite good.

6.6 Conclusions of the roughness analysis

The roughness characteristics of coated sample plates have been analysed with a UBM optical measurement system. An analysis methodology has been developed which applies the moving average 'boxcar' method to filter the data. The bandwidth limits which have been used in the analysis are 2.5&50 and 5&50. Larger cut-off lengths have not been included due to the restricted evaluation length of the roughness profile. As will be seen in Chapter 7, this is not a drawback since the effective cut-off lengths of hydrodynamical importance lie between 2.5 and 5mm for the coated surfaces analysed in this work.

Based upon the results of the analysis carried out, the following general conclusions are made with regards to the roughness characteristics of the different coatings:

1. The amplitude parameters of the sprayed Foul Release surfaces are lower than those of the rollered Foul Release surfaces and the SPC surfaces.
2. The rollered Foul Release surfaces display a roughness height distribution which is considerably more leptokurtic than the sprayed Foul Release surfaces. The greater number of high peaks on the rollered Foul Release surfaces is expected to engender higher drag than sprayed Foul Release surfaces.
3. The texture of the Foul Release surfaces is significantly different from SPC surfaces. Longer wavelengths characterise the 'open' texture of the Foul Release surface. This is particularly evident in parameters such as the mean absolute slope angle Sa, the fractal dimension FD and the correlation lengths. It is also clear from plots of the power spectra and the autocorrelation function.
4. A typical Foul Release coating scheme has a different build-up than a SPC scheme. A typical primer has a 'closed' texture characterised by short wavelengths, much like SPC surfaces. The tiecoat in a Foul Release scheme alters the texture of the surface and decreases the amplitude parameters moderately. The subsequent topcoat further decreases the amplitude parameters. In the SPC scheme, the texture is not changed significantly. Each subsequent coat of SPC increases the amplitude parameters significantly.
5. Extrapolation of the Rt measurements to a cut-off length of 50mm using the Fractal dimension as scaling parameter showed a fairly good agreement with the AHR measurements obtained with the BMT Hull Roughness Analyser. However, it is thought that the optical measurement system does not make contact with the surface

is a bonus over the stylus instrument with regards to the elastic nature of the Foul Release surfaces.

6. A correlation analysis of a selection of the roughness parameters has shown that many of them are interrelated. The interrelationships derived here correspond well to those reported in literature.
7. The parameters Sa and FD do not depend on the cut-off length and seem more robust than other parameters.
8. To the Author's knowledge, this is the first time the Fractal Dimension has been systematically included in the roughness analysis of marine coatings. It is a useful parameter which is thought to reveal some of the inherent characteristics of the material of the coatings. Its inclusion in the analysis allows scaling of the amplitude parameters to different cut-off lengths.

Chapter 7: Correlation of roughness, drag and boundary-layer characteristics

7.1 Introduction

This chapter investigates whether there is a correlation between the roughness and drag characteristics of the painted surfaces that have been tested and analysed. The results of the towing tank experiments (Chapter 3) and the water tunnel experiments (Chapter 5) are combined to obtain a set of roughness functions. These roughness functions are correlated with the roughness characteristics analysed in Chapter 6.

The methodology used for the correlation of roughness and drag, which is described in Section 7.2, is a semi-empirical approach which assumes that painted surfaces obey the Colebrook-White law in the transitional flow regime. The roughness functions of the surfaces used in the towing tank experiments, are obtained using Granville's overall method (Granville, 1987) in Section 7.3. The correlation of the gathered data is carried out in Section 7.4 with several roughness measures suggested in Section 7.2. A critical discussion of the appropriateness of the Colebrook-White law is given in Section 7.5 and some observations are made in relation to regular roughness in Section 7.6. Alternatives to the semi-empirical correlation approach are mentioned in Section 7.7 and a summary of the findings is presented in Section 7.9.

7.2 A semi-empirical approach to the correlation of roughness and drag.

As mentioned in Chapter 2, the ITTC (1990, p. 252) has adopted the formula suggested by Townsin et al. (1984) to correlate the roughness with the added resistance of new ships:

$$10^3 \cdot \Delta C_F = 44[(h/L)^{1/3} - 10 \cdot Re^{-1/3}] + 0.125 \qquad (7.1)$$

where h is the Average Hull Roughness measured by the BMT Hull Roughness Analyser. Dey (1989) has confirmed that the roughness function $\Delta U/U_\tau$, which is directly related to the added resistance, correlates well with Rt50 for new, moderately rough surfaces (Rt50 < 225μm) and that Rt50 is adequate for quality control as well as for measuring the approximate power penalties due to roughness. Townsin and Dey (1990) argued that the reason why a single roughness parameter Rt50, could well predict the added resistance of a wide range of new ship surfaces, is that their texture is fairly similar, allowing for differences in method of application, paint rheology and the application environment. New ships have several coats of paint, the number and composition of which do not vary greatly (Dey, 1989, p. 185).

In contrast, if on top of painting, a surface undergoes processes such as deterioration, corrosion, mechanical damage as occurs on a ship hull in service, the overall texture of a surface must have an influence on the added resistance that surface causes. Additional surface metrology parameters are needed to properly characterise those surfaces and to correlate roughness with drag.

However, the experiments presented in Chapter 3 have shown that the added resistance of a *new* surface coated with a Foul Release system does *not* correlate with Rt50. It is noted that the physical composition of a Foul Release system, which has been described in Section 2.5, and therefore also the texture of a Foul Release system is very different from those of newly applied toxic antifoulings such as a tin-free SPC, which has been demonstrated in Chapter 6.

It is expected that this fundamental difference between Foul Release and SPC systems in terms of their roughness must have repercussions on the respective added resistance of the coatings.

Traditionally, a semi-empirical approach has been employed to correlate roughness and drag. Ship hull surfaces have been considered as 'engineering surfaces' for which the roughness function is described by the Colebrook-White law, given by Equation 4.36:

$$\Delta U^+ = \frac{1}{\kappa} \ln(1 + \frac{C_1}{B_1} h^+) \qquad (7.2)$$

where h^+ is the roughness Reynolds number, C_1 is a constant which depends on the chosen measure of roughness, and B_1 is a universal constant. In essence, the Colebrook-White law was conceived as a simple interpolation formula between the hydraulically smooth ($\Delta U^+ = 0$) and the fully rough (ΔU^+ varies linearly with $\ln h^+$) region, so that:

$$y_1 = \frac{B_1 \nu}{U_\tau} + C_1 h \tag{7.3}$$

whereby y_1 is the 'effective hydraulic wall' which is defined as that conceptual distance for which the velocity laws valid in the overlap region satisfy $U = 0$. If $h = 0$, $y_1 = B_1\nu/U_\tau$ and from substitution of this condition in the smooth-wall log law (Equation 4.19) it follows that:

$$B = -\frac{1}{\kappa} \ln B_1 \tag{7.4}$$

or $B_1 = 0.128735$ using the Stanford conventions. Conversely, in the fully rough flow regime h becomes so large that the surface resistance becomes independent of viscosity and $y_1 = C_1 h$. Substitution of this condition in Equation 4.34 gives:

$$\chi_r = -\frac{1}{\kappa} \ln C_1 \tag{7.5}$$

Consequently, the Colebrook-White law may also be written as:

$$\Delta U^+ = \frac{1}{\kappa} \ln(1 + e^{-\kappa(\chi_r - B)} h^+) \tag{7.6}$$

Thus, by plotting ΔU^+ versus $\ln(h^+)$ for a particular surface which obeys the Colebrook-White law, the value of Nikuradse's roughness function in the fully rough region, χ_r, may readily be determined from the intercept with the ΔU^+-axis, as shown in Figure 7.1.

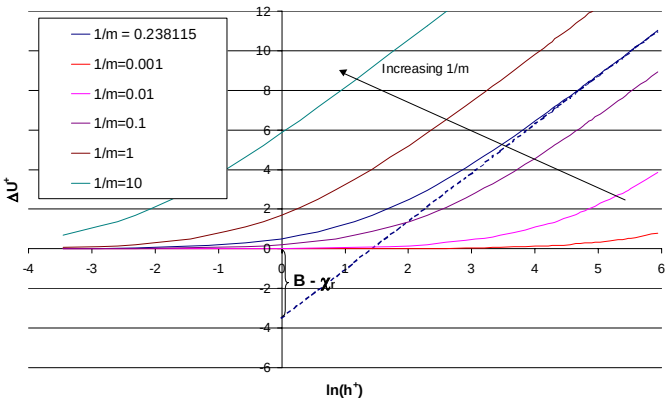

Figure 7.1. Properties of the Colebrook-White law.

Figure 7.1 shows that an increase of the parameter $1/m = C_1/B_1$ (i.e. a decrease of χ_r) shifts the values to the left along the abscissa. Schlichting's equivalent sand-roughness

method relies on Equation 4.33 and determines the equivalent sand roughness h_s of a particular surface with a characteristic roughness measure h, by replacing the experimentally obtained value χ_r of that surface with the value 8.5 obtained for Nikuradse's sand by:

$$\frac{1}{\kappa}\ln\frac{h_s}{h} = 8.5 - \chi_r \tag{7.7}$$

For many engineering surfaces, it is difficult to obtain experimental values of χ_r in laboratory conditions, but if a surface is known to obey the Colebrook-White law in the transitional flow regime, χ_r can readily be determined and from substitution of Equation 7.5 into Equation 7.7 it follows that:

$$\frac{h_s}{m_s} = \frac{h}{m} \tag{7.8}$$

whereby $1/m_s = 0.238115$. Hence the parameters h/m are shifted to h_s/m_s, which is equivalent to Hama's formulation of the Colebrook-White law which he expressed in decimal logarithms (cf. Hama, 1954). Note that one could choose any other set of parameters h and m provided they obey Equation 7.8. This does not affect the roughness function ΔU^+ (only its position along the abscissa), but it does affect the roughness function χ. The advantage of using ΔU^+ as a roughness function is that it can be determined unambiguously from the boundary-layer velocity profile alone, whereas χ involves the choice of a roughness measure h. This is no problem for regular roughness but it becomes problematic in the case of irregular roughness. As yet, it is not entirely clear which parameters that characterise aspects of the topography of irregular roughness are relevant to describe the influence on the near-wall flow.

The experimental results of, for example, Musker (1977), Johansson (1985) and Walderhaug (1986) suggest that a lot of painted surfaces obey the Colebrook-White law. If a painted surface is known to follow the Colebrook-White law, the roughness of that surface can be correlated with its drag in two different ways.

In the first approach (Grigson, 1981; Grigson, 1982), h is set to be a clear height parameter of the surface, which in the case of ship hull surfaces comes down to the AHR value determined by the BMT Hull Roughness Analyser. As mentioned, it has long been recognised that a roughness height alone cannot completely describe the irregular features of a painted surface (Todd, 1951) and produce a universal curve for the roughness function. Musker (1977) showed that h = Rt50 did not correlate with the roughness function of 5 replicated ship hull surfaces. Several other researchers (e.g. Byrne, 1980; Grigson, 1981 and

1982, Walderhaug, 1986) have noted the influence of the texture of the surface (i.e. surfaces with nominally the same AHR can exhibit significantly different drag depending on their texture). Consequently, Grigson (1981, 1982) incorporated this textural influence in the parameter m. Thus, Equations 4.30 and 4.33 are re-written as:

$$\chi = \frac{1}{\kappa}\ln h^{+} + B_0(h^{+}, \alpha, \beta, ...) \tag{7.9}$$

whereby h = AHR and since χ is independent of h in the fully rough flow region, m = m(α, β,...). By plotting the roughness functions obtained from flow measurements for many different surfaces in the form of Equation 7.2, Grigson (1982) established that an increase in m has a favourable influence on drag. However, the dependence of m on parameters α, β, ... and what these may be in terms of roughness parameters was not clear.

Several researchers have approached the effect of random and irregular roughness on flow and frictional resistance from an alternative approach (e.g. Musker and Lewkowicz, 1978; Byrne, 1980; Walderhaug, 1986; Medhurst 1989; Dey, 1989). In this approach, m is effectively kept constant and h is no longer considered to be purely a height parameter. Instead, h becomes a *characteristic measure* with a dimension of length (which is required to keep h^{+} dimensionless) that is a combination of several roughness parameters (both amplitude and texture) which are considered to have an influence on the near-wall boundary-layer flow.

Musker (1977) introduced a combined parameter $h' = Rq(1+a\cdot Sa)(1+b\cdot Sk\cdot Ku)$ whereby Rq is the RMS height, Sk and Ku are the skewness and kurtosis respectively of the roughness height profile distribution (which have been included as a measure of departure from a Gaussian surface), Sa is the mean slope angle based on a digitising interval equal to the correlation length $\tau_{0.5}$ and a and b are empirical constants. Thus, in h' the texture part is predominantly a function of the average slope Sa. Musker found the best correlation for his pipe flow experiments when the long wavelength cut-off was reduced to 2mm, taking a and b as 0.5 and 0.2 respectively.

Mosaad (1986) found that good correlation of his experiments was obtained with a simplified form of the parameter h' in which he used the parameter λ_{PC} to account for the texture. Another simplified form of h', h' = Rq(1+0.3Sa) whereby Rq and Sa were calculated for bandwidth parameters 2/50, was proposed by the Newcastle Ship Performance Group in the 1980s (Dey, 1989, p. 179) on the basis that the departure of the roughness height

distributions from a Gaussian distribution can be neglected since Sk and Ku are notoriously unreliable (Thomas, 1982).

Walderhaug (1986) attempted to correlate the roughness effect with the turbulence production in the boundary layer. He proposed to use a roughness height at an interval equal to the spacing of streamwise streaks of vorticity close to the wall, which are important in the turbulence production process (cf. Section 4.2). The distance between these streaks is about 100 wall units ν/U_τ (Meng, 1998), which would correspond to about 1mm on a model, so that Walderhaug proposed an 'effective' roughness parameter $k_E = (k/\lambda)_1(Rt50\text{-}k_{adm})$ whereby $(k/\lambda)_1$ is the amplitude/wavelength ratio at λ = 1mm and k_{adm} is the admissible roughness height (Schlichting, 1979). Walderhaug took k_{adm} to be approximately equal to the viscous sublayer, i.e. 2.5 wall units, so that it is usually very small compared to Rt50. It is important to note that the parameter $(k/\lambda)_1$ takes both the height and slope over 1mm into account (Dey, 1989, p. 181).

Since the roughness profile of a surface is always random in nature, random process theories and techniques such as Fourier analysis can be used as a tool for roughness analysis. The principal feature of Fourier analysis is the representation of the profile by the sum of a large number of harmonic components in which the amplitude and phase angle are random variables. By using suitable numerical techniques, such as Fast Fourier Transforms, an amplitude spectrum can be constructed with respect to wavenumber (Hearn and Metcalfe, 1995). The main advantage of this method is that several important parameters can be obtained from the even moments of the spectrum (cf. Chapter 6). However, it is important to give the bandwidth parameters (long and short wavelength cut-off) with which the roughness parameters or spectral moments were obtained since none of these are intrinsic to a surface.

Byrne (1980) therefore proposed that a suitable texture parameter for the characterisation of a rough surface should be the bandwidth parameter α.

Medhurst (1989, 1990) stated that four general characteristics of a rough surface intuitively seem likely to affect the roughness function:

- A measure of the size or scale of the roughness; a height parameter should serve for this purpose
- A measure for the slope or sharpness of individual roughness elements
- The range of frequencies composing the roughness profile
- The long wavelength cut-off applied to a particular surface

Dey (1989) carried out drag measurements of four painted surfaces using a rotor apparatus. In addition, he collected the roughness profiles of 24 surfaces for which the roughness function, ΔU^+, had been measured in different flow rigs. He also calculated the roughness function deduced from the total friction measurements of the rough flat planes reported by Todd (1951), using Granville's overall method (1987). Having thus gathered a sizeable collection of data, he looked for the best correlation between the drag and roughness, using Equation 7.2 for different forms of the characteristic roughness measure h. He tried Rt, Ra^2/λ_{PC}, $(m_o m_2)^{1/2}$, $(\alpha m_0)^{1/2}$ but found the best correlation for the whole range of surfaces for $h = (\alpha m_0 m_2)^{1/2} = (m_0^2 m_2/m_4)^{1/2}$ in which the texture is accounted for by the factor $(m_2/m_4)^{0.5}$. As mentioned in Chapter 6, the first three even spectral moments are the variances of amplitude, slope and curvature, so that m_2 and m_4 account for the texture of the surface. The resulting best fit found by Dey is given by Equation 7.10, and is shown in Figure 7.2:

$$\Delta U^+ = \frac{1}{\kappa}\ln(1 + 0.18h^+) \tag{7.10}$$

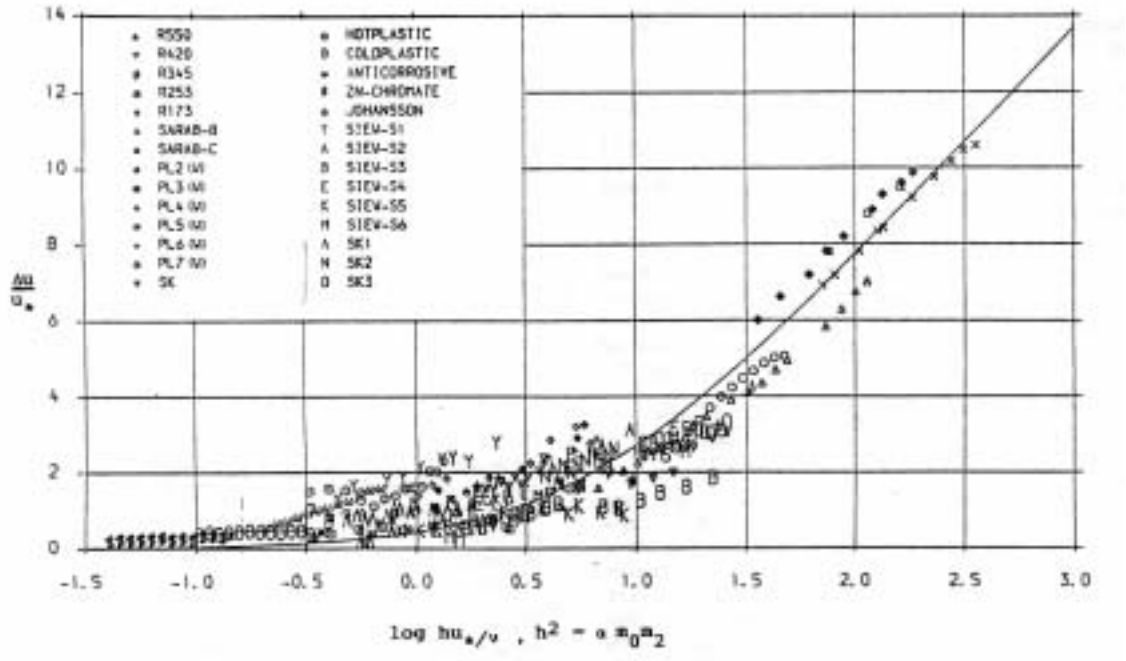

Figure 7.2 Dey's correlation of ΔU^+ with $h = (\alpha m_0 m_2)^{1/2}$ for 28 different surfaces.

It is very important to note that the results shown in Figure 7.2 were not measured at one particular long wavelength cut-off, but for a cut-off length which depended on the roughness of the surface initially measured for a long wavelength cut-off of 50mm. An 'effective long wavelength cut-off', which increases as the surface gets rougher, is then

determined from an empirical relationship which had been established by Dey to give the best correlation:

$$\left(2\pi / L_{c,e}\right)^{0.25} = 1.13 - 0.0065\sqrt{m_0 m_2} \tag{7.11}$$

On the basis of this effective long wavelength cut-off, the roughness profiles then have to be re-analysed so that finally the roughness function can be obtained with Equation 7.10.

Dey's method will be applied in Section 7.4 on the present data, looking for that characteristic measure which gives the best correlation with the roughness function of the different surfaces. The optical measurement system used for the present analysis is limited to an evaluation length of 100mm, which is too small to calculate the roughness parameters for L_c = 50mm while at the same time providing a large enough window width for the boxcar moving average filter employed by Dey and Medhurst (cf. Section 6.4.4). However, this is not very important, since an investigation of the effective cut-off wavelengths used by Dey for his smoothest surfaces lie between 2.5 and 5mm. These are the cut-off lengths which have been used in the present analysis. First, however, the frictional resistance data obtained in the towing tank experiments (cf. Chapter 3) will be converted into roughness functions in the following Section.

7.3 The roughness functions of the surfaces tested in the towing tank experiments

While the roughness functions ΔU^+ have been calculated for the flat plate surfaces tested in the water tunnel experiments (Chapter 5), they remain to be calculated for the surfaces tested in the towing tank experiments (Chapter 3).

The roughness function at the trailing edge of a plate can be calculated from the total frictional resistance coefficient C_F by using Granville's overall method (Granville, 1987). The roughness function and roughness Reynolds number are obtained at the same value of $Re \cdot C_F$ using the equations:

$$\Delta U^+ = \left(\sqrt{\frac{2}{C_F}}\right)_s - \left(\sqrt{\frac{2}{C_F}}\right)_r + 19.7\left[\left(\sqrt{\frac{C_F}{2}}\right)_r - \left(\sqrt{\frac{C_F}{2}}\right)_s\right] + 2.5B_1'\left(\sqrt{\frac{C_F}{2}}\right)_r \tag{7.12}$$

and

$$h^+ = \left(\frac{Re\,C_F}{2}\right)\left(\frac{h}{L}\right)\left(\sqrt{\frac{2}{C_F}}\right)_r\left[1 - 2.5\left(\sqrt{\frac{C_F}{2}}\right)_r + 2.5\left(3.75 + B_1'\right)\left(\frac{C_F}{2}\right)_r\right] \tag{7.13}$$

Here B_1' is the slope of ΔU^+ plotted against $\ln(h^+)$ and is evaluated by iteration starting from $B_1' = 0$. In general, the number of iterations required, is less than four.

Two considerations are important. Firstly, ΔU^+ is obtained from comparing a smooth with a rough surface in an analogue experiment. Therefore, the tested aluminium surfaces serve as the smooth reference. Secondly, the results have to be compared at the same value of $Re \cdot C_F$.

The frictional resistance coefficients have been obtained in Chapter 3 by subtracting the wave resistance values computed by the CFD code SHIPFLOW, from the total resistance values measured from the experiments. It is presumed that the wave resistance remains unchanged for the different surfaces. Furthermore, it is considered that the wave resistance computed by the CFD code is accurate, which is supported by the fact that the total resistance values computed by the CFD code agree with the measured values for the aluminium surface, and by the good agreement between the computed and the measured wave profiles, in the case of the second set of measurements carried out in Spain. In addition, the comparison of the experimental analysis with the CFD results has shown that the frictional resistance for the aluminium surface corresponds to the Schoenherr friction line. This is supported by the theory behind both the CFD method as by Granville's overall correlation method used here

(Granville, 1987). As initial roughness measures of h, the Average Hull Roughness value measured by the BMT Hull Roughness Analyser has been used. It is clear from Equations 7.9 and 7.10 that the use of a different roughness parameter h for the same surface will only affect the abscissae h^+ and not the ordinates ΔU^+.

For the Newcastle University towing tank series with the 2.55m long plate, values of ΔU^+ were calculated for $10000 < Re \cdot C_F < 22000$, using linear interpolation of $(2/C_F)^{1/2}$ for each tested surface.

For the CEHIPAR towing tank series with the 6.3m long plate, values of ΔU^+ were calculated for $50000 < Re \cdot C_F < 100000$, using the Schoenherr line as smooth reference (cf. Section 3.3) and evaluated directly at the appropriate $Re \cdot C_F$ for each measured data point of the coated surfaces.

It can be useful for comparison with other experiments to determine the equivalent sand-roughness of the surfaces. This can be done following Ligrani's method (Schultz, 1998):

$$\Delta U^+ = \left[\frac{1}{\kappa}\ln\left(h_s^+\right) + C - B\right]\sin\left(\frac{\pi}{2}Q\right) \tag{7.14}$$

where: $Q = 0$ for $h_s^+ < h_{smooth}^+ = 2.25$

$Q = \ln(h_s^+ / h_{smooth}^+)/\ln(h_{rough}^+ / h_{smooth}^+)$

$Q = 1$ for $h_s^+ > h_{rough}^+ = 90$

and $C = 5$, $B = 8.5$, $\kappa = 0.41$. Thus, the equivalent sand-roughness can be determined by iteration once ΔU^+ is known. Table 7-1 lists the average values of the roughness function and the equivalent sand-roughness over the respective $Re \cdot C_F$ ranges for both sets of surfaces.

Table 7-1. Average values of ΔU^+ and h_s^+

	ΔU/Uτ	ksUτ/ν
NCLFR	0.20	5.29
NCLSPC	2.17	14.57
SPFR	0.21	5.32
SPSPC	0.62	7.16

7.4 Correlation of the roughness and drag measurements

In this Section, a semi-empirical approach is used to correlate the roughness and drag measurements. The roughness functions ΔU^+ are plotted against the roughness Reynolds number h^+, whereby h is a characteristic measure of the roughness of the surface with the dimension of length. It is important to note that the semi-empirical approach looks for a parameter or combination of parameters for which h gives the best correlation with ΔU^+ in the form of the Colebrook-White Equation (7.2).

A number of parameters has been suggested in Section 7.2 to make up the parameter h. The most evident parameter is h = Rt50. Rt50 is known to give a satisfactory correlation for smooth (Rt50 < 225μm) newly-applied SPC surfaces. The use of Rt emphasises the fact that the largest peaks of the roughness profile are known to have the greatest effect on the fluid flow. In the manufacturing industry, the use of Ra is more widespread than Rt, while Rq is more significant from a statistical point of view (Thomas, 1999), but, as seen in Section 6.5.4 it is possible to replace one amplitude parameter by the other at any particular cut-off length since they are highly correlated. Figure 7.3 presents the correlation of Rt50 with the roughness functions of the different surfaces presently analysed, along with the surfaces tested by Dey (1989) and Pazouki (2001) in a rotating drum.

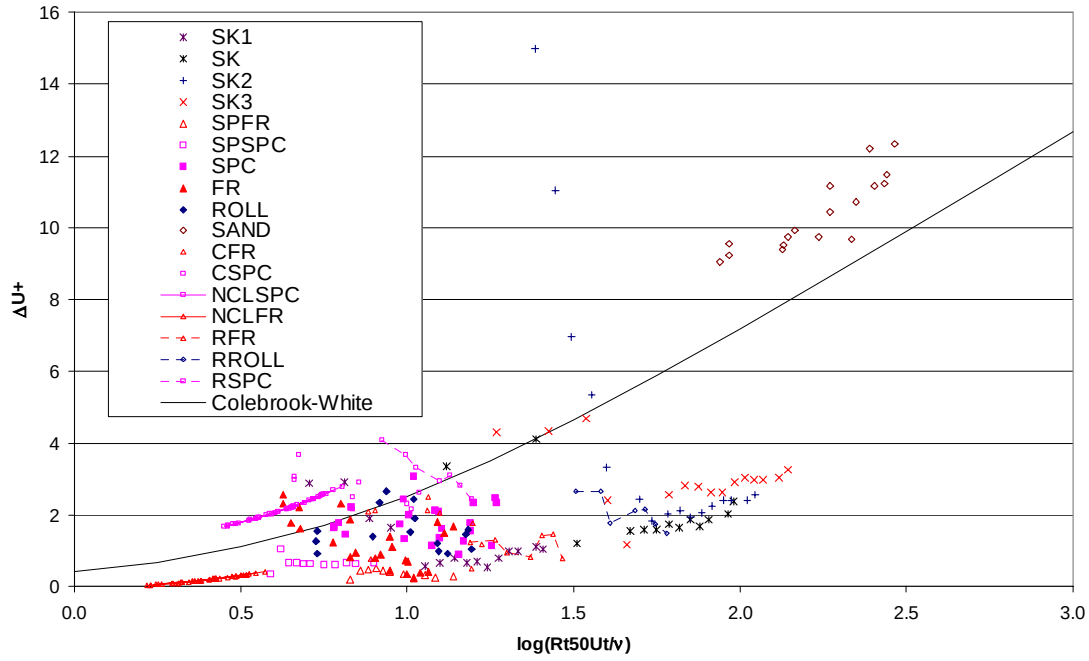

Figure 7.3. The roughness function correlated with Rt50, or the Average Hull Roughness.

The Colebrook-White function in the form of Equation 7.7 has been included in Figure 7.3 to give an indication of the correlation. The Rt50 values used in the correlation were obtained using the BMT Hull Roughness Analyser. In the case of Pazouki's surfaces (the R-series, cf. Chapter 6), the Rt50 values were obtained from extrapolation, as described and tabulated in Section 6.5.5. Figure 7.3 shows that there is no strict correlation for the surfaces analysed presently. The Foul Release surfaces extend over a wide range of the Reynolds roughness number while their roughness functions overall lie below those of the SPC surfaces.

It is obvious from Table 6.2 to Table 6.4 that Rt2.5 is expected to give a better correlation. Figure 7.4 shows the roughness functions of the same surfaces correlated with Rt2.5.

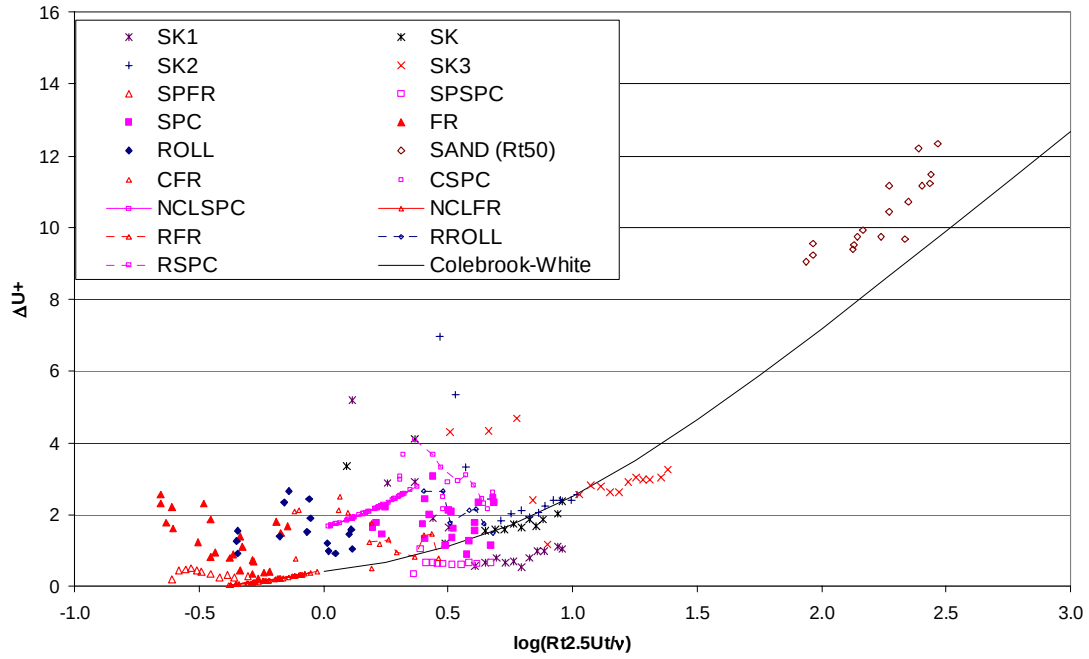

Figure 7.4. The roughness function correlated with Rt2.5 (and Rt50 for the SAND surface).

In Figure 7.4 the SAND surface is still correlated with Rt50 since it is a very rough surface with a much higher effective cut-off length than the other surfaces. Figure 7.4 shows that the correlation is much better than Figure 7.3. Overall, The sprayed Foul Release and SPC surfaces clearly fall in a different area. However, RFR, RROLL and CFR exhibit a higher roughness Reynolds than the correlation would predict

Dey (1989) used the spectral moments to correlate at effective cut-off wavelengths. Figure 7.5 and Figure 7.6 correlate the roughness function with $h^2 = \alpha m_0 m_2$ for a cut-off length of 5 and 2.5mm respectively.

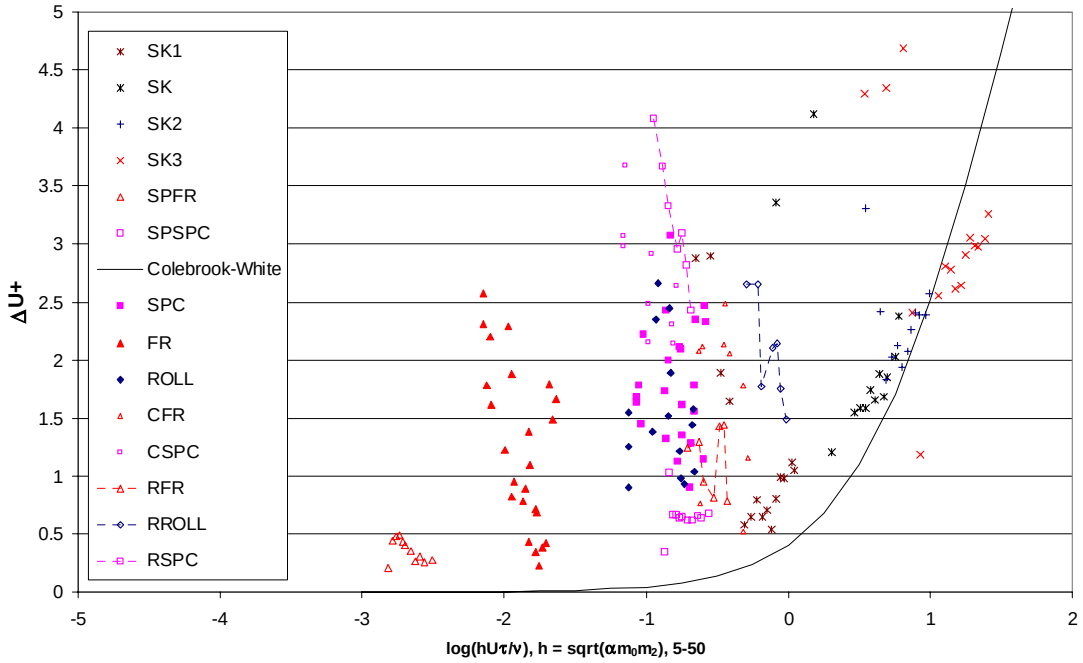

Figure 7.5. The roughness function correlated with $h^2 = \alpha m_0 m_2$ for bandwidth parameters 5/50.

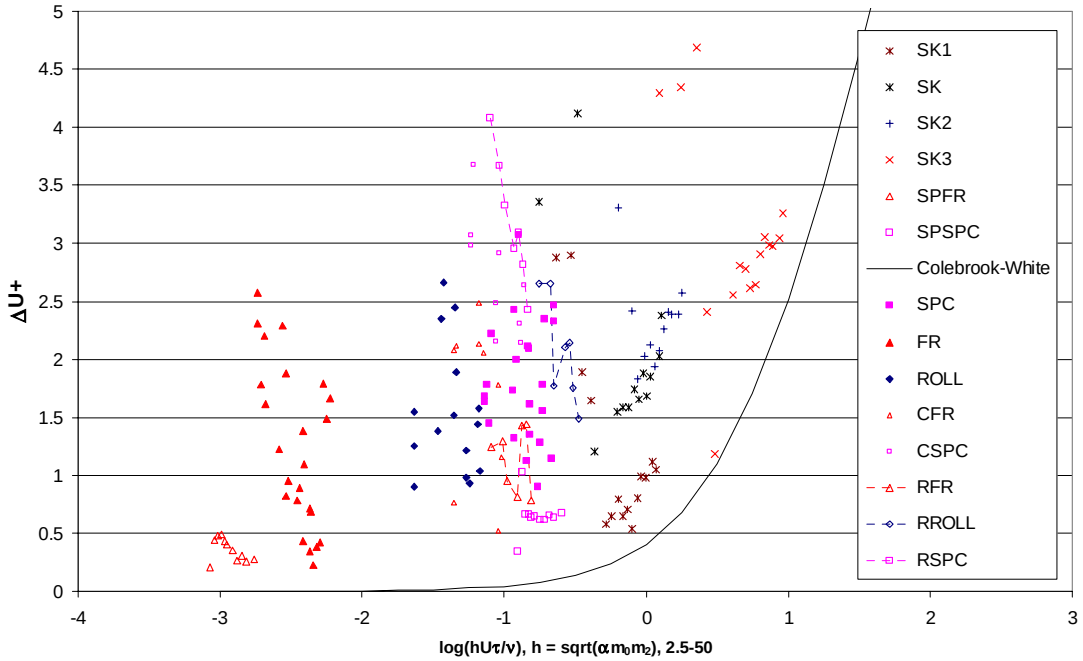

Figure 7.6. The roughness function correlated with $h^2 = \alpha m_0 m_2$ for bandwidth parameters 2.5/50.

The reason behind the choice of $h^2 = \alpha m_0 m_2$ is that the bandwidth parameter and the spectral moments m_0, m_2 and m_4 are related to height, slope and curvature. Hence the characteristic measure $h^2 = \alpha m_0 m_2$ also includes the texture of the surface in the correlation with the roughness function.

The effective cut-off lengths for the present surfaces lie between 2.5 and 5mm, whereby the Foul Release surfaces will lie very close to 2.5mm. Comparison of Figure 7.5 and Figure 7.6 shows that the change of the cut-off length hardly influences the roughness Reynolds numbers of the SPC surfaces. The overall correlation is better in Figure 7.6 but there is an overlap around $\log(h^+) = -1$.

It was noted in Section 6.5.1 that the Foul Release and SPC surfaces displayed a significant difference in the mean absolute slope angle Sa. It was therefore decided to test whether Sa can be used as a texture parameter capable of distinguishing between the Foul Release and other antifoulings. It was noted in Figure 6.26 and Table 6.7 that for the 46 surfaces studied in Sections 6.5.3 and 6.5.4, Sa not only correlates well with $m_2^{1/2}$, but also with $m_4^{1/2}$ at bandwidth parameters 5&50. Table 7-2 shows the 28 surfaces which Dey (1989) re-calculated at their effective cut-off length along with the present surfaces at an effective cut-off length of 2.5mm. Based on these data, Figure 7.7 and Figure 7.8 show that Sa still correlates both with $m_2^{1/2}$ and $m_4^{1/2}$ at the effective cut-off lengths. As a result the texture parameter suggested by Dey (1989), $(m_2/m_4)^{1/2}$ becomes nearly constant for the present data (equal to $24.5 \cdot Sa^{0.05}$ according to the least-squares regression lines).

Table 7-3 compared with Table 6-14, shows the important effect that the effective cut-off length has on the correlation of the parameters, particularly on α.

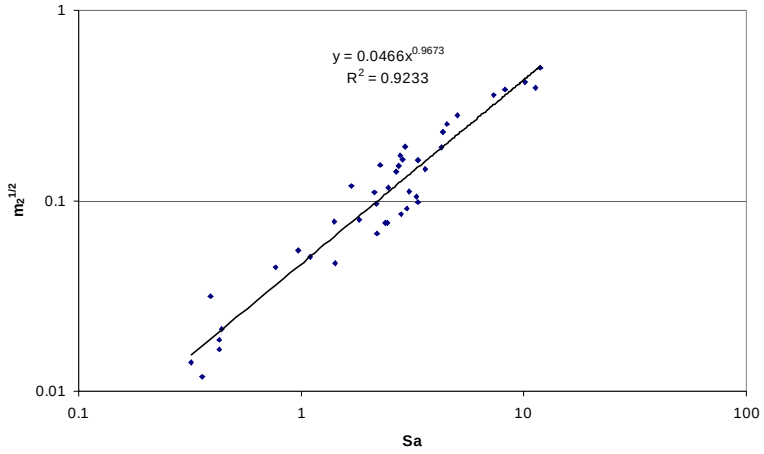

Figure 7.7. Correlation of Sa with $m_2^{1/2}$ for the data tabulated in Table 7-2.

Table 7-2. Comparison of 41 different surfaces at their effective cut-off length.

Surface (5/50)	Ra (μm)	Rq (μm)	Rt (μm)	Sa (degrees)	τ1/e (mm)	m0^0.5 (μm)	m2^0.5 (rad)	m4^0.5 (rad^2/μm)	α	
SK (4.0)	10.65	13.91	35.4	1.68	0.49316	1.44E+01	1.19E-01	4.47E-03	25.38	Dey (1989)
SK1 (4.0)	5.95	7.51	29.68	2.38	0.39214	7.71E+00	7.68E-02	3.16E-03	17.29	
SK2 (4.5)	16.22	20.94	56.25	2.27	0.59353	2.14E+01	1.55E-01	6.32E-03	33.31	
SK3 (5.0)	29.94	38.54	115.84	4.33	0.57619	3.92E+01	2.31E-01	8.94E-03	45.35	
JOHANSSON (4.0)	8.05	10.57	30.03	1.41	0.44964	1.08E+01	7.81E-02	3.16E-03	29.88	
R550 (10.0)	58.25	76.09	300.08	11.31	0.70117	7.78E+01	3.91E-01	1.38E-02	47.39	
R420 (5.5)	28.26	36.89	123.65	4.52	0.59798	3.74E+01	2.54E-01	1.00E-02	36.54	
R345 (6.0)	34.03	43.76	155.22	5.06	0.57392	4.43E+01	2.82E-01	1.18E-02	46.46	
R253 (4.5)	13.91	18.48	66.73	3.34	0.36708	1.87E+01	1.63E-01	6.32E-03	18.85	
R173 (4.25)	14.05	17.73	64.29	3.6	0.42077	1.83E+01	1.47E-01	6.32E-03	27.75	
PL2 (4.0)	9.57	12.05	36.22	1.82	0.39853	1.21E+01	7.94E-02	3.16E-03	30.63	
PL3 (4.0)	12.54	16.34	46.41	2.18	0.44998	1.64E+01	9.64E-02	3.16E-03	40.87	
PL4 (4.0)	18.45	23.42	64.91	2.74	0.47498	2.34E+01	1.53E-01	5.48E-03	35.08	
PL5 (4.0)	10.72	13.63	40.03	2.13	0.37967	1.36E+01	1.10E-01	4.47E-03	22.64	
PL6 (4.5)	21.76	28.23	88.13	4.26	0.44142	2.84E+01	1.92E-01	7.07E-03	29.85	
PL7 (35.0)	125.81	150.05	604.74	11.84	2.08975	1.52E+02	5.02E-01	1.73E-02	109.24	
ZINC-CHROMATE (4.0)	3.49	4.63	19.13	1.42	0.19871	4.99E+00	4.69E-02	1.41E-03	9.9	
COLD-PLASTIC (4.0)	5.17	6.64	19.73	0.97	0.42512	6.75E+00	5.48E-02	2.24E-03	25.03	
ANTICORROSIVE (4.0)	8.22	10.49	42.22	3.31	0.19676	1.08E+01	1.06E-01	3.16E-03	10.68	
HOT-PLASTIC (10.0)	60.98	76.93	279.86	8.25	0.73498	8.21E+01	3.86E-01	1.34E-02	53.17	
SIEW-S1 (4.0)	13.76	17.75	59.62	3.05	0.40374	1.79E+01	1.12E-01	3.16E-03	30.39	
SIEW-S2 (4.5)	16.33	20.95	61.9	2.67	0.53022	21.04757	1.43E-01	5.48E-03	32.18	
SIEW-S3 (4.5)	19.74	26.36	72.41	2.93	0.53315	2.69E+01	1.92E-01	7.75E-03	35.44	
SIEW-S4 (4.5)	17.77	23.31	65.83	2.78	0.49933	2.35E+01	1.73E-01	7.07E-03	28.54	
SIEW-S5 (4.5)	14.7	19	55.93	2.47	0.50799	1.94E+01	1.17E-01	4.47E-03	37.9	
SIEW-S6 (4.5)	19.43	24.5	69.45	2.86	0.52739	2.46E+01	1.64E-01	6.32E-03	36.84	
RS-LIM										
RWS-LIM										
RW-LIM										
SARABCHI-A										
SARABCHI-B (50)	149.71	185.51	863.08	10.15	1.91563	1.81E+02	4.21E-01	1.41E-02	255.61	
SARABCHI-C (16)	104.08	130.88	486.25	7.33	1.24243	1.37E+02	3.61E-01	1.30E-02	194.36	
R550*										
FR (2.5)	0.51	0.59	2.68	0.36	0.32	6.56E-01	1.20E-02	5.59E-04	8.32	Present analysis
FRT (2.5)	0.57	0.76	3.97	0.44	0.136	8.94E-01	2.11E-02	9.73E-04	4.83	
CFR (2.5)	1.26	1.32	4.94	0.39	0.715	1.92E+00	3.16E-02	1.37E-03	21.9	
SPFR (2.5)	0.28	0.39	2.26	0.32	0.035	4.24E-01	1.41E-02	6.72E-04	2.09	
RFR (2.5)	1.92	2.47	10.71	0.77	0.339	3.73E+00	4.49E-02	1.64E-03	11.58	
ROLL (2.5)	1.11	1.26	5.03	0.43	0.455	2.95E+00	1.87E-02	6.02E-04	22.11	
ROLLT (2.5)	0.87	1.05	4.64	0.43	0.344	2.11E+00	1.66E-02	6.97E-04	17.23	
RROLL (2.5)	4	4.69	17.68	1.1	0.408	5.38E+00	5.09E-02	2.07E-03	20.05	
SPC (2.5)	3.41	4.22	17.98	2.82	0.125	4.40E+00	8.51E-02	3.59E-03	4.84	
SPCT (2.5)	3.39	4.33	19.42	2.99	0.122	4.78E+00	9.13E-02	3.81E-03	4.7	
CSPC (2.5)	2.33	2.92	13.14	2.44	0.058	2.93E+00	7.67E-02	3.39E-03	2.86	
SPSPC (2.5)	4.38	5.41	23.24	3.35	0.122	5.47E+00	9.89E-02	4.10E-03	5.24	
RSPC (2.5)	2.71	3.38	14.86	2.2	0.112	3.47E+00	6.72E-02	2.82E-03	4.68	

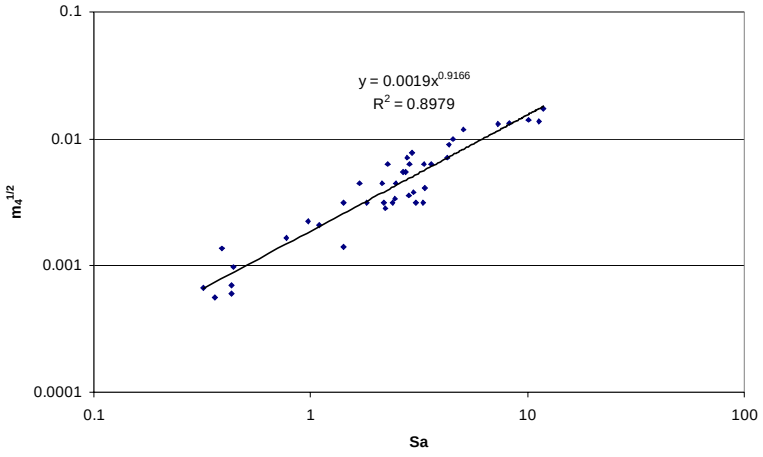

Figure 7.8. Correlation of Sa with $m_4^{1/2}$ for the data tabulated in Table 7-2.

Table 7-3. Correlation table for selected roughness parameters at effective cut-off length (cf. Table 6-14)

R	Ra	Rq	Rt	Sa	τ1/e	m0^0.5	m2^0.5	m4^0.5	α
Ra	1.000	1.000	0.992	0.884	0.929	0.999	0.899	0.865	0.922
Rq	1.000	1.000	0.992	0.887	0.923	0.999	0.905	0.871	0.925
Rt	0.992	0.992	1.000	0.864	0.914	0.988	0.861	0.823	0.931
Sa	0.884	0.887	0.864	1.000	0.756	0.890	0.960	0.937	0.685
τ1/e	0.929	0.923	0.914	0.756	1.000	0.921	0.806	0.772	0.862
m0^0.5	0.999	0.999	0.988	0.890	0.921	1.000	0.909	0.876	0.921
m2^0.5	0.899	0.905	0.861	0.960	0.806	0.909	1.000	0.993	0.726
m4^0.5	0.865	0.871	0.823	0.937	0.772	0.876	0.993	1.000	0.693
α	0.922	0.925	0.931	0.685	0.862	0.921	0.726	0.693	1.000

Therefore it is suggested not to include the curvature when accounting for the texture of the surfaces but to use only a slope parameter. There is no particular preference to which slope parameter (e.g. Sa, Sq, $m_2^{1/2}$…) should be used but in the present analysis the choice is made for Δa/2, which is strictly non-dimensional (rather than in degrees) and the physical meaning of which is easier explained to people who are not familiar with spectra. Grigson pointed out (in Collatz, 1986) that a slope parameter alone cannot completely account for the textural influence, but this is by-passed by measuring the roughness parameters at an effective cut-off length which increases as the surface gets rougher.

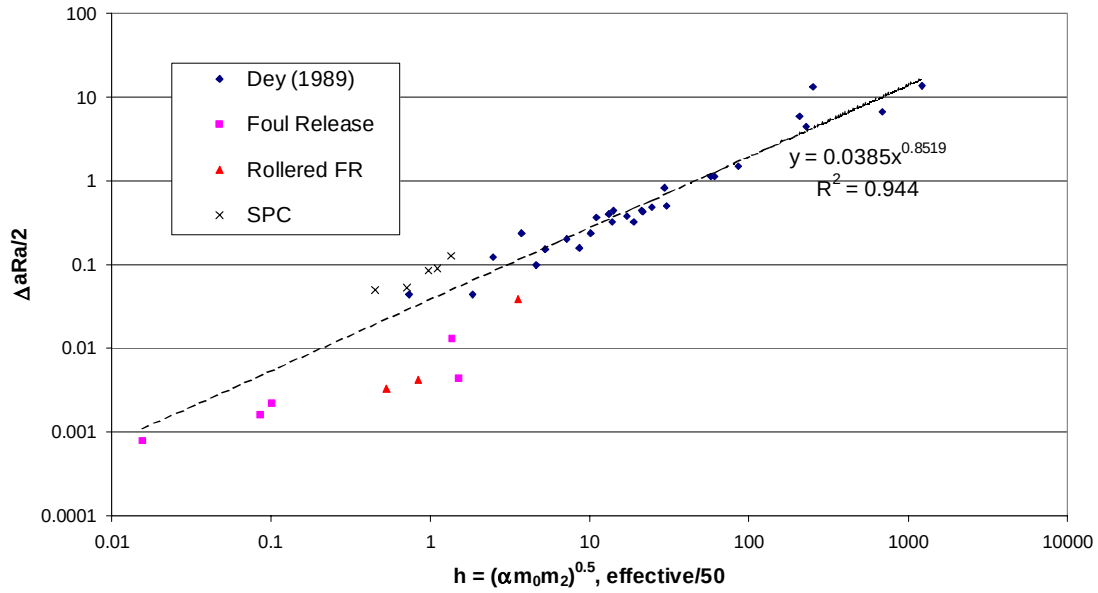

Figure 7.9. The correlation of $h = (\alpha m_0 m_2)^{1/2}$ with h = ΔaRa/2 (both in microns) for the data at effective cut-off length listed in Table 7-2.

Figure 7.9 correlates $h = (\alpha m_0 m_2)^{1/2}$ with the suggested parameter h = ΔaRa/2 for the data at effective cut-off lengths listed in Table 7-2 and shows that the suggested characteristic measure will be able to correlate all the data collected by Dey and shown in Figure 7.2.

Crucially, however, Figure 7.9 shows that h = ΔaRa/2 makes a clear distinction between the Foul Release and the Tin-free SPC, which h = $(\alpha m_0 m_2)^{1/2}$ does not. The suggested characteristic measure is now significantly smaller and will shift the data considerably to the left.

Figure 7.10 shows the correlation of the roughness functions for a selection of the 38 tested surfaces correlated with h = Ra·Δa/2 at their effective cut-off length (taken to be 2.5mm for the present data).

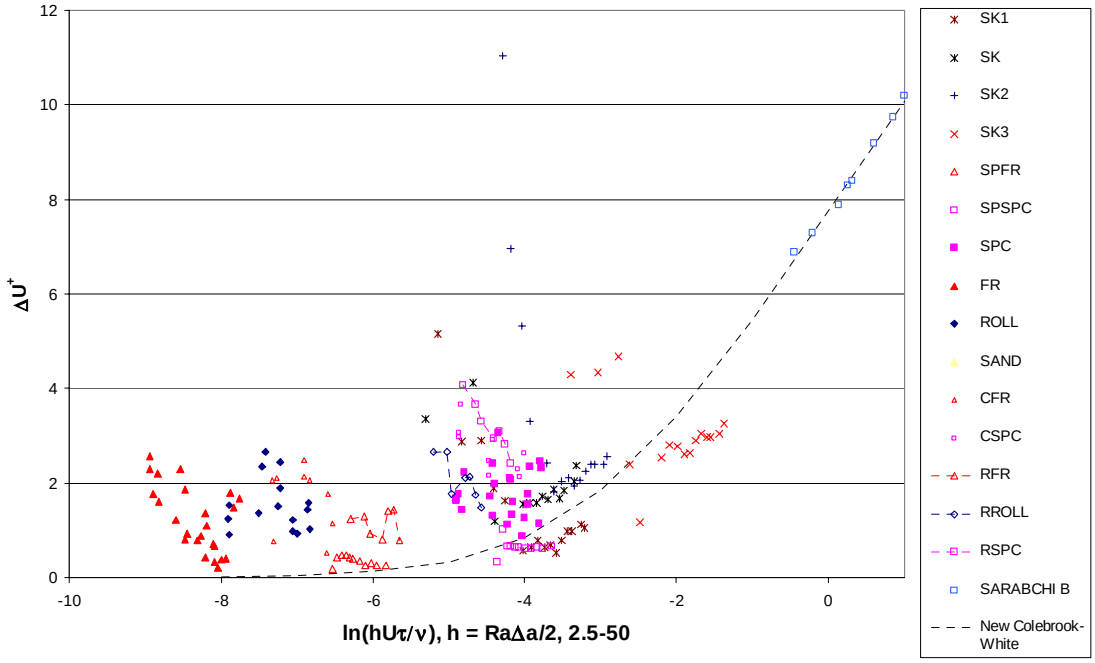

Figure 7.10. The roughness function correlated with h = ΔaRa/2 for bandwidth parameters effective/50.

Figure 7.10 shows that by using h = Ra·Δa/2, the Foul Release and SPC surfaces are now clearly and logically separated from each other. A new Colebrook-White function has been calculated by the inclusion of the SARABCHI-B surface. This surface was made of sandpaper on which three coats of paint were applied in order to simulate a very rough painted surface (Musker and Sarabchi, 1980). This surface was effectively tested in the fully rough region. The inclusion of these data allows a very easy determination of $C_1/B_1 = 1/m$ (cf. Figure 7.1) and the function valid for the new characteristic measure is:

$$\Delta U^+ = \frac{1}{\kappa}\ln(1+22.56h^+) \qquad (7.15)$$

whereby h = Ra·Δa/2 is taken at an effective cut-off length which increases with Ra and at a sampling interval of 50 microns.

7.5 Discussion of the correlation with the Colebrook-White law

The previous Section has shown that to an extent the roughness characteristics of the 8 surfaces analysed in this study and of the 28 surfaces collected by Dey (1989) correlate with the respective roughness functions. Nevertheless, the collapse of the data shown in Figure 7.10 is not entirely convincing.

The SPFR data are not really problematic. As mentioned in Section 3.4.1.4, the sample plates from which the roughness parameters have been calculated are not representative of the tested surface. However, by scaling back from the AHR measurements on the actual surface according to the principles explained in Section 6.5.2, one can estimate with good confidence that the parameter $h = Ra \cdot \Delta a/2$ increases by a factor 28, which is approximately equal to the shift of 3 to the right on the abscissa which has been applied in Figure 7.10. This quantity is a direct indication of how poor surface preparation can affect the roughness Reynolds number in comparison with best-practice paint application.

Mention can be made here of the wave-piercing catamaran model experiments (cf. Section 3.4). In view of the present findings (Section 7.4 and Section 6.5), it may be said that the single coat of Tin-free SPC is expected to give lower drag than a full Foul Release scheme, particularly if the Foul Release has been applied by rollering. Additionally, the local thickness of the Foul Release scheme at areas of high curvature on the model cannot be said to be representative of the roughness Reynolds numbers observed in full-scale. It is expected that large model tests (so that the paint thickness does not build up on high-curvature areas) whereby the Foul Release is applied by spraying and at least two coats of Tin-free SPC are applied, exhibit lower drag for Foul Release systems.

A short remark about the rotor experiments is at this point also appropriate. The RROLL and RSPC surfaces tested by Pazouki (2001) give roughness functions which are comparable to the surfaces tested by Dey (1989) even though the latter are rougher in terms of $h = Ra \cdot \Delta a/2$. Pazouki (2001) has pointed out that the experimental procedure and the use of different instrumentation may have had an influence. The experimental procedure may have had an influence in that the values of the roughness function are perhaps slightly too high in the case of Pazouki's surfaces due to end effects. More significantly, Pazouki also mentioned the effect of instrumentation on different rpm readings. Pazouki observed fluctuating rpm readings during his experiments, but additional measurements with the same tachometer,

which Dey and Medhurst used for their rotor experiments (Medhurst, 1989), demonstrated that the roughness function increased with roughness Reynolds number rather than fluctuate as observed for RFR, RSPC and RROLL (Pazouki, *pers. comm., 12/8/2001*).

The roughness function is a parameter which is very sensitive to rpm readings in the case of rotor experiments and to the friction velocity values in the case of the LDV water tunnel experiments. For example, if in the case of FR2pos2 the friction velocity would increase by 1%, the roughness function would increase from 1.48 to 1.73, which is an increase of nearly 17%. This is of the same order as the relative uncertainties determined on the SPC surface by replicate measurements (cf. Appendix C).

However, it should be realised that the roughness functions of the surfaces tested in the boundary-layer experiments are *local* roughness functions measured at individual locations. At any location the roughness can be expected to change significantly thus influencing the roughness function. In contrast, the *overall* roughness functions calculated from the towing tank and rotor experiments are values which have been measured over the entire wetted surface of the plates and cylinders respectively.

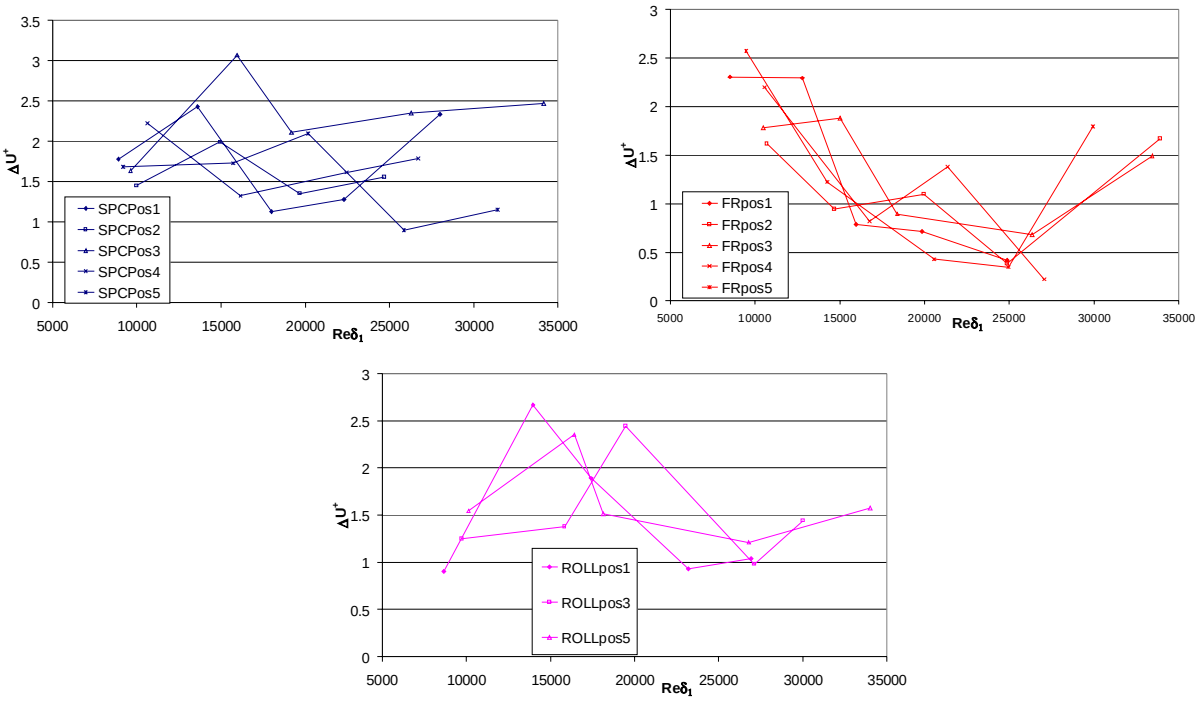

Figure 7.11. Roughness functions versus $Re_{\delta 1}$ at each location of the surfaces SPC, FR and ROLL.

Figure 7.11 shows the roughness functions versus $Re_{\delta 1}$ at each different measurement location for the surfaces SPC, FR and ROLL. Ignoring the difference between the average and

unknown local roughness (thus allowing for lateral displacement if re-plotted against roughness Reynolds number), the curves should nevertheless show the same trend with increasing Reynolds number. While this is the case for the FR surface and to a lesser extent for the ROLL surface, it is more problematic in the case of the SPC surface. However, even for the FR surface (and allowing for the experimental uncertainties), the curves do not show a monotonic increase with Reynolds number as would be expected from the Colebrook-White law, but exhibit inflections.

In his later publications on the correlation between roughness and drag, Grigson (1987, 1992), Grigson showed that many surfaces on close inspection do not exhibit Colebrook-White behaviour, but that instead the roughness function for many surfaces is a complicated function with many points of inflection in the transitional flow region. He also severely criticised Equation 7.10 and Figure 7.2 by stating that in the important region (low-drag surfaces for which $\Delta U^+ < 2$) the agreement is not good. Grigson (1992) closely inspected several of the surfaces shown in Figure 7.2 (e.g. the surfaces from Todd, 1950 and Walderhaug, 1986, and one from Musker, 1977) and showed that the roughness functions had inflections and were therefore not following Equation 7.2. Consequently, Grigson went as far as to say that information about the geometry of the roughness of a surface is not relevant and that instead one should only determine the roughness function for a particular surface experimentally. A database of roughness functions in addition to quality checks of the paint application by inspection should then suffice to determine the added drag.

If Grigson's recommendations are observed, the present analysis can conclude from the roughness functions and the quality inspections that the Foul Release surfaces studied here exhibit less drag than SPC surfaces for a fairly wide range of application (best-practice to poor surface preparation). In contrast, the SPC surfaces can be said to all have been of similar (good to excellent) quality, but the surfaces show a rather wider band of roughness function values. However, the Author believes that if one takes the effort of determining the roughness function experimentally, one might as well take the little extra effort of gathering roughness data. This information can then be analysed and help to improve on the correlation between roughness and drag. One should also aim at determining the roughness function at full-scale roughness Reynolds numbers because the extrapolation towards higher Reynolds numbers is also a factor of uncertainty (and consequently roughness measurements are relevant in any

analysis). One is still not sure whether all surfaces indeed reach the fully rough region (Raupach et al., 1991). Grigson (1982) therefore points out that the range of roughness Reynolds numbers tested in the laboratory should lie within the range at full scale.

The Colebrook-White law is only one (simple) form of interpolation between the hydraulically smooth and the fully rough region. The Ligrani method which was briefly (and uncritically) applied to find the equivalent sand roughness in Section 7.3 is another, which puts the condition of reaching the fully rough region at $h_s^+ = 90$ and becoming hydraulically smooth at $h_s^+ = 2.25$. Bandyopadhyay (1987) gives an interpolation formula for h-type roughness, which only depends on the value of the roughness function at the upper limit of the transition regime, i.e. ΔU_u^+ at a roughness Reynolds number h_u^+:

$$\frac{\Delta U^+}{\Delta U_u^+} = 0.5\left[1 - \cos\left(\pi \frac{h^+}{h_u^+}\right)\right] \tag{7.16}$$

whereby h is the height of the roughness elements and h_u^+ depends on the density and aspect ratio of the elements. For this type of roughness, Bandyopadhyay has given an explanation for the physical significance of h_u^+ in terms of vortex shedding. If in the case of irregularly rough surfaces like ship hulls, h is taken as the AHR (i.e. an average of Rt50), the onset of the fully rough regime, h_u^+, will vary with the texture of the surface (Lewkowicz and Musker, 1978). When the characteristic measure h is taken as a combined amplitude and texture parameter for a specific class of surfaces like in the present work, the onset of the fully rough regime is expected to occur at the same h_u^+ for those surfaces.

As yet, there is no explanation for the physical mechanisms which determine the behaviour of rough surfaces in the transitional (or intermediate) flow regime and it is plausible to expect one coated surface to behave differently from another. Colebrook's assumption was that 'engineering' surfaces can all be expected to behave similarly (whereas sand surfaces behave differently). As such, the Colebrook-White law has found wide application and for example has recently been applied for pipe flow experiments (e.g. Perry et al., 2001). The present analysis, and the data collected by other researchers, show that despite the fairly wide margins, the Colebrook-White law nevertheless gives a reasonable correlation between roughness and drag for coated surfaces. However, when using these results in order to predict added drag at full scale, the relatively wide margins of error must be borne in mind.

7.6 Regular roughness viewed as an asymptotic case of irregular roughness

The basic argument in the semi-empirical approach used to correlate roughness function with roughness Reynolds number was the assumption that surfaces with irregular roughness obey the Colebrook-White law, given by Equation 7.2 and discussed in the previous section. This law was derived from an asymptotic matching process whereby the roughness function of a smooth surface is equal to zero and the roughness function in the fully rough regime only depends on the geometry of surface and not on the Reynolds number. An asymptotic matching process was also encountered in Chapter 4 in the derivation of the logarithmic law of the wall.

Instead of looking at the roughness function in asymptotic cases, one may also look at the geometry of the surface in an asymptotic form and observe that regular or geometrical roughness is an asymptotic case of irregular roughness.

It was mentioned in Chapter 4 that there is a great deal more information available on the flow behaviour over regular rough surfaces than over irregular rough surfaces. It may be useful to see whether the literature on regular roughness can give further information on the flow and drag behaviour observed over the irregular rough surfaces analysed in Chapter 6.

The main conclusion from Chapter 6 was that the main characteristic which distinguishes the roughness of Foul Release surfaces from SPC surfaces, is its texture. Several researchers have considered the roughness density of geometrical elements as a texture parameter. The influence of roughness density on the turbulent boundary layer in the fully rough region was studied by Bettermann (1966) and Dvorak (1969). The correlation devised by Dvorak and Bettermann was later improved by Simpson (1973). Similar work carried out in meteorological boundary layers was mentioned in Yaglom (1979) and Raupach et al. (1991). More recently this topic of research has been extended experimentally by Sigal and Danberg (1990) and theoretically by Trunev (1999).

Looking at the roughness profiles in Appendix E.3, one may view the roughness profiles as an irregular case of triangular roughness sketched in Figure 7.12. Imagine a surface of evaluation length L entirely made up of a number N of roughness triangles with height Ra. Therefore, one could use, as suggested by Simpson (1973), a texture parameter which is the area perpendicular to the flow divided by the area of the surface. Per unit width, it is equal to

N·Ra/L in this case. If one observes that the mean absolute slope is equal to $\Delta a = Ra/(L/2N)$, the roughness density parameter as a measure of texture is equal to $\Delta a/2$.

Therefore, a characteristic measure of such a surface which incorporates the (average) height and texture is $h = Ra \cdot \Delta a/2$. One might also use the RMS slope and height, or take Rt as an amplitude parameter. As seen in Section 6.4, these parameters are highly correlated with Ra and Δa.

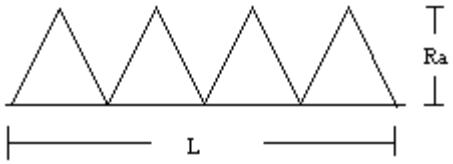

Figure 7.12. Sketch of geometrical roughness consisting of N triangles over a length L with an average height Ra

One could therefore draw a parallel with the approach used in regular roughness and Grigson's approach for irregular roughness using the characteristic measure suggested here. For regular roughness, the height parameter becomes Ra and the roughness function χ_r in the fully rough flow region was related by several researchers to the textural influence $\Delta a/2$ in the fully rough flow region. This would correspond to Grigson's factor 1/m in the transitional flow regime using (individual) Colebrook-White functions for irregular rough surfaces. Grigson noted (1982) that low drag surfaces display higher m values, which is in accordance to the observations made here.

One does not even have to postulate that a particular surface obeys the Colebrook-White law. Even if a surface would not follow a Colebrook-White law in the transitional flow region, the value of the roughness function χ_r to which χ converges in the fully rough flow region would then determine 1/m of a unique *conceptual* Colebrook-White function for that surface. However, to use this function to predict the values of the roughness function in the transitional flow regime would imply very high uncertainties.

To summarise, the texture parameter $\Delta a/2$ which has been suggested here to correlate drag and roughness characteristics of coated surfaces, has also been used for that purpose in the case of regular roughness of varying configurations.

It is important to point out that this parameter can only account for a limited class of rough surfaces. For example, the parameter cannot be applied for 'rough' surfaces which do not add drag. One example is the application of a random arrangement of bumps on a smooth surface which can lead to up to 12% drag reduction; however, if the bumps are arranged in an aligned pattern they lead to drag enhancement (Carpenter, 1997; Sirovich and Karlsson, 1997). Another obvious example are 'riblets', which are basically grooved surfaces which can reduce drag by as much as 10% (Nieuwstadt et al., 1989; Walsh, 1990; Choi, 1998). The grooves on the surfaces aim to confine and order the streaks in the viscous sublayer. The optimum results are obtained from riblets with triangular and semi-circular cross sections of the order of viscous sublayer thickness of the boundary layer (Bechert and Bartenwerfer, 1989, Bechert et al., 1997). The possible effects of misalignment between the free stream direction and the grooves are very important. Results showed that there was very little change in the drag reduction performance up to a yaw angle of 15 degrees, but no net drag reduction was observed from a ribbed surface yawed more than 30 degrees (Nieuwstadt et al., 1991; Choi, 1991). Viewed as special cases of roughness, drag reduction has also been reported for wavy surfaces with a small amplitude-to-sublayer-thickness ratio (Himeno and Noudo, 1988) and d-type roughness with longitudinal ribs placed within transverse grooves (Osaka and Mochizuki, 1991).

The correlation of drag and roughness in general must therefore involve aspects such as roughness distribution and alignment. Ultimately, one should be able to predict the added drag of a surface in the transitional flow regime if (sufficient) details on the roughness on that surface are known. The fine details which determine whether a surface follows the Colebrook-White law, whether there is a region for which drag reduction occurs etc., are at present not known. The semi-empirical approach used here can only try to match experimentally determined drag and roughness results, and then only for a restricted class of surfaces. It is likely that the ultimate solution to this problem will not be solved in a semi-empirical manner, but by resolving the physical mechanisms which govern the flow over rough surfaces, as discussed in Section 7.7.

7.7 Alternative approaches to the correlation of roughness and drag

In the previous Sections of this Chapter, a semi-empirical approach based on the Colebrook-White law in the transitional flow region has been used to correlate the roughness characteristics of a surface with the roughness function. This approach has been used by several researchers for coated ship hull surfaces, but other methods of correlating drag and roughness have been used in the aeronautical sciences and in the study of heat transfer.

As mentioned in Section 7.2, the classic approach is the use of the equivalent sandgrain roughness, originally devised by Schlichting in 1936 (Schlichting, 1979). If a surface is known to exhibit a certain roughness function, an equivalent sandgrain roughness h_s is attributed to that surface as characteristic measure of roughness. If the roughness function is not known a priori, correlation of the sand-grain roughness with the geometry of the roughness like the relationships devised by Bettermann (1966), Dvorak (1969) and Simpson (1973) may be used to predict the increase in drag. In the previous Section, it was shown that this is very similar to the semi-empirical method used in this Chapter. However, just like the semi-empirical approach, the classic approach suffers from the fact that the roughness function does not correlate very well with the roughness measure and that little is known of the bahaviour in the transitional flow region.

An alternative approach to predict rough-wall skin friction is the discrete element approach (Musker, 1991). In this approach, the effects of a collection of individual roughness elements on the flow are generally considered by including a form drag term in the momentum equation (cf. Chapter 4) and by accounting for the blockage effect of the roughness elements on the flow. The division in form drag and viscous drag of the roughness elements was originally also mentioned by Schlichting in 1936 (Schlichting, 1979), and was later developed by other researchers (e.g. Liepmann and Goddard, 1957; Lewis, 1975; Coleman et al., 1984; Taylor et al., 1985; Trunev, 1999).

At one point, this approach will eventually involve near-wall physics to model the interaction between the boundary-layer flow and the rough wall.

In this study the emphasis has been on approaching the problem from a study of the roughness characteristics and by evaluating a promising characteristic measure against the collected roughness functions. Conversely, one may attempt to find length scales which seem relevant from the flow behaviour in the boundary layer. In the case of the equivalent sand roughness it is known that the fully rough region is reached for $h_s^+ = 70$ to 90, but this value

also depends on the surface geometry (Raupach et al., 1991). From a physical point of view it is not clear how these values relate to the rough-wall geometry. Relevant length scales were proposed by Walderhaug (1986) and Musker (1977) in order to derive the long-wavelength cut-off length. Musker assumed that the integral length scale, which is an indication of the size of the largest eddies in the boundary layer, is directly influenced by wall roughness and therefore relevant in scaling the roughness. As mentioned in Section 5.2.4.8, both Musker (1977) and Kutlar and Lewkowicz (1990) found that the integral length scales increased for rough surfaces at $y/\delta = 0.05$ which is the region of major turbulence production and collapsed for the different surfaces (to about 0.4δ) further away from the wall. This difference was not observed for the present boundary-layer experiments, not even for the SAND surface, but Raupach et al. (1991) mention that very close to the wall ($y/h = 1$) the integral length scale becomes equal to the height of the roughness elements, so that it seems to be a very relevant parameter. The effective cut-off length, so effective in correlating rougher surfaces in the present and in Dey's (1989) analysis, therefore may well be related to the integral length scale.

One may also contemplate how the rough wall interacts with the coherent structures in the turbulent boundary layer, as Walderhaug did (1986). In particular, one may envisage that the rough wall essentially interacts with the near-wall streamwise vortices (cf. Section 4.2), shown in Figure 4.2. These vortices precede the eruption and bursting process which is the main contributor to the turbulence production. It may be expected that a rough wall which protrudes through the viscous sublayer will promote the instability of the streamwise vortices, thus hastening the eruptions.

The vortices are known to have a characteristic wavelength of approximately 100 wall units, i.e. $\lambda^+ = 100$ (Meng, 1998). Since the main differences between the Foul Release and the SPC surfaces lie in the texture of the surfaces, one may compare the characteristic wavenumber of the streamwise vortices with the power spectra of the roughness distributions of the surfaces shown in Figure 6.11 and Figure 6.13.

The water tunnel experiments carried out in Section 5.2 were carried out for wall units ν/U_τ between approximately 3 and 20μm for the smooth surface, so that the streamwise vortices would extend over a characteristic wavelength between 0.3 and 2mm, equivalent to wavenumbers between 3 and 21rad/mm. If one compares this with the typical power spectra for both surfaces shown in Figure 6.11 and Figure 6.13, one notices that the wavenumber range 3-20rad/mm contributes little to the total power of the Foul Release surface, whereas

the contribution is significant to the total power of the SPC surface. Figure 7.13 and Figure 7.14 clarify this by plotting the cumulative normalised spectral moments for both surfaces (at 5/50; except for m_0' which shifts slightly to the right, the cumulative spectral moments do not change for 2.5/50). The cumulative spectral moment of order n is given by:

$$m_n' = m_n(\omega') = \int_0^{\omega'} \omega^n S(\omega) d\omega \qquad (7.15)$$

where ω' may assume any value between 0 and ω_h.

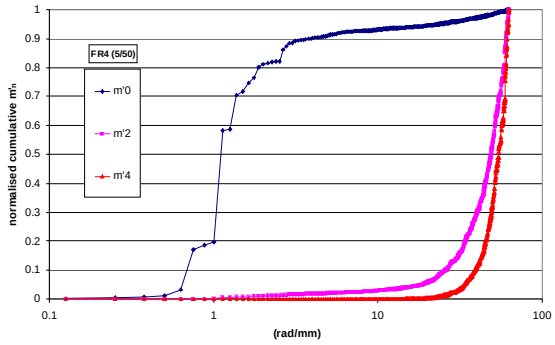

Figure 7.13. Cumulative normalised spectral moments for FR4 (5/50).

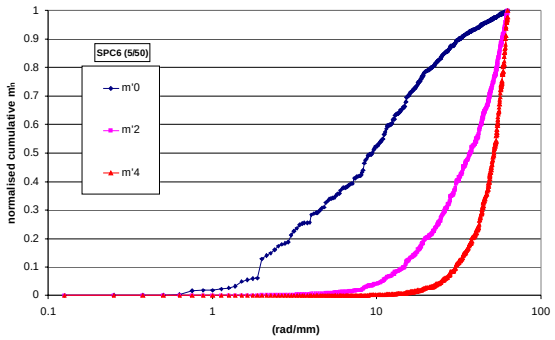

Figure 7.14. Cumulative normalised spectral moments for SPC6 (5/50).

Figure 7.13 shows that for the Foul Release surface 90% of the total power is contributed by wavenumbers below 3rad/mm and 95% by wavenumbers below 20rad/mm. In contrast, Figure 7.14 shows that for the SPC surface higher wavenumbers contribute more to the total power; wavenumbers below 3rad/mm contribute 21% to the total power, wavenumbers below 20rad/mm contribute 79%. Low wavenumbers contribute little to the second spectral moments. Wavenumbers below 20rad/mm contribute 5% to the total for the Foul Release surface and 20% for the SPC surface; below 3rad/mm the figures are 1.5% and 0.3% respectively. According to Hearn and Metcalfe (1995), this indicates that low wavenumbers are of such negligible slope that their hydrodynamic influence can be discounted, thus justifying a cut-off length of 2.5 to 5mm for the surfaces considered here. In addition, they point out that the cumulative fourth spectral moment rises so sharply that it is unstable and not very suitable to be included in a characteristic measure h.

It is interesting to note that, if the spectra of marine surfaces indeed follow a power law, given by Equation 6.8, the cumulative normalised spectral moments, will only depend on the Fractal Dimension (and ω'/ω_h), but not on the topothesy (or scaling factor) G. A lower Fractal Dimension implies that less power is contributed by higher wavenumbers. Based on the

cumulative normalised second spectral moment, theoretically expressed by $(\omega'/\omega_h)^{2FD-2}$, the cut-off length for which the contribution to m'_2 falls below a certain level increases as FD decreases. Figure 7.15 shows the cumulative normalised spectral moments based on Equation 6.8 for FD = 1.265 and FD = 1.6, and shows that there is quite discrepancy with Figure 7.13 and Figure 7.14, which is mainly due to the fact that the lowest wavenumbers fall below the power law predictions (cf. Figure 6.14). Nevertheless, the observations made in connection with Figure 7.13 and Figure 7.14 generally hold.

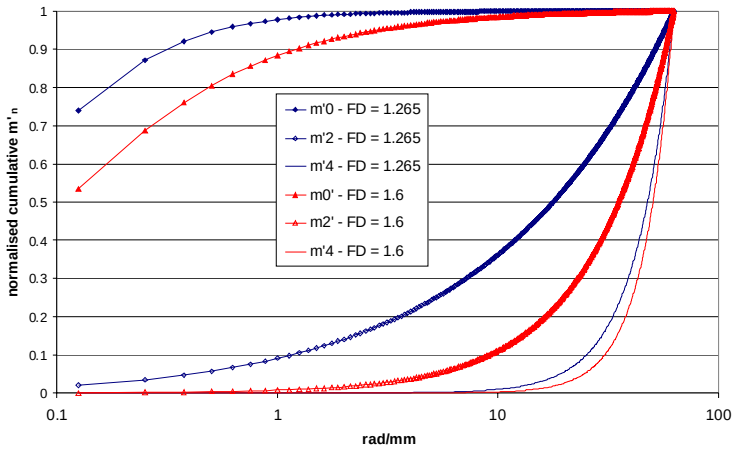

Figure 7.15. Cumulative normalised spectral moments calculated from Equation 6.8.

The cut-off length for the present surfaces agrees with the observations made regarding m'_2. For rougher surfaces, an effective cut-off length has been introduced which is much longer than would be predicted from this analysis. However, it is likely that the effective cut-off length accounts for the (possibly) more violent 'ejections' and the larger size of the eddies in the near-wall, and should rather be related to the integral length scale

One may assume that wavelengths longer than $\lambda^+ = 100$ will not influence the near-wall streaks, but shorter wavelengths may act to 'trip' the streaks, promoting their instability and hastening their ejections. When the surface becomes rougher, it may be expected that short-wavelength roughness trips the streaks so quickly that they are effectively no longer detectable in the near-wall, but ejections will remain present and may be relatively 'violent'. This conceptualisation would be in accordance with the observations of coherent motions on rough-wall turbulent boundary layers discussed by Grass et al. (1991) and Raupach et al. (1991). Djenidi and Antonia (1997), however, believe that other mechanisms than the creation

and regeneration of vortices are involved over certain types of roughnesses whereby bursts are not being set off by conditions in the sublayer.

In other words, the texture of the SPC surface is such that it is likely to interfere much more than a Foul Release surface with the streamwise vortices in the turbulent boundary layer. This is expected to hasten the eruption and bursting process, resulting in higher turbulence production and consequently higher skin friction.

7.8 The prediction of drag from roughness characteristics

From a practical point of view, the measurement of the roughness of a ship hull will often evoke expectations to predict the (added) frictional drag of that ship and the cost penalties involved. Equation 7.1, which was specifically derived for this purpose (Townsin et al., 1984), would become inappropriate if the new parameter h suggested here to incorporate the texture of the surface is introduced.

Medhurst (1989) gives an interesting account as to how Equation 7.1 was derived. Following the work of Musker (1977), Medhurst put a lot of effort into developing a software package which was able to predict the boundary layer behaviour on a ship based on an integral method which incorporated a Colebrook-White friction relation. The Colebrook-White law was derived from the roughness characteristics of different investigated surfaces and as such was a precursor of Equation 7.10 or Equation 7.15 (using a different characteristic measure h and a different constant m). The ΔC_F values predicted with this software package for a number of different ships were compared with available full-scale data. Equation 7.1 eventually resulted as a regression line from these data.

It falls outside the scope of this work to develop a boundary layer prediction method or to incorporate the new friction relation 7.15 into an existing boundary layer prediction method in order to derive a new relationship between ΔC_F and h.

It is the Author's personal opinion that Equation 7.15 needs full-scale validation before the development of such a relationship can be usefully applied. This will inevitably require the recording of digital roughness profiles from ship hull surfaces in order to calculate Δa or other texture parameters. The current practice of measuring ship hull roughness will therefore have to be modified and this issue will be addressed in Section 8.2. One also has to point out that the use of Equation 7.15 will always be controversial since it assumes that all painted surfaces follow the Colebrook-White law in the transitional flow regime (wherein most ships operate). Further validation of this is also required.

Nevertheless, if one wishes to know how a set of values h and ΔU relate to a set of Re and C_F, one could use a chart for flat plates, like Figure 7.16, taken from Granville (1958). This flat plate approach assumes that the added drag on a ship due to roughness is equal to the added drag on a flat plate with the same length and wetted surface, in the same philosophy as the ITTC approach (1957, 1978) adopted from Froude (1874b) for 'smooth' ships. The effect

of roughness is currently adopted by the ITTC in an entirely different way, but this approach is suggested here for reasons of simplicity and brevity. Tokunaga and Baba (1983) have compared a flat plate approach with a two-dimensional boundary-layer prediction theory and concluded that a flat plate approximation may serve as a practical prediction tool within acceptable accuracy. Their approach was based on the scaling laws established by Sasajima et al. (1965) and Sasajima and Himeno (1965). In the present approach, hydrodynamic similarity between model and ship scale is achieved by adjusting the Reynolds number and the non-dimensional roughness parameter L/h simultaneously, not taking Froude's similarity law into consideration (Nakato et al., 1985).

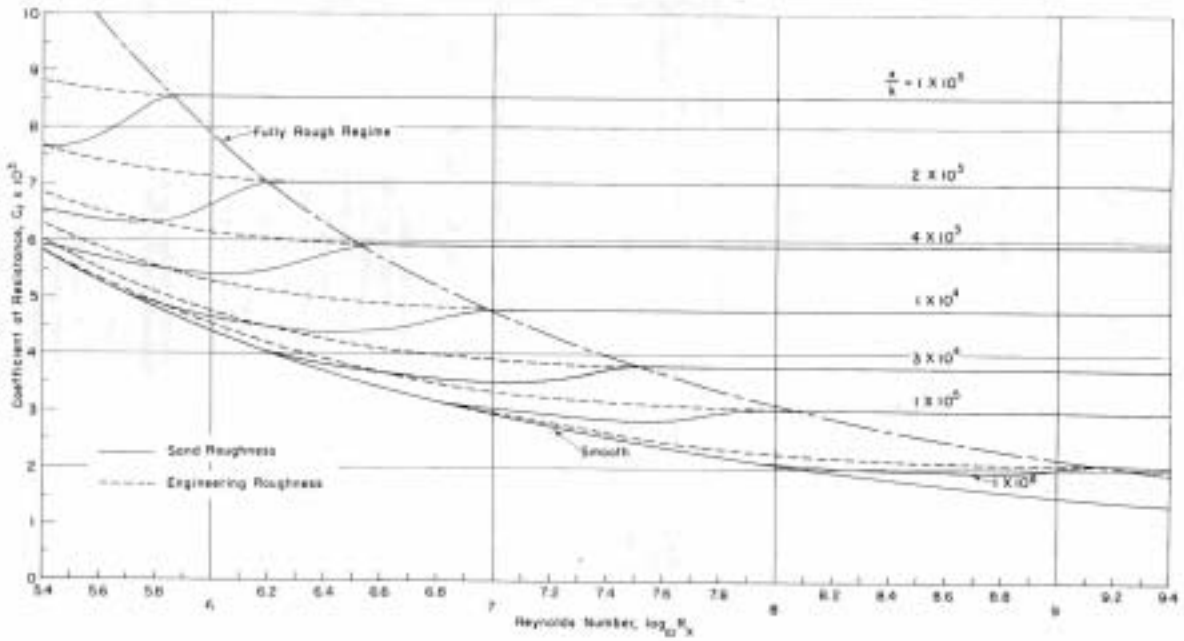

Figure 7.16. Granville's chart to predict the drag of rough flat plates (From Granville, 1958).

Granville (1958) used the Colebrook-White law to draw the lines of 'engineering roughness' in Figure 7.16. He assumed that χ_r would be equal to 7.2, so that by using Equation 7.8, the current values of h have to be multiplied by a factor 56 to comply. Consequently, as can be seen from Figure 7.9 the range of h-values analysed here would approximately lie between 0.1 (Foul Release) and 1000μm (Sarabchi C).

The prediction of ship boundary layers has evolved significantly since the advent of sophisticated CFD tools. The incorporation into these purpose-built packages of Equation 7.15 as a friction relation to account for the effect of roughness is therefore an attractive avenue of further research (Patel, 1998; Leer-Andersen, 1999).

7.9 Summary of the correlation of roughness, drag and boundary-layer characteristics

A semi-empirical approach based on the Colebrook-White law in the transitional flow region has been applied to correlate the roughness characteristics of the different surfaces with their roughness functions. This approach involves the selection of a characteristic roughness measure h which gives the best correlation assuming that the roughness function of the surfaces obeys the Colebrook-White law.

The characteristic which was found to give to best correlation for the present surfaces is $h = Ra \cdot \Delta a/2$ for a cut-off length of 2.5mm. This characteristic measure involves both the texture and amplitude characteristics of the rough surfaces, which is necessary in order to correlate the Foul Release surfaces.

The achieved correlation between roughness and drag is a reasonably good indication, but when used to predict the added drag in full-scale, reservations have to be made about the accuracy because the margins of error are fairly large.

From a qualitative point of view the roughness and drag of the present experiments are correlated and explained satisfactorily.

It is noted that the correlation of roughness and drag of a surface eventually will have to involve the near-wall physics of the turbulent boundary layer. It is expected that a rough wall will interact with the coherent streamwise vortices near the wall. The protuberances of a rough wall may be expected to destabilise the vortices more quickly, thus hastening the eruption and bursting process, increasing the turbulence production and ultimately causing higher friction. Typically, the streamwise vortices extend over 100 wall units. It is noted that from correlating the data of the boundary-layer experiments with the rough-wall characteristics, that the wavenumber range of the streamwise vortices overlap with the wavenumber range of the roughness distribution much more for the SPC surface than they do for the Foul Release surface. In addition, it is thought that the integral length scale can give a relevant roughness scale, which may well be connected to the effective cut-off length employed here.

The prediction of added resistance at large Reynolds numbers is only given in the case of rough flat plates, using Granville (1958). It is recommended that Equation 7.15 will be incorporated in ship boundary layer prediction methods and validated against full-scale data.

Chapter 8: Conclusions and Recommendations

8.1 Conclusions

The present investigation has systematically compared the drag, boundary-layer and roughness characteristics of marine surfaces coated with two types of antifouling paint systems: a Foul Release system and a Tin-free SPC system. This work had 5 principal objectives in mind. The first objective was to provide an in-depth literature review of present-day antifoulings and the implications of paint application on ship performance. The second objective was to provide a systematic set of resistance data for Foul Release and Tin-free SPC systems, whereas the third objective was to investigate the boundary-layer characteristics of these coatings. The fourth objective was to carry out an in-depth analysis of the roughness characteristics of the tested coatings and the fifth objective was to investigate whether there was a correlation between the drag, boundary-layer and roughness characteristics of these two antifouling systems.

The literature review given in Chapter 2 has indicated that a good understanding of the drag, boundary-layer and roughness characteristics of Tin-free SPC and Foul Release systems is timely as these systems are currently the best alternatives to TBT-SPCs, which will be banned from application by 2003. These antifouling systems work by entirely different principles. Tin-free SPC coatings rely on the steady release of toxins to kill off any fouling organisms which have attached to the surface. The Foul-Release systems studied in this work are silicone elastomers which by virtue of their low surface-energy prevent firm attachment of fouling organisms. The low surface energy is a direct consequence of the high mobility of the molecules around the polymeric backbone, which in turn may be expected to have repercussions on the roughness characteristics of the coatings. Moreover, since fouling organisms in general prefer to settle and attach more strongly on rough surfaces, Foul Release surfaces may partly rely on their smoothness to be effective. This work has investigated whether these idiosyncratic characteristics of Foul Release systems have repercussions on the drag, boundary-layer and roughness characteristics compared to Tin-free SPC systems.

While antifouling paints are an essential component to keep a seagoing vessel economic, the application of paint will add resistance to the smooth unpainted hull surface. In view of the impending TBT ban, several alternative antifoulings have been commercialised

over the last decade. To the Author's knowledge, this work is the first to present systematic resistance, boundary-layer and roughness data on two of the best of these alternatives currently available.

In Chapter 3, three sets of towing tank experiments were carried out, two with plates of different size and one with a wave-piercing catamaran model. The first two sets of experiments showed that the Foul Release system exhibits less drag than the Tin-free SPC system. In an extension to this work, rotor experiments with coated cylinders carried out by Pazouki (2001) also confirmed these findings. The experiments with the catamaran model showed an increase of resistance for the Foul Release system compared to the Tin-free SPC system. This was caused by the application choices. Firstly, only one (thin) coat of Tin-free SPC was applied and which has been shown to give lower drag than the two coats applied for all other experiments (cf. Section 6.5.3). Secondly, the Foul Release system was applied by rollering which virtually eliminates any drag benefits sprayed Foul Release systems have over Tin-free SPC systems.

The friction of a surface in fluid flow is caused by the viscous effects and turbulence production in the boundary layer close to the surface. A study of the boundary-layer characteristics of the coatings is therefore relevant. A literature review on rough-wall turbulent boundary layers has been presented in Chapter 4 to provide a theoretical basis for the analysis of the boundary-layer experiments presented in Chapter 5. It is noted that compared to regular roughness, relatively little boundary-layer experiments have been carried out for irregular rough surfaces. The boundary-layer experiments reported in this work were carried out in two different water tunnels using LDV equipment and to the Author's knowledge this is the first time LDV equipment has been used for boundary-layer experiments for antifoulings or for marine coated surfaces in general and reported in the open literature. An outer-layer similarity method and the Reynolds stress method were used to determine the friction velocity and both methods showed good agreement with each other. The experiments showed that the friction velocity for the sprayed Foul Release surfaces is significantly lower than for the rollered Foul Release or sprayed Tin-free SPC surfaces. This indicates that at the same streamwise Reynolds number the ratio of the inner layer to the outer layer is smaller for Foul Release surfaces than for the other coated surfaces. The inner layer is that part of the boundary layer where major turbulence (and hence drag) production occurs. The roughness functions were determined for the different surfaces and confirmed the findings from the drag tests carried out with friction planes that the Foul Release surfaces

exhibit less drag than Tin-free SPC surfaces. The turbulence characteristics scale on the friction velocity and increase with roughness in the inner layer when scaled with the free-stream velocity (although this is not entirely clear with regards to the turbulence intensities within the experimental uncertainty). In the inner layer, the integral length scale determined from spectra and autocorrelation functions is expected to increase with roughness, but such a trend was not observed here. Acquiring more accurate near-wall flow measurements and structural boundary-layer information obtained by flow visualisation and conditional analysis could possibly reveal more differences between the coatings and this is recommended as future work in Section 8.2.

A detailed roughness analysis of coated sample plates was carried out in Chapter 6 with a UBM optical measurement system. The methodology which was developed applies a moving average 'boxcar method' to filter the data. The bandwidth limits which have been used in the analysis are 2.5&50 and 5&50. Larger cut-off lengths have not been included due to the restricted evaluation length of the roughness profile. This is not a drawback since the effective cut-off lengths, below which the roughness is estimated to influence the flow hydrodynamics, lie between 2.5 and 5mm for the coated surfaces analysed in this work.

This roughness analysis has revealed that when the profiles are filtered, the amplitude parameters of the sprayed Foul Release surfaces are lower than those of the rollered Foul Release surfaces and the SPC surfaces. The rollered Foul Release surfaces display a roughness height distribution which is considerably more leptokurtic than the sprayed Foul Release surfaces. The greater number of high peaks on the rollered Foul Release surfaces is expected to engender higher drag than sprayed Foul Release surfaces.

The main difference between the Foul Release and the Tin-free SPC systems lies in the texture characteristics. Whereas the Tin-free SPC surface displays a typical 'closed texture', the 'open' texture of the Foul Release surface is caused by a greater proportion of long wavelengths. This is particularly evident in parameters such as the mean absolute slope angle Sa, the Fractal Dimension FD and the correlation lengths. The character of the texture is particularly evident from plots of the power spectra and the autocorrelation function. The spectra of the coated surfaces seem to follow a power law which is dependent on the Fractal Dimension and an implication of self-affine behaviour. A surface with an 'open texture' will therefore have a lower Fractal Dimension than a surface with a 'closed texture'. There is relatively little data available in literature on the influence of texture of irregular surfaces on drag, but one source (Grigson, 1982) shows that open textures have a beneficial effect on

drag. It is believed that the rheology of the paint (which is significantly different for Foul Release systems than for Tin-free SPC systems as is clear from a parameter such as the viscosity) has a direct effect on its texture, whereas amplitudes depend significantly on the application quality. Correlation of the texture parameters with the amplitude parameters, however, shows that the two are inter-related so that bad application can be expected to have a knock-on effect on the texture parameters.

A typical Foul Release coating scheme has a different build-up than a SPC scheme. A typical primer has a 'closed' texture characterised by short wavelengths, much like SPC surfaces. The tiecoat in a Foul Release scheme alters the texture of the surface and decreases the amplitude parameters moderately. The subsequent topcoat further decreases the amplitude parameters. In the SPC scheme, the final texture is not changed significantly. Each subsequent coat of SPC increases the amplitude parameters significantly.

Extrapolation of the maximum amplitudes (Rt) to a cut-off length of 50mm using the Fractal Dimension as scaling parameter showed fairly good agreement with the AHR measurements obtained with the BMT Hull Roughness Analyser. Some suggestions concerning future roughness measurements will be made in the following Section. To the Author's knowledge, this is the first time that the Fractal Dimension has been systematically included in the roughness analysis of marine coatings. The Author believes that it is a useful parameter that reveals some of the inherent characteristics of the material of the coatings. Its inclusion in the analysis allows scaling of the amplitude parameters to different cut-off lengths. The Fractal Dimensions do not seem to depend on the application and seem to be ca. 1.2-1.3 for the Foul Release surfaces and ca. 1.6 for the Tin-free SPC surfaces.

In Chapter 7, it was demonstrated that the roughness characteristics correlate qualitatively with the drag differences observed in the experiments reported in Chapter 3 and Chapter 5. A semi-empirical approach has been applied to correlate the roughness characteristics of the different surfaces with their roughness functions. This approach involves the selection of a characteristic roughness measure h which gives the best correlation assuming that the roughness function of the surfaces obeys the Colebrook-White law.

The characteristic measure which was found to give the best correlation for the present surfaces is $h = Ra \cdot \Delta a/2$ for a cut-off length of 2.5mm. This characteristic measure incorporates both the texture and amplitude characteristics of the rough surfaces.

The appropriateness of using the Colebrook-White law has been discussed and it is noted that the correlation of roughness and drag of a surface eventually will have to involve

the near-wall physics of the turbulent boundary layer. The integral length scale is a physical boundary-layer length scale which has been suggested to be related to the cut-off length used in roughness analysis (Musker, 1977). However, as mentioned, clear differences in the integral length scales were not observed in the present boundary-layer experiments.

It is expected that a rough wall will interact with the coherent streamwise vortices near the wall. The protuberances of a rough wall may be expected to destabilise the vortices more quickly, thus hastening the eruption and bursting process, increasing the turbulence production and ultimately causing higher friction. Typically, the streamwise vortices extend over 100 wall units (cf. Figure 4.2). Correlating of the data of the boundary-layer experiments with the rough-wall characteristics shows that the wavenumber range of the streamwise vortices overlap with the wavenumber range of the roughness distribution much more for the SPC surface than they do for the Foul Release surface.

In conclusion, this work has established that there are fundamental differences between the Foul Release and Tin-free SPC coatings in terms of drag, roughness and friction velocity. From a qualitative point of view, the experiments have shown that because of these differences, a typical application by the same operator of a newly sprayed Foul Release system will result in less added drag than a newly applied Tin-free SPC system.

8.2 Recommendations for further work

From a quantitative point of view the correlation between roughness and drag was not entirely satisfactory and further work is recommended. The ultimate objective of this field of research is to correlate drag and roughness satisfactorily, which would then allow the prediction of the full-scale added drag of a ship if enough information on the condition of its hull is available.

It is recommended that more data (both roughness function and characteristic measure h) are collected on coated surfaces. It is particularly important to obtain data from surfaces representative of in-service ship hull conditions. This is a logical extension of the present work, which needs to be addressed before any predictions of added drag can be made satisfactorily. This issue is complicated by the fact that antifouling coatings prevent macro-fouling but not the formation of slime films.

The behaviour of rough (and by extension coated) surfaces in the transitional flow regime is at present not physically explained. The Colebrook-White law is an empirical law and it has to be established whether this law is unambiguously valid for coated surfaces.

The roughness functions of coated surfaces have to be incorporated in boundary layer prediction methods. This has been suggested by many researchers in CFD (Patel, 1998; Leer-Andersen, 1999; Date and Turnock, 2000) and the present data may serve for that purpose provided they will be validated and refined if necessary.

The acquisition of roughness data in the future will only be useful if texture parameters are also measured. While a non-contact instrument in the long term is preferable to contact instruments, it is thought that the BMT Hull Roughness Analyser with its virtual monopoly in dockyard use can relatively easily be adapted to store digital roughness profiles, which can then be used to calculate the desired roughness parameters. It is thought worthwhile to pursue the modification of the instrument by 2003, so that useful measurements can be taken to monitor the quality of ship hulls in the TBT-transition period between 2003 and 2008. This issue has been discussed with BMT.

It would be worthwhile to further investigate the merits and uses of the Fractal Dimension of coated surfaces. It seems interesting to try to relate it with the Fractal Dimension of the instantaneous velocity profiles in the turbulent boundary layer (Sreenivasan

and Meneveau, 1986; Tsuji et al., 1994; Nicolleau, 1996), perhaps by observing how the latter evolve in boundary-layers over walls with different Fractal Dimension.

An attempt has been made to correlate the surface characteristics with the physical phenomena in the turbulent boundary layer. The Author would suggest carrying out further research in the study of coherent motions over the different coated surfaces.

Coherent motions can be studied experimentally, by statistical analysis or numerically (Robinson, 1991). Experimentally, flow visualisation techniques using dye, particles and bubbles have been the most successful because they give much higher information density for a given area of volume than probe techniques. The most successful probe techniques have employed multiple sensors separated in space. Highly resolved temporal sequences are required for most forms of conditional signal processing. As a result, single-point instrumentation such as LDV is rarely used for structure measurements compared with the widespread use of multi-sensor hot-wire and hot-film arrays. In recent years, PIV techniques have emerged which are able to resolve the required scales.

A rich variety of statistical-analysis tools is used to study turbulent coherent motions. These techniques are used to detect and characterize the four-dimensional (space + time) structure and to quantify the contributions of the structures to the gross statistical properties of the flow. A number of conditional-sampling techniques have evolved to filter turbulence events with certain predefined characteristics. Among the most popular are the Variable-Interval Time Average (VITA) method, the u'v' quadrant method and proper orthogonal decomposition. Key aspects of conditional sampling techniques for turbulence structures have been reviewed by for example Antonia (1981).

Numerical methods used in the study of coherent motions are Large Eddy Simulations (LES) and Direct Numerical Simulations (DNS). These methods, however, are currently not applicable on irregular rough surfaces.

The Author would therefore suggest to study the coherent motions over coated surfaces both experimentally by PIV (provided the required resolutions can be met) and statistically by conditional sampling techniques. This can be combined with further LDV measurements as carried out in this work, which aim to get more accurate data closer to the wall. This can be done for the experimental set-up used in Chapter 5 by adding a beam expander, which would reduce the probe volume and allow more readings closer to the wall, and by extending the boundary layer plate, which would thicken the boundary layer.

References

Adrian, R.J. (1996), Laser velocimetry. In: *Fluid Mechanics Measurements (2nd Edition)*, R. J. Goldstein (Ed.), Philadelphia, PA, Taylor & Francis**,** pp. 175-299.

Aertssen, G. (1955), Further sea trials on the Lubumbashi. *Transactions of the Institution of Naval Architects,* Vol. 97, pp. 502-530.

Allan, J.F. and Cutland, R.S. (1956), The effect of roughness on ship resistance. *Transactions of the North-East Coast Institution of Engineers and Shipbuilders,* Vol. 72, pp. 257-278.

Anderson, C.D. (1993), Self-polishing antifoulings: a scientific perspective. *Proceedings of Ship Repair and Conversion 93*.

Anderson, C.D. and Hunter, J.E. (2000), Whither antifouling paints after TBT? *NAV 2000 International Conference on Ship and Shipping Research, 13th Congress,* Paper 3.7. Venice, Italy, 19-22 September 2000.

Anderson, C.D. (2000), Antifoulings: Regulatory and Technological Update. Newcastle-upon-Tyne, External Lecture at the University of Newcastle-upon-Tyne, 12 December 2000.

Antonia, R.A. and Luxton, R.E. (1971), The response of a turbulent boundary layer to a step change in surface roughness. Part 1. Smooth-to-rough. *Journal of Fluid Mechanics,* Vol. 48, pp. 721-761.

Antonia, R.A. and Luxton, R.E. (1972), The response of a turbulent boundary layer to a step change in surface roughness. Part 2. Rough-to-smooth. *Journal of Fluid Mechanics,* Vol. 53, pp. 737-757.

Antonia, R.A. (1981), Conditional sampling in turbulence measurement. *Annual Review of Fluid Mechanics,* Vol. 13, pp. 131-156.

Antonia, R.A. and Krogstad, P.-A. (2001), Turbulence structure in boundary layers over different types of surface roughness. *Fluid Dynamics Research,* Vol. 28, pp. 139-157.

Atlar, M. and Korkut, E. (1997). Emerson Cavitation Tunnel inflow characteristics based on 2-D Laser Doppler Anemometry analysis, *Report No. MT-1997-001*, University of Newcastle-upon-Tyne, Newcastle-upon-Tyne.

Atlar, M. (2000), A history of the Emerson Cavitation Tunnel and its role in propeller cavitation research. *NCT '50 International Conference on Propeller Cavitation,* pp. 3-34. Newcastle upon Tyne, 3-5 April 2000.

Baier, R.E. (1970), Surface properties influencing biological adhesion. In: *Adhesion in Biological Systems*, R. S. Manly (Ed.), Academic Press**,** pp. 15-48.

Baier, R.E., Meyer, A.E. and Forsberg, R.L. (1997), Certification of properties of nontoxic fouling-release coatings exposed to abrasion and long-term immersion. *Naval Research Reviews,* Vol. 49, pp. 60-65.

Baldwin, L. (1997), Improving coating processes in the shipbuilding industry. *Protective Coatings Europe,* Vol. 2, No. 6, pp. 23-25.

Bandyopadhyay, P.R. (1987), Rough-wall turbulent boundary layers in the transition regime. *Journal of Fluid Mechanics,* Vol. 180, pp. 231-266.

Barenblatt, G.I. (1993), Scaling laws for fully developed turbulent shear flows. Part 1. Basic hypothesis and analysis. *Journal of Fluid Mechanics,* Vol. 248, pp. 513-520.

Barenblatt, G.I. and Prostokishin, V.M. (1993), Scaling laws for fully developed turbulent shear flows. Part 2. Processing of experimental data. *Journal of Fluid Mechanics,* Vol. 248, pp. 521-529.

Barthlott, W. and Neinhuis, C. (1997), Purity of the sacred lotus, or escape from contamination in biological surfaces. *Planta,* Vol. 202, pp. 1-8.

Bechert, D.W. and Bartenwerfer, M. (1989), The viscous flow on surfaces with longitudinal ribs. *Journal of Fluid Mechanics,* Vol. 206, pp. 105-129.

Bechert, D.W., Bruse, M., Hage, W., Hoeven, J.G.T.v.d. and Hoppe, G. (1997), Experiments on drag-reducing surfaces and their optimization with an adjustable geometry. *Journal of Fluid Mechanics,* Vol. 338, pp. 59-87.

Belmabrouk, H. (2000), A theoretical investigation of the exactness of Taylor length scale estimates from two-point LDV. *Experimental Thermal and Fluid Science,* Vol. 22, pp. 45-53.

Bendat, J.S. and Piersol, A.G. (1993). *Engineering Applications of Correlation and Spectral Analysis*. New York, John Wiley & Sons, Inc.

Bengough, G.D. and Shepheard, V.G. (1943), The corrosion and fouling of ships. *Transactions of the Institution of Naval Architects,* Vol. 85, pp. 1-34.

Berntsson, K.M., Andreasson, H., Jonsson, P.G., Larsson, L., Ring, K., Petronis, S. and Gatenholm, P. (2000), Reduction of barnacle recruitment on micro-textured surfaces: analysis of effective topographic characteristics and evaluation of skin friction. *Biofouling: the Journal of Bioadhesion and Biofilm Research,* Vol. 16, pp. 245-261.

Bertram, V. (2000), Past, present and prospects of antifouling. *32nd WEGEMT School on Marine Coatings,* pp. 85-97. Plymouth, UK, 10-14 July 2000.

Bettermann, D. (1966), Contribution à l'étude de la convection forcée turbulente le long de plaques rugueuses. *International Journal of Heat and Mass Transfer,* Vol. 9, pp. 153-164 (In French).

BMT (1986). *Recommended Practice for the Protection and Painting of Ships*, Wallsend Research Station.

Bogard, D.G. and Thole, K.A. (1998), Wall-bounded turbulent flows. In: *The Handbook of Fluid Dynamics*, R. W. Johnson (Ed.), CRC Press – Springer, pp.13.49-13.63.

Bohlander, G.S. (1991), Biofilm effects on drag: measurements on ships. *Polymers in a Marine Environment. The Institute of Marine Engineers Third International Conference,* Paper 16. London.

Bowden, B.S. and Davison, N.J. (1974). Resistance increments due to hull roughness associated with form factor extrapolation methods, *Technical Memo 380*, National Maritime Institute.

Brady, R.F., Griffith, J.R., Love, K.S. and Field, D.E. (1989), Non-toxic alternatives to antifouling coatings. *Polymers in a Marine Environment. The Institute of Marine Engineers Third International Conference,* Paper 26. London.

Brady, R.F. (1997), In search of non-stick coatings. *Chemistry and Industry,* pp. 219-222, 17 March 1997.

Brady, R.F. and Singer, I.L. (2000), Mechanical factors favoring release from fouling release coatings. *Biofouling,* Vol. 15, pp. 73-81.

Brady, R.F. (2000), No more tin. *Protective Coatings Europe,* Vol. 5, No. 6, pp. 42-49.

Buchave, P., George, W.K. and Lumley, J.L. (1979), The measurement of turbulence with the Laser-Doppler Anemometer. *Annual Review of Fluid Mechanics,* Vol. 11, pp. 443-503.

Byrne, D. (1980). The Hull Roughness of Ships in Service, *MSc Dissertation*, Department of Marine Technology, University of Newcastle-upon-Tyne, Newcastle-upon-Tyne.

Callow, M.E., Pitchers, R.A. and Milne, A. (1986), The control of fouling by non-biocidal systems. In: *Algal Biofouling*, L. V. Evans and K. D. Hoagland (Ed.), Amsterdam, Elsevier**,** Chapter 10.

Candries, M., Atlar, M., Mitchell, G.H.G. and Lamb, D. (1998). Flat plane towing experiments with two coatings, *Report No. MT-1998-034*, University of Newcastle-upon-Tyne, Newcastle-upon-Tyne.

Candries, M. (1998). Recent developments in surface technology and the effect on roughness and drag, *MSc Dissertation*, Department of Marine Technology, University of Newcastle-upon-Tyne and University of Ghent (Erasmus/Socrates Programme), Ghent, Belgium.

Candries, M. and Atlar, M. (2000). Influence of two different antifoulings on the resistance and roughness of a flat plate, *MT-2000-012*, University of Newcastle-upon-Tyne, Newcastle-upon-Tyne.

Candries, M. and Atlar, M. (2000b). Experiments with a wave-piercing catamaran model: the effect of three different paints, *MT-2000-067*, Department of Marine Technology, University of Newcastle-upon-Tyne, Newcastle-upon-Tyne.

Candries, M., Atlar, M. and Paterson, I. (2001). Experimental investigation of the turbulent boundary layer over painted surfaces using Laser Doppler Velocimetry. Part 1: Experiments carried out in the Emerson Cavitation Tunnel, *MT-2001-015*, Department of Marine Technology, University of Newcastle-upon-Tyne, Newcastle-upon-Tyne.

Candries, M. and Atlar, M. (2001). Experimental investigation of the turbulent boundary layer over painted surfaces using Laser Doppler Velocimetry. Part 2: Experiments carried out in the CEHIPAR Cavitation Tunnel, *MT-2001-016*, Department of Marine Technology, University of Newcastle-upon-Tyne, Newcastle-upon-Tyne.

Canham, H.J.S. (1975), Resistance, propulsion and wake tests with HMS Penelope. *Transactions of the Royal Institution of Naval Architects,* Vol. 117, pp. 61-94.

Cantwell, B.J. (1981), Organized motion in turbulent flow. *Annual Review of Fluid Mechanics,* Vol. 13, pp. 457-515.

Carpenter, P. (1997), The right sort of roughness. *Nature,* Vol. 388, pp. 713-714.

Cebeci, T. and Smith, A.M.O. (1974). *Analysis of Turbulent Boundary Layers*. New York, Academic Press. 404 pages.

Champ, M.A. (2000), A review of organotin regulatory strategies, pending actions, related costs and benefits. *The Science of the Total Environment,* Vol. 258, pp. 21-71.

Chaplin, P.D. (1967), The analysis of hull surface roughness records. *European Shipbuilding,* Vol. 16, pp. 40-47.

Choi, K.-S. (1991), Drag reduction by riblets for marine applications. *Transactions of the Royal Institution of Naval Architects,* Vol. 133, pp. 269-282.

Choi, K.-S., Yang, X., Clayton, B.R., Glover, E.J., Atlar, M., Semenov, B.N. and Kulik, V.M. (1997), Turbulent drag reduction using compliant surfaces. *Proceedings of the Royal Society of London, A,* Vol. 453, pp. 2229-2240.

Choi, K.-S. (1998), European drag reduction research - recent developments and current status. *International Symposium on Seawater Drag Reduction,* pp. 13-17. Newport, Rhode Island, July 22-24.

Chuah, K.B., Dey, S.K., Thomas, T.R. and Townsin, R.L. (1990), A digital hull roughness analyser. *International Workshop on Marine Roughness and Drag,* Paper No. 3. London, 29 March 1990.

Claisse, D. and Alzieu, C. (1993), Copper contamination as a result of antifouling paint regulation? *Marine Pollution Bulletin,* Vol. 26, pp. 395-397.

Clare, A. (1995), Natural ways to banish barnacles. *New Scientist,* Vol. 145, No. 1965, pp. 38-41, http://www.biology.bham.ac.uk/biofoulnet.

Clare, A.S. (1996), Marine natural product antifoulants: status and potential. *Biofouling: the Journal of Bioadhesion and Biofilm Research,* Vol. 9, No. 3.

Clauser, F.H. (1954), Turbulent boundary layer in adverse pressure gradients. *Journal of the Aeronautical Sciences,* Vol. 21, pp. 91-108.

Clauser, F.H. (1956), The turbulent boundary layer. *Advances in Applied Mechanics,* Vol. 4, pp. 1-51.

Colebrook, C.F. and White, C.M. (1937), Experiments with fluid friction in roughened pipes. *Proceedings of the Royal Society of London, A,* Vol. 161, pp. 367-381.

Colebrook, C.F. (1939), Turbulent flows in pipes with particular reference to the transition region between the smooth and rough pipe flows. *Journal of the Institution of Civil Engineers,* No. 11, pp. 133-155.

Coleman, H.W., Hodge, B.K. and Taylor, R.P. (1984), A revaluation of Schlichting's surface roughness experiment. *Journal of Fluids Engineering, Transactions of the ASME,* Vol. 106, pp. 60-65.

Coleman, H.W. and Steele, W.G. (1999). *Experimentation and Uncertainty Analysis for Engineers*. New York, John Wiley & Sons.

Coles, D.E. (1956), The law of the wake in the turbulent boundary layer. *Journal of Fluid Mechanics,* Vol. 1, pp. 191-226.

Collatz, G. (1986), Zum Widerstandsgesetz glatter und rauher Oberflächen. *Schiffstechnik,* Vol. 33, pp. 75-110 (In German).

Conn, J.F.C., Lackenby, H. and Walker, W.P. (1953), BSRA resistance experiments on the 'Lucy Ashton': Part 2. *Transactions of the Royal Institution of Naval Architects,* Vol. 95, pp. 350-436.

Corrsin, S. and Kistler, A.L. (1955). The free-steam boundaries of turbulent flows, *Report No. 1244*, National Advisory Committee for Aeronautics,

Cowling, M.J., Hodgkiess, T., Parr, A.C.S., Smith, M.J. and Marrs, S.J. (2000), An alternative approach to antifouling based on analogues of natural processes. *The Science of the Total Environment,* Vol. 258, pp. 129-137.

Crisp, D.J. and Walker, G. (1985), Marine organisms and adhesion. *Polymers in a Marine Environment. The Institute of Marine Engineers,* Paper 34. London.

Culver, H.B. and Grant, G. (1924, 1935). *The Book of Old Ships and Something of their Evolution and Romance*. Garden City, NY, Garden City Publishing Company Inc. 306 pages.

Czimmek, D.W. and Sandor, L.W. (1985), Economic and technical feasibility of copper-nickel sheathing. *Marine Technology,* Vol. 22, pp. 142-154.

Date, J.C. and Turnock, S.R. (2000), Computational Fluid Dynamics estimation of skin frction experienced by a plane moving through water. *Transactions of the Royal Institution of Naval Architects,* Vol. 142.

Davis, A. and Williamson, P. (1995), Marine biofouling: a sticky problem. *NERC News,* April 1996, http://www.biology.bham.ac.uk/biofoulnet.

Denny, M.E. (1951), BSRA resistance experiments on the 'Lucy Ashton': Part 1. Full scale measurements. *Transactions of the Institution of Naval Architects,* Vol. 93, pp. 40-57.

Dey, S.K. (1989). Parametric Representation of Hull Painted Surfaces and the Correlation with Fluid Drag, *PhD Thesis*, Department of Marine Technology, University of Newcastle-upon-Tyne, Newcastle-upon-Tyne.

Djenidi, J. and Antonia, R.A. (1997), Reynolds stress producing motions in smooth and rough wall boundary layers. In: *Self-Sustaining Mechanisms of Wall Turbulence*, R. L. Panton (Ed.), Southampton, Computational Mechanics Publications**,** pp. 181-199.

Durst, F., Jovenovic, J. and Sender, J. (1995), LDA measurements in the near-wall region of a turbulent pipe flow. *Journal of Fluid Mechanics,* Vol. 295, pp. 305-335.

Durst, F., Fischer, M., Jovanovic, J. and Kikura, H. (1998), Investigate low Reynolds number, fully developed turbulent plane channel flows. *Journal of Fluids Engineering, Transactions of the ASME,* Vol. 120, pp. 496-503.

Dvorak, F.A. (1969), Calculation of a turbulent boundary layer on rough surfaces in pressure gradient. *American Institute of Aeronautics and Astronautics Journal,* Vol. 7, pp. 1752-1759.

Edwards, R.V. (1987), Report of the special panel on statistical particle bias problems in laser anemometry. *Journal of Fluids Engineering, Transactions of the ASME,* Vol. 109, pp. 89-93.

Edyvean, R.G.J. (1982). Fouling and Corrosion by Microalgae, *PhD Thesis*, University of Newcastle-upon-Tyne, Newcastle-upon-Tyne.

Egan, B. (1987), Marine microbial adhesion and its consequences. In: *Microbes in the Sea*, M. A. Sleigh (Ed.), Ellis Horwood Ltd.

El-Labbad, A.F. (1987). Techno-economic Analysis of the Problems of the Bottom Maintenance of Ships, *MPhil Thesis*, Marine Technology, University of Newcastle-upon-Tyne, Newcastle-upon-Tyne.

Estarlich, F.F., Lewey, S.A., Nevell, T.G., Thorpe, A.A., Tsibouklis, J. and Upton, A.C. (2000), The surface properties of some silicone and fluorosilicone coating materials immersed in seawater. *Biofouling: the Journal of Bioadhesion and Biofilm Research,* Vol. 6, pp. 263-275.

Evans, S.M., Birchenough, A.C. and Brancato, M.S. (2000), The TBT ban: out of the frying pan into the fire? *Marine Pollution Bulletin,* Vol. 40, pp. 204-211.

Evans, S.M. and Birchenough, A.C. (2000), Imposex in marine snails: what is it and what does it tell us about the health of the marine environment? *ENSUS 2000 international Conference on Marine Science and Technology for Environmental Sustainability,* pp. 104-108. Newcastle-upon-Tyne.

Feiereisen, W.J. and Acharya, M. (1986), Modeling of transition and surface roughness effects in boundary-layer flows. *American Institute of Aeronautics and Astronautics Journal,* Vol. 24, pp. 1642-1649.

Fingerson, L.M. and Menon, R.K. (1998), Laser doppler velocimetry. In: *The Handbook of Fluid Dynamics*, R. W. Johnson (Ed.), CRC Press - Springer**,** Chapter 35.

Fischer, E.C., Castelli, V.J., Rodgers, S.D. and Bleile, H.R. (1984), Technology for control of marine biofouling - a review. In: *Marine Biodeterioration: An Interdisciplinary Study*, J. D. Gostlow and R. C. Tipper (Ed.), Maryland, USA, Naval Institute Press.

Fitzsimmons, P.A. and Ellis, J. (1990), A two-parameter roughness analyser and performance monitoring software. *International Workshop on Marine Roughness and Drag,* Paper No. 4. London, 29 March 1990.

Fletcher, R.L. and Chamberlain, A.H.L. (1975), Marine fouling algae. In: *Microbial Aspects of the Deterioration of Materials*, R. J. Gilbert and D. W. Lovelock (Ed.), pp. 59-81, London, Academic Press Inc.

Forbes, P. (2001), Lotus revolution. *The Guardian,* Wednesday May 2, 2001.

Froude, W. (1872), Experiments on the surface-friction experienced by a plane moving through water. In: *British Association for the Advancement of Science*, In: The Collected Papers of William Froude, Institution of Naval Architects, 1955, pp. 138-146.

Froude, W. (1874), Experiments for the determination of the frictional resistance of water on a surface under various conditions. In: *Report to the Admiralty and British Association for the Advancement of Science* (Ed.), In: Collected Papers of William Froude, Institution of Naval Architects, 1955, London, pp. 345-353.

Froude, W. (1874b), On experiments with H.M.S. Greyhound. *Transactions of the Institution of Naval Architects,* Vol. 15, pp. 36-73.

Furuya, Y., Miyata, M. and Fujita, H. (1976), Turbulent boundary layer and flow resistance on plates roughened by wires. *Journal of Fluids Engineering, Transactions of the ASME,* Vol. 98, pp. 635-644.

Gad-el-Hak, M. (1986), Boundary layer interactions with compliant coatings: an overview. *Applied Mechanics Review,* Vol. 39, pp. 511-523.

Gad-el-Hak, M. and Bandyopadhyay, P.R. (1994), Reynolds number effects in wall-bounded turbulent flows. *Applied Mechanics Review,* Vol. 49, pp. 307-365.

Gad-el-Hak, M. (1996), Compliant coatings: a decade of progress. *Applied Mechanics Review,* Vol. 49, pp. S147-S157.

Gad-el-Hak, M. (1998), Compliant coatings: the simpler alternative. *International Symposium on Seawater Drag Reduction,* pp. 197-204. Newport, Rhode Island.

Gangadharan, S.N., Schultz, M., Collino, B., Clark, A. and Wimberly, C.R. (2001), Experimental investigation of *Enteromorpha clathrata* bioflouling on lifting surfaces of marine vehicles. *Marine Technology,* Vol. 38, pp. 31-50.

Ganti, S. and Bhushan, B. (1995), Generalized fractal analysis and its applications to engineering surfaces. *Wear,* Vol. 180, pp. 17-34.

Gawn, R.W.L. (1942), Roughened hull surface. *Transactions of the North-East Coast Institution of Engineers and Shipbuilders,* Vol. 58, pp. 245-272.

Gawn, R.W.L. (1955), An evaluation of the work of William Froude. In: *The Papers of William Froude*(Ed.), London, The Institution of Naval Architects**,** pp. xv-xxiv.

George, W.K. and Castillo, L. (1997), Zero pressure gradient turbulent boundary layer. *Applied Mechanics Review,* Vol. 50, pp. 689-729.

Graham, D.P. (1947), Use of plastic ship bottom paints. *Transactions of the Society of Naval Architects and Marine Engineers,* Vol. 55, pp. 202-243.

Granville, P.S. (1958), The frictional resistance and turbulent boundary layer of rough surfaces. *Journal of Ship Research,* Vol. 3, pp. 52-74.

Granville, P.S. (1987), Three indirect methods for the drag characterization of arbitrarily rough surfaces on flat plates. *Journal of Ship Research,* Vol. 31, pp. 70-77.

Grass, A.J. (1971), Structural features of turbulent flow over smooth and rough boundaries. *Journal of Fluid Mechanics,* Vol. 50, pp. 233-255.

Grass, A.J., Stuart, R.J. and Mansour-Tehrani, M. (1991), Vortical structures and coherent motion in turbulent flow over smooth and rough boundaries. *Proceedings of the Royal Society of London, A,* Vol. 336, pp. 35-66.

Griffith, J.R. (1985), The fouling release concept: a viable alternative to toxic antifouling coatings? *Polymers in a Marine Environment. The Institute of Marine Engineers,* Paper 38. London.

Griffith, J.R. and Bultman, J.D. (1997), Exterior hull coatings in transition: antifouling paints and fouling release coatings. *Naval Research Reviews,* Vol. 49, pp. 35-38.

Grigson, C.W.B. (1981), The drag coefficients of a range of ship surfaces. *Transactions of the Royal Institution of Naval Architects,* Vol. 123, pp. 195-208.

Grigson, C.W.B. (1982), The drag coefficients of a range of ship surfaces II. *Transactions of the Royal Institution of Naval Architects,* Vol. 124, pp. 183-198.

Grigson, C. (1985), The drag at ship scale of planes having any quality of roughness. *Journal of Ship Research,* Vol. 29, pp. 94-104.

Grigson, C. (1987), The full-scale viscous drag of actual ship surfaces and the effect of quality of roughness on predicted power. *Journal of Ship Research,* Vol. 31, pp. 189-206.

Grigson, C. (1992), Drag losses of new ships caused by hull finish. *Journal of Ship Research,* Vol. 36, pp. 182-196.

Guerrero, A. (2000). Towing tank test with a large friction plate, CEHIPAR, El Pardo, Madrid.

Hama, F.R. (1954), Boundary layer characteristics for smooth and rough surfaces. *Transactions of the Society of Naval Architects and Marine Engineers,* Vol. 62, pp. 333-358.

Hanratty, T.J. and Campbell, J.A. (1996), Measurement of wall shear stress. In: *Fluid Mechanics Measurements (2nd Edition)*, R. J. Goldstein (Ed.), Philadelphia, PA, Taylor & Francis, pp. 575-648.

Hearn, G.E. and Metcalfe, A.V. (1995). *Spectral Analysis in Engineering. Concepts and Cases*. London, Arnold. 307 pages.

Himeno, Y. and Noudo, H. (1988), Effect of wavy roughness on wall turbulence damping. *Journal of the Kansai Society of Naval Architects,* Vol. 209, pp. 37-46.

Hinze, J.O. (1975). *Turbulence*. New York, McGraw-Hill.

Holzapfel, A.C.A. (1904), Ships' Composition. *Transactions of the Institution of Naval Architects,* Vol. 46, pp. 252-272.

Hughes, G. and Allan, J.F. (1951), Turbulence stimulation on ship models. *Transactions of the Society of Naval Architects and Marine Engineers,* Vol. 59, pp. 281-314.

Hunter, J.E. and Cain, P. (1996), Antifouling coatings in the 1990s - environmental, economic and legislative aspects. *IMAS 96 Shipping and the Environment: Is Compromise Inevitable?* Paper 16. London.

Hussain, A.K.M.F. (1986), Coherent structures and turbulence. *Journal of Fluid Mechanics,* Vol. 173, pp. 303-356.

I.T.T.C. (1990), *Proceedings of the 19th International Towing Tank Conference, Report of the Powering Performance Committee,* pp. 235-287. Madrid, Spain, 16-22 September 1990.

IMO (2001). IMO adopts Convention on Control of Harmful Anti-fouling Systems on Ships, *Briefing 27/2001,* International Maritime Organization, London, http://www.imo.org.

Johansson, L.-E. (1985), The local effect of hull roughness on skin friction calculation based on floating element data and three-dimensional boundary layer theory. *Transactions of the Royal Institution of Naval Architects,* Vol. 127, pp. 187-201.

Kan, S., Shiba, H., Tsuchida, K. and Yokoo, K. (1958), Effect of fouling of a ship's hull and propeller upon propulsive performance. *International Shipbuilding Progress,* Vol. 5, pp. 15-34.

Karlsson, R.I. (1978), The effect of irregular surface roughness on the frictional resistance of ships. *International Symposium on Ship Viscous Resistance,* Paper 9. Göteburg.

Kim, H.T., Kline, S.J. and Reynolds, W.C. (1971), The production of turbulence near a smooth wall in a turbulent boundary layer. *Journal of Fluid Mechanics,* Vol. 50, pp. 133-160.

Kim, S.Y. and Lewkowicz, A.K. (1992), Computation of the surface roughness effects on a slender ship-hull. *International Shipbuilding Progress,* Vol. 39, pp. 5-18.

Klebanoff, P.S. (1955). Characteristics of turbulence in a boundary layer with zero pressure gradient, *NACA Report No. 1247*, National Advisory Committee for Aeronautics.

Kohl, J.G. and Singer, I.L. (1999), Pull-off behavior of epoxy bonded to silicone duplex coatings. *Progress in Organic Coatings,* Vol. 36, pp. 15-20.

Kovach, B.S. and Swain, G.F. (1998), A boat mounted foil to measure the drag properties of antifouling coatings applied to static immersion panels. *Proceedings of the International Symposium on Seawater Drag Reduction,* pp. 169-173. Newport, Rhode Island, July 22-24.

Kramer, M.O. (1957), Boundary-layer stabilization by distributed damping. *Journal of the Aeronautical Sciences,* Vol. 24, pp. 459-460.

Kramer, M.O. (1960), Boundary layer stabilization by distributed damping. *Journal of the American Society of Naval Engineers,* Vol. 72, pp. 25-33.

Kramer, M.O. (1961), The dolphin's secret. *Naval Engineer Journal,* Vol. 73, pp. 103-107.

Kramer, M.O. (1962), Boundary layer stabilization by distributed damping. *Naval Engineers Journal,* Vol. 74, pp. 341-348.

Krogstad, P.-A., Antonia, R.A. and Browne, L.W.B. (1992), Comparison between rough- and smooth-wall turbulent boundary layers. *Journal of Fluid Mechanics,* Vol. 245, pp. 599-617.

Krogstad, P.-A. and Antonia, R.A. (1994), Structure of turbulent boundary layers on smooth and rough walls. *Journal of Fluid Mechanics,* Vol. 277, pp. 1-21.

Krstajic, N., Jovic, V.D., Bilen, B. and Nikolic, Z. (1992), An attempt for providing simultaneous cathodic protection and antifouling of ships in sea water. *International Shipbuilding Progress,* Vol. 39, pp. 279-285.

Kutlar, A.I. and Lewkowicz, A.K. (1990), Investigation of the effect of a paint coat on the turbulence near a rough flat plate. *Marine Roughness and Drag Workshop,* Paper 6. London,

Lackenby, H. (1955), B.S.R.A. resistance experiments on the Lucy Ashton. Part III. The ship-model correlation for the shaft-appendage conditions. *Transactions of the Institution of Naval Architects,* Vol. 97, pp. 109-166.

Lackenby, H. (1962), Resistance of ships with special reference to skin friction and hull surface condition. The 34th Thomas Lowe Gray Lecture. *Proceedings of the Institute of Mechanical Engineers,* Vol. 176, pp. 981-1014.

Lamble, J.H. (1936), On the effects of changes in 'degree of wetting' and 'degree of turbulence' on skin frictional resistance and wake of models. *Transactions of the Institution of Naval Architects,* Vol. 78, pp. 125-136.

Leer-Andersen, M. (1999). Two Studies of Ship Flows : A. Skin Friction Measurements on Fouled and Structured surfaces, *Licentiate of Engineering*, Department of Naval Architecture and Ocean Engineering, Chalmers University of Technology, Gothenburg.

Lewes, V.B. (1889), The corrosion and fouling of steel and iron. *Transactions of the Institution of Naval Architects,* Vol. 30, pp. 362-389.

Lewis, M.J. (1975), An elementary analysis for predicting the momentum and heat transfer characteristics of a hydraulically rough surface. *Journal of Heat Transfer,* Vol. 97, pp. 249-254.

Lewkowicz, A.K. and Musker, A.J. (1978), The surface roughness and turbulent wall friction on ship hulls: interaction in the viscous sublayer. *International Symposium on Ship Viscous Resistance,* Paper 10. Göteburg.

Lewthwaite, J.C., Molland, A.F. and Thomas, K.W. (1985), An investigation into the variation of ship skin frictional resistance with fouling. *Transactions of the Royal Institution of Naval Architects,* Vol. 127, pp. 269-284.

Liepmann, H.W. and Goddard, F.E. (1957), Note on the Mach number effect upon the skin friction of rough surfaces. *Journal of the Aeronautical Sciences,* Vol. 24, p. 784.

Ligrani, P.M., Moffat, R.J. and Kays, W.M. (1983), Artificially thickened turbulent boundary layers for studying heat transfer and skin friction on rough surfaces. *Journal of Fluids Engineering, Transactions of the ASME,* Vol. 105, pp. 146-153.

Ligrani, P.M. and Moffat, R.J. (1986), Structure of transitionally rough and fully rough turbulent boundary layers. *Journal of Fluid Mechanics,* Vol. 162, pp. 69-98.

Loeb, G.I., Laster, D. and Gracik, T. (1984), The influence of microbial fouling films on hydrodynamic drag of rotating disks. In: *Marine Biodeterioration: An Interdisciplinary Study*, J. D. Gostlow and R. C. Tipper (Ed.), Maryland, USA, Naval Institute Press.

Longuet-Higgins, M.S. (1957), Statistical properties of an isotropic random surface. *Philosophical Transactions of the Royal Society A,* Vol. 250, pp. 157-174.

Majumdar, A. and Bhushan, B. (1990), Role of fractal geometry in roughness characterization and contact mechanics of surfaces. *Journal of Tribology,* Vol. 112, pp. 205-216.

Mallet, R. (1872), On the corrosion and fouling of iron ships. *Transactions of the Institution of Naval Architects,* Vol. 13, pp. 90-162.

Mandelbrot, B.B. (1967), How long is the coast of Britain? Statistical self-similarity and the Fractional Dimension. *Science,* Vol. 156, pp. 636-638.

Manen, J.D.v. and Oossanen, P.v. (1988), Resistance. In: *Principles of Naval Architecture, Second Revision*, E. V. Lewis (Ed.), S.N.A.M.E., Vol. 2**,** Chapter 5, p. 58.

Mason, R.L., Gunst, R.F. and Hess, J.L. (1989). *Statistical Design and Analysis of Experiments with Applications to Engineering and Science*. New York, Wiley.

Matias, J.R. (2001), Novel, ecologically safe and economically viable natural alternatives to Tributyl Tin. *Proceedings of AddCoat 2001 Conference Paint Research Association,* Orlando, Fla., 29-31 January 2001, http://www.poseidonsciences.com/.

McEntee, W. (1915), Variation of frictional resistance of ships with condition of wetted surface. *Transactions of the Society of Naval Architects and Marine Engineers,* Vol. 24, pp. 37-42.

McLaughlin, D.K. and Tiederman, W.G. (1973), Biasing correction for individual realisation of laser anemometer measurements in turbulent flows. *Physics of Fluids,* Vol. 16, pp. 2082-2088.

Medhurst, J.S. (1989). The Systematic Measurement and Correlation of the Frictional Resistance and Topography of Ship Hull Coatings, with Particular Reference to Ablative Antifoulings, *PhD Thesis*, Marine Technology, University of Newcastle-upon-Tyne, Newcastle-upon-Tyne.

Medhurst, J.S. (1990), Outline of a draft international standard for the measurement and characterisation of roughness topography in fluid flow. *Marine Roughness and Drag Workshop,* Paper 11. London.

Meng, J.C.S. (1998), Engineering insight of near-wall microturbulence for drag reduction and derivation of a design map for seawater electromagnetic turbulence control. *International Symposium on Seawater Drag Reduction,* pp. 359-367. Newport, Rhode Island, July, 22-24.

MER (1999), The cost of TBT-contaminated waste disposal. *Marine Engineers Review,* July/August 1999, pp. 22-24.

MER (2001), Antifouling cover-up. *Marine Engineers Review,* June 2001, pp. 12-15.

Meyer, A.E., Baier, R.E. and King, R.W. (1988), Initial fouling of nontoxic coatings in fresh, brackish and sea water. *The Canadian Journal of Chemical Engineering,* Vol. 66, pp. 55-62.

Millett, J. and Anderson, C.D. (1997), Fighting fast ferry fouling. *Fast '97, Conference Papers,* Vol. 1, pp. 493-495.

Millikan, C.B. (1939), A critical discussion of turbulent flows in channels and circular tubes. *Proceedings of the 5th International Congress for Applied Mechanics,* pp. 386-392.

Milne, A. (1982). On the corrosion and fouling of iron ships: 110 years on. Presentation given to the North East Coast Institution of Engineers and Shipbuilders, Junior Section, *Unpublished Transcript*, Newcastle-upon-Tyne, 11th March 1982.

Milne, A. and Callow, M.E. (1985), Non-biocidal antifouling processes. *Polymers in a Marine Environmnet. The Institute of Marine Engineers,* Paper 37. London.

Milne, A. (1990), Roughness and drag from the marine paint chemist's viewpoint. *Marine Roughness and Drag Workshop,* Paper 12. London.

Milne, A. (1991), Ablation and after: the law and the profits. *Polymers in a Marine Environment. The Institute of Marine Engineers Third International Conference,* Paper 17. London.

Monin, A.S. and Yaglom, A.M. (1971). *Statistical Fluid Mechanics: Mechanics of Turbulence*. Cambridge, Massachusetts, MIT Press. Volume 1.

Morison, S.E. (1942). *Admiral of the Ocean Sea*, Oxford University Press. 680 pages.

Mosaad, M.A. (1986). Marine Propeller Roughness Penalties, *PhD Thesis*, Department of Marine Technology, University of Newcastle-upon-Tyne, Newcastle-upon-Tyne.

Mosaad, M.A. (1990), Experiments and applications on the effects of propeller surface roughness. *Marine Roughness and Drag Workshop,* Paper 2. London.

Musker, A.J. (1977). Turbulent shear flows near irregularly rough surfaces with particular reference to ships' hulls, *PhD Thesis*, University of Liverpool, Liverpool.

Musker, A.J. and Lewkowicz, A.K. (1978), The effect of ship hull roughness on the development of turbulent boundary layers. *International Symposium on Ship Viscous Resistance,* Paper 11. Göteburg.

Musker, A.J. and Sarabchi, K. (1980), Wall-friction and profilometry aspects of coating an irregularly rough surface. *International Shipbuilding Progress,* Vol. 27, pp. 30-35.

Musker, A.J. (1990), Turbulence measurements in a shear-layer associated with a ship-hull roughness. *International Workshop on Marine Roughness and Drag,* Paper 10. London, 29 March 1990.

Musker, A.J. (1991), The hull roughness problem. *Dynamics of Marine Vehicles and Structures in Waves,* pp. 93-108. Uxbridge, UK, 24-27 June 1990.

Nakato, M., Onogi, H., Himeno, Y., Tanaka, I. and Suzuki, T. (1985), Resistance increase due to surface roughness. *Naval Hydrodynamics: 15th Symposium,* pp. 553-568. Hamburg, 2-7 September.

Neinhuis, C. and Barthlott, W. (1997), Characterization and distribution of water-repellent, self-cleaning plant surfaces. *Annals of Botany,* Vol. 79, pp. 667-677.

Nicolleau, F. (1996), Numerical determination of turbulent fractal dimensions. *Physics of Fluids,* Vol. 8, pp. 2661-2670.

Nieuwstadt, F.T.M., Hoeven, J.G.T.v.d., Leijdens, H. and Krishna Prasad, K. (1989), Some experiments on riblet surfaces in a towing tank. In: *Drag Reduction in Fluid Flows: Techniques for Friction Control*, Sellin and Moses (Ed.), pp. 85-92, Ellis Horwood Ltd.

Nieuwstadt, F.T.M., Wolthers, W., Leijdens, H., Prasad, K.K. and Manen, A.D.S.-v. (1991), Some further experiments on riblet surfaces in a towing tank. In: *Recent Developments in Turbulence Management*, K.-S. Choi (Ed.), pp. 113-123, Dordrecht, Kluwer.

Nikuradse, J. (1933). The laws of flows in rough pipes. Translated in: *NACA TM 1291*, National Advisory Committee for Aeronautics.

Nygren, C. (2001), Experience with TBT-free antifouling paint. *Consolidation of Technical Advances in the Protective and Marine Coatings Industry; Proceedings of the PCE 2001 Conference,* pp. 343-354. Antwerp, Belgium, 27-29 March 2001.

Osaka, H. and Mochizuki, S. (1991), Turbulent drag reduction of a d-type rough wall boundary layer with longitudinal ribs placed within the traverse grooves. In: *Recent developments in turbulence management*, K.-S. Choi (Ed.), Kluwer Academic Publishers**,** pp. 163-180.

Patel, V.C. (1998), Perspective: flow at high reynolds number and over rough surfaces - Achilles heel of CFD. *Journal of Fluids Engineering, Transactions of the ASME,* Vol. 120, pp. 434-444.

Pazouki, K. (2001). The ban on TBT-SPC and its alternatives; their characteristics on surface roughness and drag, *MSc Dissertation*, Department of Marine Technology, University of Newcastle-upon-Tyne, Newcastle-upon-Tyne.

Perry, A.E. and Joubert, P.N. (1963), Rough wall boundary layers in adverse pressure gradients. *Journal of Fluid Mechanics,* Vol. 17, pp. 193-211.

Perry, A.E., Schofield, W.H. and Joubert, P.N. (1969), Rough wall turbulent boundary layers. *Journal of Fluid Mechanics,* Vol. 37, pp. 383-413.

Perry, A.E., Lim, K.L. and Henbest, S.M. (1987), An experimental study of the turbulence structure in smooth- and rough-wall boundary layers. *Journal of Fluid Mechanics,* Vol. 177, pp. 437-466.

Perry, A.E. and Li, J.D. (1990), The attached-eddy hypothesis in turbulent boundary layers. *Journal of Fluid Mechanics,* Vol. 218, pp. 405-438.

Perry, A.E., Hafez, S. and Chong, M.S. (2001), A possible reinterpretation of the Princeton superpipe data. *Journal of Fluid Mechanics,* Vol. 439, pp. 395-401.

Raupach, M.R., Antonia, R.A. and Rajagopalan, S. (1991), Rough-wall turbulent boundary layers. *Applied Mechanics Review,* Vol. 44, pp. 1-25.

Reynolds, A.J. (1974). *Turbulent Flows in Engineering*. London, John Wiley & Sons.

Robinson, S.K. (1991), Coherent motions in the turbulent boundary layer. *Annual Review of Fluid Mechanics,* Vol. 23, pp. 601-639.

Sakamoto, S., Takemoto, I., Wakabayashi, H., Milne, A. and Lenny, P. (1983), Ship roughness, new and in-service, and the role of Self-Polishing antifoulings. *PRADS '83 - Proceedings of the second International Symposium on Practical Design in Shipbuilding,* pp. 265-274. Tokyo and Seoul.

Sasajima, H., Terao, T., Yoko, K., Nakato, M. and A.Ogawa (1965), Experimental investigation into roughness of hull surface and increase of skin friction resistance. *Journal of the Society of Naval Architects of Japan,* Vol. 117, pp. 58-71 (in Japanese).

Sasajima, H. and Himeno, Y. (1965), Scale correction for roughness effect. *Journal of the Society of Naval Architects of Japan,* Vol. 118, pp. 66-70 (in Japanese).

Sayles, R.S. and Thomas, T.R. (1978), Surface topography as a nonstationary random process. *Nature,* Vol. 271, pp. 431-434.

Schetz, J.A. (1993). *Boundary Layer Analysis*. New Jersey, Prentice-Hall Inc.

Schlichting, H. (1979 (reprint 1987)). *Boundary-layer Theory*, McGraw-Hill.

Schoenherr, K.E. (1932), Resistance of flat surfaces moving through a fluid. *Transactions of the Society of Naval Architects and Marine Engineers,* Vol. 40, pp. 279-312.

Schultz, M.P. and Swain, G.F. (1998), The effects of biofilms on turbulent boundary layer structure. *Proceedings of the International Symposium on Seawater Drag Reduction,* pp. 175-181. Newport, Rhode Island, July 22-24.

Schultz, M.P. (1998). The Effect of Biofilms on Turbulent Boundary Layers, *DPhil Thesis*, Florida Institute of Technology, Melbourne, Florida.

Schultz, M.P., Kavanagh, C.J. and Swain, G.W. (1999), Hydrodynamic forces on barnacles: implications on detachment from fouling-release surfaces. *Biofouling,* Vol. 13, pp. 323-335.

Schultz, M.P. and Swain, G.W. (1999), The effect of biofilms on turbulent boundary layers. *Journal of Fluids Engineering, Transactions of the ASME,* Vol. 121, pp. 44-51.

Schultz, M.P. and Swain, G.W. (2000), The influence of biofilms on skin friction drag. *Biofouling,* Vol. 15, pp. 129-139.

Schultz, M.P. (2000), Turbulent boundary layers on surfaces covered with filamentous algae. *Journal of Fluids Engineering, Transactions of the ASME,* Vol. 122, pp. 357-362.

Semenov, B.N. (1972). Interaction of an elastic boundary with the viscous sublayer of a turbulent boundary layer, *NASA-TT-F-14391 (translation from Russian by Translation Consultants Ltd.).*

Semenov, B.N. (1996), Analysis of four types of viscoelastic materials for turbulent drag reduction. In: *Emerging Techniques in Drag Reduction*, K.-S. Choi, K. K. Prasad and T. V. Truong (Ed.), pp. 187-206, London, Mechanical Engineering Publications Ltd.

SHIPFLOW (1999). *Training Course Syllabus*. Gothenburg, Sweden, Flowtech International AB.

Sigal, A. and Danberg, J.E. (1990), New correlation of roughness density effect on the turbulent boundary layer. *American Institute of Aeronautics and Astronautics Journal,* Vol. 28, pp. 554-556.

Simpson, R.L. (1973), A generalized correlation of roughness density effect on the turbulent boundary layer. *American Institute of Aeronautics and Astronautics Journal,* Vol. 11, pp. 242-244.

Singer, I.L., Kohl, J.G. and Patterson, M. (2000), Mechanical aspects of silicone coatings for hard foulant control. *Biofouling,* Vol. 6, pp. 301-309.

Sirovich, L. and Karlsson, S. (1997), Turbulent drag reduction by passive means. *Nature,* Vol. 388, pp. 753-755.

Smith, S.L. (1955), BSRA resistance experiments on the *Lucy Ashton.* Part IV. Miscellaneous investigations and general appraisal. *Transactions of the Institution of Naval Architects,* Vol. 97, pp. 525-548.

Spalding, D.B. (1961), A single formula for the 'law of the wall'. *Journal of Applied Mechanics, Transactions of the ASME Series E,* Vol. 28, pp. 455-458.

Sreenivasan, K.R. and Meneveau, C. (1986), The fractal facets of turbulence. *Journal of Fluid Mechanics,* Vol. 173, pp. 357-386.

Stemp, W.J. and Stemp, M. (2001), UBM laser profilometry and lithic use-wear analysis: a variable length scale investigation of surface topography. *Journal of Archaeological Science,* Vol. 28, pp. 81-88.

Stevens, S.A. (1937), The increase in frictional resistance due to the action of water on bottom paint. *Journal of the American Society of Naval Engineers,* Vol. 49, pp. 585-588.

Stevens, C., Powell, D.E., Mäkelä, P. and Karman, C. (2001), Fate and effects of Polydimethylsiloxane (PDMS) in marine environments. *Marine Pollution Bulletin,* Vol. 42, pp. 536-543.

Strandenes, S.P. (2000), The second order effects on commercial shipping restrictions on the use of TBT. *The Science of the Total Environment,* Vol. 258, pp. 111-117.

Swain, G. (1999), Redefining antifouling coatings. *Journal of Protective Coatings and Linings,* Vol. 16, No. 9, pp. 26-35.

Tachie, M.F., Bergstrom, D.J. and Balachandar, R. (2000), Rough wall turbulent boundary layers in shallow open channel flow. *Journal of Fluids Engineering, Transactions of the ASME,* Vol. 122, pp. 533-541.

Tachie, M.F. (2000). Open channel turbulent boundary layers and wall jets on rough surfaces, *PhD Thesis*, Department of Mechanical Engineering, University of Saskatchewan, Saskatoon.

Taylor, R.P., Coleman, H.W. and Hodge, B.K. (1985), Prediction of turbulent rough-wall skin friction using a discrete element approach. *Journal of Fluids Engineering, Transactions of the ASME,* Vol. 107, pp. 251-257.

Thibaut, T. and Meinesz, A. (2000), Are the Mediterranean ascoglossan molluscs *Oxynoe olivacea* and *Lobiger serradifalci* suitable agents for a biological control against the invading tropical alga *Caulerpa taxifolia*? *Comptes Rendus de l'Académie des Sciences - Series III - Sciences de la Vie,* Vol. 323, pp. 477-488.

Thomas, T.R. (1982). *Rough Surfaces*. London, Longman Group Ltd.

Thomas, T.R. (1999). *Rough Surfaces, Second Edition*. London, Imperial College Press.

Todd, F.H. (1951), Skin friction resistance and the effects of surface roughness. *Transactions of the Society of Naval Architects and Marine Engineers,* Vol. 59, pp. 315-374.

Tokunaga, K. and Baba, E. (1983), Approximate calculation of ship frictional resistance due to surface roughness. *Journal of the Society of Naval Architects of Japan,* Vol. 152, pp. 55-61.

Townsend, A.A. (1956). *The Structure of Turbulent Shear Flow*. Cambridge, Cambridge University Press.

Townsin, R.L., Byrne, D., Milne, A. and Svensen, T. (1980), Speed, power and roughness: the economics of outer bottom maintenance. *Transactions of the Royal Institution of Naval Architects,* Vol. 122, pp. 459-483.

Townsin, R.L., Byrne, D., Svensen, T.E. and Milne, A. (1981), Estimating the technical and economic penalties of hull and propeller roughness. *Transactions of the Society of Naval Architects and Marine Engineers,* Vol. 89, pp. 295-318.

Townsin, R.L., Medhurst, J.S., Hamlin, N.A. and Sedat, B.S. (1984), Progress in calculating the resistance of ships with homogeneous or distributed roughness. *N.E.C.I.E.S. Century Conference on Marine Propulsion,* Paper 6.

Townsin, R.L., Byrne, D., Svensen, T.E. and Milne, A. (1986), Fuel economy due to improvements in ship hull roughness 1976-1986. *International Shipbuilding Progress,* Vol. 33, pp. 127-130.

Townsin, R.L. (1986), Penalties of rough underwater surfaces. *The Motor Ship,* Vol. 66, pp. 46-52.

Townsin, R.L. (1987), Efficient underwater surfaces. *Transactions of the Institute of Marine Engineers,* Vol. 99, Paper 30.

Townsin, R.L. (1990), The ITTC correlation allowance: the evidence re-examined and supplemented. *Marine Roughness and Drag Workshop,* Paper 9. London.

Townsin, R.L. and Dey, S.K. (1990), The correlation of roughness drag with surface characteristics. *Marine Roughness and Drag Workshop,* Paper 8. London.

Trunev, A.P. (1999). *Theory of Turbulence and Model of Turbulence Transport in the Atmospheric Surface Layer*, SRC RAS, Sochi, Russia. 160 pages.

Tsuji, T. and Nakamura, I. (1994), The fractal aspect of an isovelocity set and its relationship to bursting phenomena in the turbulent boundary layer. *Physics of Fluids,* Vol. 6, pp. 3429-3441.

Vincent, H.L. and Bausch, G.G. (1997), Silicon fouling release coatings. *Naval Research Reviews,* Vol. 49, pp. 39-45.

Walderhaug, H. (1986), Paint roughness effects on skin friction. *International Shipbuilding Progress,* Vol. 33, pp. 96-100.

Walsh, M.J. (1990), Riblets. In: *Viscous Drag Reduction in Boundary Layers*, D. M. Bushnell and J. N. Hefner (Ed.), Washington DC, AIAA, 123, pp. 203-261.

Watanabe, S., Nagamatsu, N., Yokoo, K. and Kawakami, Y. (1969), The aumentation in frictional resistance due to slime (B.S.R.A. Translation No. 3454). *Journal of the Kansai Society of Naval Architects,* Vol. 131, pp. 45.

Watanabe, K., Yanuar, Ohkido, K. and Mizunuma, H. (1996), Drag reduction through square and rectangular ducts with highly water-repellent walls. *Proceedings of the ASME Fluids Engineering Division Summer Meeting 1996, Volume 2,* pp. 115-119. San Diego, California.

Watanabe, K., Yanuar and Udagawa, H. (1999), Drag reduction of Newtonian fluid in a circular pipe with a highly water-repellent wall. *Journal of Fluid Mechanics,* Vol. 381, pp. 225-238.

Watermann, B., Daehne, B., Michaelis, H., Sievers, S., Dannenberg, R. and Wiegemann, M. (2001). *Performance of biocide-free antifouling paints. Volume 1: Application of test paints and inspections of 2000*, WWF Germany, Coastal and Marine Division.

West, E.E. (1973). The effect of surface preparation and repainting procedures on the frictional resistance of old ship bottom plates as predicted from NSRDC friction plane model 4125, *Report 4084*, Naval Ship Research and Development Center, Bethesda, Maryland.

White, A.H. (1999). A technical and economic evaluation of two different coating systems on high speed catamarans, *MEng Dissertation*, Department of Marine Technology, University of Newcastle-upon-Tyne, Newcastle-upon-Tyne.

Whitehouse, D.J. (1994). *Handbook of Surface Metrology*. Bristol, Institute of Physics Publishing. 988 pages.

Whitehouse, D.J. (2001), Fractal or fiction. *Wear,* Vol. 249, pp. 345-353.

Williams, H. (1923), Notes on fouling of ships' bottoms and the effect on fuel consumption. *Journal of the American Society of Naval Engineers,* Vol. 35, pp. 357-374.

Woods Hole Oceanographic Institution (WHOI) (1952). *Marine Fouling and its Prevention*. Annapolis, Maryland, US Naval Institute.

Wu, J.-J. (2000), Characterization of fractal surfaces. *Wear,* Vol. 239, pp. 36-47.

Yaglom, A.M. (1979), Similarity laws for constant-pressure and pressure-gradient turbulent wall flows. *Annual Review of Fluid Mechanics,* Vol. 11, pp. 505-540.